

**REAL TIME WATER PIPES
LEAK DETECTION USING
ELECTROMAGNETIC WAVES
FOR THE WATER INDUSTRY**

**BY
JUNG HEAN GOH**



**A thesis submitted in partial fulfillment of the requirements of
Liverpool John Moores University for the degree of
Doctor of Philosophy**

**LIVERPOOL JOHN MOOES UNIVERSITY
UNITED KINGDOM**

MAY 2011

CONTAINS

PULLOUTS

Acknowledgement

I would like to express my sincere gratitude for the friendships and support that has made my time here at Liverpool John Moores University (LJMU) the most rewarding experience. This dissertation would not have been possible without the countless individuals who have both inspired and supported me along the way.

First I would like to give my sincere thanks to my supervisor, Dr. Andrew Shaw and Professor Ahmed I. Al-Shamma'a, both of them have given me the chance to participate in this project. Furthermore, both of them have been an excellent mentor and a constant source of knowledge, motivation, and encouragement throughout my graduate studies. Professor Ahmed I. Al-Shamma'a also has given the lecture about electromagnetic waves propagation and antenna in my MSc studies. My deepest thanks go to my family, who has given me unconditional love, patience, and support throughout the year.

Finally, I also want thanks to the RF and Microwaves research group staffs for their various assistance of the components, measurement equipments and instruments I needed in this project especially Jeff and Steve.

Abstract

This project concerns the use of an electromagnetic sensor for the detection of leaks/cracks in water pipes. As old metal pipes corrode they start to become brittle, resulting in the potential for cracks to appear in the pipes. In addition corrosion can build up resulting in a restricted flow of water in the pipe. Using an electromagnetic (EM) wave sensor to monitor the signal reflected from the pipes in real time, provides the necessary information to determine where a leak in the pipe has occurred. Analysis of the reflected signal can provide the operator with information about the condition and position of a leak within the pipe. This is the first time research has been carried using EM waves for leak detection in water pipelines. This project involves the design and construction of an EM sensor operating at frequencies in the range of 240MHz to 560MHz, and at a power of 0dBm. The sensor is launched into the water pipeline through any existing hydrant and is moved along the pipeline to check for leaks. The simulation software High Frequency Structure Simulator (HFSS) was used to model the pipe section as a circular waveguide cavity, and also for antenna simulation. The monopole and loop antenna were designed to determine the best antenna for this project. The printed circuit board (PCB) design package Eagle was used to provide the surface mount layout for the sensor, and the PCB board was fabricated by using a computer numerical control (CNC) routing machine. Finally the graphical interface package LabVIEW was used to control the frequency sweep for the sensor and to capture the data from the sensor. Based on the findings of this project, the EM wave sensor could be used to determine a leak up to a 0.9 correlation limit using low cost RF electronic devices.

Contents

List of Figures	vii
List of Tables	xiv
List of Acronyms	xv
List of Symbols	xvii
Chapter 1: Introduction	1
1.1 Introduction	1
1.2 Project Aim and Objectives	2
1.3 Current Technology	3
1.4 Electromagnetic Theory for Leak Detection	7
1.5 Project Overview	9
1.6 Research Methodology	10
Chapter 2: Electromagnetic Waves	14
2.1 Electromagnetic Waves	14
2.2 Maxwell's Equations	15
2.3 Electromagnetic Waves Spectrum	18
2.4 Characteristic Impedance of Free Space	20
2.5 Polarisation	20
2.5.1 Linear Polarisation	21
2.5.2 Circular Polarisation	22
2.5.3 Elliptical Polarisation	22
2.6 Transmission Lines	23

2.6.1 Coaxial Cable	24
2.6.2 Microstrip	27
2.7 General Transmission Line Equations	28
2.8 Voltage Standing Wave Ratio (VSWR)	31
2.9 Waveguide	32
2.9.1 Rectangular Waveguide	32
2.9.2 Circular Waveguide	35
2.10 Scattering Parameters (S-Parameters)	38
2.11 Water Pipe as Transmission Line	39
Chapter 3: Antenna	42
3.1 Antenna	42
3.2 Monopole Antenna	43
3.3 Loop Antenna	45
3.4 Microstrip Patch Antenna	47
3.5 Directivity and Gain	48
3.6 Antenna Used for the Project	49
Chapter 4: High Frequency Structure Simulator (HFSS) and LabVIEW	56
4.1 High Frequency Structure Simulator (HFSS)	56
4.1.1 Transverse Electric (TE) and Transverse Magnetic (TM) modes	59
4.1.2 A Simple Monopole Antenna Design	60
4.2 LabVIEW	64
4.2.1 Pearson Correlation	67

4.2.2 LabVIEW Programming	70
4.2.3 LabVIEW Control Systems	72
Chapter 5: Water Pipe Simulations, Experiments and Results	76
5.1 Water Pipe Simulation for Monopole Antenna	76
5.2 Water Pipe Experiment for Monopole Antenna	78
5.3 Water Pipe Simulation for Loop Antenna	80
5.4 Water Pipe Experiment for Loop Antenna	83
5.5 Water Pipe Leak Simulation	85
5.6 Experiments for Leak Detection	88
5.7 Gap Detection	90
Chapter 6: Prototype Demonstrator Design and Construction	94
6.1 90 Degree Bent Loop Antenna	94
6.2 Prototype Demonstrator Design	96
6.3 Prototype Demonstrator Design with Electronics Subsystem	99
6.4 Field Trial at Balfour Beatty Test Facility	102
Chapter 7: PCB Design with Leak Detection Trial	111
7.1 Eagle PCB Design Software	111
7.2 CNC Routing Machine	113
7.3 EM wave Sensor	115
7.4 Experiments for Reference Signal	118
7.5 Experiments for Leak Detection	123
7.6 Location for Leakage	131

Chapter 8: Conclusion	133
10.1 Future Work	136
References	137
Appendix A: Source Code for LabVIEW Programme	
Appendix B: Results for Leak Detection	

List of Figures

Figure 1.1: Flow chart for the project	3
Figure 1.2: Listening stick, (a) stainless steel, (b) wood	4
Figure 1.3: Ground Microphone & Listening Stick, Aquascope 3	5
Figure 1.4: Ground penetrating radar	7
Figure 1.5: Electromagnetic mode patterns in a circular waveguide	8
Figure 1.6: Block diagram of the leak detection system	9
Figure 2.1: Electromagnetic waves propagation in free space	14
Figure 2.2: Gauss's law	16
Figure 2.3: Gauss's law for magnetism	17
Figure 2.4: Ampere's law	17
Figure 2.5: Faraday's law	18
Figure 2.6: Electromagnetic waves spectrum	18
Figure 2.7: Linear polarization	21
Figure 2.8: Circular polarization	22
Figure 2.9: Elliptical polarization	23
Figure 2.10: Transmission line	24
Figure 2.11: Coaxial cable	24
Figure 2.12: Dimension for coaxial cable	25
Figure 2.13: TEM mode in coaxial cable	26
Figure 2.14: Field, charge and current distributions along the coaxial cable	26
Figure 2.15: Microstrip transmission lines	28
Figure 2.16: Equivalent circuit of a transmission line	29
Figure 2.17: Rectangular waveguide	32

Figure 4.6: The variation of the attenuation for the TM_{01} mode in a 4 inch cast iron pipe filled with distilled water	61
Figure 4.7: $ S_{11} $ and $ S_{21} $ signal versus antenna length by HFSS simulation	62
Figure 4.8: Monopole antenna design with dielectric plug by HFSS simulation	63
Figure 4.9: $ S_{11} $ and $ S_{21} $ signal versus antenna length with dielectric plug	63
Figure 4.10: User interface (Front Panel)	65
Figure 4.11: Graphical code (Block Diagram)	66
Figure 4.12: VI icons with connector	66
Figure 4.13: Possible Pearson correlation outputs	68
Figure 4.14: False data created as example with a Pearson correlation of 1 indicating identical shape but with difference amplitude (average) and the red panel indicates inspection required	69
Figure 4.15: False data created as example with identical shape and amplitude therefore panel indicates no further inspection required	69
Figure 4.16: Flow chart for the LabVIEW program for the EM wave sensor	70
Figure 4.17: Front Panel of the LabVIEW program for the EM wave Sensor	71
Figure 4.18: Block diagram of LabVIEW system	73
Figure 4.19: Experimental setup for the LabVIEW system	74
Figure 4.20: Comparison between LabVIEW and the VNA	74
Figure 5.1: HFSS model of 4 inch cast iron pipe with two 50mm monopole antenna	76
Figure 5.2: HFSS simulation result of the reflection signal $ S_{11} $ for the monopole antenna	77
Figure 5.3: HFSS simulation result of the transmission signal $ S_{21} $ for the monopole antenna	77
Figure 5.4: Monopole antenna experiment setup for water pipe	78

Figure 5.5: Reflection signal $ S_{11} $ of experiment and HFSS for monopole antenna	79
Figure 5.6: Transmission signal $ S_{21} $ of experiment and HFSS for monopole antenna	80
Figure 5.7: HFSS model of 4 inch cast iron pipe with two 28mm diameter loop antenna	81
Figure 5.8: HFSS simulation result of the reflection signal $ S_{11} $ for the loop antenna	82
Figure 5.9: HFSS simulation result of the transmission signal $ S_{21} $ for the loop antenna	82
Figure 5.10: Loop antenna experiment setup for water pipe	83
Figure 5.11: Reflection signal $ S_{11} $ of experiment and HFSS for loop antenna	84
Figure 5.12: Transmission signal $ S_{21} $ of experiment and HFSS for loop antenna	85
Figure 5.13: HFSS simulation for water pipe leak	86
Figure 5.14: Reflection signal $ S_{11} $ of HFSS simulation result for water pipe leak	86
Figure 5.15: Transmission signal $ S_{21} $ of HFSS simulation result for water pipe leak	87
Figure 5.16: Expansion of HFSS $ S_{21} $ simulation result for water pipe leak	87
Figure 5.17: Experiment setup for water pipe leak, three pipeline sections, 4 inch diameter pipeline filled with water and with a cut through the central section of the pipe	88
Figure 5.18: Reflection signal $ S_{11} $ versus frequency for water pipe leak	89
Figure 5.19: Transmission signal $ S_{21} $ versus frequency for water pipe leak	90
Figure 5.20: Experiment setup for water pipe gap detection, two pipeline sections of 4 inch diameter filled with water with nylon ring inserts between the pipes	91
Figure 5.21: Reflection signal $ S_{11} $ for gap detection with nylon ring inserted	92

Figure 5.22: Transmission signal $ S_{21} $ for gap detection with nylon ring inserted	92
Figure 6.1: Loop antenna bent to 90 degrees from the axis of the pipe to fit with Balfour Beatty's requirements	94
Figure 6.2: Reflection signal $ S_{11} $ for bent loop antenna with nylon ring inserted	96
Figure 6.3: Setup of industrial prototype with 90 degree bent loop antenna	97
Figure 6.4: Experimental setup to test prototype demonstrator	98
Figure 6.5: Reflection signal $ S_{11} $ for the prototype demonstrator with nylon ring inserted	98
Figure 6.6: Electronics schematics for standalone EM wave sensor	100
Figure 6.7: Four electronic circuit boards assembled for EM wave sensor	100
Figure 6.8: PCB masks for the three main component boards	101
Figure 6.9: Photograph of the RF electronics for the integrated sensor, 25mm in length	101
Figure 6.10: Photograph of the RF electronics being placed into the stainless steel Housing	102
Figure 6.11: Block diagram for the overall length of the pipelines in Balfour Beatty's test facility	103
Figure 6.12: Experimental trial at Balfour Beatty's test facility	104
Figure 6.13: EM wave sensor in Perspex section with power and control cables feeding back to laptop and LabVIEW	104
Figure 6.14: Photograph of markings starting from the reducer	105
Figure 6.15: Photograph of marking ending at the access port	105
Figure 6.16: Results of reducer and start position of EM wave sensor	106
Figure 6.17: Photograph of end of Perspex section and start of straight 4 inch pipeline	107

Figure 6.18: Results of end of Perspex section and start of the straight 4 inch pipeline	107
Figure 6.19: Photograph of EM wave sensor is enter to the 'T' Piece	108
Figure 6.20: Results of EM wave sensor is enter to 'T' piece	108
Figure 6.21: Results of increaser and end position at the access port of EM wave sensor	109
Figure 7.1: Eagle library for the RF components	112
Figure 7.2: Schematic diagram for the integrated sensor	112
Figure 7.3: PCB layout for the integrated sensor	113
Figure 7.4: CNC routing machine	114
Figure 7.5: ABViewer use to open the HPGL/2 file	114
Figure 7.6: PCB board making by CNC routing machine	115
Figure 7.7: PCB circuit board for the sensor created by the CNC routing machine	116
Figure 7.8: Complete PCB circuit board with full components for the sensor	116
Figure 7.9: Block diagram for PCB circuit board sensor	117
Figure 7.10: Experimental setup to obtain the reference signal	118
Figure 7.11: LabVIEW capture the signal from the sensor	119
Figure 7.12: Frequency versus reflection signal $ S_{11} $ from the sensor	120
Figure 7.13: Reference signals from 10cm to 50cm depth in pipeline	121
Figure 7.14: Reference signals from 60cm to 100cm depth in pipeline	122
Figure 7.15: Reference signals from 110cm to 140cm depth in pipeline	122
Figure 7.16: Experimental setup for water pipe leak detection	123
Figure 7.17: Reference $ S_{11} $ plots loaded from database	124
Figure 7.18: $ S_{11} $ waveform compared for 10cm depth in pipeline	125
Figure 7.19: $ S_{11} $ waveform compared for 60cm depth in pipeline	126
Figure 7.20: $ S_{11} $ waveform compared for 70cm depth in pipeline	127

Figure 7.21: $ S_{11} $ waveform compared for 80cm depth in pipeline	128
Figure 7.22: $ S_{11} $ waveform compared for 90cm depth in pipeline	129
Figure 7.23: $ S_{11} $ waveform compared for 140cm depth in pipeline	130
Figure 7.24: Location of the leak on the 4 inch pipeline	131

List of Tables

Table 1.1: Present technology with their attribute	4
Table 2.1: Classification of frequency bands	19
Table 2.2: Values of p'_{nm} for TE modes of a circular waveguide	37
Table 2.3: Values of p_{nm} for TM modes of a circular waveguide	37
Table 4.1: Strength and significance of the correlation coefficient r	68
Table 10.1: Comparison between EM waves sensor and present technology	135

List of Acronyms

ADC	Analog to digital converter
CNC	Computer numerical control
DAC	Digital to analog converter
DAQ	Data acquisition
DSP	Digital signal processing
EM	Electromagnetic
GHz	Gigahertz
HFSS	High Frequency Structure Simulator
KCL	Kirchhoff's Current Law
KVL	Kirchhoff's Voltage Law
LabVIEW	Laboratory Virtual Instrument Engineering Workbench
LJMU	Liverpool John Moores University
MHz	Megahertz
NI	National Instrument
RF	Radio Frequency
PCB	Printed Circuit Board
PEC	Perfect Electrical Conductor
Rx	Receiver
SMA	Sub-Miniature, version A
SMD	Surface mount devices
SMT	Surface mount technology
TE	Transverse Electric
TEM	Transverse Electromagnetic

TM	Transverse Magnetic
TSB	Technology Strategy Board
Tx	Transmitter
VCO	Voltage Control Oscillator
VI	Virtual Instrument
VNA	Vector Network Analyser
VSWR	Voltage Standing Wave Ration

List of Symbols

c	Speed of light, 299792458m/s
ϵ_0	Permittivity, 8.85419×10^{-12} F/m
μ_0	Permeability, $4\pi \times 10^{-7}$ H/m
π	pi, 3.14159
η_0	Characteristic impedance of free space, $\approx 377\Omega$
ϵ_r	Permittivity
μ_r	Permeability
σ	Conductivity
Ω	Ohm
f	Frequency
f_c	Cut-off frequency
λ	Wavelength
η_e	Radiation efficiency factor of the antenna
γ	Propagation constant
α	Attenuation constant
β	Phase constant
ω	Angular frequency
ρ	Electric charges density
p_{nm}	Value of for TM modes
p'_{nm}	Value of for TE modes
B	Magnetic flux density

C	Capacitance
D	Directivity
D_E	Electric flux density
E	Electric field
G	Conductance
G_g	Gain
H	Magnetic field
J	Electric current density
L	Inductance
P_t	Total radiated power
P_{in}	Total input power accepted by the antenna
R	Resistance
U	Radiation intensity of the antenna
U_i	Radiation intensity of an isotropic source
v_p	Phase velocity
z	Distance / Direction of propagation
Z_0	Characteristic impedance
Z_L	Load impedance
$ S_{11} $	Reflected Signal Magnitude
$ S_{21} $	Transmitted Signal Magnitude
Γ	Reflection coefficient
Γ_L	Load reflection coefficient
d	Diameter
e	Exponent

i	Current
n	Number of 'pairs' of data
r	Correlation coefficient
t	Time
v	Voltage
\ln	Logarithm to base e
θ	Theta angle
Σ	Summation

Chapter 1: Introduction

1.1 Introduction

Water is a basic essential for all life on Earth. For humans, water is not only used for drinking, but also for many other parts of our daily life such as cooking, cleaning and for flushing the toilet. Although 70% of the earth is covered with water, only about 2% is fresh water [1]. In the UK, there are many water companies [2] such as United Utilities, Yorkshire Water, South East Water, Essex Water who are responsible for supplying homes and factories with clean fresh water. This is achieved by the use of underground water pipes, some of which have been in the ground for decades and have fractured. In the UK, 70% of water pipes are cast iron, with the other 30% being plastic, Perspex, concrete or some other material. There are a lot of different diameters for the cast iron pipelines including 4 inch, 6 inch and 12 inch. This project only investigated the 4 inch diameter cast iron pipelines which are commonly used for water supplies. However in principle the EM sensor has the capability of detecting pipe defects based upon the operating frequency, this can be see in chapter 7. This is the first time research by using the electromagnetic (EM) waves technique for the leak detection in the water pipelines.

The purpose of this project is to reduce the water loss from public water supply distribution networks by identifying leaks in cast iron pipes. This research has investigated whether EM waves can be used to pinpoint the location of leaks in water pipes by using an internal EM wave sensor. This sensor is launched into the live drinking water mains through any existing hydrant and deployed using a mechanical drive on the launch chamber developed by Balfour Beatty [3]. The EM sensor should be

designed and constructed to meet the needs of the water industry represented by Balfour Beatty as part of an industrial project supported by the Technology Strategy Board (TSB).

1.2 Project Aim and Objectives

The aim of this project is to design, construct and test a sensor system for mains water leak detection in cast iron pipes. The radio frequency (RF) components including the voltage controlled oscillator (VCO), power detector, voltage regulator, directional coupler and voltage amplifier are all to be fitted within the sensor.

The main objectives of this project are to understand current technology techniques that are used for leak detection, and investigate and build a new sensor system by using the RF technique sense a leak in a metallic pipeline. The RF frequencies signal allows transmission of frequencies at Megahertz (MHz) frequency in potable water.

The main factor influencing this research work is that the water industry is continuing to look for a more reliable sensing technology than is currently on the market. Currently, the EM waves technique has not been researched for real time water pipe leak detection systems, so a successful outcome to this project could lead to a patent and a marketable product. The sensor is to be deployed into the pipeline via a pressurised hydrant allowing drinking water to continue to be supplied. This mechanism restricts the overall dimensions of the sensor to 22mm in diameter and a length of not more than 100mm.

Figure 1.1 shows the flow chart for the project. The water pipeline section was treated as a circular cavity. A standalone sensor with an antenna was used to transmit an EM signal, and receive the reflected signal. HFSS was used to determine the transverse

electric (TE) and transverse magnetic (TM) modes, the reflected signal magnitude $|S_{11}|$ and transmitted magnitude signal $|S_{21}|$ for the circular cavity, and then compared these with the experimental results, which were recorded as the sensor was moved along a buried pipeline. All the readings and results that were obtained from the reflected signals were recorded using a LabVIEW program that also processed the data and decided whether a leak is present or not.

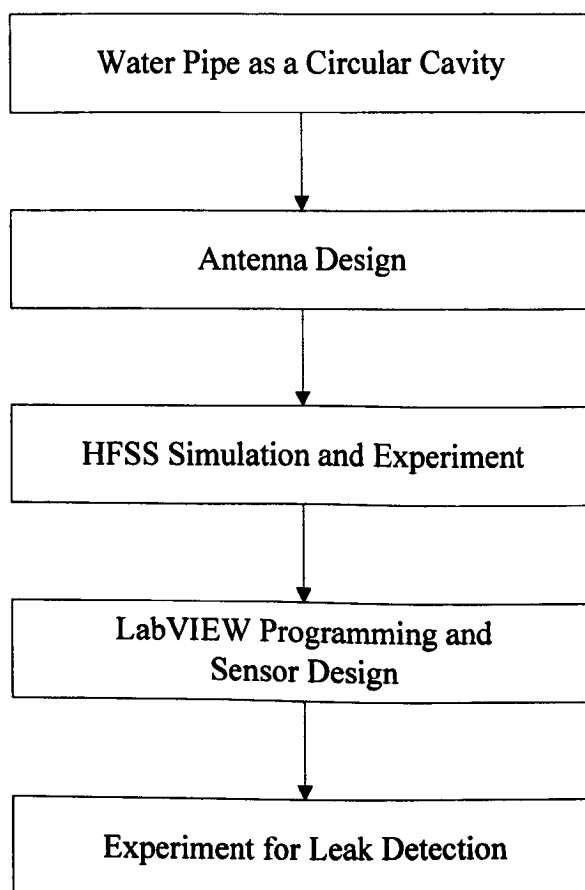


Figure 1.1: Flow chart for the project

1.3 Current Technology

The present technology used in the detection of leaks is a listening stick, ground microphone, acoustic and ground penetrating radar. All of these techniques have their advantages and limitations. Table 1.1 shows the present technology with their attribute.

Table 1.1: Present technology with their attribute

Technology Attribute	Listening Stick	Ground Microphone	Acoustic	Ground Penetrating Radar
Respond Time	Time consuming	Time consuming	Time consuming	DSP analysis take hours to complete
Reliability and Sensitivity	Not very efficient	Not very efficient	Contact point with the water pipeline	Cannot differentiate the buried object
Accuracy	Moderate success	Moderate success	Satisfactory	Over 80% [4]
Cost	Low Cost £25 [5]	Expensive £2500 [6]	Moderate £400 [7]	Very Expensive £8000 [8]

The listening stick [9] is a 1.5m (approximately) long rod made from stainless steel or wood with a 10mm diameter wooden ear piece which is shown in Figure 1.2. This technique allows the engineer to listen for the sound of escaping water from a water distribution system by placing the listening stick on the mains or fittings through the valves or hydrant. The leak noise is transmitted from the fitting to the engineer's ear. This technique is reasonably low cost with a moderate success rate on metallic pipelines but with poor result on non-metallic pipelines. This technique is time consuming and not very efficient for the leak inspection.

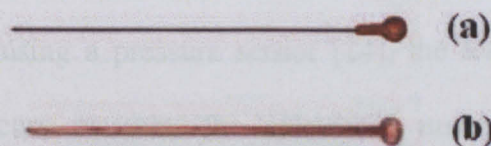


Figure 1.2: Listening stick, (a) stainless steel, (b) wood [5]

The modern versions of the “listening stick” are called ground microphones [10] which as shown in Figure 1.3. These devices are placed on the ground and amplify the sound

produced by a leak to enable easier detection. These devices have many shapes and sizes, but the device known as an ‘elephant’s foot’ is the most popular and are extremely sensitive to identify the strongest leak noise and best leak location.



Figure 1.3: Ground Microphone & Listening Stick, Aquascope 3 [11]

The acoustic [12,13] techniques are the most widely used in leak detection. They are based on the continuous analysis of the pipeline pressure, flow, temperature and density. The acoustic sensors are always placed either side of the leak at convenient access points for example hydrants to determine the leak these variables need to be known, but the wave speed for this technique is difficult to measure due to the material properties of the pipe are dependent upon temperature, so the wave speed can change from day to day. Another example is by using a pressure sensor [14], the leak is suspected when the discrepancy pattern occurs between the calculated numerical model results and measured real time values of pressure and flow at pipe ends, this is depends on its inherent thresholds and exposed a high number of failure in accuracy availability.

The acoustic failed to perform optimally within the criteria of response time, robustness, reliability, sensitivity, accuracy and cost [15]. Acoustics in water are characterized by relatively low frequencies which are limited by attenuation and a relatively slow speed of the propagation. The three primary mechanisms which attenuate acoustic signals in water are [16,17]:

- Spreading loss: occurs when the transmitted signal expands across a larger surface area as the signal propagates away from the source.
- Absorption loss: occurs because of the conversion of the energy in the propagating signal into heat, the absorption loss of signals is strongly frequency dependent and increases with frequency.
- Scattering loss: occurs when the transmission power is lost due to reflections from suspended particles in the medium.

Ground penetrating radar [18,19,20] uses low frequency EM waves to create an image of the subsurface by detecting the reflected signals from subsurface structures which as shown in Figure 1.4. It transmits the EM wave into the ground, and when the wave hits a buried object, the receiving antenna records a reflected signal. The ground penetrating radar generally operates with frequencies between 10MHz and 1000MHz [21]. The lower frequencies have longer wavelengths which are able to penetrate to a greater depth but provide lower resolution, allowing large size objects to be detected. Shorter wavelengths enable less penetration but provide higher resolution, allowing smaller size object to be detected [22]. The ground penetrating radar technique cannot differentiate whether the buried object is water, gas or oil pipeline and the digital signal processing (DSP) [23] analysis required takes hours to complete. The water companies therefore still require a quick, cost justified, large scale method of identifying areas of actual leakage.

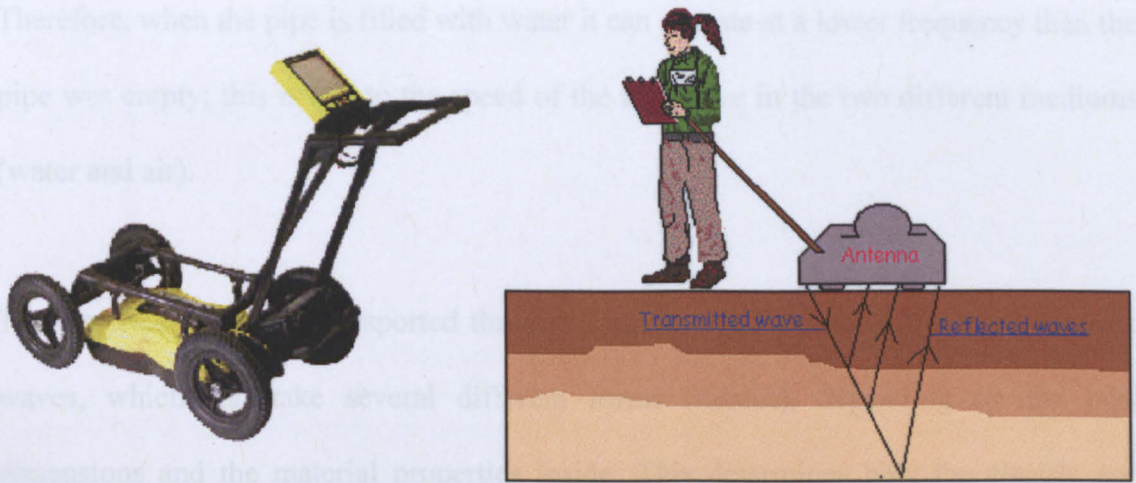


Figure 1.4: Ground penetrating radar [24,25]

Due to the limitation of the present technology this thesis outlines a new technique of using electromagnetic wave propagation within the pipeline to detect defect at the pipeline structure.

1.4 Electromagnetic Theory for Leak Detection

Water is transported in cylindrical metal pipes. The metal pipe (cast iron with concrete lining) can be treated as a circular waveguide which is a particular form of electrical transmission line that is generally used at microwave frequencies. The speed of an EM wave travels in vacuum at $3 \times 10^8 \text{ m/s}$, which is speed of light (c). The speed of an EM wave is reduced by a factor $\sqrt{\epsilon_r \mu_r}$ when it travels through a material (medium), where ϵ_r is the relative permittivity, and μ_r is the relative permeability of the material. The value of ϵ_r for the water at the frequencies considered is approximately 81 at temperature around 20°C [26], μ_r is 1, therefore, the speed of the EM wave in water is, given by 1.1.

$$c_{\text{water}} = \frac{c_{\text{vacuum}}}{\sqrt{\epsilon_r \mu_r}} = \frac{3 \times 10^8}{\sqrt{81 \times 1}} = 3.33 \times 10^7 \text{ m/s} \quad (1.1)$$

Therefore, when the pipe is filled with water it can operate at a lower frequency than the pipe was empty; this is due to the speed of the EM wave in the two different mediums (water and air).

1.5 Project Overview

The electrical power is transported through a metal pipe by means of electromagnetic waves, which can take several different forms (modes), depending on the pipe dimensions and the material properties inside. This determines how the electric and magnetic fields appear in the pipeline and hence the operational frequency. The solid line in Figure 1.5 represents electric field and the dotted line represents magnetic field of the EM wave signal.

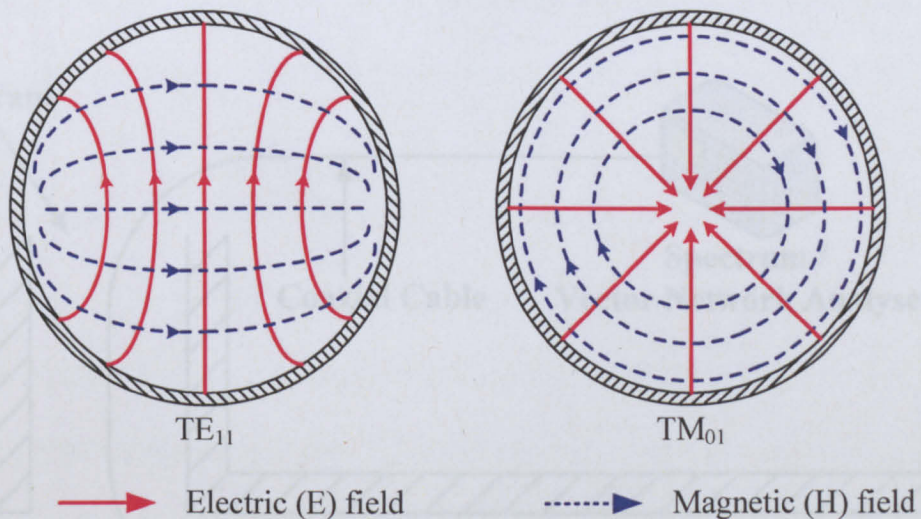


Figure 1.5: Electromagnetic mode patterns in a circular waveguide [27]

The two most important modes in the circular waveguide are known as TE_{11} (Transverse Electric) and the TM_{01} (Transverse Magnetic) modes. For a typical 4 inch metal pipe, the so called cut off frequencies below which there is no propagation is 192MHz for the TE_{11} mode and 251MHz for the TM_{01} mode. Consequently, between

192MHz and 251MHz, only the TE_{11} mode can propagate. These modes and the cut off frequencies for the 4 inch pipeline will be discussed in more detail in chapter 2.

1.5 Project Overview

The electromagnetic wave propagation method is applied and used for transmission purposes in water. It is necessary to transmit a high frequency carrier between 240MHz to 560MHz, and use the reflection signal $|S_{11}|$ to decide which water pipeline needs further investigation. The frequency range for this system will be discussed in more detail in chapter 5 and 6. Figure 1.6 shows the block diagram of the leak detection system. The EM wave sensor in cylinder form is put into the buried 4 inch pipeline through the hydrant.

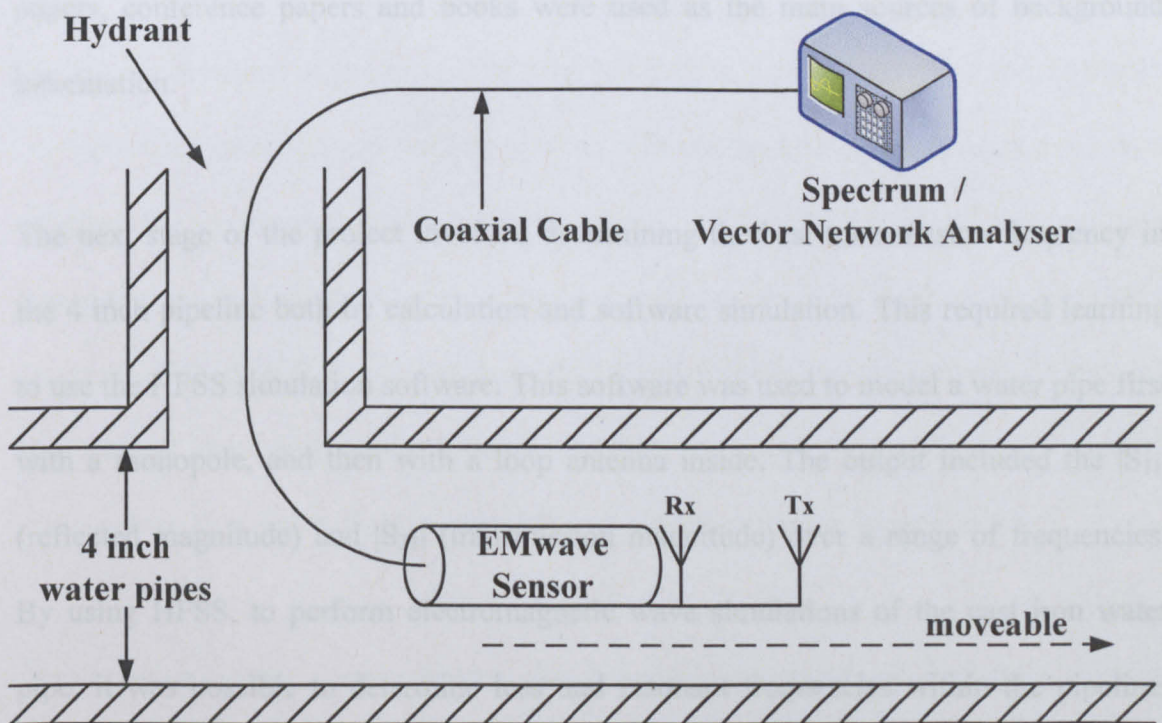


Figure 1.6: Block diagram of the leak detection system

The RF frequency sweeps from 240MHz to 560MHz using an RF integrated circuit. Then the frequency is transmitted to the water through the transmitter (Tx) and the signal is received by the receiver (Rx), and the separation between the transmitter and receiver should be at least 100mm based upon the industrial requirement. The sensor is moved along the pipeline, using the carbon fibre push rod detecting the pipe wall as it goes along. The spectrums for the reflection magnitude $|S_{11}|$ and transmission magnitude $|S_{21}|$ are measured by using a Vector Network Analyser (VNA) via the coaxial cable link from the sensor.

1.6 Research Methodology

A literature review was carried out to understand the existing technologies for pipeline leak detection as well as for EM theory, including waveguides and antennas. Journal papers, conference papers and books were used as the main sources of background information.

The next stage of the project involved determining the best transmission frequency in the 4 inch pipeline both by calculation and software simulation. This required learning to use the HFSS simulation software. This software was used to model a water pipe first with a monopole, and then with a loop antenna inside. The output included the $|S_{11}|$ (reflected magnitude) and $|S_{21}|$ (transmission magnitude) over a range of frequencies. By using HFSS, to perform electromagnetic wave simulations of the cast iron water pipe, it was possible to determine loss and resonant frequencies within the pipeline. Leaks were also simulated and the results were compared between the leak and non-leak conditions. HFSS was also used to find the best length for the monopole antenna.

The was followed by a comprehensive set of experiments to identify the resonant frequencies of the cast iron pipes filled with water and to determine suitable frequency sources, transmitter and receiver systems. This data was then compared with the HFSS simulation result. It was important to characterise the EM fields modes generated within the frequency range and determine which were best suited to act as the reference point for the leak detection.

The next step was to set up a laboratory test system with leak detection (predrilled holes) to identify the signal spectrum experimentally. It was necessary to design and construct a transmitter and receiver system to fit inside the pipeline and operate when the water was flowing past. This involved optimizing parameters including transmitter and receiver sizes, materials and power electronics.

For the construction of the prototype demonstrator, it was necessary for the sensor to have its own transmitter and receiver circuits with onboard processing power in a single housing. The system was linked to outside world by a coaxial cable and interfaced to a laptop running LabVIEW software from National Instrument (NI) to display the signal spectrum. The LabVIEW program was used to monitor the signal spectrum through the NI Compaq Data Acquisition (DAQ). The Pearson correlation method was used to compare two data sets and make a decision on whether a leak is present or not.

The laboratory testing took place at the RF and Microwave lab in LJMU. A loop antenna was used with an electronic circuit to sweep frequencies in the 240MHz to 560MHz range. This frequency range was the best for the 90 degree bent loop antenna as will be discussed in chapter 6. Another reason for using this range is that the components for MHz frequencies is always cheaper than the gigahertz (GHz) range.

Variations in the frequency response of the reflection from the pipeline were then compared to the proximity of a fault.

The next stage was an the industrial trial and the preliminary system evaluation that took place at Balfour Beatty in Derby, where they have a full scale industrial test rig. This required the PCB circuit board on to which all of the electronic components were connected to be no large than 65mm (length) \times 20mm (width).

The new PCB board for the sensor was used for final trials to prove that the system was operational in an industrial environment. This project required that the data from the EM wave sensor at a certain position along the pipeline, be compared with data from a pipeline with no leaks. The Pearson correlation theory played a major role in this experiment. This will be discussed in chapter 4. All the readings were displayed and recorded using LabVIEW. The LabVIEW programme performed the analysis and gave a recommendation based on the result obtained. This will be discussed in chapters 7. The EM wave sensor was used for the final test for leak detection. The LabVIEW program was used to monitoring how the microwave spectrum changed at a leak. Finally, the conclusion for whole thesis was written.

Summary

The present technology for leak detection such as acoustic and ground penetrating radar techniques have limitations. Therefore, an EM waves technique was undertaken to propagate inside the water pipeline. This method has not been used in any previous research. The main idea of this research project was to investigate the effectiveness of an EM wave leak detection sensor, for locating leaks in 4 inch metallic pipelines. This work also included the characterisation of leak signals in cast iron pipes, identification

of necessary improvements to existing sensor and methods, and evaluation of the potential technologies for the industry. The smaller and unique sensor was designed and put into the buried pipeline through a hydrant and the leak could be monitored and detected in real time. The project also involved extensive field tests that were carried out under controlled conditions at a specially constructed experimental leak detection facility at Balfour Beatty. The EM characteristics of leak signals were investigated, these included frequency content and attenuation rate. The experimental test for leaks signals were measured in the RF and Microwave research group laboratory at LJMU. Finally, the potential for locating leaks using alternative EM waves technology was evaluated.

Chapter 2: Electromagnetic Waves

2.1 Electromagnetic Waves

Electromagnetic (EM) waves [28,29] are waves of energy that travel through the vacuum at the speed of light, approximately $c=3 \times 10^8$ m/s. EM waves consist of two primary components, an electric (E) field and a magnetic (H) field. The electric field and magnetic field oscillate in phase perpendicular to each other and perpendicular to the direction of energy propagation (z) as shown in Figure 2.1. This is known as a Transverse Electromagnetic (TEM) Wave.

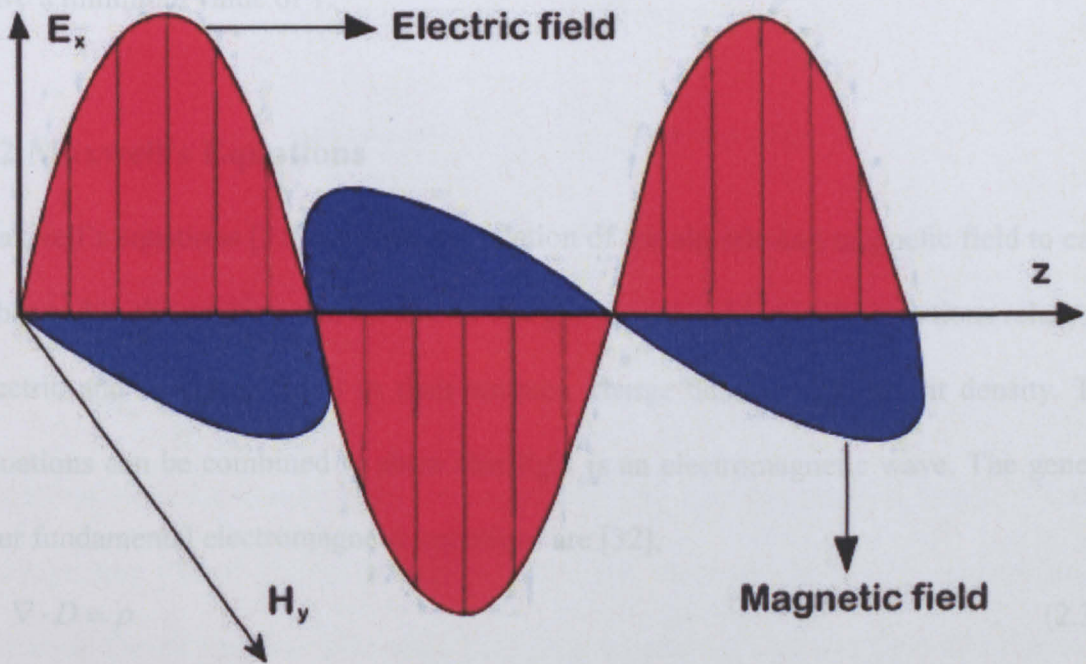


Figure 2.1: Electromagnetic waves propagation in free space [30]

EM waves can be visualised as a sinewave. The distance a wave travels to complete one cycle is known as the wavelength of the signal. If a periodic signal with a frequency

(f) travels at the speed of light (c), then the wavelength (λ) is given by equation 2.1.

$$\lambda = \frac{c}{f} \quad (2.1)$$

In vacuum and air, the speed of light is approximately $3 \times 10^8 \text{ m/s}$, but the speed of an EM wave is reduced by a factor $\sqrt{\epsilon_r \mu_r}$ when passing through other materials. The effect on the wavelength is shown in equation 2.2.

$$\lambda = \frac{c}{\sqrt{\epsilon_r \mu_r} f} \quad (2.2)$$

where ϵ_r is the relative permittivity, and μ_r is the relative permeability. As these values have a minimum value of 1.

2.2 Maxwell's Equations

Maxwell's equations [31] describe the relation of the electric and magnetic field to each other and to the position and motion of charged particles. Maxwell's equations relate the electric and magnetic fields to their sources, charge density and current density. The equations can be combined to show that light is an electromagnetic wave. The general four fundamental electromagnetic equations are [32],

$$\nabla \cdot D = \rho \quad (2.3)$$

$$\nabla \cdot B = 0 \quad (2.4)$$

$$\nabla \cdot E = -\frac{\partial B}{\partial t} \quad (2.5)$$

$$\nabla \cdot H = J + \frac{\partial D}{\partial t} \quad (2.6)$$

In the above equations, the E represents the electric field in volt per metre (Vm^{-1}) and H represents the magnetic field in ampere per metre (Am^{-1}). D is electric displacement field in coulomb per square metre (Cm^{-2}) and B is the magnetic flux density in tesla (T). J is the electric current density in ampere per square metre (Am^{-2}) and ρ is the electric charges density in coulomb per cubic metre (Cm^{-3}).

Equation 2.3 is the Gauss's Law [33] describes how an electric field is generated by electric charges. Charges with opposite signs attract each other, and charges with the same sign repel each other which is shown in Figure 2.2. The electric field tends to point away from positive charges and towards negative charges.

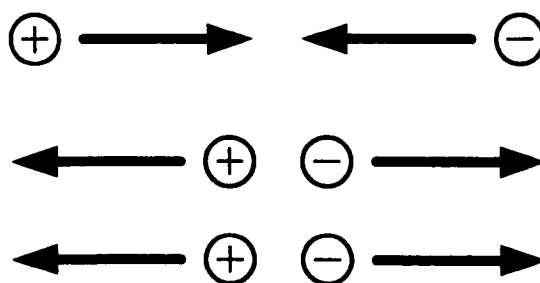


Figure 2.2: Gauss's law [34]

Equation 2.4 is the Gauss's Law for magnetism [35] describes the total magnetic field B through any closed surface is always zero. The magnetic field B is defined as the direction that the north pole to south pole on a magnet bar which as shown in Figure 2.3.

Equation 2.5 is the Ampere's Law [36] described that magnetic fields can be generated by electrical current. The direction of magnetic field is depends to the current that can be found using the right hand rule as shown in Figure 2.4. If the thumb points in the direction of the current, then the fingers show the direction of the magnetic field.

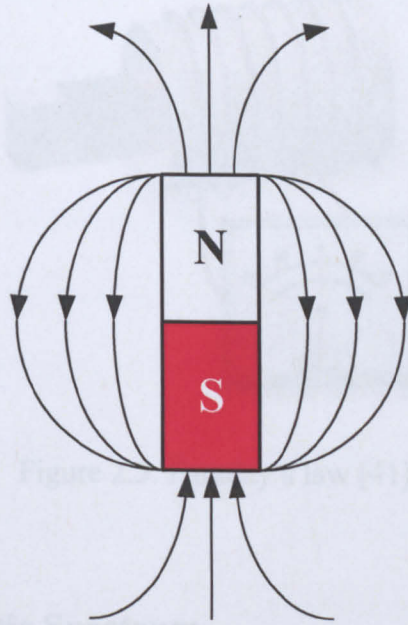


Figure 2.3: Gauss's law for magnetism [37]

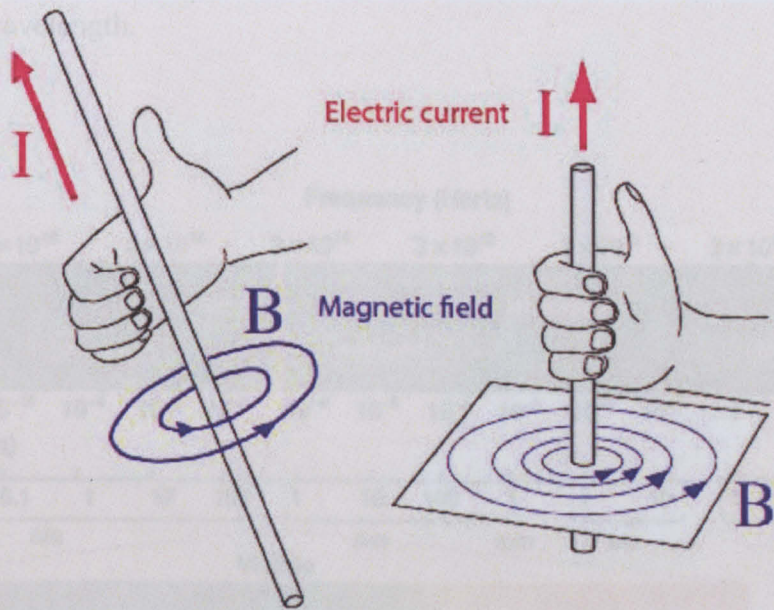


Figure 2.4: Ampere's law [38]

Equation 2.6 is the Faraday's Law [39,40] described how a changing magnetic field can create an electric field as shown in Figure 2.5. The needle of galvanometer moves when the magnet is moving backward and forward. This indicated that a current is induced in the coil. The needle immediately returns to zero when the magnet is not moving.

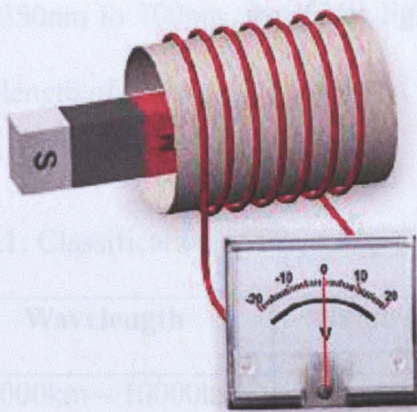


Figure 2.5: Faraday’s law [41]

2.3 The Electromagnetic Spectrum

Figure 2.6 shows the electromagnetic wave spectrum, the EM radiation [42] depends on its wavelength, the higher frequency have shorter wavelength, and lower frequency have longer wavelength.

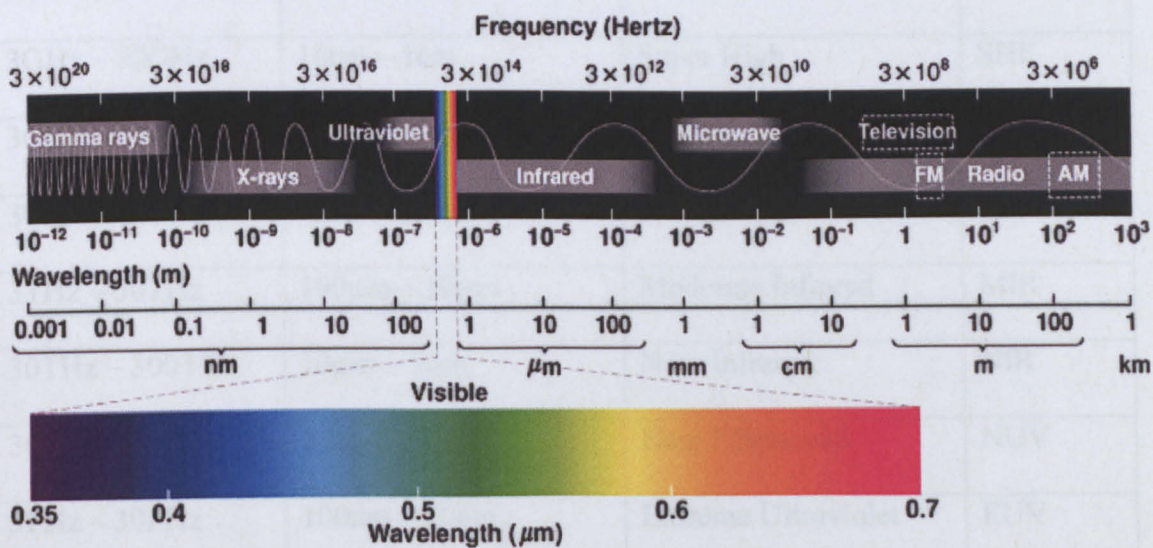


Figure 2.6: Electromagnetic waves spectrum [43]

Normally, EM radiation is classified by wavelength into radio waves, microwaves, infrared, visible light, ultraviolet, X-rays and gamma rays. The visible regions have

wavelengths ranging from 350nm to 700nm, the violet light has a wavelength 350nm and the red light has a wavelength of 700nm.

Table 2.1: Classification of frequency bands [44]

Frequency	Wavelength	Name (Frequency)	Class
3Hz – 30Hz	100000km – 10000km	Extremely Low	ELF
30Hz – 300Hz	10000km – 1000km	Super Low	SLF
300Hz – 3kHz	1000km – 100km	Ultra Low	ULF
3kHz – 30kHz	100km – 10km	Very Low	VLF
30kHz – 300kHz	10km – 1km	Low	LF
300kHz – 3MHz	1km – 100m	Medium	MF
3MHz – 30MHz	100m – 10m	High	HF
30MHz – 300MHz	10m – 1m	Very High	VHF
300MHz – 3GHz	1m – 10cm	Ultra High	UHF
3GHz – 30GHz	10cm – 1cm	Super High	SHF
30GHz – 300GHz	1cm – 1mm	Extremely High	EHF
300GHz – 3THz	1mm – 100 μ m	Far Infrared	FIR
3THz – 30THz	100 μ m – 10 μ m	Moderate Infrared	MIR
30THz – 300THz	10 μ m – 1 μ m	Near Infrared	NIR
300THz – 3PHz	1 μ m – 100nm	Near Ultraviolet	NUV
3PHz – 30PHz	100nm – 10nm	Extreme Ultraviolet	EUV
30PHz – 300PHz	10nm – 1nm	Soft X-rays	SX
300PHz – 3EHz	1nm – 100pm		
3EHz – 30EHz	100pm – 10pm	Hard X-rays	HX
30EHz – 300EHz	10pm – 1pm	Gamma Ray	Y

Table 2.1 shows the classification of frequency bands. Most microwave systems are located in the 300 MHz to 30 GHz range. High atmospheric absorption exists at some frequencies in the 30-300GHz range. However between these absorption frequency ranges there are transmission windows. For example, Missile seeker radars use such a window at 94GHz [45]. With continuing advances in microwave devices more and more microwave systems are being developed in the millimetre portion of the microwave band.

2.4 Characteristic Impedance of Free Space

Characteristic impedance [46,47] of free space (η_0) is defined as the ratio of the electric field (E) to the magnetic field (H). The unit of the electric field is volts per meter (V/m), and the unit of the magnetic field is amperes per meter (A/m). Therefore, the ratio E/H is a constant having the dimensions of V/A or ohms. In free space, the characteristic impedance (η_0) is given by equation 2.7 [48].

$$\eta_0 = \sqrt{\frac{\mu_0}{\epsilon_0}} \quad (2.7)$$

where μ_0 is the constant for permeability of free space which is $4\pi \times 10^{-7} \text{ H/m}$ and ϵ_0 is the constant for permittivity of free space which is $8.854 \times 10^{-12} \text{ F/m}$, therefore,

$$\eta_0 = \sqrt{\frac{4\pi \times 10^{-7}}{8.854 \times 10^{-12}}} = 377\Omega$$

2.5 Polarisation

The polarisation [49] of EM waves describes the time-varying behaviour of the electric field intensity vector at a given point in space. There are three types of polarisation

which are:

- Linear polarisation
- Circular polarisation
- Elliptical polarisation

Since linear and circular polarizations are different forms of an ellipse, they are sometimes all referred to as elliptical polarisation.

2.5.1 Linear Polarisation

In linear polarisation the electric field can be described by one or two components (E_x and E_y) that are exactly in phase. The ratio of the strengths of the two components is constant; therefore, the direction of the electric vector (the vector sum of these two components) is constant, and the vector traces out a single line as shown in Figure 2.7.

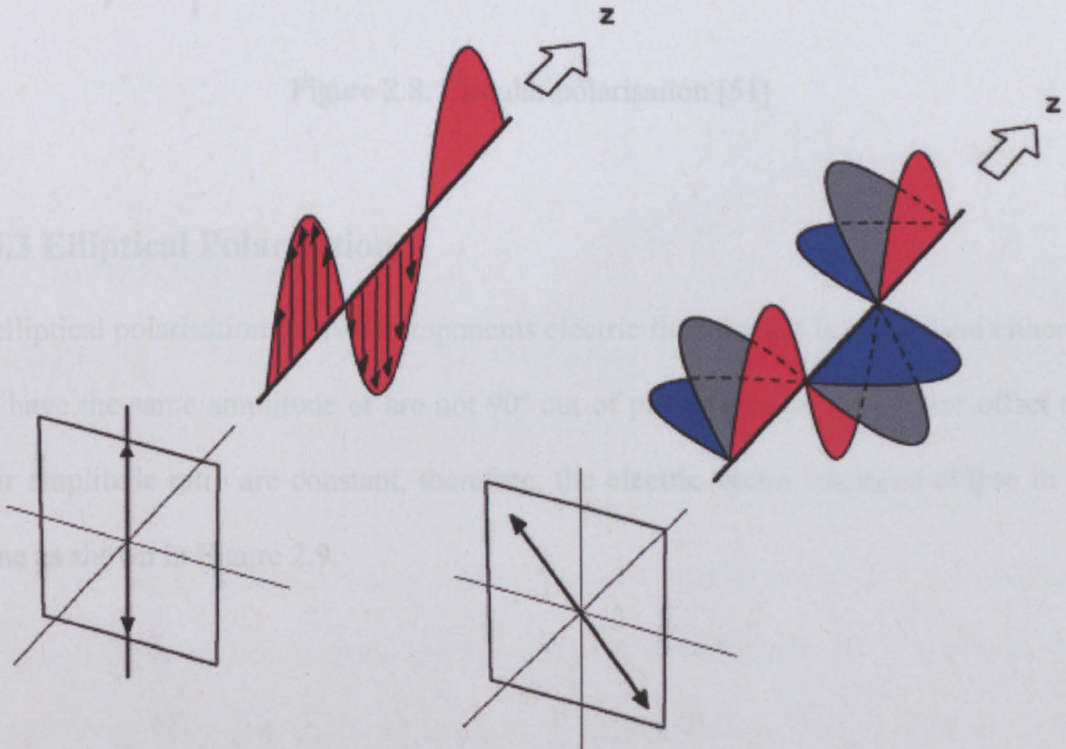


Figure 2.7: Linear polarisation [50]

2.5.2 Circular Polarisation

In circular polarisation the two electric field components have exactly the same amplitude and are exactly 90° out of phase. When one component is zero and another component is at maximum or minimum amplitude, therefore, the electric vector traces out a circle as shown in Figure 2.8.

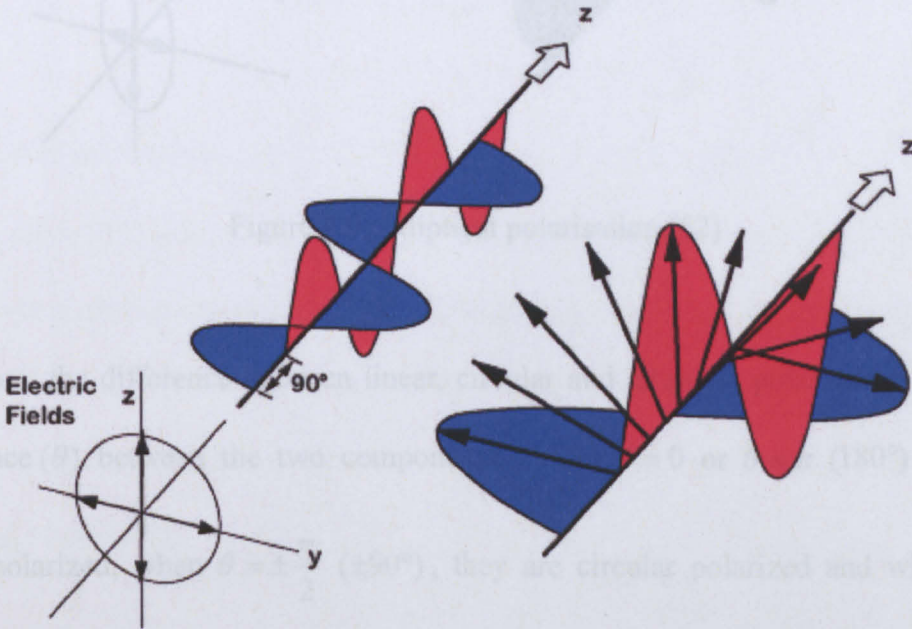


Figure 2.8: Circular polarisation [51]

2.5.3 Elliptical Polarisation

In elliptical polarisation the two components electric field are not in phase, and either do not have the same amplitude or are not 90° out of phase, though their phase offset and their amplitude ratio are constant, therefore, the electric vector traces an ellipse in the plane as shown in Figure 2.9.

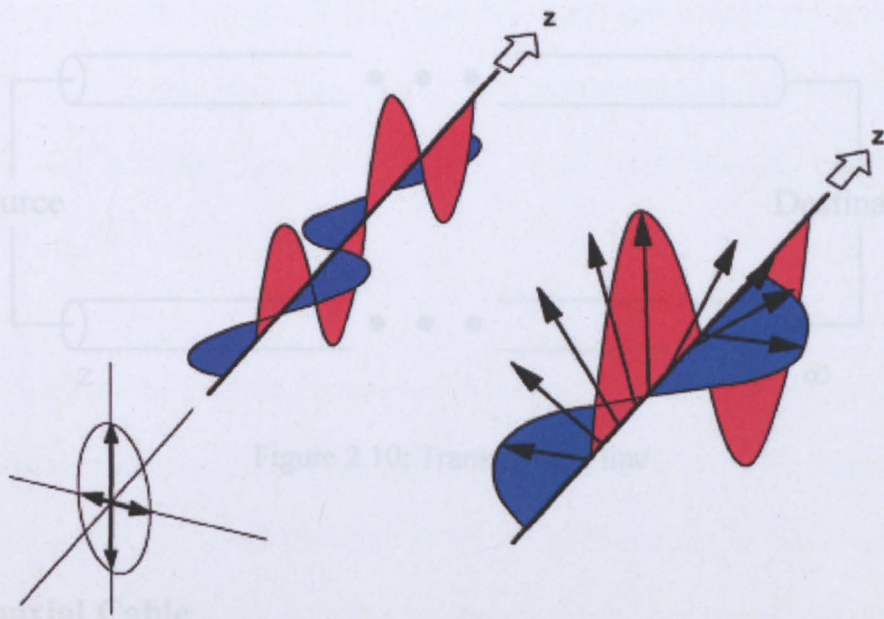


Figure 2.9: Elliptical polarisation [52]

Therefore, the difference between linear, circular and elliptical polarisation is a phase difference (θ) between the two components. When $\theta = 0$ or $\theta = \pi$ (180°), they are linear polarized, when $\theta = \pm \frac{\pi}{2}$ ($\pm 90^\circ$), they are circular polarized and when $\theta \neq 0$, $\theta \neq \pm \frac{\pi}{2}$ ($\pm 90^\circ$) or $\theta \neq \pi$ (180°) they are elliptical polarized.

2.6 Transmission Lines

Transmission line [53] is the material medium or structure that is used to transmit energy and guide wave electromagnetic fields from the source to the destination. The electrically long wires can act as antennas as shown in Figure 2.10, radiating power into their surroundings and picking up electromagnetic interference [54]. Two conductor transmission lines with a uniform geometry such as coaxial lines and parallel wire lines are used to minimize these effects and their general behaviour is more predictable. The three main type of transmission lines are coaxial cable, microstrip and waveguide.

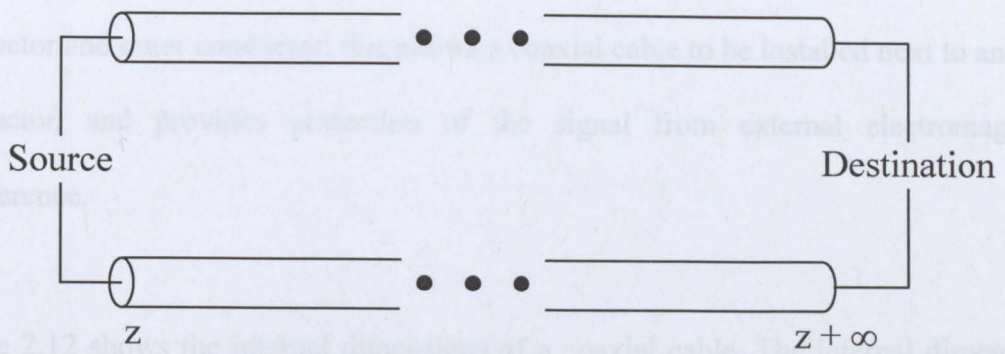


Figure 2.10: Transmission line

2.6.1 Coaxial Cable

Coaxial cable [55] is an electrical cable consisting of an inner conductor surrounded by an insulating material layer with a high dielectric constant; both the inner conductor and the insulator are surrounded by a conductive layer called the shield (outer conductor). Finally the shield is covered by another insulating layer such as a plastic sheath as shown in Figure 2.11.

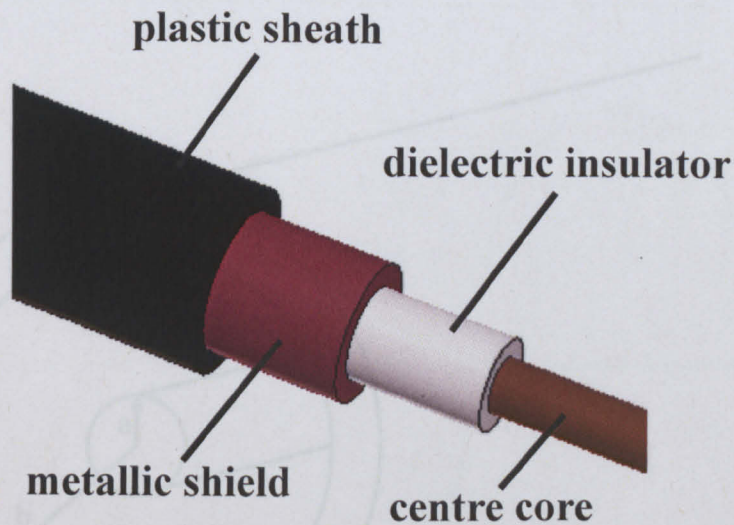


Figure 2.11: Coaxial cable [56]

The advantage for the coaxial cable is that the signal only exists between the inner conductor and outer conductor; this allows a coaxial cable to be installed next to another conductor, and provides protection of the signal from external electromagnetic interference.

Figure 2.12 shows the internal dimensions of a coaxial cable. The internal dimensions for the coaxial cable are commonly labelled by letters 'a' and 'b', where 'a' is the internal radius for inner conductor and 'b' is the internal radius to the outer conductor. Generally, if the loss of the coaxial line can be considered very small, the characteristic impedance Z_0 is given by equation 2.8 [57]. η_0 is characteristic impedance of free space and ϵ_r is the relative permittivity of the insulating material.

$$Z_0 = \frac{1}{2\pi} \sqrt{\frac{\mu}{\epsilon}} \ln \frac{b}{a} \quad (2.8)$$

$$Z_0 = \frac{\eta_0}{2\pi\sqrt{\epsilon_r}} \ln \frac{b}{a} = \frac{60}{\sqrt{\epsilon_r}} \ln \frac{b}{a}$$

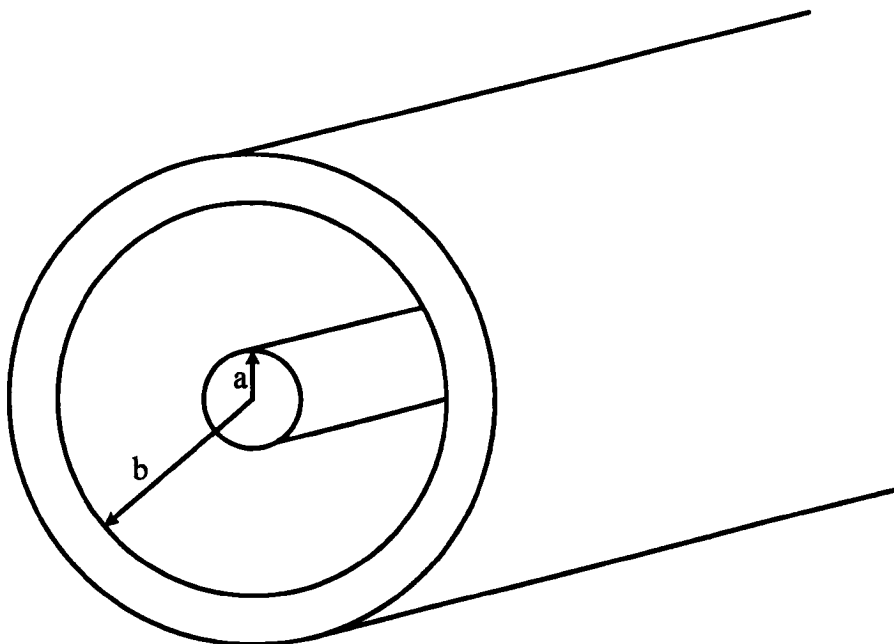


Figure 2.12: Dimension for coaxial cable [58]

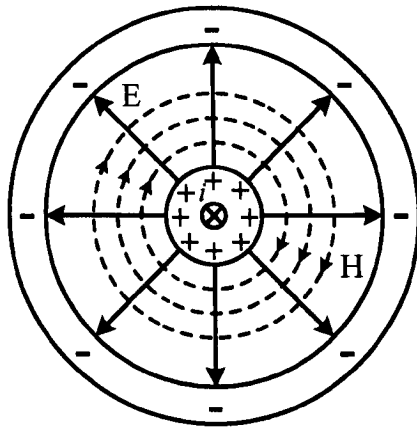


Figure 2.13: TEM mode in coaxial cable [59]

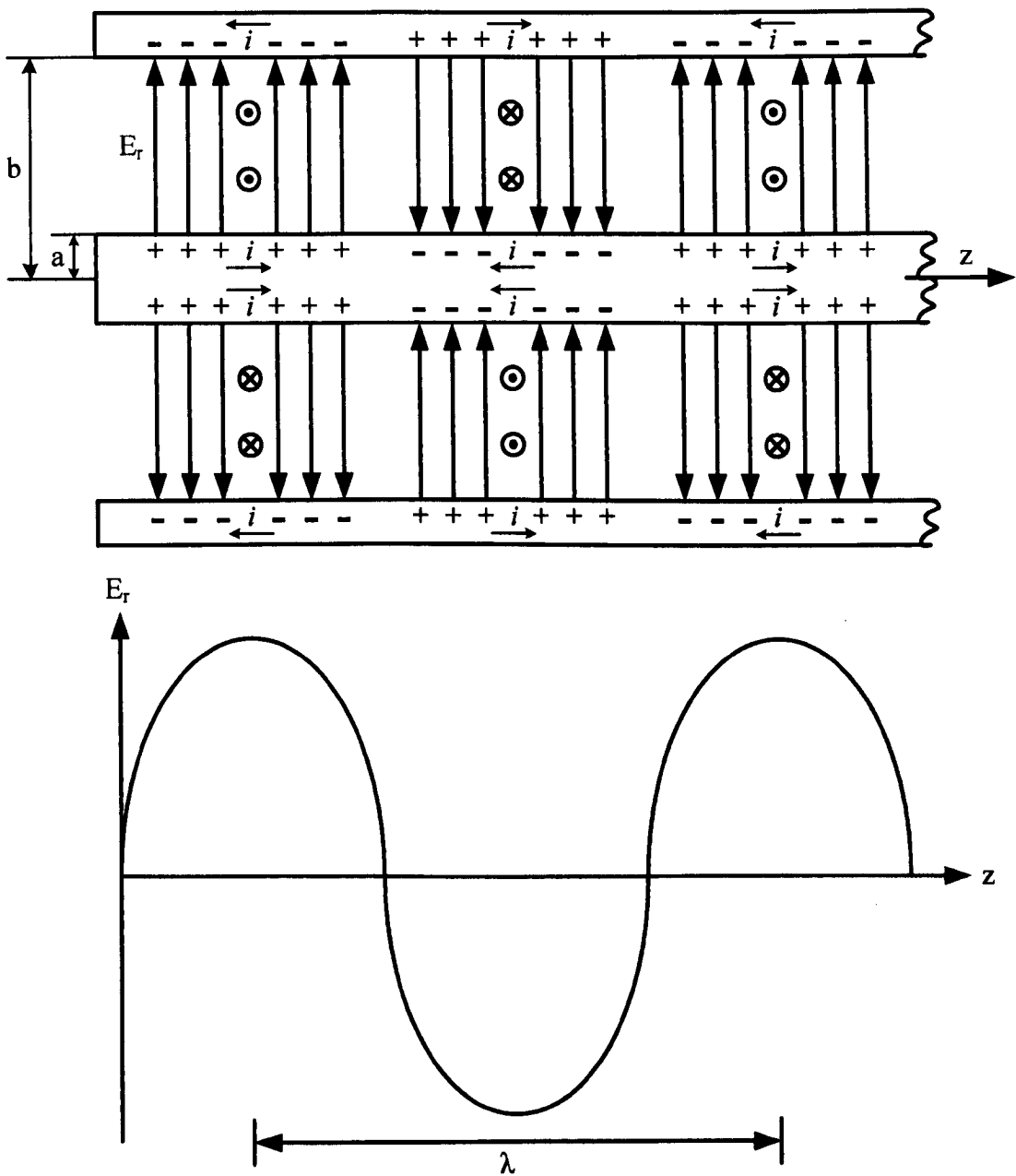


Figure 2.14: Field, charge and current distributions along the coaxial cable [60]

Figure 2.13 shows the TEM mode in a coaxial cable. When the circuit dimensions approach that of the wavelength instead of using voltage and current waveforms, E field and H field are more appropriate. The electric field (E) lines in coaxial cable go from one conductor to the other and must join the conductors at right angles, and the magnetic fields (H) are circular. The electric and magnetic field lines are as shown in Figure 2.13. The solid lines represent the electric field, the dotted lines represent the magnetic field and the current (i) in the coaxial cable is represented by the symbols positive (+) and negative (-). Figure 2.14 shows the distributions of field, charge and current along the coaxial cable, 'z' is the direction of propagation of the EM power, and λ is the wavelength of EM waves.

2.6.2 Microstrip

Microstrip [61] is useful because it can be fabricated using standard printed circuit board (PCB) techniques. It allows the combination of transmission lines with electronic devices such as resistors, capacitors, inductors and transistors. The advantage of microstrip transmission lines is that it simplifies the problem of making many connections in a complex RF or microwave circuit. Microstrip [62] consists of a conductor, an insulator, and a flat plate called the ground plan which shown in Figure 2.15. Microstrip is like a coaxial cable that has been cut and laid out flat so that the ground plane on the bottom is like the outer conductor. The strip on the top is like the inner conductor, and the space between the conductor and ground plane is the insulator.

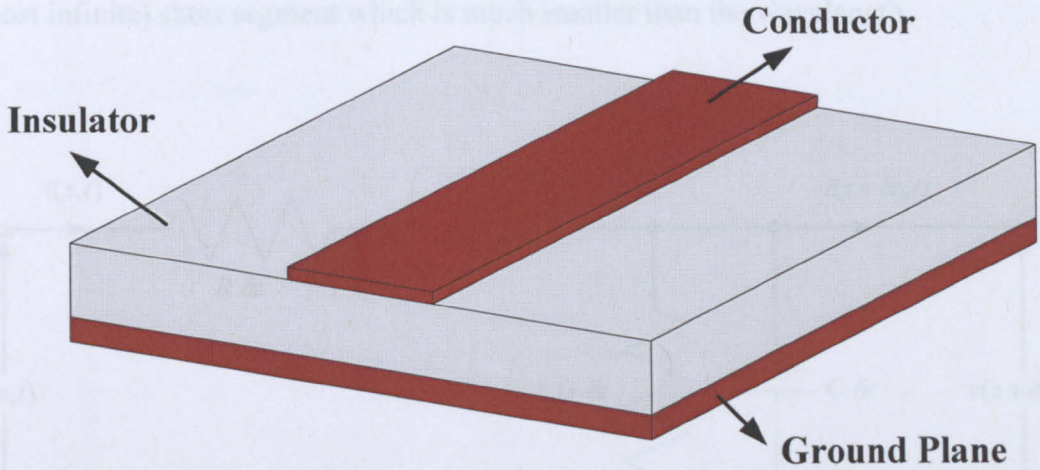


Figure 2.15: Microstrip transmission lines [63]

2.7 General Transmission Line Equations

A uniform transmission line [64] is a distributed system, as every bit of length introduces some capacitance and some inductance. In a real transmission cable, the conductor will not be perfect and therefore it will have some resistance per unit length (R), and the dielectric which separates the conductors will not be a perfect insulator and therefore will have some conductance per unit length (G).

Figure 2.16 shows the equivalent electric circuit of a very short section (δz) of transmission line, where,

R is series resistance per unit length, in Ω/m

L is series inductance per unit length, in H/m

G is shunt conductance per unit length, in S/m

C is shunt capacitance per unit length, in F/m

The voltage v and the current i are functions of distance z as well as of time t . The δz is very small distance of length when the transmission line is divide into many

(almost infinite) short segment which is much smaller than the wavelength.

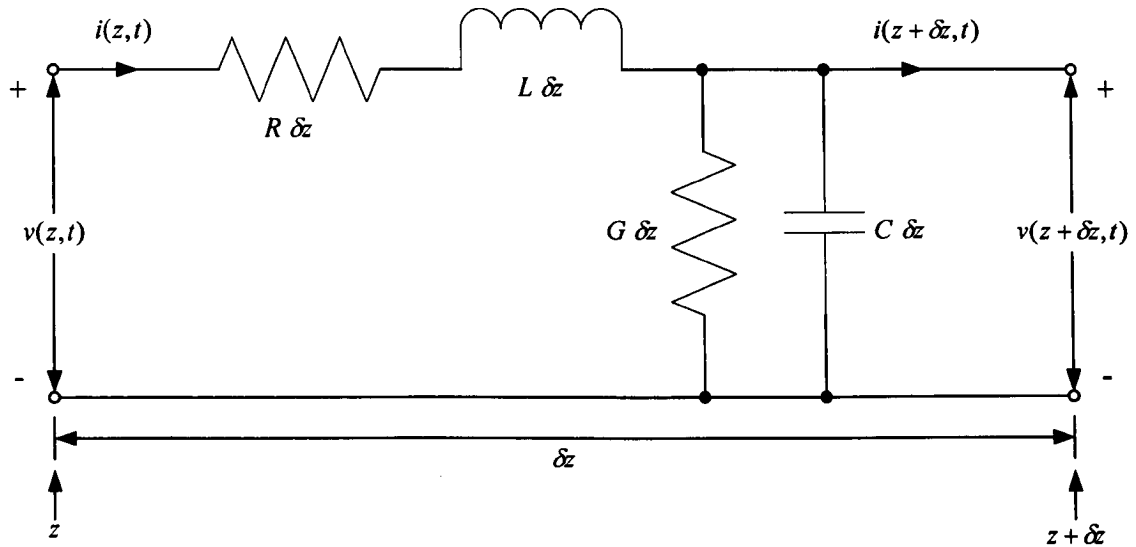


Figure 2.16: Equivalent circuit of a transmission line

By Kirchhoff's Voltage Law (KVL),

$$v(z, t) = R \delta z i(z, t) + L \delta z \frac{\partial i(z, t)}{\partial t} + v(z + \delta z, t) \quad (2.9)$$

By Kirchhoff's Current Law (KCL),

$$i(z, t) = G \delta z v(z + \delta z, t) + C \delta z \frac{\partial v(z + \delta z, t)}{\partial t} + i(z + \delta z, t) \quad (2.10)$$

then,

$$\gamma = \alpha + j\beta = \sqrt{(R + j\omega L)(G + j\omega C)} \quad (2.11)$$

γ is the propagation constant whose real and imaginary parts, α is the attenuation constant, in Np/m, and β is the phase constant, in rad/m, of the transmission line. V^+ and I^+ are the forward travelling wave, V^- and I^- are backward travelling wave.

The ratio of the voltage and the current at any distance z for an infinitely long line is independent of distance z is known as the characteristic impedance Z_0 .

$$Z_0 = \sqrt{\frac{R + j\omega L}{G + j\omega C}} \quad (2.12)$$

The general expressions for the characteristic impedance Z_0 in equation 3.4 and the propagation constant γ in equation 2.12 are relatively complicated. In the lossless line case, $R = 0$ and $G = 0$,

(a) characteristic impedance Z_0 ,

$$Z_0 = \sqrt{\frac{0 + j\omega L}{0 + j\omega C}} = \sqrt{\frac{j\omega L}{j\omega C}} = \sqrt{\frac{L}{C}} \quad (2.13)$$

(b) propagation constant γ ,

$$\gamma = \sqrt{(j\omega L)(j\omega C)} = j\omega\sqrt{LC}$$

$$\gamma = \alpha + j\beta$$

$$\alpha = 0,$$

$$\beta = \omega\sqrt{LC} \quad (2.14)$$

(c) phase velocity v_p ,

$$v_p = \frac{\omega}{\beta} = \frac{\omega}{\omega\sqrt{LC}} = \frac{1}{\sqrt{LC}} \quad (2.15)$$

If a load impedance Z_L is placed at the end of the transmission line and make the position $z = 0$, then the equation,

$$Z_L = \frac{V(0)}{I(0)} = \frac{V^+ + V^-}{\frac{V^+}{Z_0} - \frac{V^-}{Z_0}} = Z_0 \left(\frac{V^+ + V^-}{V^+ - V^-} \right) \quad (2.16)$$

$$Z_L(V^+ - V^-) = Z_0(V^+ + V^-)$$

$$V^+Z_L - V^-Z_L = V^+Z_0 + V^-Z_0$$

$$V^+(Z_L - Z_0) = V^-(Z_L + Z_0)$$

When a transmission line is terminated in a load impedance Z_L different from the characteristic impedance Z_0 , both the incident wave and a reflected wave exist. The ratio V^-/V^+ of the complex amplitudes of the reflected and incident voltage waves at the load is known as load reflection coefficient Γ_L [65], therefore,

$$\Gamma_L = \frac{V^-}{V^+} = \frac{(Z_L - Z_0)}{(Z_L + Z_0)} \quad (2.17)$$

2.8 Voltage Standing Wave Ratio (VSWR)

The reflection coefficient Γ is a complex number describing both the magnitude and phase of the reflected signal with the imaginary part of the reflection coefficient Γ set to zero, a real part of reflection coefficient of '1' represents a perfect open circuit, a reflection coefficient of '-1' represents a perfect short circuit and reflection coefficient of '0' is represents a perfect match with the load impedance $Z_L = Z_0$. Therefore, no reflection will occur in this case which is the aim in most systems. The reflection coefficient is related to the voltage standing wave ratio (VSWR).

The VSWR [66] is the ratio of maximum voltage to minimum voltage on a line, which indicates how good the impedance match is. A VSWR of '1' represents a perfect

matched line and this number increases for a poorly matched line which represents wasted energy. The VSWR and the reflected power are a different way of expressing the same thing. The relationship between VSWR and reflection coefficient is shown in equation 2.18 [67].

$$VSWR = \frac{|V_{\max}|}{|V_{\min}|} = \frac{1+|\Gamma|}{1-|\Gamma|} \quad (2.18)$$

VSWR is the mismatch ratio of power available from an ideal source to the power in the mismatched load. The VSWR was used to know whether the antenna is match to 50Ω (common used), if not, the matching circuit might be applied and make the antenna match to 50Ω .

2.9 Waveguide

Waveguide [68] is a hollow conducting tube to contain the EM energy and usually constructed in rectangular or circular cross section. There are two most common types of waveguides, rectangular and circular.

2.9.1 Rectangular Waveguide

Figure 2.17 shows the rectangular waveguide [69,70]. The internal dimensions for the rectangular waveguide are commonly labelled by letters 'a' and 'b', where 'a' is the width and 'b' is the height of the waveguide.

Different configurations of the E field and H field can exist in a waveguide and these are known as modes. The two types of modes that usually exist in the waveguides are transverse electric (TE) and transverse magnetic (TM) modes. The difference between the two types is defined by the component of the wave which is transverse to the

direction of propagation. TE modes only have a magnetic field component and no electric field component in the direction of propagation. TM modes only have an electric field component and no magnetic field component in the direction of propagation. Figure 2.18 is explained the subscript notation that often used to express more information about the mode for the EM waves propagation in waveguide.

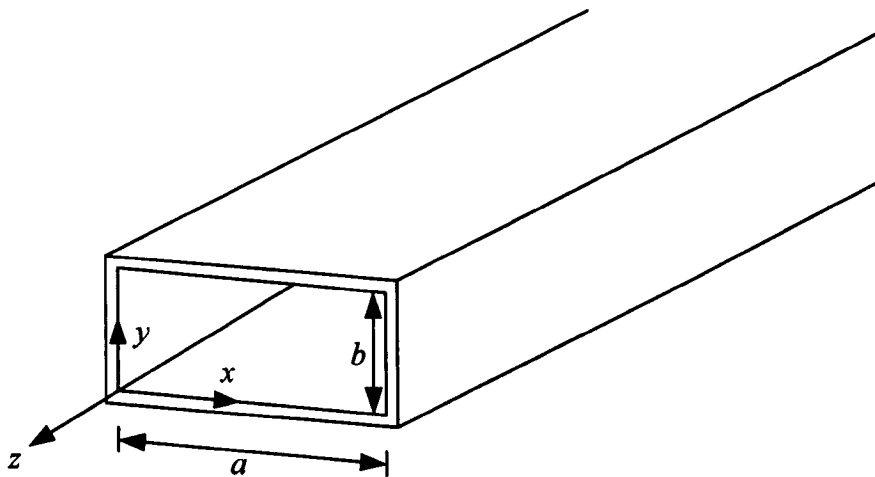


Figure 2.17: Rectangular waveguide [71]

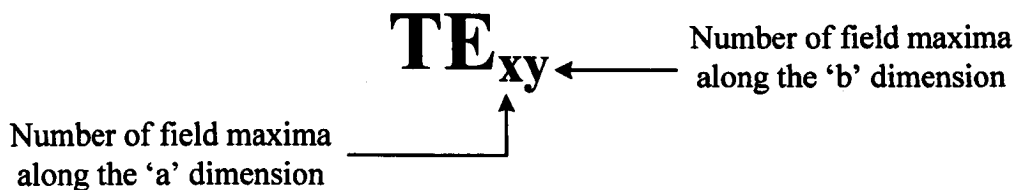


Figure 2.18: An explanation for mode subscript notation which used in waveguide

Figure 2.19 and Figure 2.20 shows a few of the configurations for TE and TM modes in rectangular waveguide. The most common and fundamental mode is TE_{10} . The solid lines in Figure 2.19 represent the direction of the electric field and the dotted lines in Figure 2.20 represent the direction of the magnetic field.

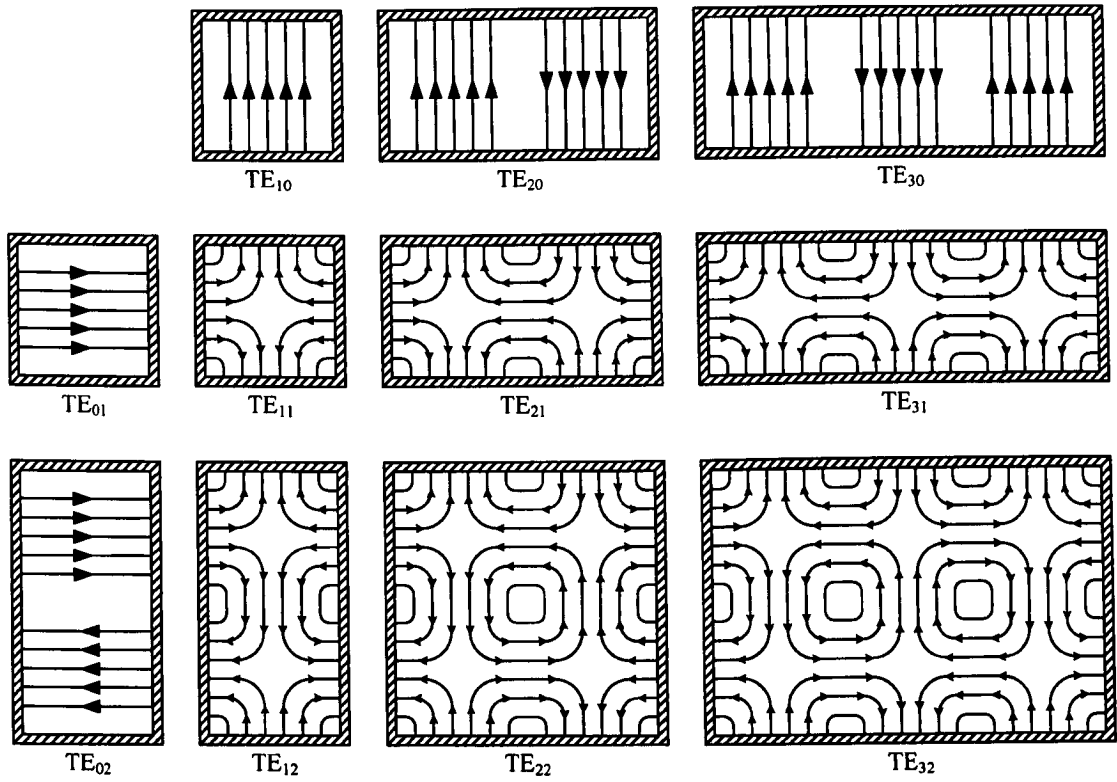


Figure 2.19: TE modes in rectangular waveguide [72,73]

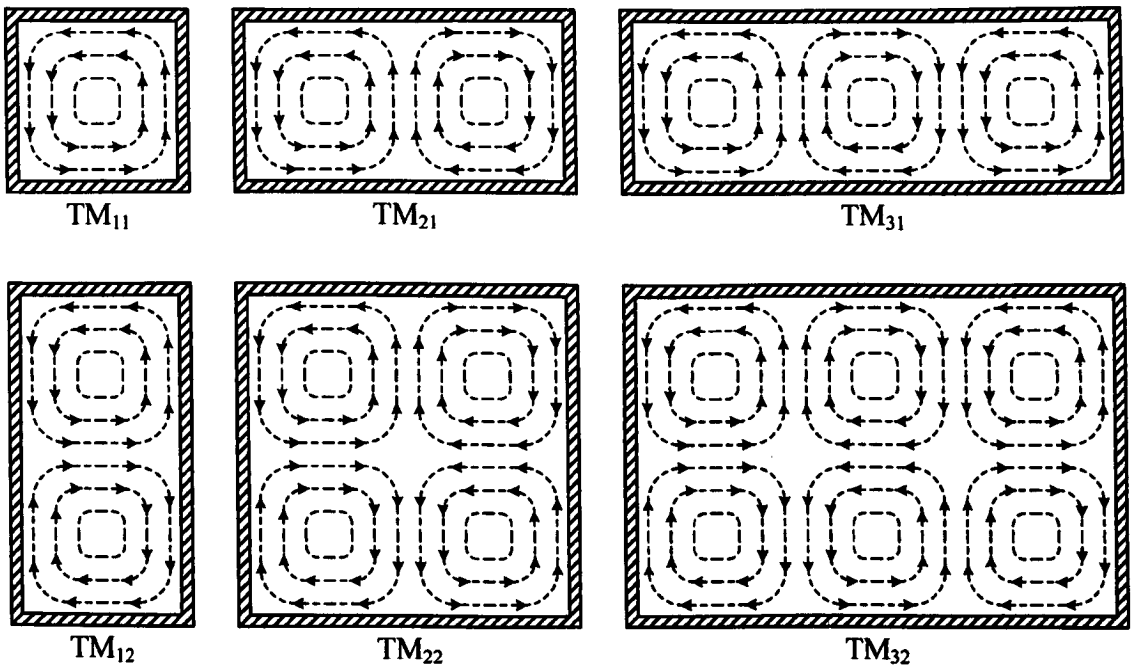


Figure 2.20: TM modes in rectangular waveguide [74]

2.9.2 Circular Waveguide

Figure 2.21 shows a circular waveguide [75,76] and the internal radius for the circular waveguide is labelled by letter 'a'. Different modes of propagation also exist in circular waveguide with each mode describing a unique field configuration.

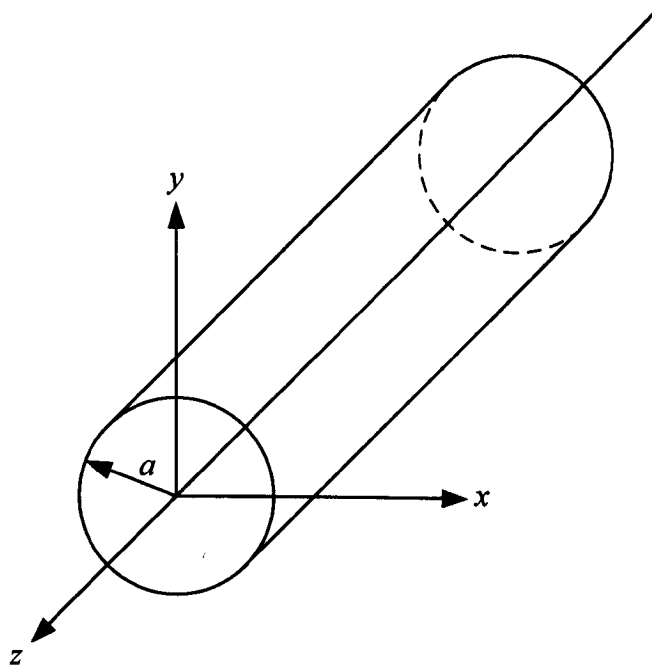


Figure 2.21: Circular waveguide [77]

Figure 2.22 shows some possible configurations for TE and TM modes in circular waveguide. The solid lines in Figure 2.22 represent the direction of the electric field and the dotted represent the direction of the magnetic field.

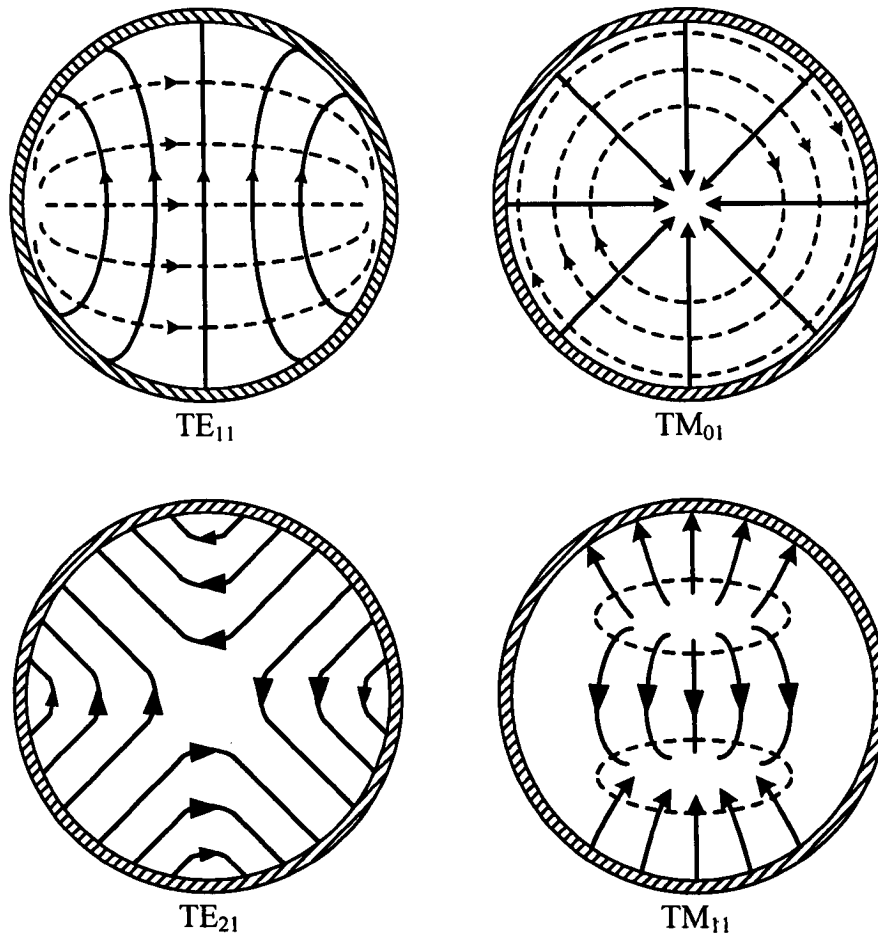


Figure 2.22: TE and TM mode in circular waveguide [78,79]

TE or transverse electric modes have electric fields in the transverse plane across the waveguide. The magnetic field in the TE modes runs both transversely and axially along the waveguide. The TM or transverse magnetic modes have magnetic fields that exist only in the transverse cross section of the guide, whereas the electric fields extend in the transverse and axial directions along the guide. The cut-off frequency for each mode depends on the diameter of the waveguide.

The equation for the cut-off frequency given by Pozar [80] for the TE modes of a circular waveguide is,

$$f_{c_{nm}} = \frac{p'_{nm}}{2\pi a \sqrt{\mu\epsilon}} \quad (2.18)$$

where a is the radius of the circular waveguide and the values of p'_{nm} for TE modes are shown in Table 2.2.

Table 2.2: Values of p'_{nm} for TE modes of a circular waveguide

n	p'_{n1}	p'_{n2}	p'_{n3}
0	3.832	7.016	10.174
1	1.841	5.331	8.536
2	3.054	6.706	9.970

The equation for cut-off frequency given by Pozar [81] for the TM modes of a circular waveguide is,

$$f_{c_{nm}} = \frac{p_{nm}}{2\pi a \sqrt{\mu\epsilon}} \quad (2.19)$$

where a is the radius of the circular waveguide and the values of p_{nm} for TM modes are shown in Table 2.3.

Table 2.3: Values of p_{nm} for TM modes of a circular waveguide

n	p_{n1}	p_{n2}	p_{n3}
0	2.405	5.520	8.654
1	3.832	7.016	10.174
2	5.135	8.417	11.620

2.10 Scattering Parameters (S-Parameters)

Scattering parameters or S-parameters [82,83] are another way of specifying return loss and insertion loss. Figure 2.23 shows RF or microwave signals entering and exiting a cavity in both directions. If an RF or microwave signal is incident on the input side of the cavity, some of the signal is reflected and some is transmitted through the cavity. The ratio of the reflected signal to the incident signal is the reflection coefficient. The ratio of the transmitted signal to the incident signal is the transmission coefficient.

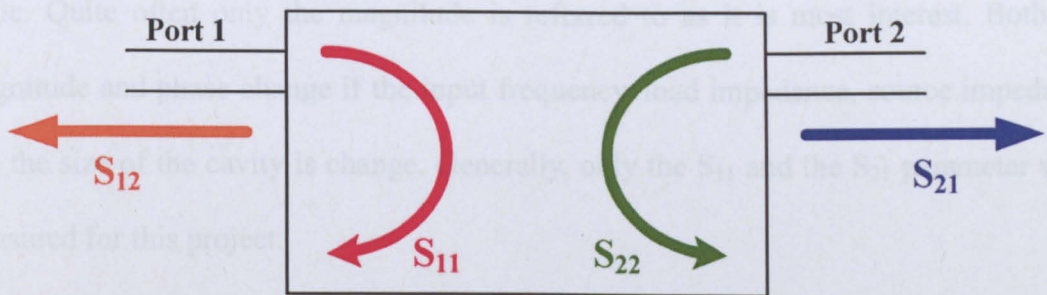


Figure 2.23: Block diagram for S-parameter

In Figure 2.23, the reflection and transmission coefficients are specified in both directions as follows:

Port 1: Input Port

Port 2: Output Port

S_{11} : Input reflection coefficient

S_{12} : Reverse transmission coefficient

S_{21} : Forward transmission coefficient

S_{22} : Output reflection coefficient

S_{11} is the signal reflected at input port 1 as a ratio of the signal incident at the same input port 1. S_{12} is the signal exiting at input port 1 as a ratio of the signal incident at

output port 2. S_{21} is the signal exiting at output port 2 as a ratio of the signal incident at input port 1. S_{22} is the signal reflected at input port 2 as a ratio of the signal incident at the same input port 2.

The transmitted and reflected wave will generally have a change in amplitude and phase from the incident wave. Normally, the transmitted and the reflected wave will be at the same frequency as the incident wave. The S-parameters are complex because they have magnitude and phase. The real part is the magnitude and the imaginary part is the phase angle. Quite often only the magnitude is referred to as it is most interest. Both the magnitude and phase change if the input frequency, load impedance, source impedance and the size of the cavity is change. Generally, only the S_{11} and the S_{21} parameter were measured for this project.

2.11 Water Pipe as Transmission Line

In this project, the water is transported through metal pipes with a circular cross section. The metal pipe can considered as a circular waveguide. The metal pipe can still act as a waveguide if the metal pipe is full filled of water. In this situation, the minimum frequency that propagates through the water pipe is much lower by 192MHz. The cut-off frequency is nine times lower than that of an empty pipe, this is because of the high dielectric constant (ϵ_r) of water which is approximately 81 at temperature around 20°C [26], therefore $\sqrt{\epsilon_r} = \sqrt{81} = 9$. This value is temperature dependant but the temperature for underground water is nearly constant.

Several different modes occur when RF power is propagated through a water pipe. The two most common modes in the circular waveguide are the TE_{11} mode and the TM_{01}

mode. These two modes in circular water pipes are different from electromagnetic waves in free space because they have to be higher than a certain minimum frequency in order to be able to propagate through the water pipe based upon the pipe diameter. The cut-off frequency for TE₁₁ mode for the 4 inch metal pipe can be calculated by using the equation 2.18, the radius for the metal pipe is 50.8mm and the value for p'_{11} from Table 2.2 is 1.841, therefore,

$$f_{c_{11}} = \frac{p'_{11}}{2\pi a \sqrt{\mu_0 \epsilon_0 \times \epsilon_r}}$$

$$f_{c_{11}} = \frac{1.841}{2\pi \times 50.8 \times 10^{-3} \sqrt{4\pi \times 10^{-7} \times 8.854 \times 10^{-12} \times 81}}$$

$$f_{c_{11}} \approx 192 \text{ MHz}$$

The cut-off frequency for TM₀₁ mode for the 4 inch metal pipe can be calculated by using the equation 2.19, the radius for the metal pipe is 50.8mm and the value for p_{01} from Table 2.3 is 2.405, therefore,

$$f_{c_{01}} = \frac{p_{01}}{2\pi a \sqrt{\mu_0 \epsilon_0 \times \epsilon_r}}$$

$$f_{c_{01}} = \frac{2.405}{2\pi \times 50.8 \times 10^{-3} \sqrt{4\pi \times 10^{-7} \times 8.854 \times 10^{-12} \times 81}}$$

$$f_{c_{01}} \approx 251 \text{ MHz}$$

Therefore, for a typical 4 inch metal pipe, there is no propagation below the cut-off frequency of 192MHz for the TE₁₁ mode and 251MHz for the TM₀₁ mode. Consequently, only the TE₁₁ mode can propagate at frequencies between 192MHz and 251MHz.

The propagation of electromagnetic waves through the water pipe was affected by the purity of the drinking water, and the propagation will also depend on the type of material which is used to fabricate the pipes. If the material for the pipe is cast iron, then being a ferromagnetic it will have a high permeability. Therefore, the ohmic losses in the walls of the waveguide could be large, unless the permeability drops to a low value at high frequency.

To generate the TE_{11} mode in the water pipe, a monopole antenna or a probe has to be inserted transversely into the pipe. The design of the monopole antenna has been investigated using High Frequency Structure Simulator (HFSS) software and will be discussed in chapter 4.

Summary

Maxwell's equations which can be used to describe EM waves can be solved by using the simulation software HFSS for a particular set of boundary conditions. The frequency that was used for this project was between 240MHz and 560MHz due to the physical properties of the pipes and the water, this will be discussed further in chapter 5 and 6. Only a single wave was used for propagation in the water pipe, hence only the linear polarisation was created when the waves are travelling along the pipeline. Coaxial cables are used for the wave transmission between the antennas and the source and the detector. The transmission line equation to explain this process and the importance of matching has been included. It was necessary to understand the simpler rectangular cavity modes prior to considering the more complex circular cavity modes. The TE_{11} and TM_{01} modes have been used in the circular water pipe because of these two modes have a better resonance peak compared to other modes. The cut-off frequency for the TE_{11} mode is at 192MHz and for TM_{01} mode is at 251MHz.

Chapter 3: Antenna

3.1 Antenna

An antenna is made using a conductor and is generally in the form of a rod or wire that is used for radiating or receiving radio waves [84]. It acts as a transitional structure between a guiding device such as transmission line and free space. In this way they are unlike transmission lines, which are designed to prevent the field radiating away.

The transmitter radiates electromagnetic energy into free space and the receiver collects electromagnetic energy from free space [85]. The same antenna design can be used for transmission or reception. Every antenna will have a certain amount of radiation resistance also known as antenna impedance. For the best condition operation, the transmitter and receiver should be matched to the antenna impedance. Mismatched components will result in signal reflection, a $VSWR > 1$ and a loss of transmission power. Many types of antenna are designed with a 50Ω impedance which is standard for RF and microwave systems. The matching network can be used for mismatch component to achieve a match to the 50Ω antenna impedance.

Most antennas are resonant devices which operate efficiently over the relative frequency bandwidths. Power is radiated more readily at high frequencies because the wavelength is comparable with the dimensions of the antenna, and charges are accelerated to a greater extent because of the faster changes in the electric field.

The characteristics of an antenna are determined by the shape, size and the material

used. The three most common types of antenna are the monopole, loop and microstrip patch antenna.

3.2 Monopole Antenna

The dipole [86,87] antenna is made by a two wire transmission line, where the two currents in the conductors are of sinusoidal distribution and equal in amplitude and in opposite direction. No radiation occurs from the transmission line for the dipole antenna due to the canceling effects as shown in Figure 3.1, the currents in the angle of the dipole are in the same direction and they will produce radiation in the horizontal direction. The length of this antenna is equal to half of its wavelength.

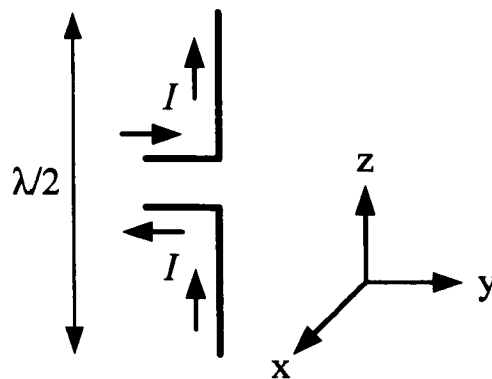


Figure 3.1: Dipole antenna [88]

A monopole [89,90] antenna is a type of radio antenna formed by replacing a dipole antenna with a ground plane. Figure 3.2 shows the monopole antenna result from applying the image theory to the dipole. According to this theory, the combination of the element and its image acts identically to a dipole of length L if a ground plane is placed below a single element of length $L/2$ except that the radiation occurs only in the space above the plane. Therefore, the monopole antenna behaves like a dipole if the ground plane is large enough.

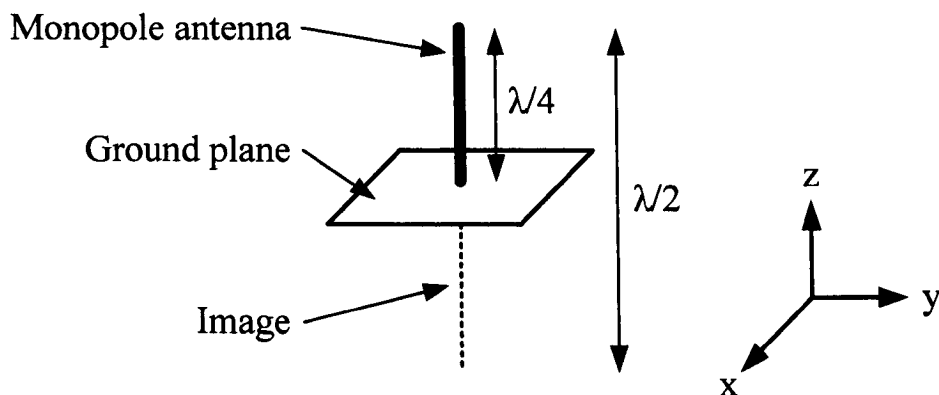


Figure 3.2: Monopole antenna

The directivity for the monopole antenna is doubled and the radiation resistance is halved compared to the dipole antenna [91]. Therefore, a half wave dipole can be approximated by a quarter wave monopole. The monopole antenna is very useful for mobile antennas where the ground plane can be a car body or the mobile phone handset case for example.

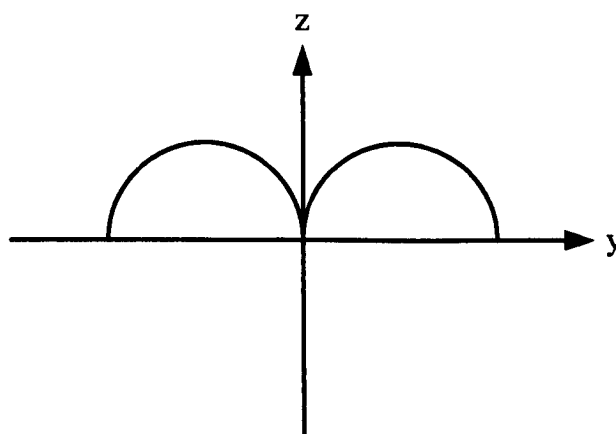


Figure 3.3: Radiation pattern of monopole antenna

Monopole antennas [92] have a low input resistance and the directive gain with reference to an isotropic antenna is 5.19dBi where the gain is twice for a half wave

dipole antenna which is 3dBi. The radiation pattern [93] for the monopole antenna is shown in Figure 3.3. The wavelength of the monopole antenna is given by equation 3.1,

$$\frac{\lambda}{4} = L \quad (3.1)$$

where L is the length of the monopole antenna in metres (m), and the frequency of monopole antenna is given in equation 3.2

$$f = \frac{c}{\lambda} \quad (3.2)$$

3.3 Loop Antenna

The loop antenna is a directional type antenna which consists of one or more complete turns of a conductor [94]. There are many different forms for the loop antenna, such as rectangle, square, triangle, ellipse, circle, etc. Figure 3.4 shows a circular loop antenna with radius r . A loop antenna has a continuous conducting path leading from one conductor of a two wire transmission line to the other conductor. All planar loops are directional antennas with a sharp null.

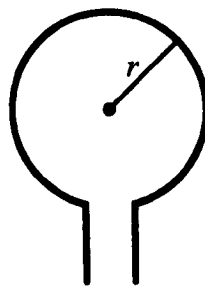


Figure 3.4: Circular loop antenna

A small loop antenna [95] is considered less than a quarter of a wavelength in circumference. Most directional receiving loops are about 1/10 of a wavelength. The small loop is also known as magnetic loop because it is more sensitive to the magnetic component of the electromagnetic wave.

The loop antenna has a very low radiation resistance because it acts as an inductive component like a large inductor. The advantages of the loop antenna is that it strongly responds to the magnetic field (H) of the EM waves, and is less affected by the man-made interference because it has a strong electric field (E). The loop antenna also picks up less noise, providing a better signal to noise ratio (SNR).

Figure 3.5 shows the radiation pattern of a circular loop antenna. The radiation pattern of the antenna is the strength of the radiated field in different directions at a constant distance for the antenna. The loop antenna has identical radiation patterns with E and H interchanged. Therefore, the horizontal loop is horizontally polarized.

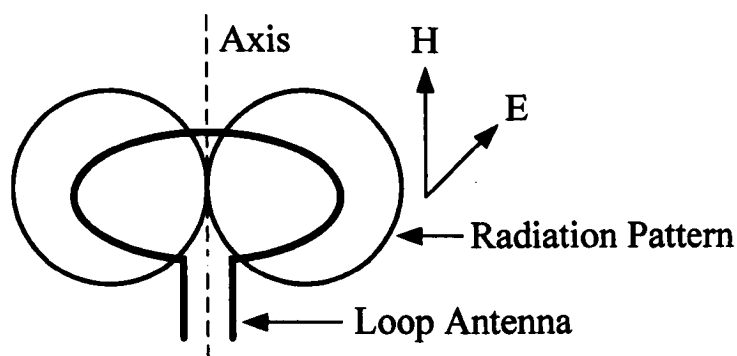


Figure 3.5: Radiation pattern of loop antenna [96]

The wavelength of the loop antenna is given by equation 3.3 [97],

$$\lambda = \pi d \quad (3.3)$$

where d is the diameter of the loop antenna in metres (m), and the equation for the frequency of a loop antenna is the same as equation 3.2.

3.4 Microstrip Patch Antenna

The basic concept of a microstrip patch antenna [98,99] is driven against a ground plane which as shown in Figure 3.6. Normally, the simplest patch antenna uses a patch with the dielectric loading included over a larger ground plane separated by a constant thickness and their dielectric substrate are usually in the range $2.2 \leq \epsilon_r \leq 12$. The largest ground planes will produce more stable patterns and lower environmental sensitivity and this will course to make the antenna bigger. This is not uncommon for the ground plane to be larger than the active patch.

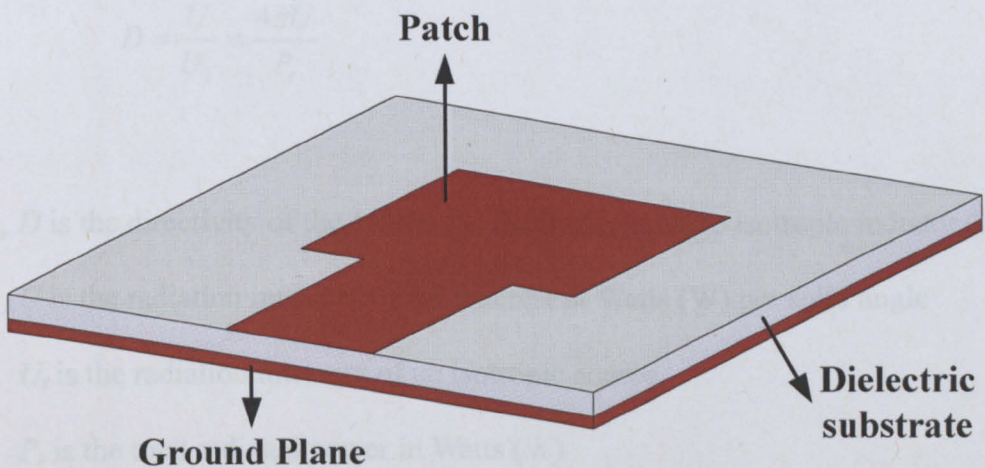


Figure 3.6: Microstrip patch antenna

This antenna can be fed via coaxial cable or waveguide transmission arrangement. The advantages for patch antenna are possible to generating sum and difference radiation patterns and this approach has been used with both semicircular and rectangular patches in combination. The disadvantages for this antenna are a low-profile, low gain, low power, low efficiency and narrow frequency bandwidth. The patch antenna is suitable

for planar and nonplanar surfaces, simple and low cost to manufacture using modern printed circuit technology. Patch antennas are simple to fabricate and easy to modify and customize. When a particular patch shape and mode are selected, they are very versatile in terms of resonant frequency, polarization, pattern and impedance.

3.5 Directivity and Gain

The directivity is a measurement of the concentration of radiated power in a particular direction. The directivity of an antenna has been defined by [100,101] as “the ratio of the radiation intensity in a given direction from the antenna to be radiation intensity averaged over all directions”. The directivity of a nonisotropic source is equal to the ratio of its radiation intensity in a given direction, over that of an isotropic source. The directivity is given in equation 3.4 [102],

$$D = \frac{U}{U_i} = \frac{4\pi U}{P_t} \quad (3.4)$$

where, D is the directivity of the antenna in decibel relative to isotropic radiator (dBi)

U is the radiation intensity of the antenna in Watts (W) per solid angle

U_i is the radiation intensity of an isotropic source

P_t is the total radiated power in Watts (W)

Antenna gain is a parameter which closely related to the directivity of the antenna. The gain of an antenna has been defined by [103] as “the ratio of the radiation intensity in a given direction from the antenna to the total input power accepted by the antenna divided by 4π ”. If the direction is not specified, the direction of maximum radiation is implied. The gain is given in equation 3.5 [104],

$$G_g = \frac{4\pi U}{P_{in}} = \frac{P_t}{P_{in}} D = \eta_e D \quad (3.5)$$

where, G_g is the gain of the antenna in decibel (dB)

P_{in} is the total input power accepted by the antenna in watt (W)

η_e is the radiation efficiency factor of the antenna (equation 3.6) and is the ratio of the radiated power to the input power accepted by the antenna.

$$\eta_e = \frac{P_t}{P_{in}} \quad (3.6)$$

3.6 Antenna Used for the Project

A monopole antenna with a length of 50mm and a loop antenna with a diameter of 28mm were used in this project. The material for the antenna was copper and the conductivity is 5.8×10^7 S/m [105]. The reason for using 50mm monopole antenna will be discussed more detail in chapter 4 and those for the 28mm diameter loop antenna will be discussed in chapter 5. Figure 3.7 shows the monopole antenna that was used in this project.

The wavelength of this monopole antenna can be calculated by using the equation 3.1.

Therefore,

$$\frac{\lambda}{4} = L$$

$$\lambda = 4(0.05) = 0.2m$$

The frequency of this monopole antenna can be calculated by using the equation 3.2,

$$f = \frac{3 \times 10^8}{0.2} = 1.5 \text{GHz}$$

If the monopole antenna is in water, then the wavelength of this antenna is reduced by a factor $\sqrt{\epsilon_r \mu_r}$, where ϵ_r is the relative permittivity in F/m , and μ_r is the relative permeability in H/m . The ϵ_r for the water at room temperature is 81 and μ_r is 1. The conductivity for fresh water is 0.01 S/m [105]. Therefore, the frequency in water can be calculated as,

$$f = \frac{c}{\sqrt{\epsilon_r \mu_r} \cdot \lambda} = \frac{3 \times 10^8}{\sqrt{81 \times 1} \times 0.2} = 167 \text{MHz}$$

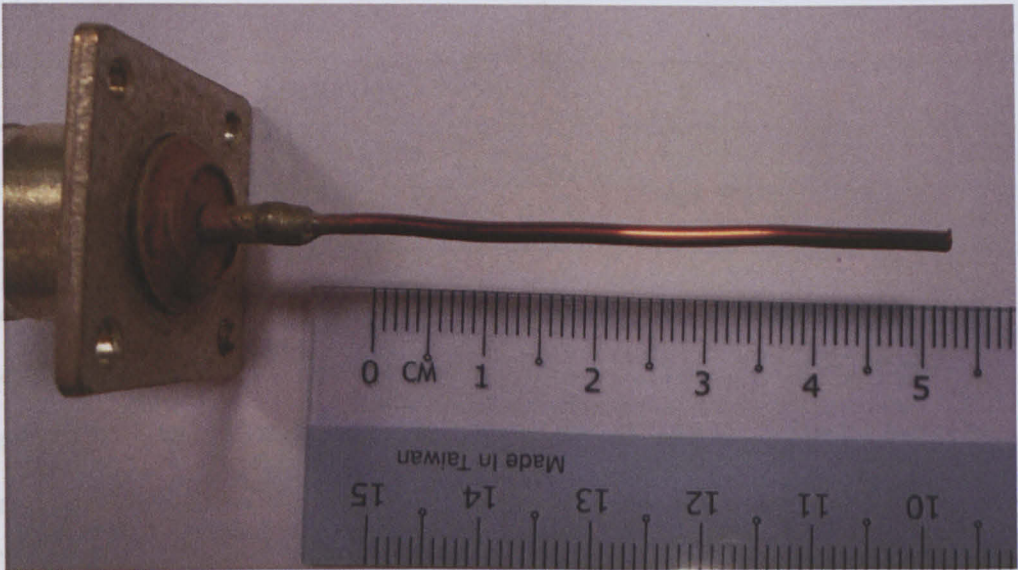


Figure 3.7: Monopole antenna with 50mm of length

The monopole antenna shown in Figure 3.7 was connected to a VNA via a coaxial cable which as shown in Figure 3.8. The water tank is filled with water and the measurement for the antenna was taken in air and water. Figure 3.9 shows the reflection magnitude $|S_{11}|$ for the antenna in air. The best transmission frequency for this monopole antenna was found to be 1.55GHz, which is close to the theoretical frequency of 1.5GHz.

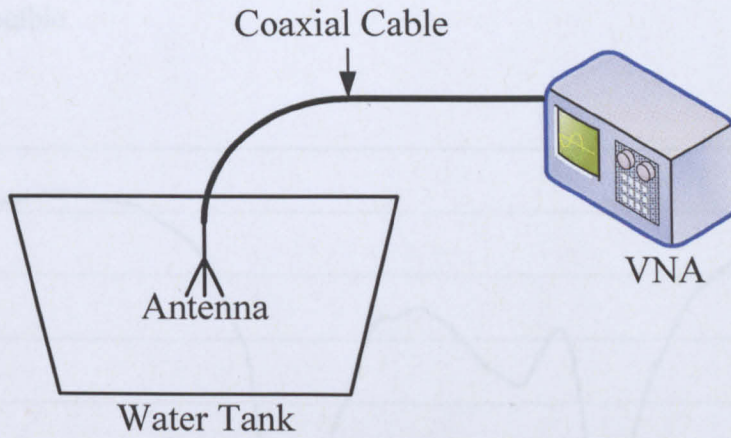


Figure 3.8: Experimental for antenna measurement

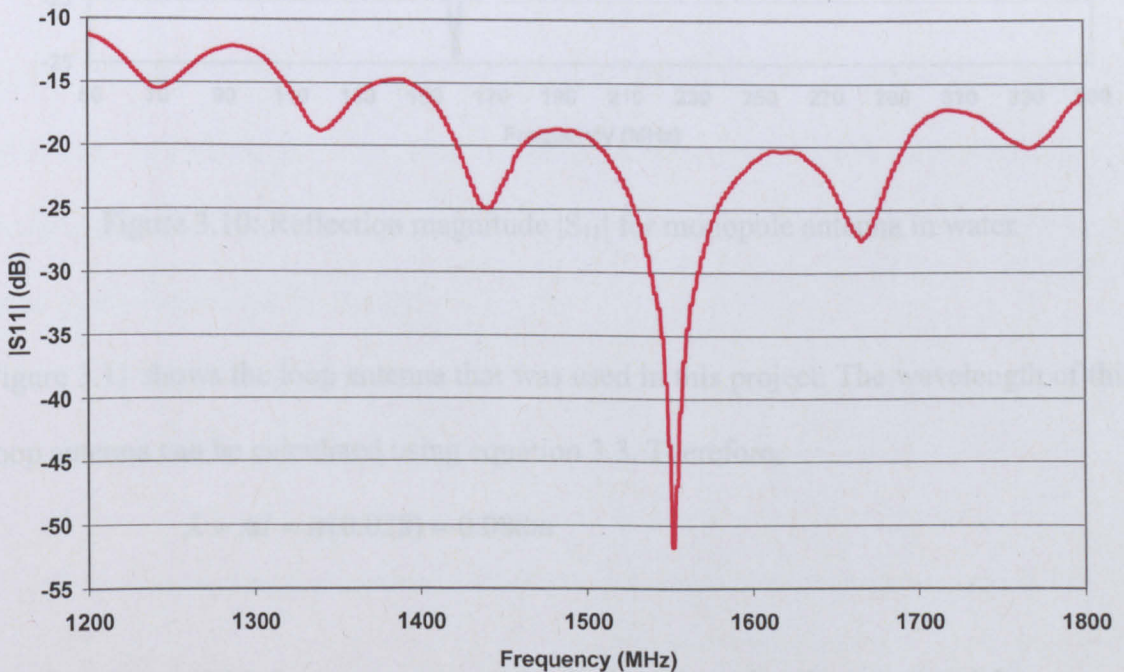
Figure 3.9: Reflection magnitude $|S_{11}|$ for monopole antenna in atmosphere

Figure 3.10 shows the reflection magnitude $|S_{11}|$ for a monopole antenna in water. The best transmission frequency for this monopole antenna in water was 160MHz. and from the theoretical frequency is 167MHz, this is because of the relative permittivity and the temperature (16°C) for the water is slightly different in practical, and the monopole

antenna which made is not perfectly straight enough, but the 160MHz from practical is consider acceptable.



Figure 3.10: Reflection magnitude $|S_{11}|$ for monopole antenna in water

Figure 3.11 shows the loop antenna that was used in this project. The wavelength of this loop antenna can be calculated using equation 3.3. Therefore,

$$\lambda = \pi d = \pi(0.028) = 0.088m$$

The frequency of this loop antenna can be calculated by using the equation 3.2,

$$f = \frac{c}{\lambda} = \frac{3 \times 10^8}{0.088} = 3.4GHz$$

Then, the frequency in water can be calculated as,

$$f = \frac{c}{\sqrt{\epsilon_r \mu_r} \cdot \lambda} = \frac{3 \times 10^8}{\sqrt{81 \times 1} \times 0.088} = 379MHz$$

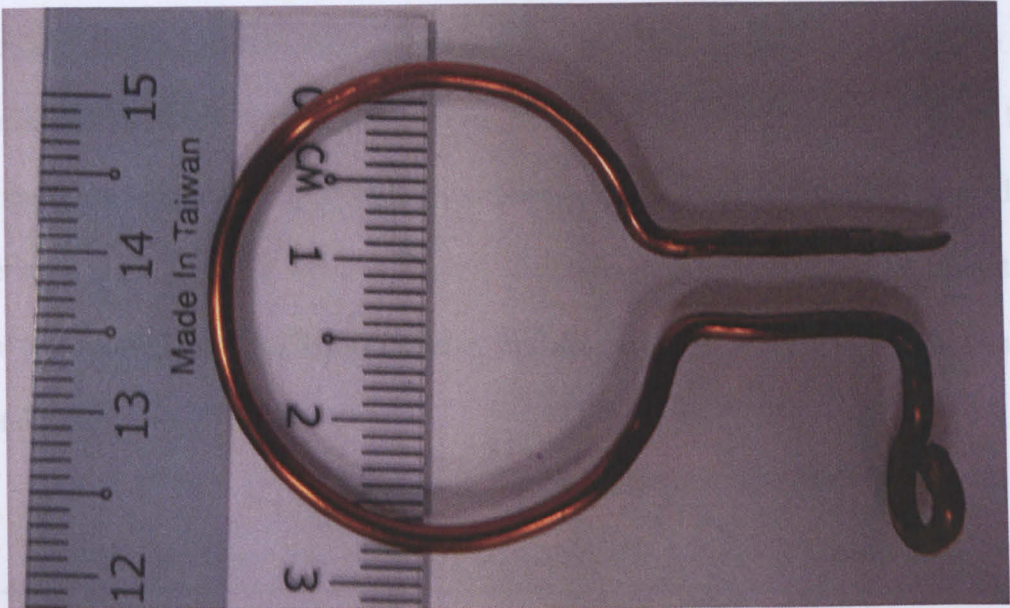


Figure 3.11: Loop antenna with 28mm of diameter

Again, the loop antenna shown in Figure 3.11 was attached to the VNA to see the reflection magnitude $|S_{11}|$ for loop antenna in atmosphere. The best transmission frequency for this loop antenna was 3.4GHz as shown in Figure 3.12, which is exactly same as the theoretical frequency.

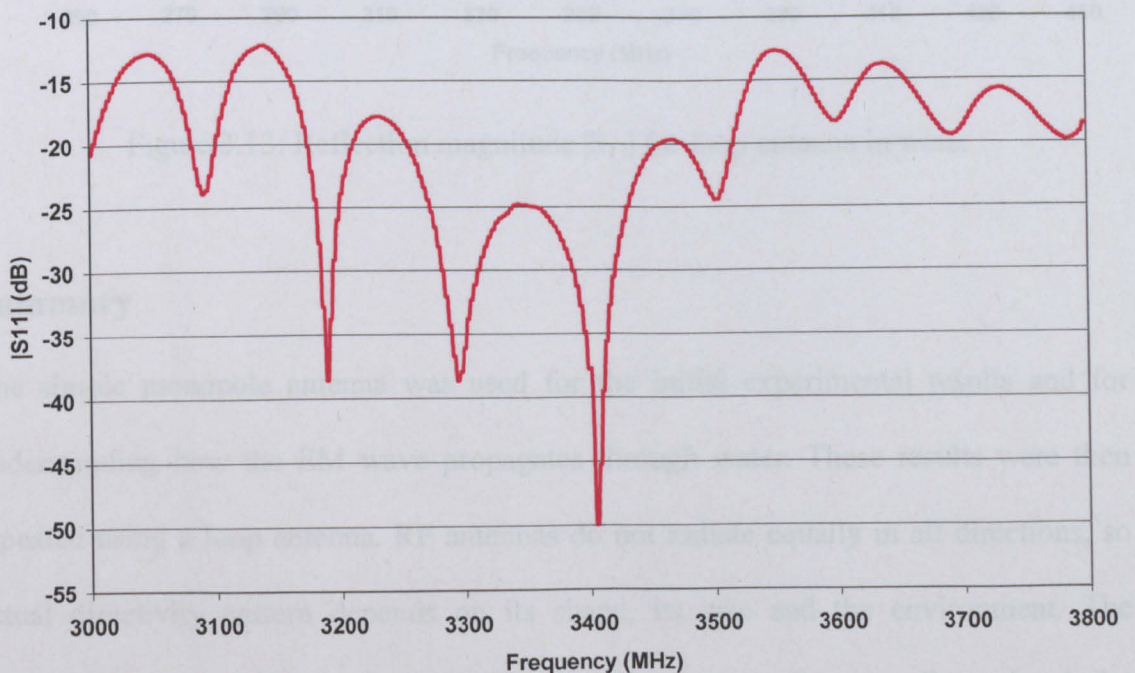


Figure 3.12: Reflection magnitude $|S_{11}|$ for loop antenna in atmosphere

Figure 3.13 shows the reflection magnitude $|S_{11}|$ for loop antenna in water. The best transmission frequency for this loop antenna in water was 360MHz. This different from the theoretical frequency (379MHz), because of the relative permittivity and the temperature (16°C) for the water is slightly different in practical, and the loop antenna which was made is not perfectly circular, but the 360MHz from practical is consider acceptable.

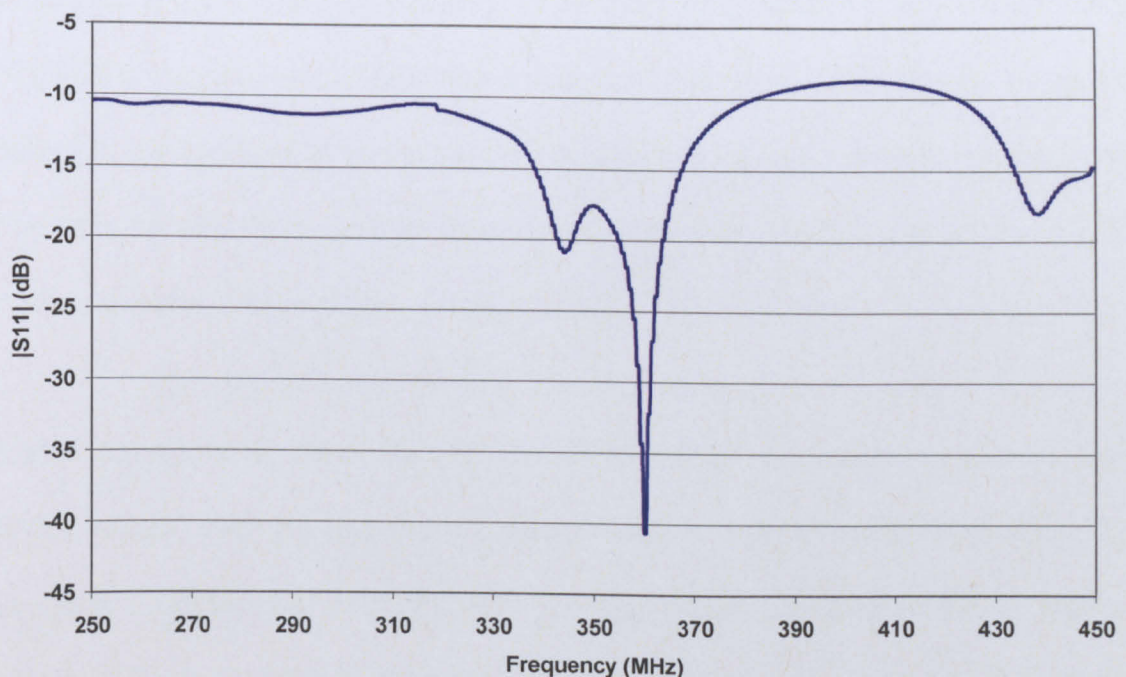


Figure 3.13: Reflection magnitude $|S_{11}|$ for loop antenna in water

Summary

The simple monopole antenna was used for the initial experimental results and for understanding how the EM wave propagates through water. These results were then repeated using a loop antenna. RF antennas do not radiate equally in all directions, so actual directivity pattern depends on its shape, its size and the environment. The directivity can be shown using a polar diagram. This is normally a two dimensional plot around an antenna showing the intensity of the radiation at each point for a particular

plane. The peak frequency for the 50mm monopole antenna was 167MHz by calculation, and 160MHz by experiment, a 4.2% difference. For the loop antenna which had a diameter of 28mm, the peak frequency was 379MHz by calculation, but 360MHz by experiment, a 5% difference. Therefore, there is good agreement for the best transmission frequency between the theoretical calculation and experimental results.

Chapter 4: High Frequency Structure Simulator (HFSS) and LabVIEW

4.1 High Frequency Structure Simulator (HFSS)

High Frequency Structure Simulator (HFSS) is a 3D full wave electromagnetic field simulation software which can be used to designed RF structures [106]. The advantage of HFSS is that it allows complex geometries to be created. HFSS can also be used to design IC packages, PCB interconnects, antennas and RF and microwave components. The outputs of HFSS include S-parameter, Full-Wave SPICE extraction and 3D electromagnetic field simulation [107].

Figure 4.1 shows the flow chart for the HFSS design and simulation process. Each HFSS design [108,109] includes a geometric model, with material assignments. The boundary condition and excitation setup enables planes, faces, or interfaces between objects to be assigned material properties, or designated as a wave port. The solution type and frequency range are required before the design can be simulation. The analysis process then automatically creates a mesh for the design and solves Maxwell's equation using the design parameters. It repeats this process as required using a higher resolution mesh until the results converge. Finally the output is presented as 2D or 3D reports and field plots. Figure 4.2 shows the main window for HFSS. Figure 4.3 shows the material selection window. The parameters such as permittivity and conductivity for each material are shown. Users can also add their own materials if they are not provided in the database.

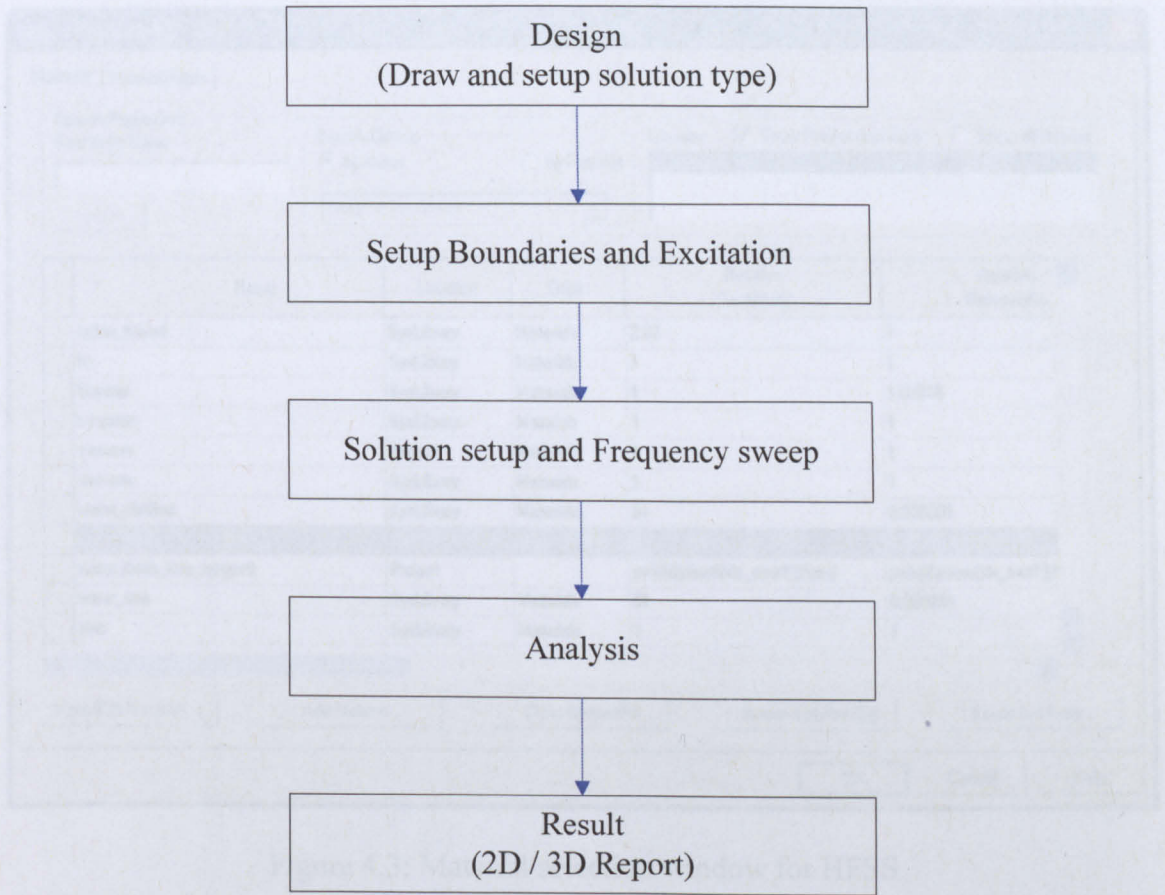


Figure 4.1: Flow chart for the HFSS design and simulation process

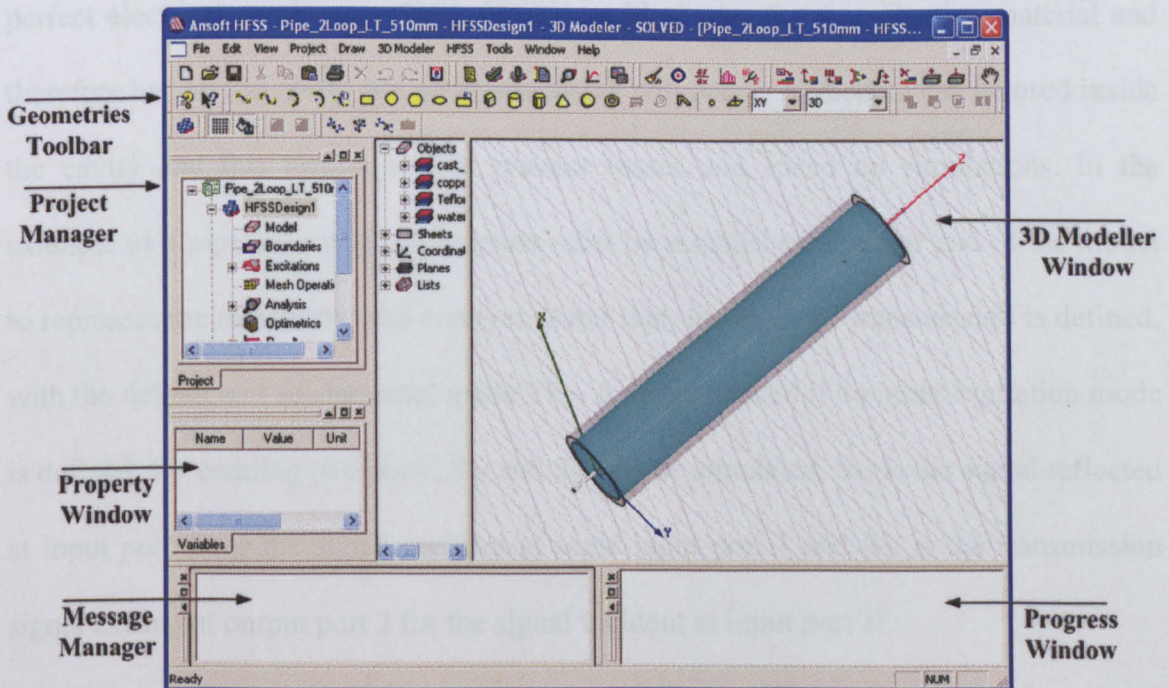


Figure 4.2: Main window for HFSS

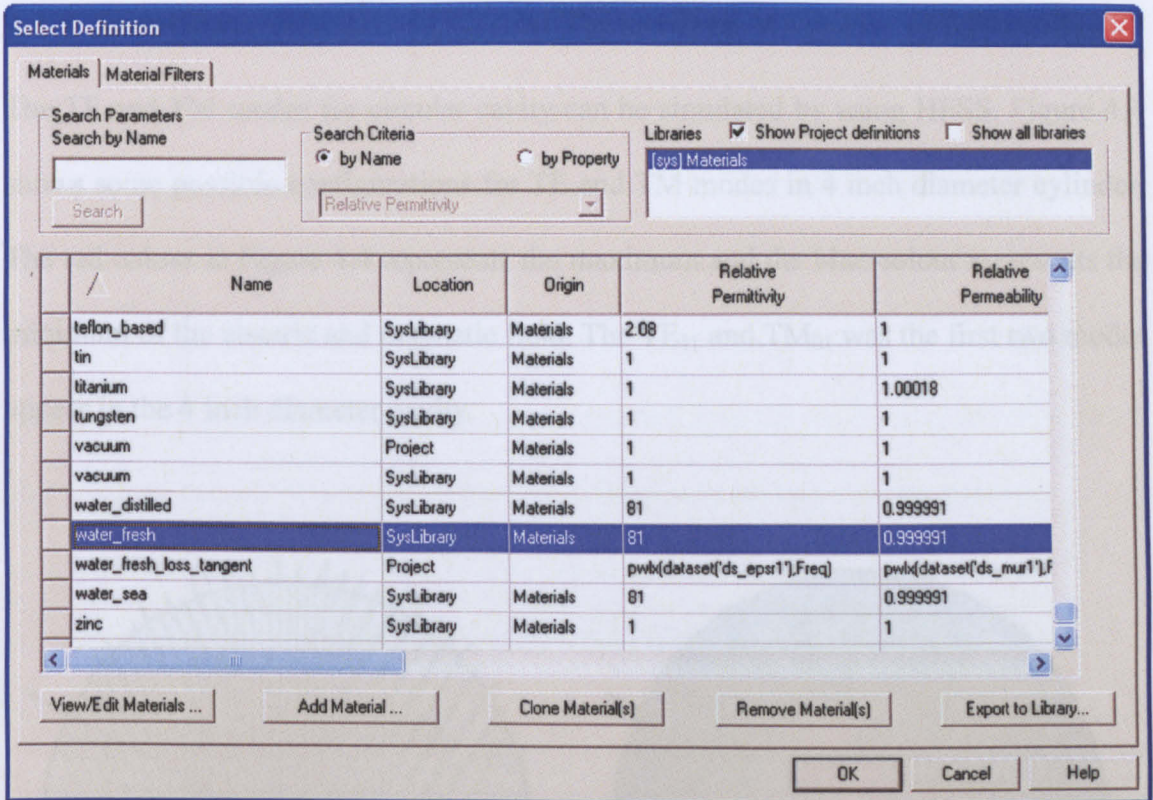


Figure 4.3: Material selection window for HFSS

One of the materials is available to create the walls of a waveguide or a cavity is called perfect electrical conductor (PEC). PEC is an ideal case for a conductive material and therefore has no resistivity and no ohmic losses will occur. A vacuum can be used inside the cavity and this technique will prevent losses and speed up simulations. In the example of a pipeline cavity, wave ports must be established at either end of the model to represent the transmitter and receiver. After that, the mode of transmission is defined, with the default and fundamental mode TE_{11} for pipe created if no other excitation mode is defined. By creating two ports, S_{11} and S_{21} can be simulated. S_{11} is the signal reflected at input port 1 for the signal incident at same input port 1 and S_{21} is the transmission signal exiting at output port 2 for the signal incident at input port 1.

4.1.1 Transverse Electric (TE) and Transverse Magnetic (TM) modes

The TE and TM modes for circular cavity can be simulated by using HFSS. Figure 4.4 shows some possible configurations for TE and TM modes in 4 inch diameter cylinder. The red colour in Figure 4.4 represents the maximum and the blue colour represents the minimum of the electric and magnetic field. The TE_{11} and TM_{01} was the first two modes appear in the 4 inch diameter cavity.

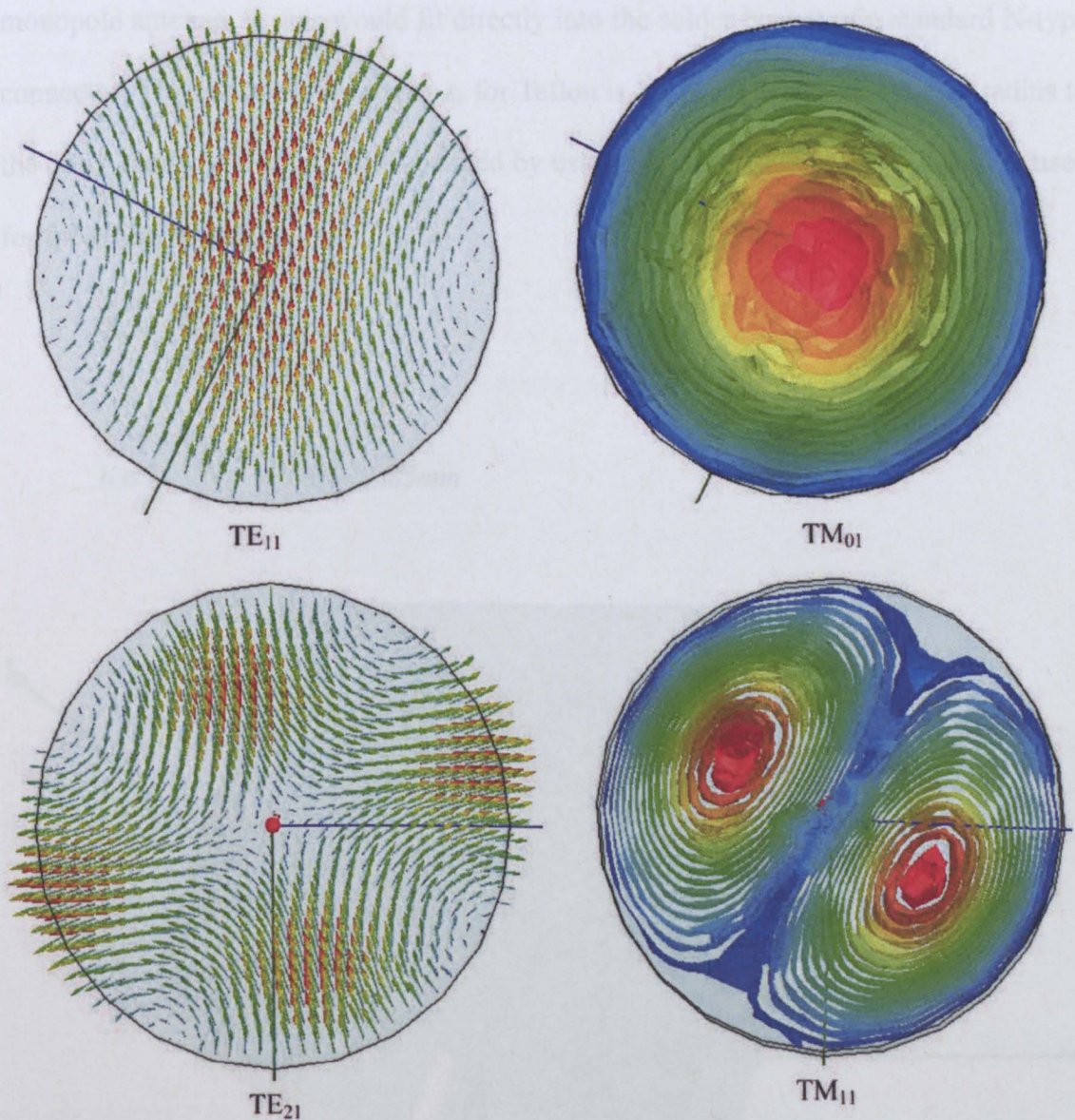


Figure 4.4: TE and TM mode in 4 inch diameter cylinder

4.1.2 A Simple Monopole Antenna Design

The simple monopole antenna for this project can be designed by using the HFSS software. Figure 4.5 shows the monopole antenna design using HFSS simulation. A 4 inch diameter cast iron cylinder with a length of 510mm was filled with fresh water and two monopole antennas were connected by 50Ω coaxial cable in each port. The monopole antenna's effectiveness at coupling power into the fresh water depends on the length of antenna. For practical reasons, 1.7mm was chosen for the diameter of the monopole antenna, as this would fit directly into the solder bucket of a standard N-type connector. The relative permittivity ϵ_r for Teflon is 2.1 [105]. Then the internal radius to the outer conductor 'b' can be calculated by using equation 2.8 and this radius was used for the HFSS modeling.

$$Z_0 = \frac{60}{\sqrt{\epsilon_r}} \ln \frac{b}{a}$$

$$b = e^{\left(\frac{50 \times \sqrt{2.1}}{60}\right)} \times 0.85 = 2.85 \text{mm}$$

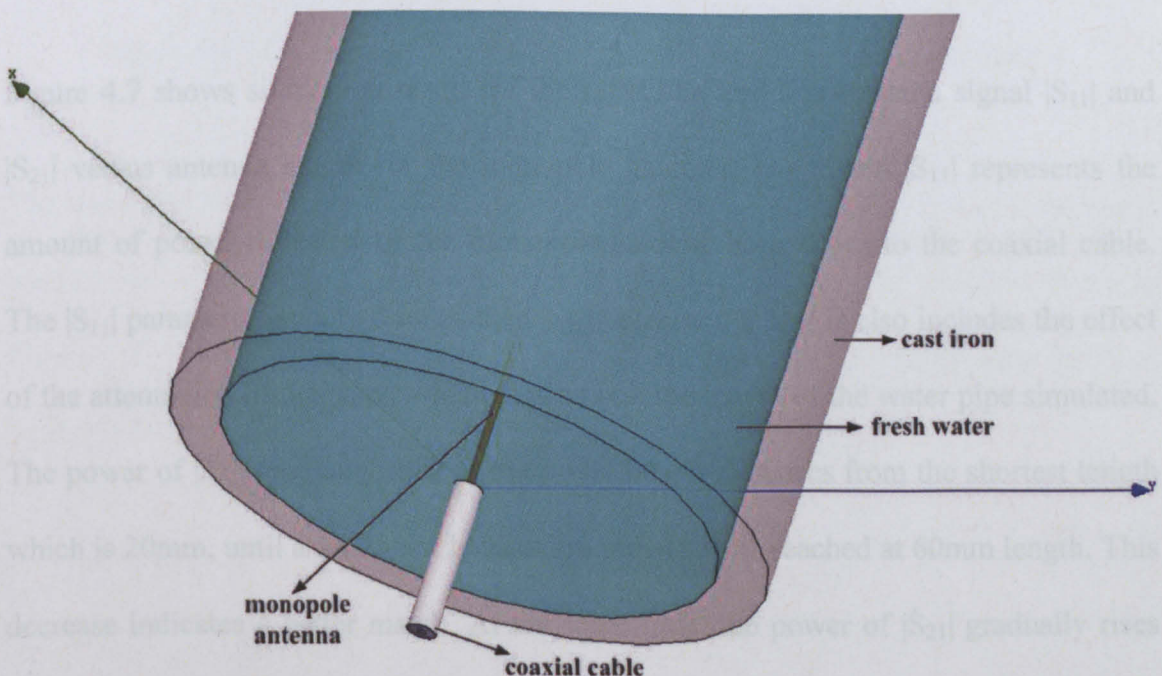


Figure 4.5: Monopole antenna design by HFSS simulation

The simulation was carried out with the length of the antenna are a variable for a frequency of 320MHz. The 320MHz frequency is the minimum attenuation level for the 4 inch cast iron pipe which is shown in Figure 4.6.

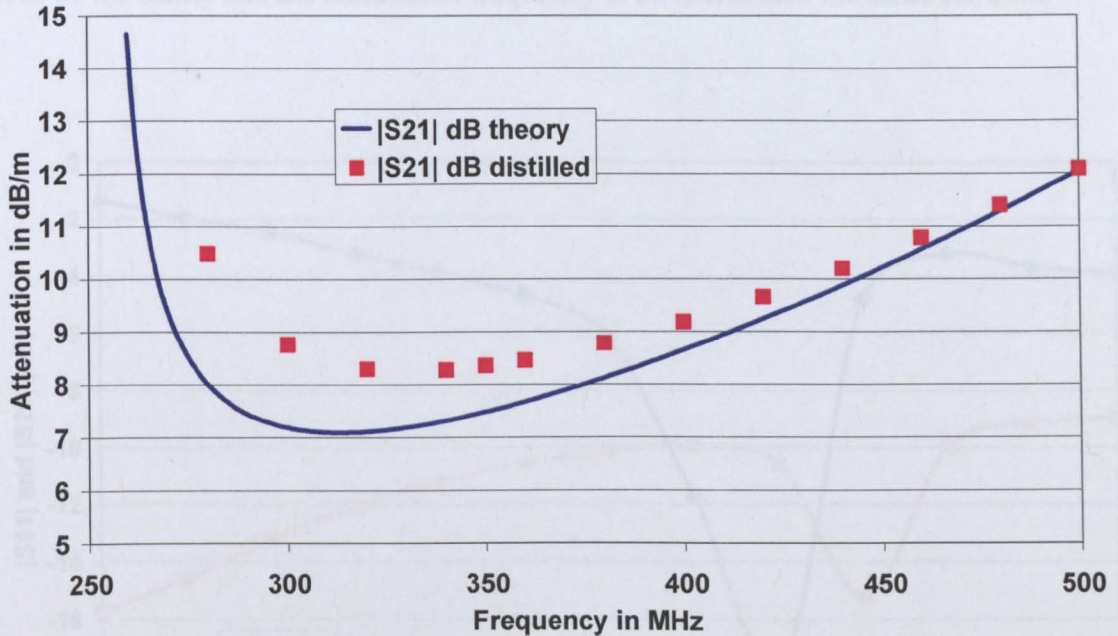


Figure 4.6: The variation of the attenuation for the TM_{01} mode in a 4 inch cast iron pipe filled with distilled water [110]

Figure 4.7 shows simulation result for the reflection and transmission signal $|S_{11}|$ and $|S_{21}|$ versus antenna length for the monopole antenna. The signal $|S_{11}|$ represents the amount of power reflected by the monopole antenna back down to the coaxial cable. The $|S_{11}|$ parameter is more interest than $|S_{21}|$ because the $|S_{21}|$ is also includes the effect of the attenuation of the water which depends on the length of the water pipe simulated. The power of $|S_{11}|$ gradually falls as the probe length increases from the shortest length which is 20mm, until a minimum level at around -18dB is reached at 60mm length. This decrease indicates a better match. At the same time, the power of $|S_{21}|$ gradually rises from a low level at around -16dB when the length of the antenna is 20mm, until a

maximum level at around -10dB is reached at 55mm length. This indicates a better transmission. Therefore, it is possible to choose two antenna lengths having the same value for $|S_{21}|$ on either side of the minimum but having two very different values of $|S_{11}|$. For both these probe lengths, the attenuation in the water and cast iron pipe wall will be the same, and the simulation frequency is 320MHz also the same for both.

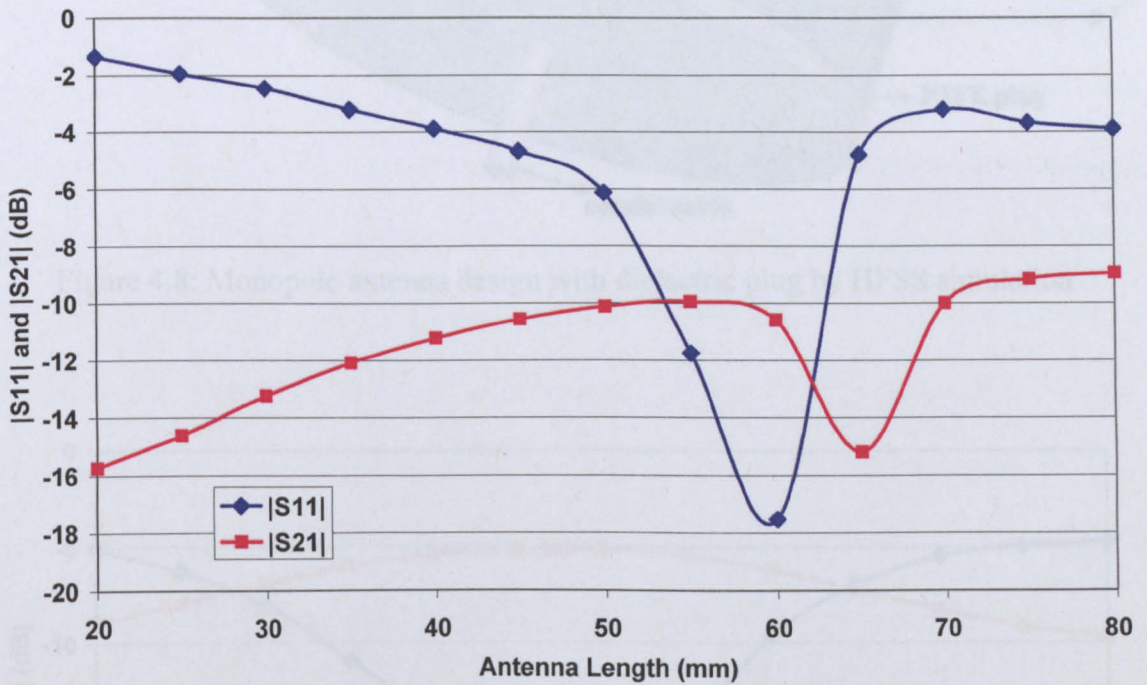


Figure 4.7: $|S_{11}|$ and $|S_{21}|$ signal versus antenna length by HFSS simulation

The transition from the TEM mode in the coaxial cable to the TM_{01} mode in the water pipe can be substantially eased by the introduction of a dielectric plug which is shown in Figure 4.8. The simulation result of $|S_{11}|$ and $|S_{21}|$ versus antenna length using HFSS at 310MHz is shown in Figure 4.9.

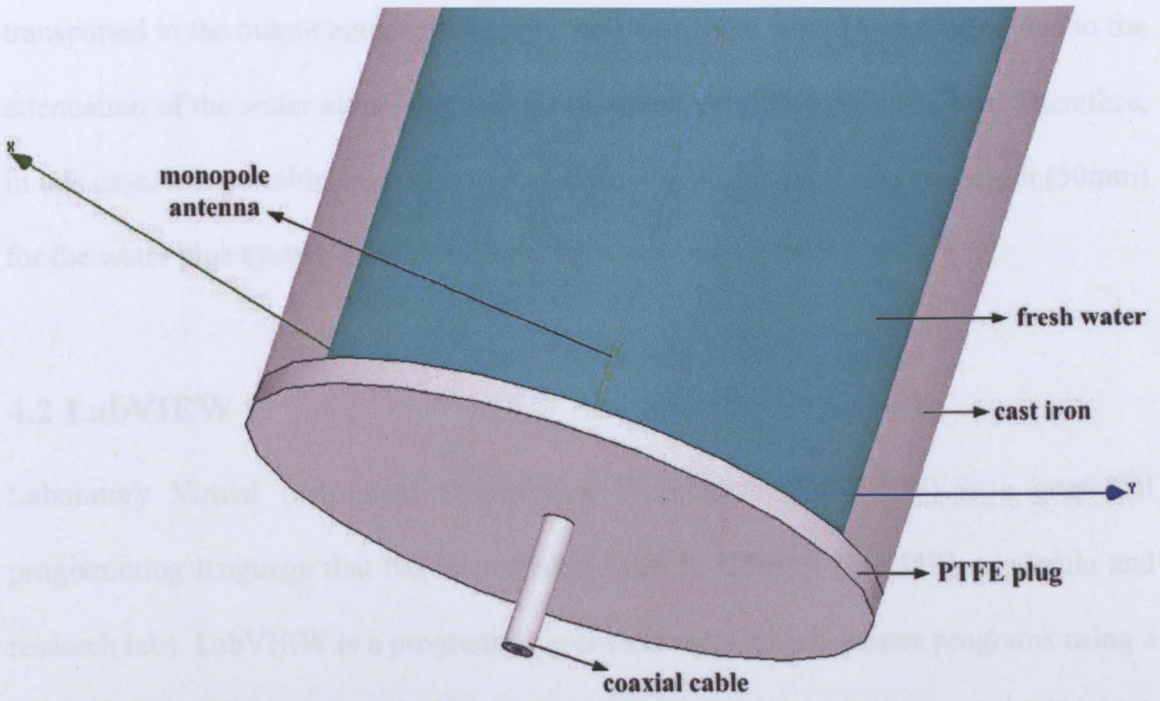


Figure 4.8: Monopole antenna design with dielectric plug by HFSS simulation

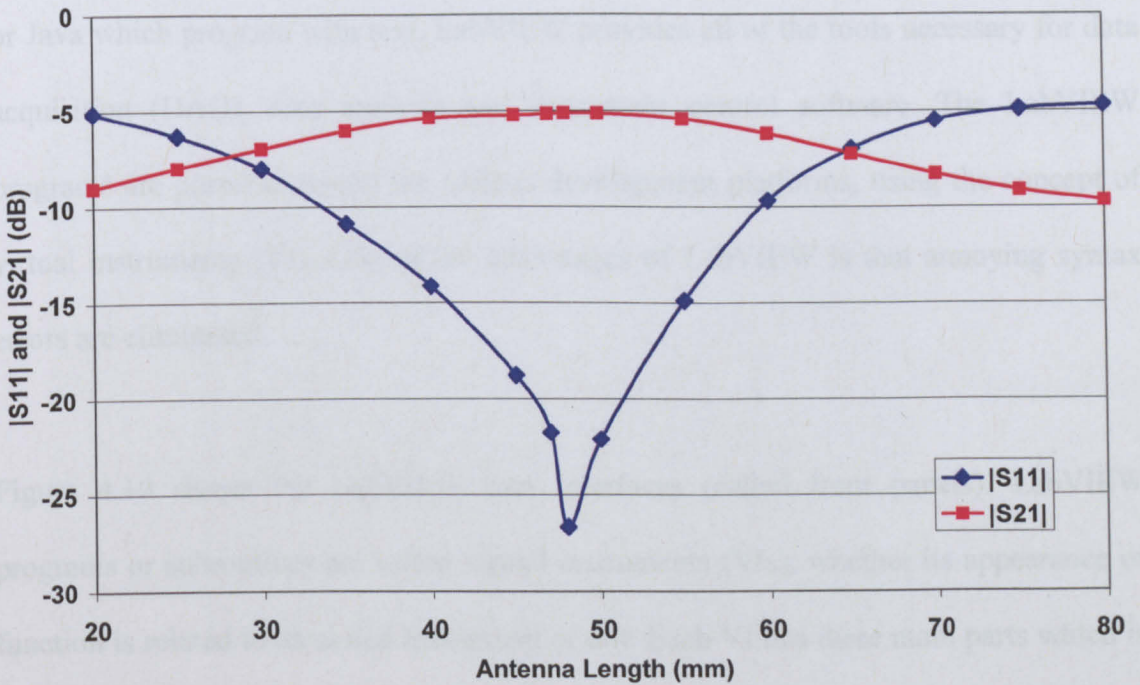


Figure 4.9: $|S_{11}|$ and $|S_{21}|$ signal versus antenna length with dielectric plug

As can be seen the results do not show the anomalies observed in Figure 4.7, and when the antenna length is well matched which is from 48mm to 50mm long, the power

transported to the output agrees reasonably well with what would be expected due to the attenuation of the water alone, this is indicating that very little power is lost. Therefore, in this case, it is possible to choose two antenna lengths having the same length (50mm) for the water pipe system and this will be discussed in chapter 5.

4.2 LabVIEW

Laboratory Virtual Instrument Engineering Workbench (LabVIEW) is a graphical programming language that has been widely used in industry [111,112], academia and research labs. LabVIEW is a programming environment which creates programs using a graphical notation in which functional nodes are connected via wires through which data flows. The graphical block diagram of a LabVIEW program is compiled into machine code. LabVIEW differs from traditional programming languages like C, C++ or Java which program with text. LabVIEW provides all of the tools necessary for data acquisition (DAQ), data analysis and instrument control software. The LabVIEW programs are portable among the various development platforms, using the concept of virtual instruments (VI). One of the advantages of LabVIEW is that annoying syntax errors are eliminated.

Figure 4.10 shows the LabVIEW user interfaces (called front panels). LabVIEW programs or subroutines are called virtual instruments (VIs), whether its appearance or function is related to an actual instrument or not. Each VI has three main parts which is a front panel, a block diagram, and an icon.

The front panel is the interactive user interface of a VI. The front panel can contain knobs, push buttons, graphs, and many other controls which are user inputs and indicators which are program outputs. Both the controls and indicators allow an

operator to input data into or extract data from a running virtual instrument. However, the front panel can also serve as a programmatic interface. Thus a virtual instrument can either be run as a program, with the front panel serving as a user interface, or, when dropped as a node onto the block diagram, the front panel defines the inputs and outputs for the given node through the connector pane. This implies each VI can be easily tested before being embedded as a subroutine into a larger program. The data can be inputted using a mouse and keyboard, and then view the results produced by the program on the screen.

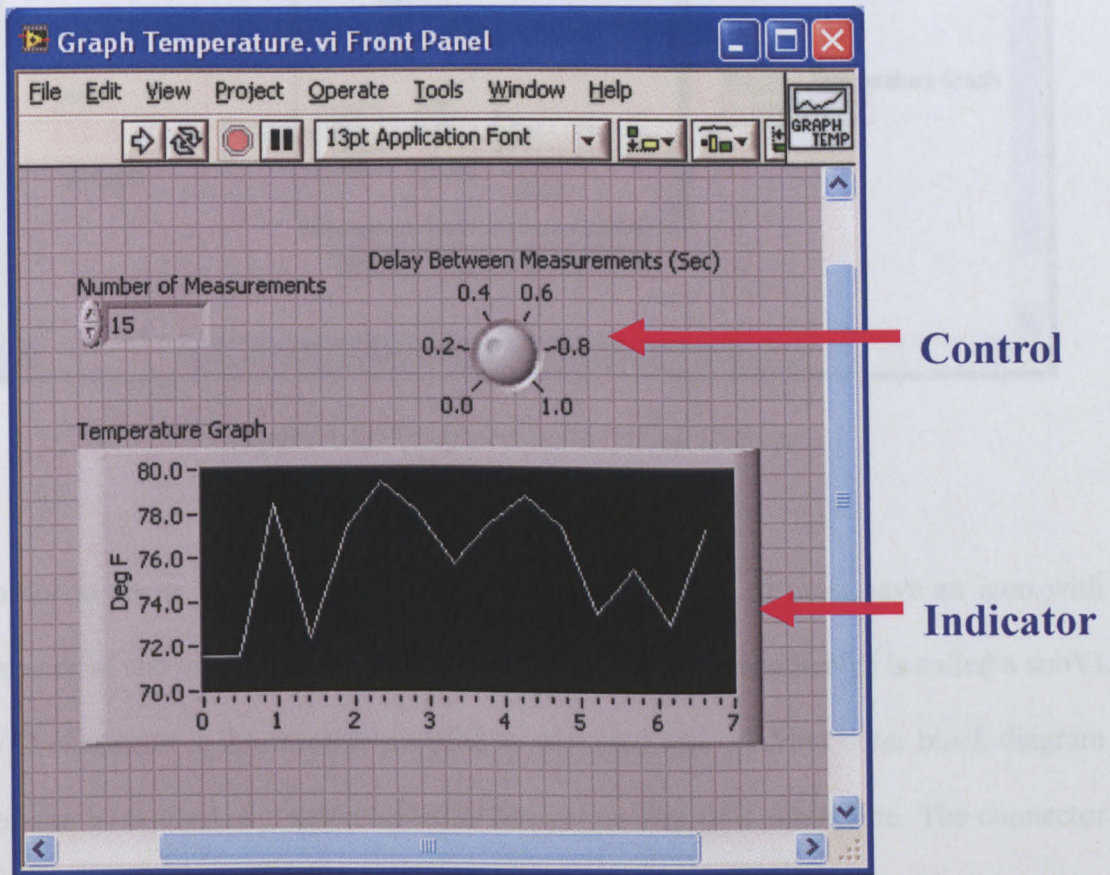


Figure 4.10: User interface (Front Panel)

The block diagram is the VI's source code which is constructed in LabVIEW's graphical programming language as shown in Figure 4.11. The block diagram is the actual executable program. The components of a block diagram are built-in functions,

constants, and program execution control structures. A wires was drew to connect the appropriate objects together to define the flow of data between two objects. The front panel objects have corresponding terminals on the block diagram, and therefore data can pass from the user to the program and back to the user.

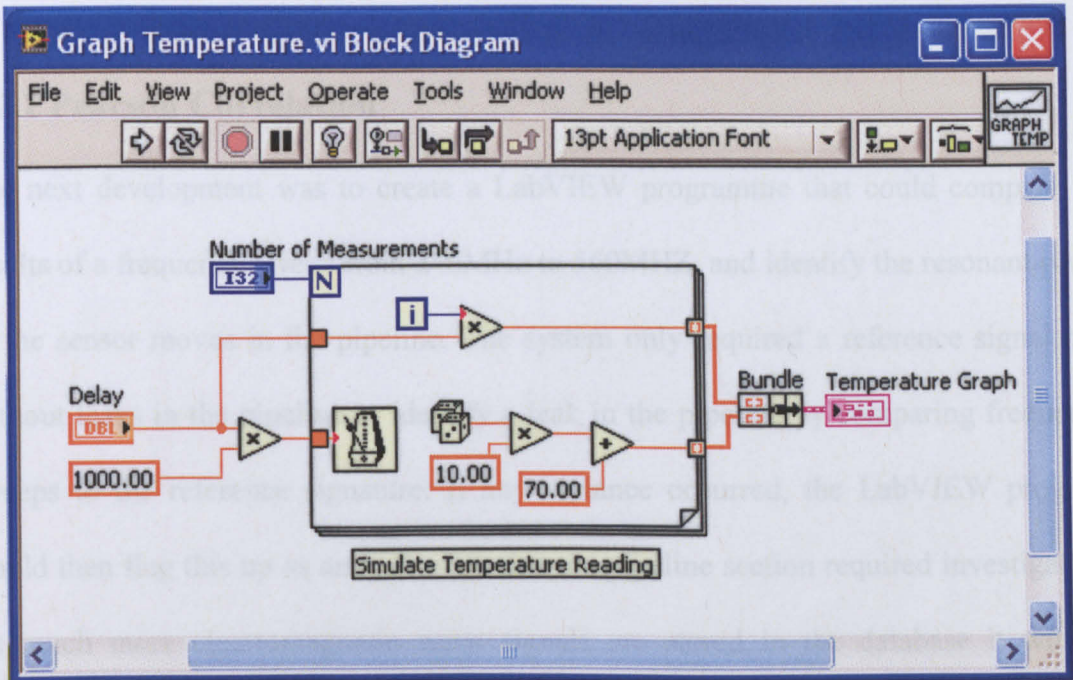


Figure 4.11: Graphical code (Block Diagram)

In order to use a VI as a subroutine in the block diagram, it must have an icon with connector as shown in Figure 4.12. A VI that is used within another VI is called a subVI. A VI's connector is the mechanism used to wire data into VI from other block diagram when the VI is used as a subVI much like parameters of a subroutine. The connector defines the inputs and outputs of the VI.

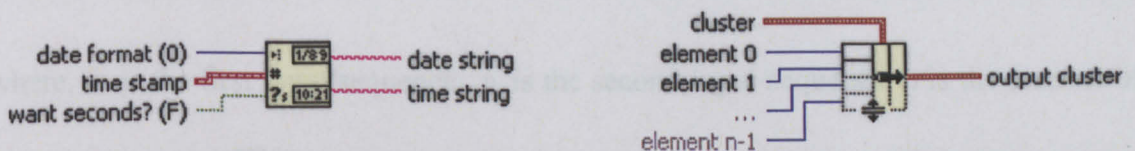


Figure 4.12: VI icons with connector

The graphical approach also allows non-programmers to build programs by dragging and dropping virtual representations of lab equipment with which they are already familiar. The LabVIEW programming environment, with the examples included and the documentation makes it simple to create small applications. The most advanced LabVIEW development systems offer the possibility of building standalone applications.

4.2.1 Pearson Correlation

The next development was to create a LabVIEW programme that could compare the results of a frequency sweep from 240MHz to 560MHz, and identify the resonant peaks as the sensor moves in the pipeline. The system only required a reference signal plot without leaks in the pipeline to identify a leak in the pipeline by comparing frequency sweeps to the reference signature. If any variance occurred, the LabVIEW program would then flag this up as an indication that the pipeline section required investigation. As much more electromagnetic wave signals are stored in the database it will be possible to have a catalogue of known discontinuities such as ‘T’ pieces, reducers and Perspex to cast iron pipe work.

Pearson correlation [113] is the most appropriate algorithm to use when comparing two data sets which map the amplitudes for both the frequency sweeps. The equation for correlation r is given by equation 6.1 [114],

$$r = \frac{n \sum xy - \sum x \sum y}{\sqrt{[n \sum x^2 - (\sum x)^2][n \sum y^2 - (\sum y)^2]}} \quad (4.1)$$

where, x is the first input sequence, y is the second input sequence, n is the number of ‘pairs’ of data and \sum is the summation.

The possible outputs will look like those shown in Figure 4.13. The gradients of the graphs indicate how the data sets are related. A gradient of +1 indicates that the data sets have perfect correlation, -1 indicates that the data sets have perfect negative correlation and 0 indicates that there is no correlation. Table 4.1 shows the general categories indicate the strength and significance [115] of the correlation coefficient r .

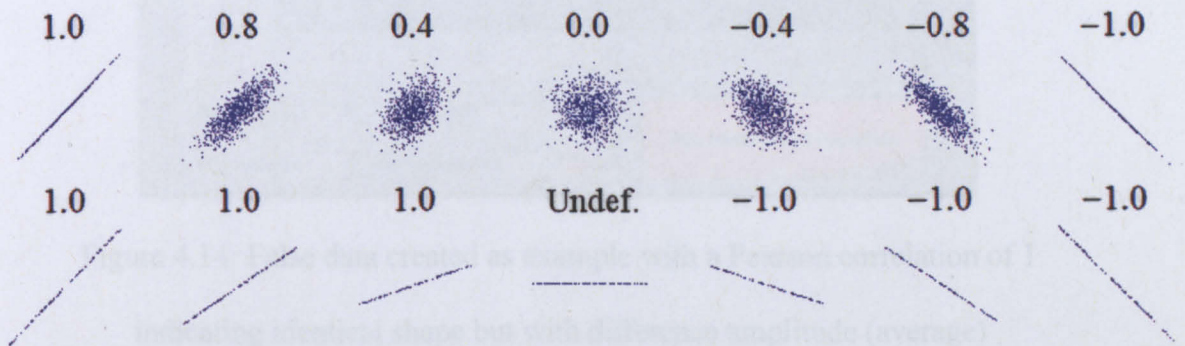


Figure 4.13: Possible Pearson correlation outputs [116]

Table 4.1: Strength and significance of the correlation coefficient r [117]

Coefficient, r	Strength and significance
0.0 to 0.2	Very weak to negligible correlation
0.2 to 0.4	Weak, low correlation (not very significant)
0.4 to 0.7	Moderate correlation
0.7 to 0.9	Strong, high correlation
0.9 to 1.0	Very strong correlation

Figure 4.14 shows the false data created as example of perfect correlation with an identical shape but with a difference in amplitude. The red panel shows inspection required. Therefore the mean of the data set is also used to distinguish between these sets. Figure 4.15 shows the false data created as example of data captured with identical shape and amplitude, therefore, the green panel shows no further inspection required.

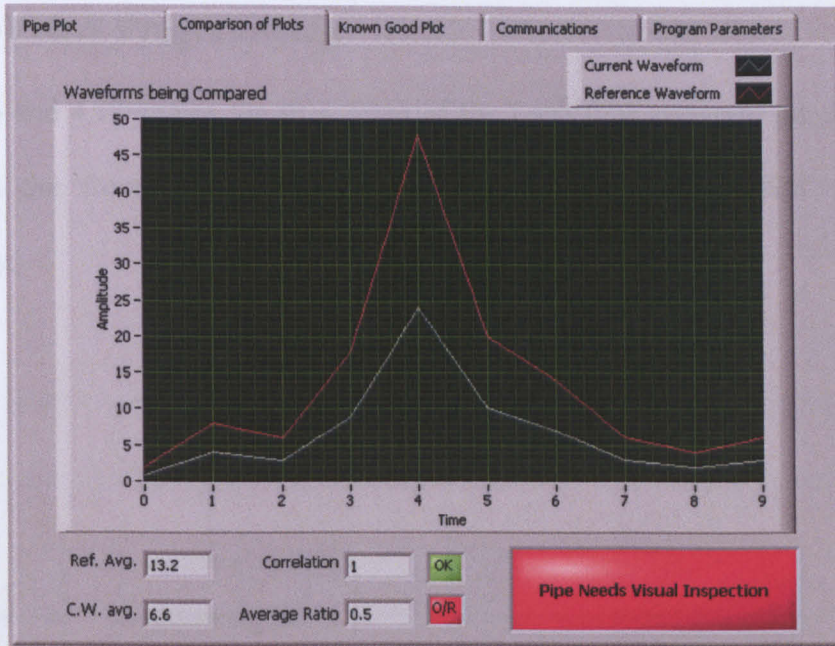


Figure 4.14: False data created as example with a Pearson correlation of 1 indicating identical shape but with difference amplitude (average) and the red panel indicates inspection required

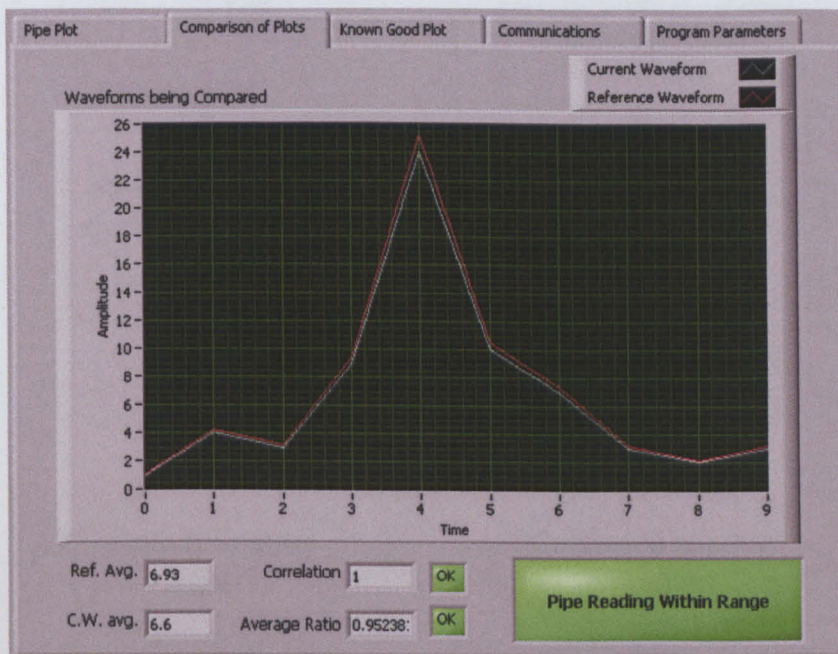


Figure 4.15: False data created as example with identical shape and amplitude therefore panel indicates no further inspection required

4.2.2 LabVIEW Programming

Figure 4.16 and 4.17 shows the flow chart of the LabVIEW program for the EM wave sensor and the front panel of the LabVIEW program for the EM wave sensor respectively.

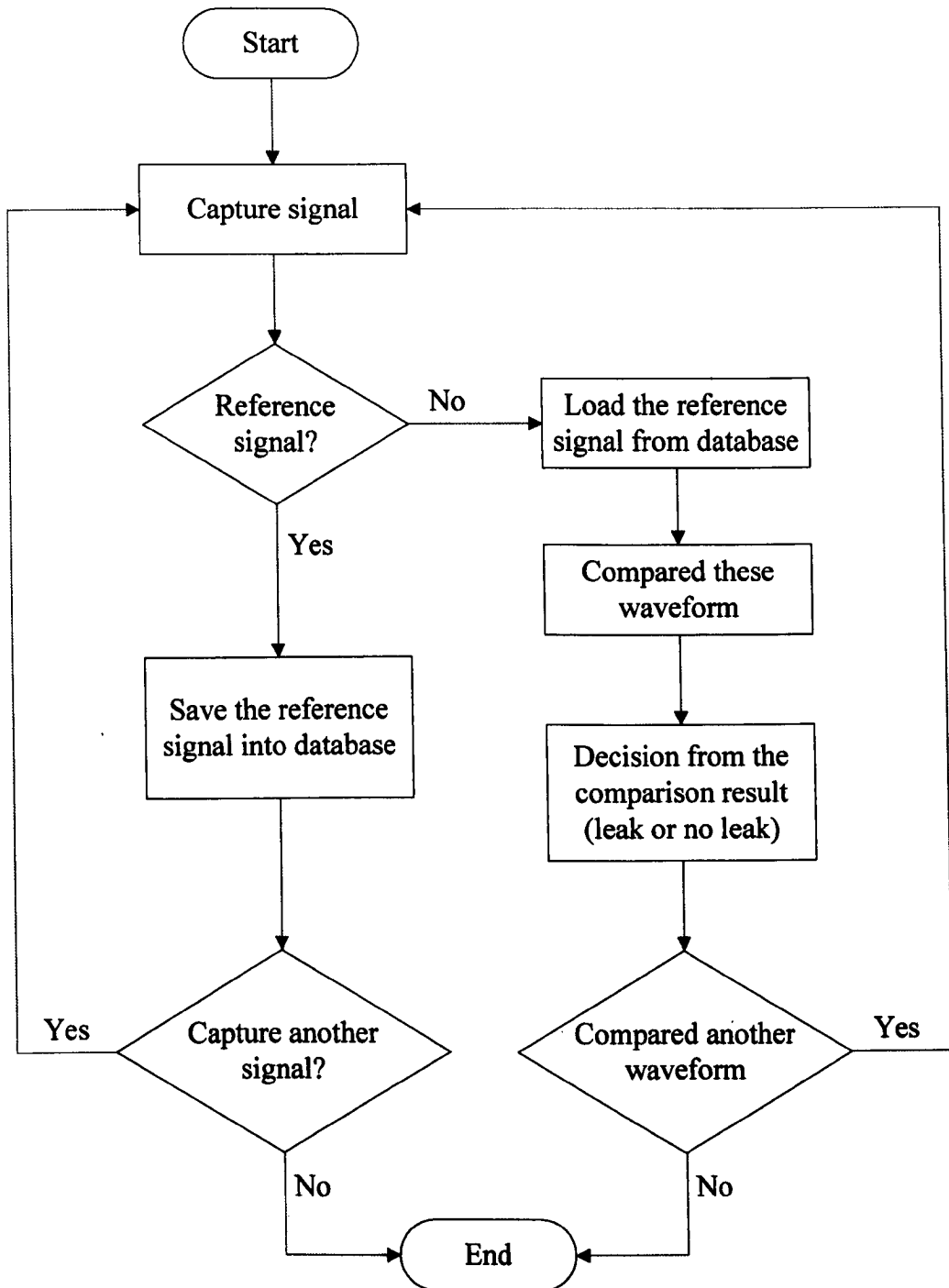


Figure 4.16: Flow chart for the LabVIEW program for the EM wave sensor

This programme is able to capture the output voltage supply from 0 to 8 volt and the detected voltage from 0 to 2 volt in capture tab. The spectrum for reflected signal $|S_{11}|$ is plotted in $|S_{11}|$ vs Frequency Plot tab. The $|S_{11}|$ Reference Plot tab is used to load the reference signal plot without leaks which is stored in a database. The final $|S_{11}|$ Waveform Compared tab is the decision panel which to indicate whether further inspection is required for the pipeline. The demonstration for this program will be discussed in chapter 7. The full source code for this LabVIEW programme is shown in appendix A.

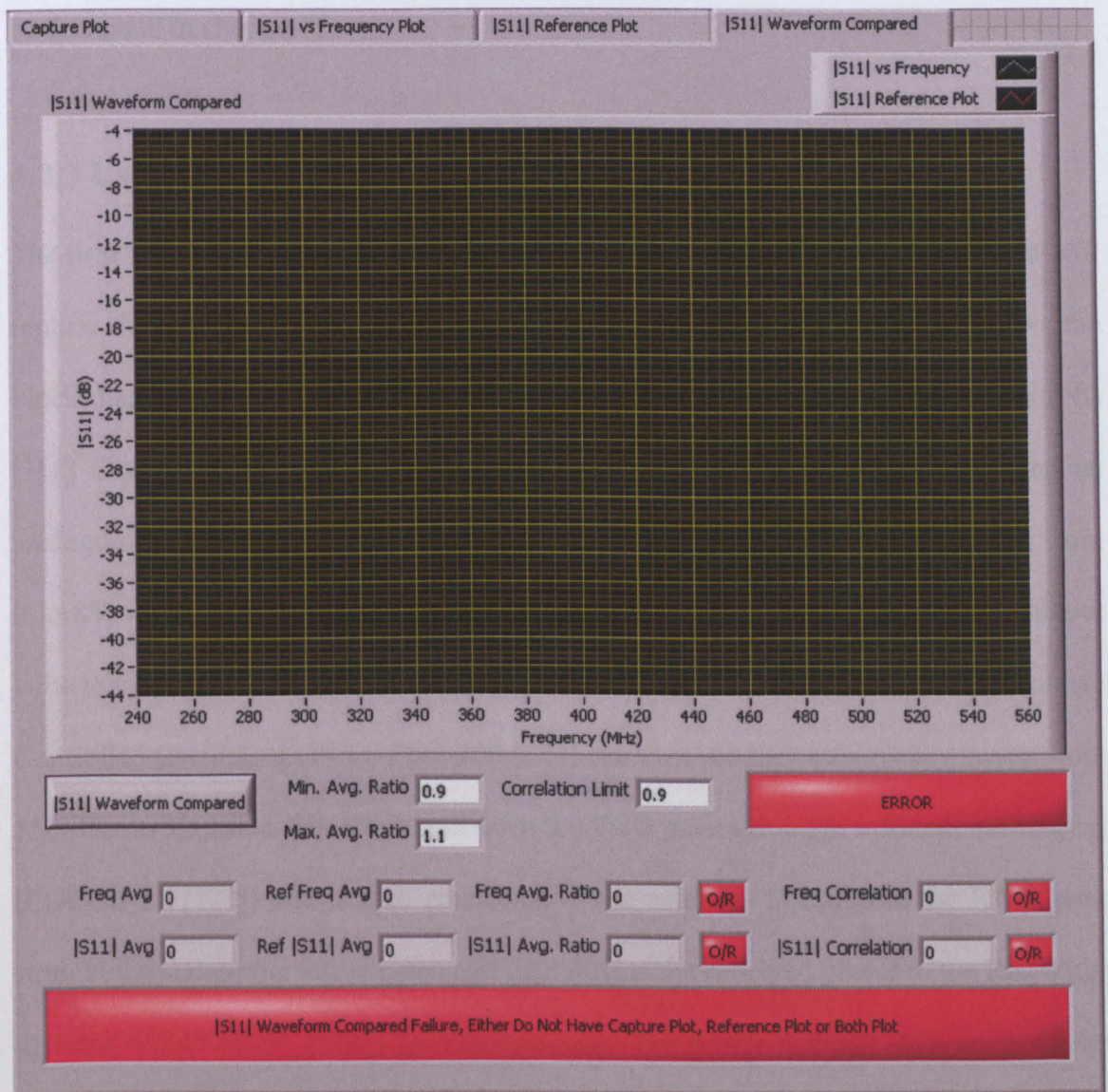


Figure 4.17: Front Panel of the LabVIEW program for the EM wave Sensor

From Table 4.1, the correlation coefficient 0.9 indicates as a very strong correlation. Therefore, this value was chosen for the initial correlation limit for this project. If this limit provided a poor relationship between the two sequences of data, then the limit would need to be reduced. If the limit provides a good relationship, then it is possible that the limit could be increased to ensure that the data sequences do match. It was found by experiment that the 0.9 limit provided a good relationship between the two sequences of data, but increasing the limit above 0.9 often provided a poorer relationship between the two sequences of data. Therefore, a correlation limit of 0.9 was found to be the best limit for this project. The experiment for the correlation limit will be discussed in chapter 7.

4.2.3 LabVIEW Control Systems

The next stage is to implement a LabVIEW control of the electronic modules that will replace the expensive VNA over the required frequency range. Figure 4.18 shows the block diagram of the LabVIEW system. The system uses a National Instruments (NI) [118] Compaq DAQ system with an analogue input module (NI9205 [119]) and an analogue output module (NI9264 [120]). This produces an output voltage ranging from 0 to 8V, which is then amplified. The amplifier (CA3140MZ [121]) produces an output voltage range from 0 to 16V which gives the full range of frequency output. The Voltage Controlled Oscillators (VCO) ZOS-300 [122] can then produce a frequency sweep from 130MHz to 320MHz. The RF output from the VCO passes through a directional coupler (ZDC-10-1+ [123]) and is then connected to the antenna. This allows the RF to pass straight through to the test antenna and then directs the reflected power to the RF power detector (ZX47-60-S+ [124]) for measurement. The power detector then converts the RF signal into a DC voltage. Finally the detected voltage is recorded by the analogue input module and the reflected signal $|S_{11}|$ plot is displayed and the LabVIEW program

will make a decision whether a leak is present. To test this system against the VNA a single section of pipeline was filled with water and a bent loop antenna end cap was used which is shown in Figure 4.19.

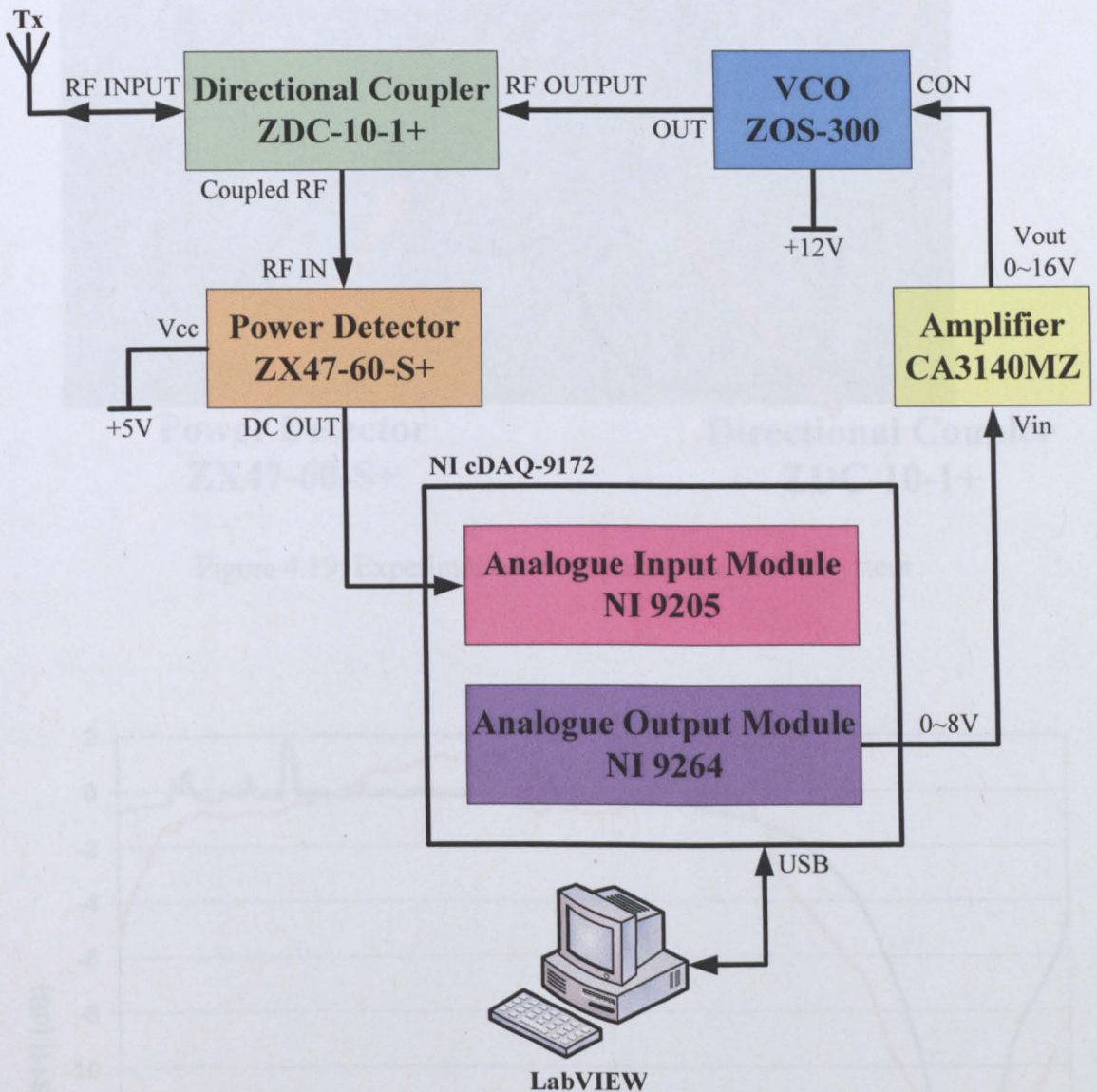


Figure 4.18: Block diagram of LabVIEW system

Figure 4.20 shows the comparison results between LabVIEW and the VNA. Both of the results are in very good agreement with each other and this shows that both the RF electronics setup and LabVIEW can successfully replace the VNA over this frequency range. This LabVIEW system will be used and discussed in chapter 6.

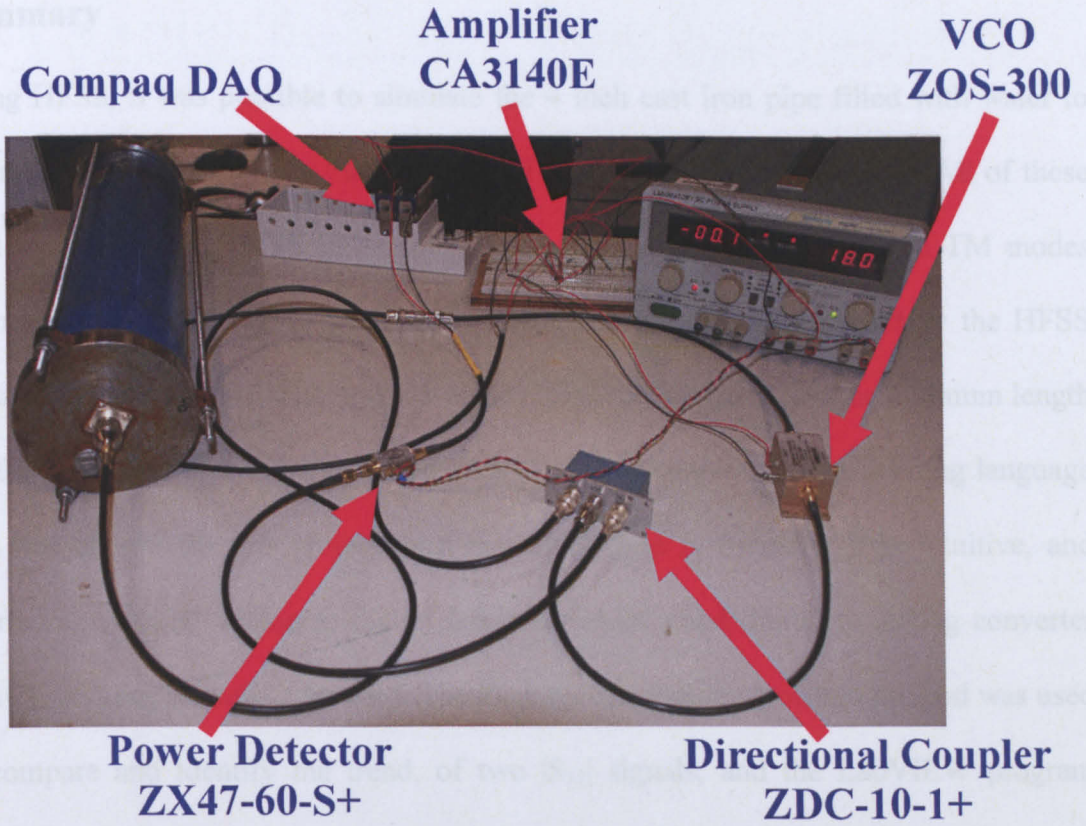


Figure 4.19: Experimental setup for the LabVIEW system

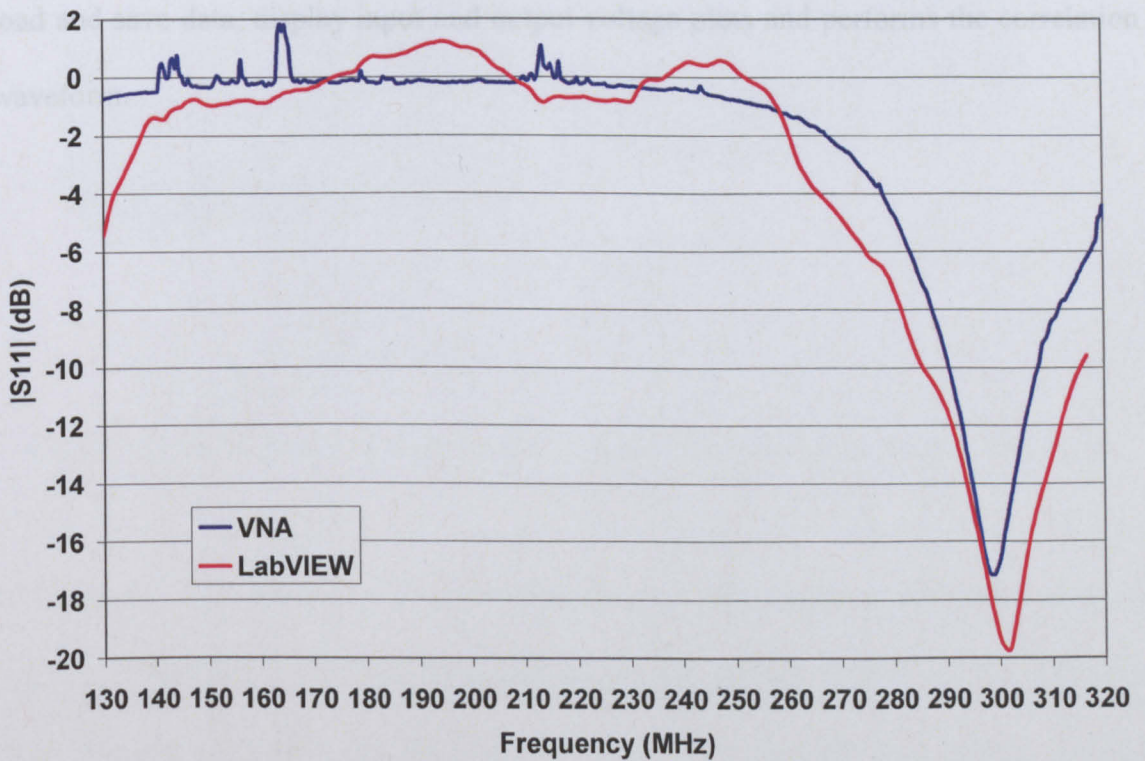


Figure 4.20: Comparison between LabVIEW and the VNA

Summary

Using HFSS, it was possible to simulate the 4 inch cast iron pipe filled with water to determine the resonances of the TE and TM modes in the circular cavity. All of these modes simulated by HFSS in Figure 4.4 are very similar to the TE and TM modes theoretical shown in Figure 2.22. This proves that the results produced by the HFSS simulation were reliable. The model was also used to determine that the optimum length for the monopole antenna was 50mm. LabVIEW is a graphical programming language that was chosen for this project as it is widely used in industry. It is intuitive, and interfacing with NI analog to digital converter (ADC) and digital to analog converter (DAC) modules is straight forward. The Pearson correlation algorithm method was used to compare and identify the trend, of two $|S_{11}|$ signals, and the LabVIEW program provided a decision on whether they matched. The RF electronics consider on individual components and modules and they were shown to successfully replace the expensive VNA equipment. The final LabVIEW program shown in Figure 6.7 could load and save data, display input and output voltage plots and performs the correlation waveform.

Chapter 5: Water Pipe Simulations,

Experiments and Results

5.1 Water Pipe Simulation for Monopole Antenna

Figure 5.1 shows the HFSS model of a 4 inch cast iron pipe with two 50mm monopole antennas. The pipe is filled with fresh water. The length for the cast iron is 510mm long. This simulation performed a virtual frequency sweep and plotted the amplitude response in dB for both $|S_{11}|$ and $|S_{21}|$ which are shown in Figures 5.2 and 5.3.

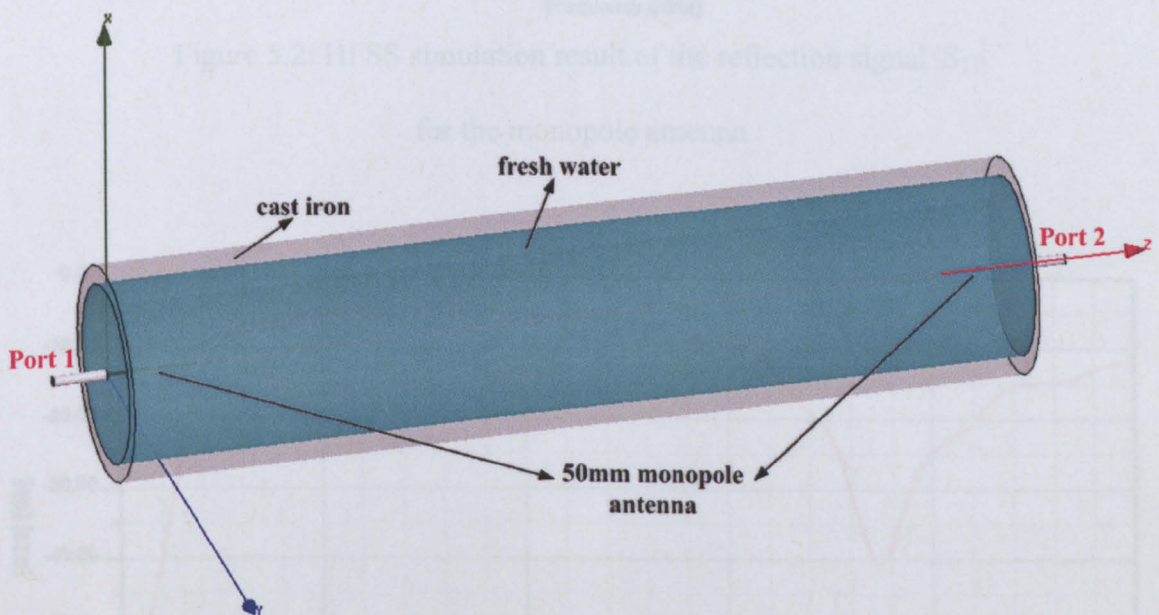


Figure 5.1: HFSS model of 4 inch cast iron pipe with two 50mm monopole antenna

In Figure 5.2, the variation of $|S_{11}|$ with frequency is very similar to the earlier result in Figure 4.9 because the 50mm long antenna should operate best at around 320MHz frequency, due to the fact that the 510mm long cast iron pipe acts as a heavily damped cavity since only a little power can be trapped in the cavity as the antennas are well

matched. This cavity effect is hardly visible in the variation of $|S_{21}|$ in Figure 5.3. The transmission loss in the well matched frequency region, is mainly due to the attenuation of the water.

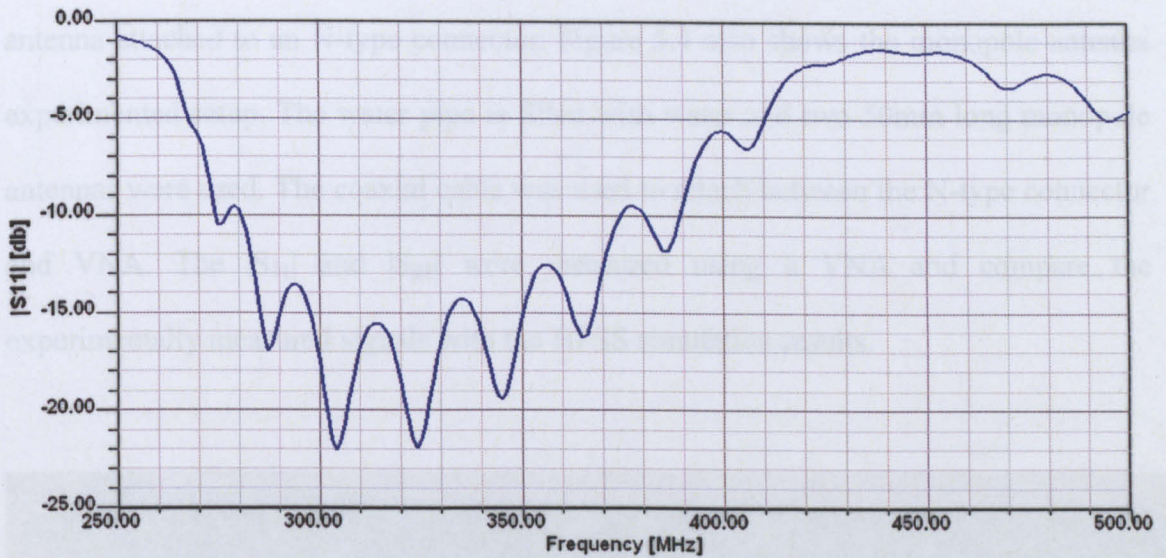


Figure 5.2: HFSS simulation result of the reflection signal $|S_{11}|$
for the monopole antenna

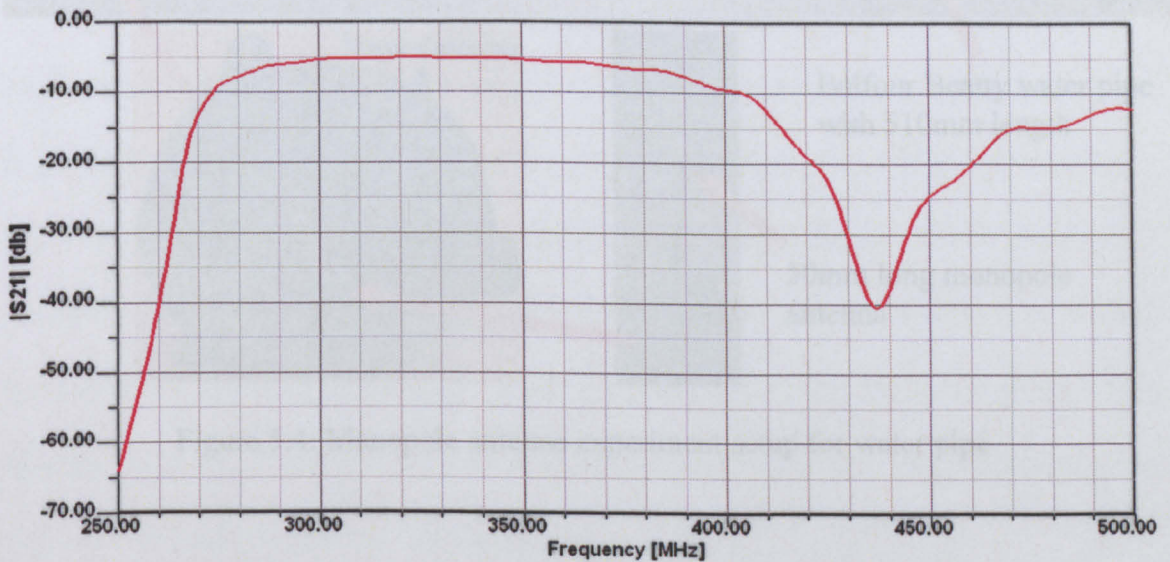


Figure 5.3: HFSS simulation result of the transmission signal $|S_{21}|$
for the monopole antenna

5.2 Water Pipe Experiment for Monopole Antenna

To validate the HFSS simulations in section 5.1, a 4 inch diameter cast iron pipe with a length of 510mm long was used as shown in Figure 5.4. To transmit an electromagnetic wave into the pipe, two mild steel end caps were made which housed a monopole antenna attached to an N-type connector. Figure 5.4 also shows the monopole antenna experimented setup. The water pipe is filled with water and two 50mm long monopole antennas were used. The coaxial cable was used to attach between the N-type connector and VNA. The $|S_{11}|$ and $|S_{21}|$ were measured using a VNA and compare the experimentally measured signals with the HFSS simulation results.

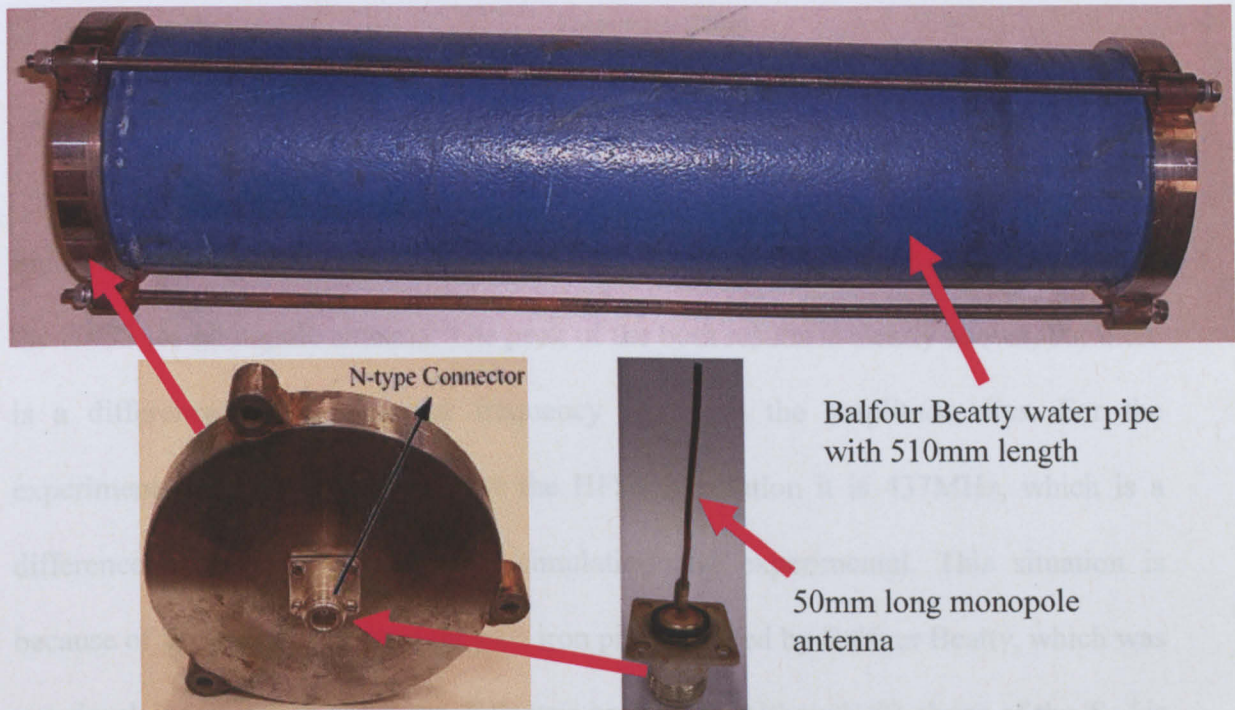


Figure 5.4: Monopole antenna experiment setup for water pipe

Figure 5.5 shows $|S_{11}|$ versus frequency of experimented and HFSS monopole antenna. Both of the experimented and simulation results have the same underlying shape. Therefore, the experimented $|S_{11}|$ was in good agreement with both the frequency and amplitude determined by the HFSS simulation and the experimental results. These show

that the operational frequency range determined by the simulation was correct.

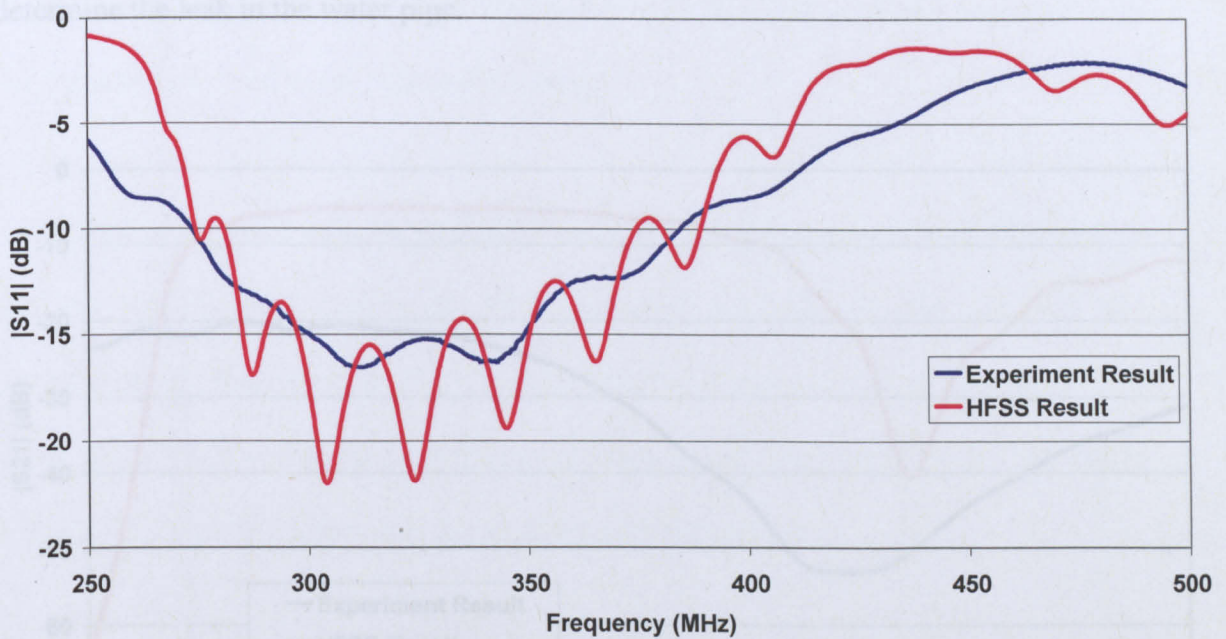


Figure 5.5: Reflection signal $|S_{11}|$ of experiment and HFSS for monopole antenna

Figure 5.6 shows the transmission signal $|S_{21}|$ versus frequency of the experimented and the HFSS for monopole antenna. The peak of the both results is clearly shown, but there is a difference in the resonant frequency at which the amplitude dips. For the experiment it is at 422MHz and for the HFSS simulation it is 437MHz, which is a difference of 3.4% between HFSS simulation and experimental. This situation is because of the concrete lines of the cast iron pipe supplied by Balfour Beatty, which was not simulated due to its unknown dielectric properties. Although the shape of the $|S_{21}|$ is slightly different, it can still be considered as a good agreement. The simulations can therefore be used to speed up the design stage.

Besides that, one of the very important factors to point out is that there is no resonance shape for the reflection signals $|S_{11}|$ that measure in Figure 5.5 and therefore, it will be

difficult to use to determine a leak. For the transmission signal $|S_{21}|$ in Figure 5.6, a clear resonant peak is shown at 422MHz, therefore the transmission signal $|S_{21}|$ is used to determine the leak in the water pipe.

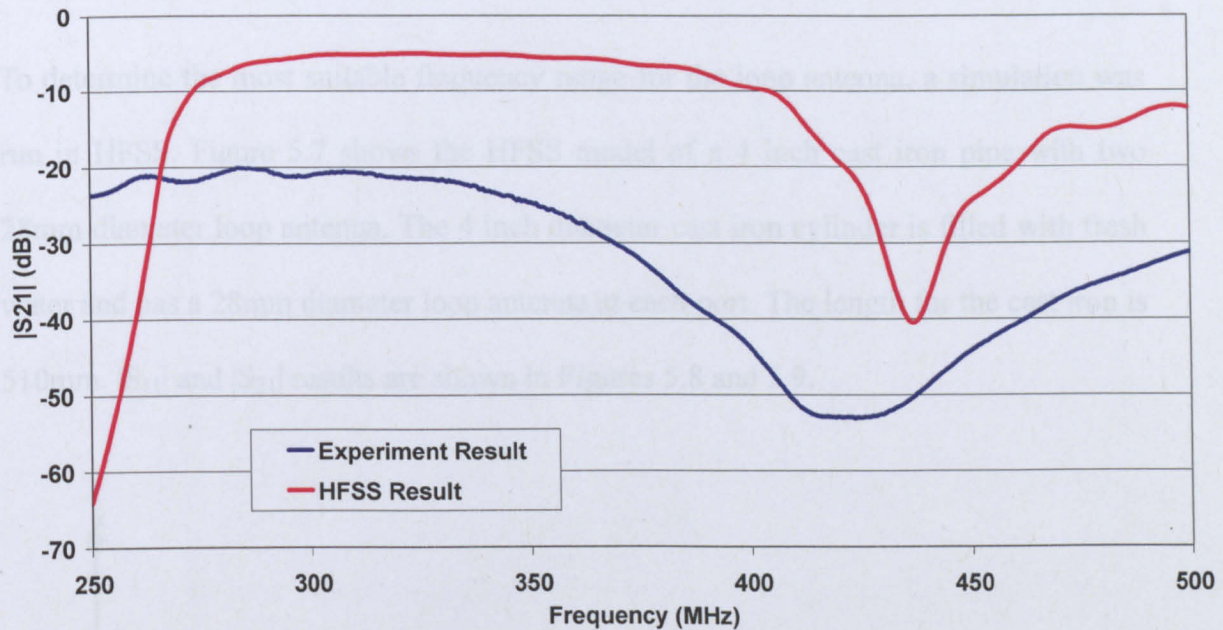


Figure 5.6: Transmission signal $|S_{21}|$ of experiment and HFSS for monopole antenna

5.3 Water Pipe Simulation for Loop Antenna

For this system to be deployed as a viable leak detector there would have to be two antennas, spaced at a reasonable distance apart. If both monopole antennas are 50mm long and the separation between the antennas is 200mm, then the overall length including the electronics part would be a minimum of 300mm long. This is much bigger than the proposed design specifications given by Balfour Beatty which is 100mm in length and 22mm in diameter. Besides that, this system would also require a cable to pass between the antennas that would interfere with the transmission path.

To overcome these problems the antenna design was changed to a loop antenna rather than a monopole. One of the advantages of changing to loop antenna is that it is mechanically stronger. The loop antenna will not be damaged so easily when put into the hydrant compared to the monopole antenna.

To determine the most suitable frequency range for the loop antenna, a simulation was run in HFSS. Figure 5.7 shows the HFSS model of a 4 inch cast iron pipe with two 28mm diameter loop antenna. The 4 inch diameter cast iron cylinder is filled with fresh water and has a 28mm diameter loop antenna at each port. The length for the cast iron is 510mm. $|S_{11}|$ and $|S_{21}|$ results are shown in Figures 5.8 and 5.9.

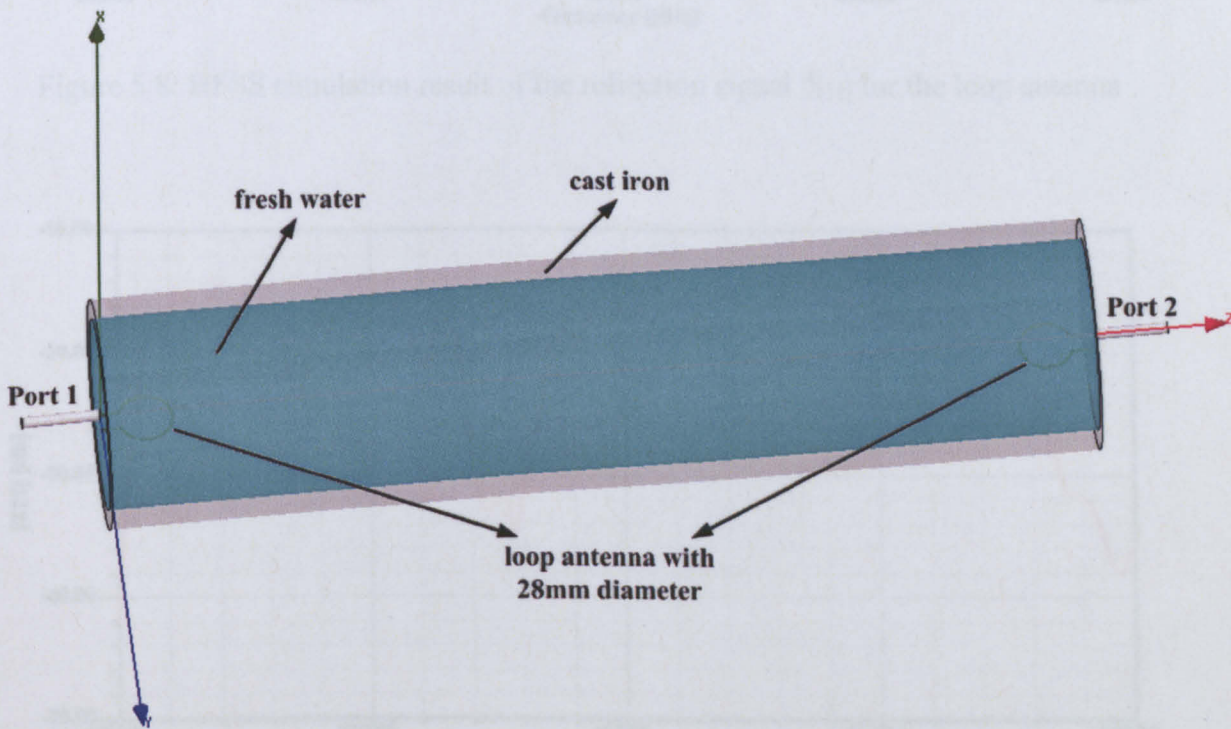


Figure 5.7: HFSS model of 4 inch cast iron pipe with two 28mm diameter loop antenna

In Figure 5.8, the peak of $|S_{11}|$ is clearly shown. The 28mm diameter loop antenna should operate best at around 480MHz. In Figure 5.9, $|S_{21}|$ have shows the best transmission between 220MHz and 330MHz and 370MHz and 560MHz.

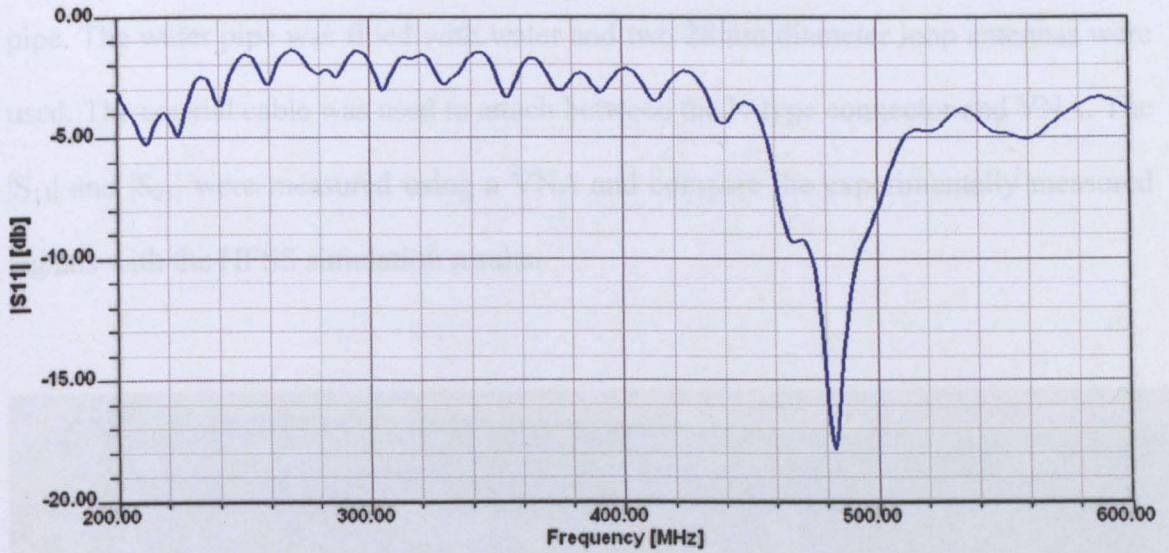


Figure 5.8: HFSS simulation result of the reflection signal $|S_{11}|$ for the loop antenna

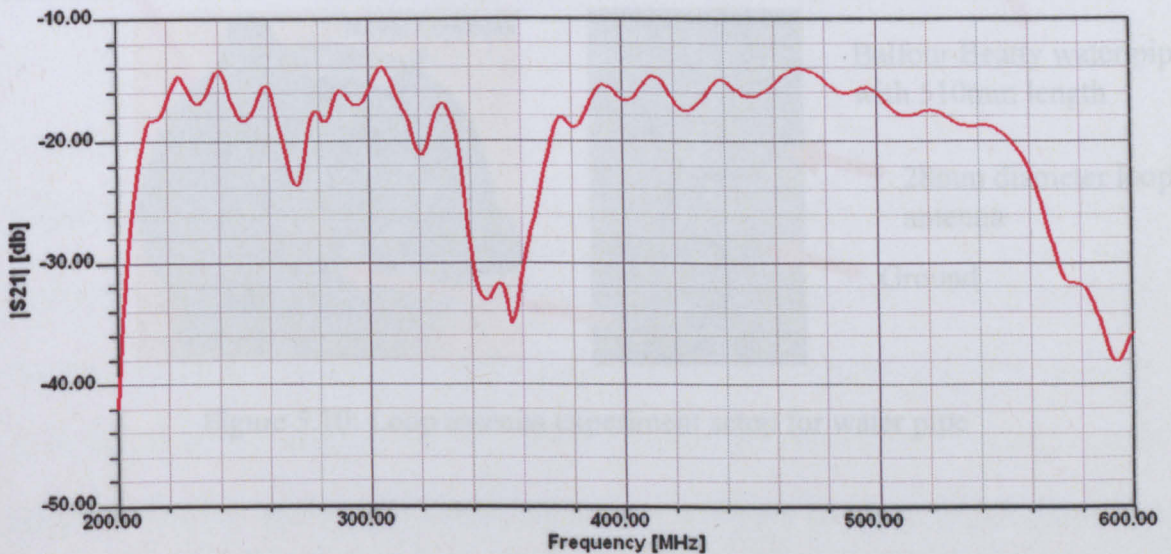


Figure 5.9: HFSS simulation result of the transmission signal $|S_{21}|$ for the loop antenna

5.4 Water Pipe Experiment for Loop Antenna

To validate the HFSS simulations for the loop antenna in section 5.3, two mild steel end caps were made which housed a loop antenna attached to an N-type connector which is shown in Figure 5.10. Figure 5.10 shows the loop antenna experiment setup for water pipe. The water pipe was filled with water and two 28mm diameter loop antennas were used. The coaxial cable was used to attach between the N-type connector and VNA. The $|S_{11}|$ and $|S_{21}|$ were measured using a VNA and compare the experimentally measured signals with the HFSS simulation results.



Figure 5.10: Loop antenna experiment setup for water pipe

Figure 5.11 shows $|S_{11}|$ versus frequency for the experiment and HFSS for loop antennas. The peak of the both results is clearly shown, but there is a difference in the resonant frequency at which the amplitude dips. For the experiment it is at 480MHz and for the HFSS simulation it is at 483MHz, which is a difference of 0.6% between HFSS simulation and experimental. Therefore, the peak of the both results was considered at

the same frequency region approximately 480MHz although the amplitude is different. Therefore, the reflection spectrum $|S_{11}|$ shows a level of agreement between the HFSS simulation and the experimental results this shows that the operational frequency range determined by simulation is correct.

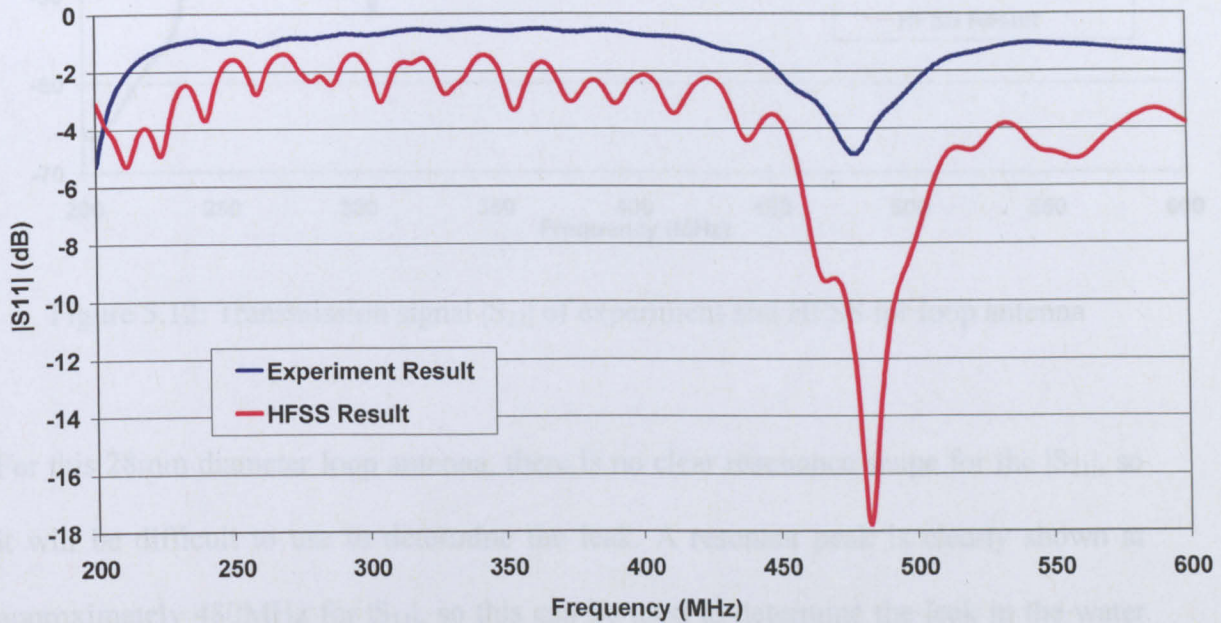


Figure 5.11: Reflection signal $|S_{11}|$ of experiment and HFSS for loop antenna

Figure 5.12 shows $|S_{21}|$ versus frequency for experimented and HFSS simulation for the loop antenna. The peak of the both results is clearly shown, but there is a difference in the resonant frequency with that on the experimental results being at 306MHz while the peak of the HFSS simulation is at 352MHz, which is a difference of 13% between HFSS simulation and experimental. Again, this situation is likely to be due to the concrete lines on the inner surface of the cast iron pipe supplied by Balfour Beatty, which was not simulated due to its unknown dielectric properties. Although the shape of the both $|S_{21}|$ results is different, it can still be considered as a good agreement.

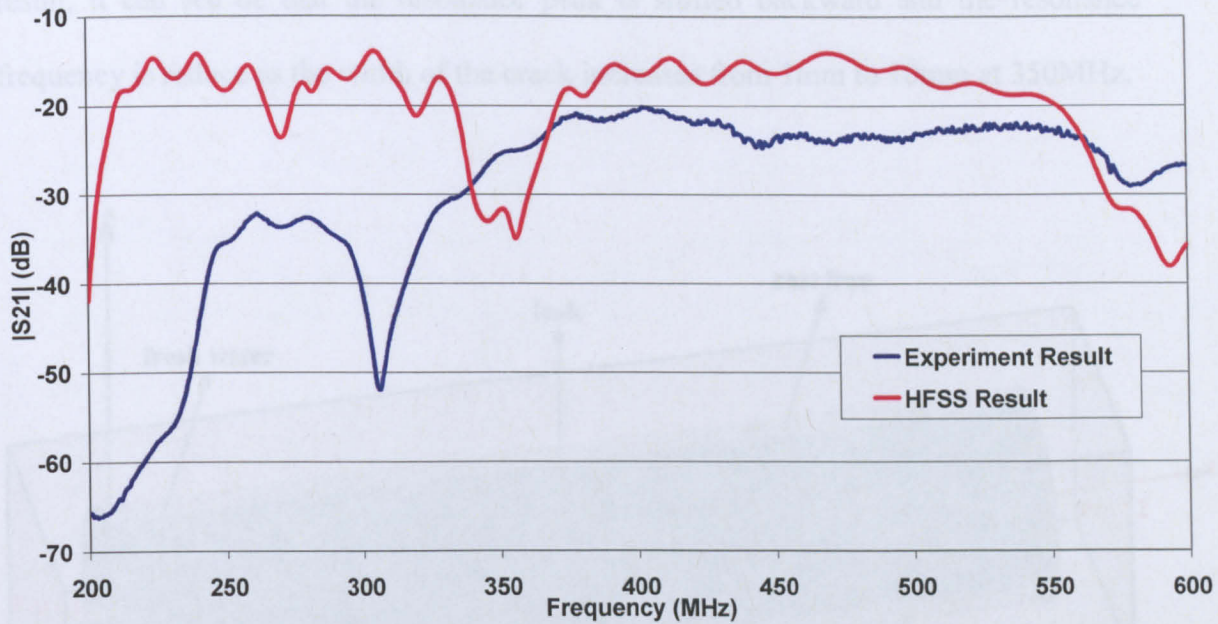


Figure 5.12: Transmission signal $|S_{21}|$ of experiment and HFSS for loop antenna

For this 28mm diameter loop antenna, there is no clear resonance shape for the $|S_{21}|$, so it will be difficult to use to determine the leak. A resonant peak is clearly shown at approximately 480MHz for $|S_{11}|$, so this can be used to determine the leak in the water pipe.

5.5 Water Pipe Leak Simulation

It was then necessary to continue the tests with a cracked pipe. A crack was made in the pipe and it was simulated using HFSS. Figure 5.13 shows the software simulation for water pipe leak. The 4 inch cast iron cylinder is filled with fresh water and 28mm diameter loop antennas at each port. A crack is made at the centre position on the cast iron cylinder. The simulation results $|S_{11}|$ and $|S_{21}|$ are shown in Figures 5.14 and 5.15.

Figure 5.14 shows $|S_{11}|$ for different crack width. The amplitude of the signals and the frequency of the resonance changes when the crack in the pipeline is made. From the

result, it can be seen that the resonance peak is shifted backward and the resonance frequency is reduced as the width of the crack increases from 1mm to 10mm at 350MHz.

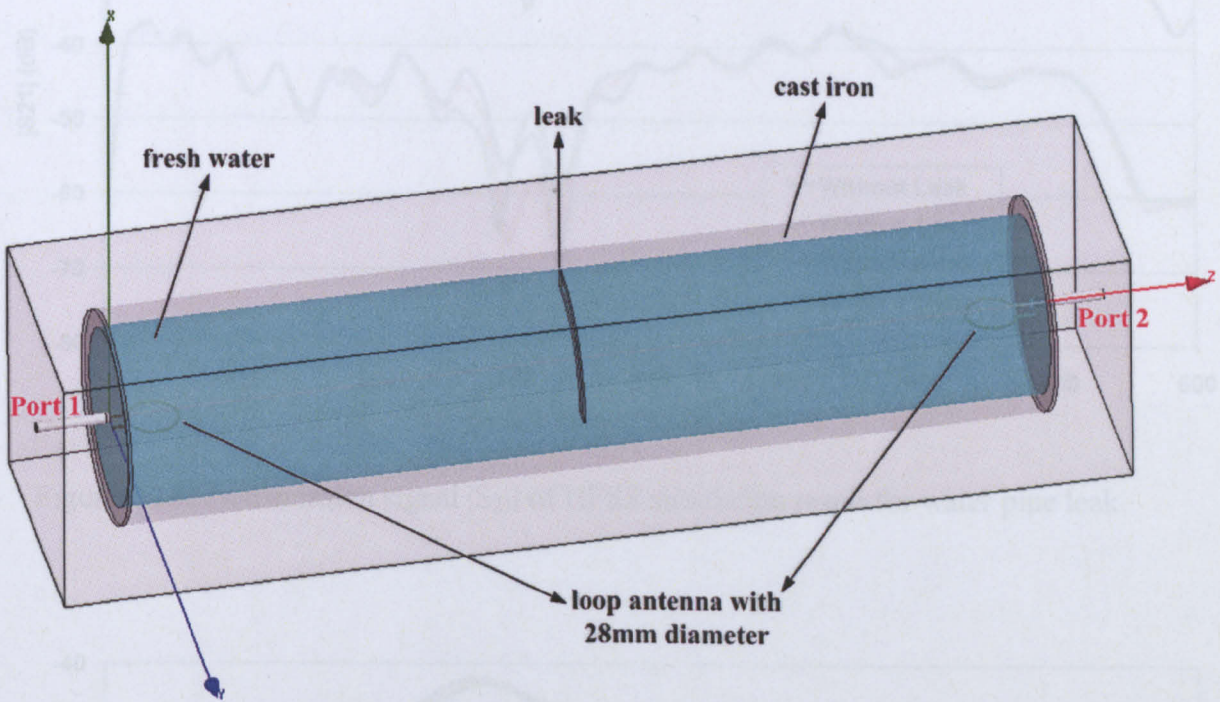


Figure 5.13: HFSS simulation for water pipe leak

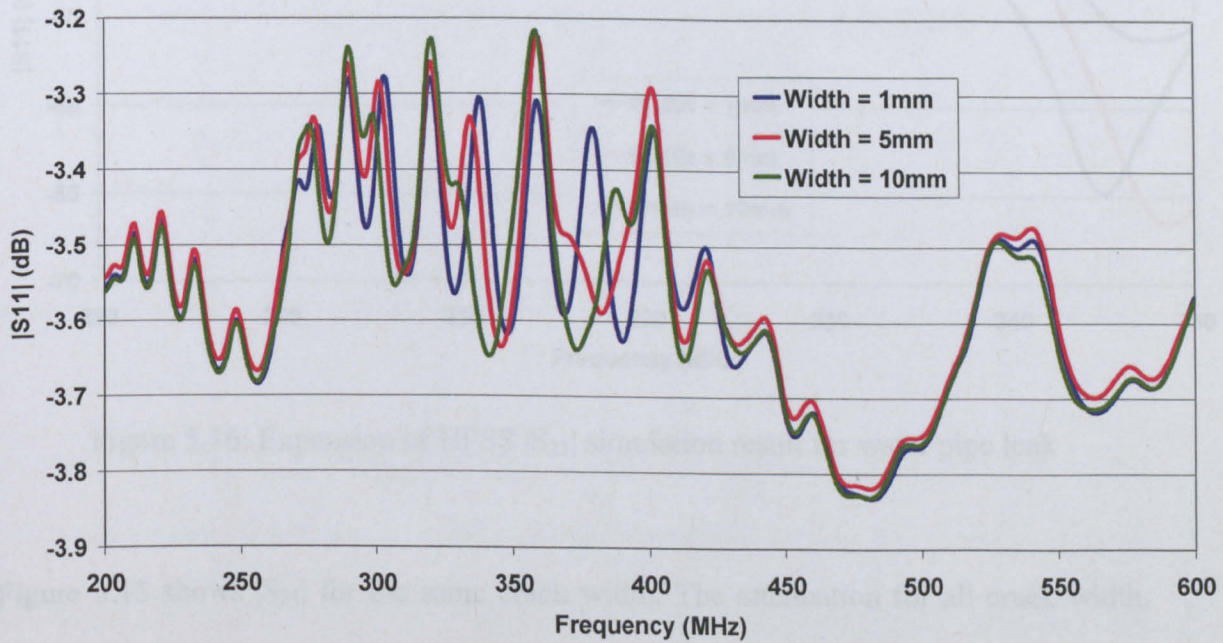


Figure 5.14: Reflection signal $|S_{11}|$ of HFSS simulation result for water pipe leak

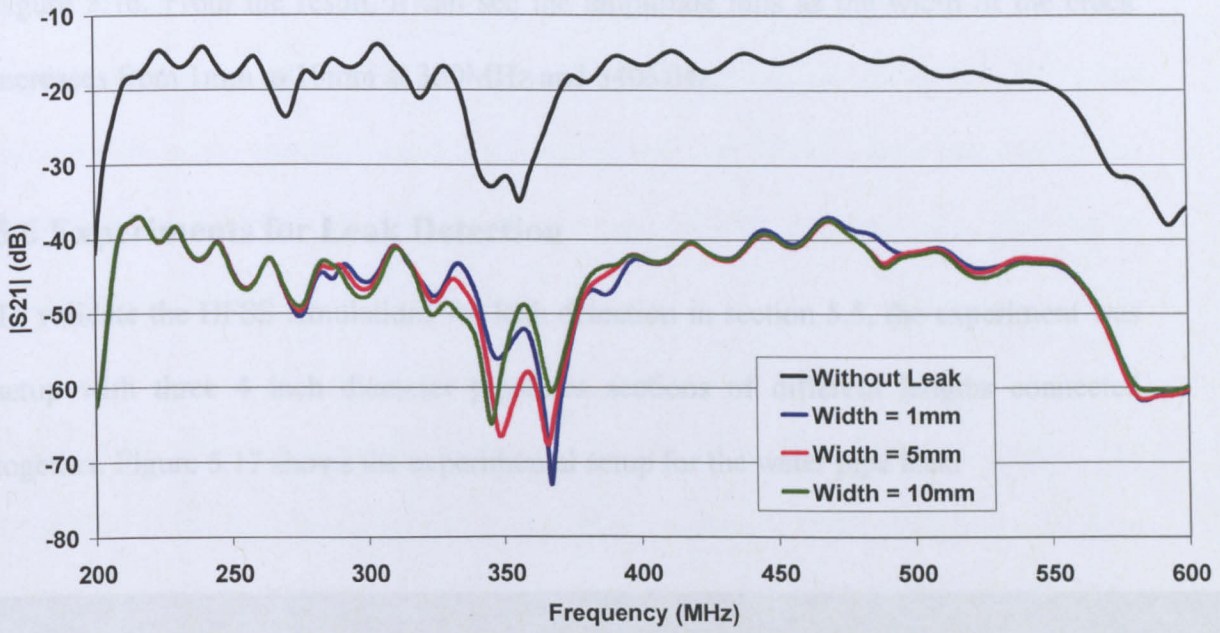


Figure 5.15: Transmission signal $|S_{21}|$ of HFSS simulation result for water pipe leak

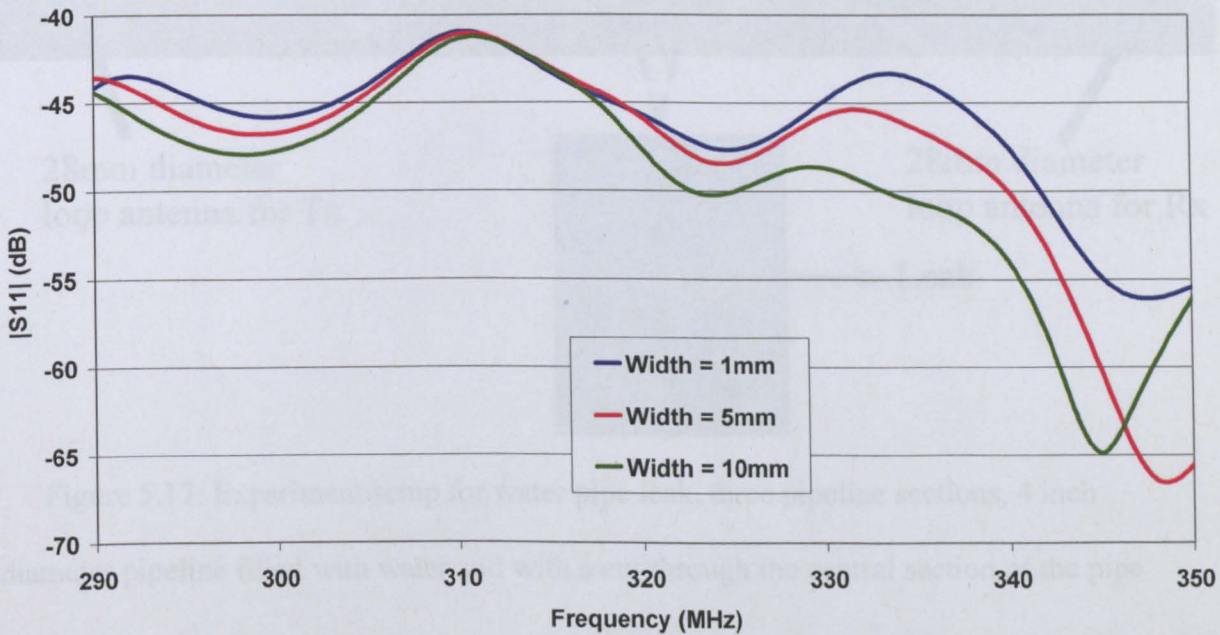


Figure 5.16: Expansion of HFSS $|S_{21}|$ simulation result for water pipe leak

Figure 5.15 shows $|S_{21}|$ for the same crack width. The attenuation for all crack width, with the signal dropping by 20dB. The signal for leak is quite difficult to see in Figure 5.15; therefore the result is expanded over the frequency range 290MHz to 350MHz in

Figure 5.16. From the result, it can see the amplitude falls as the width of the crack increases from 1mm to 10mm at 320MHz and 340MHz.

5.6 Experiments for Leak Detection

To validate the HFSS simulations for leak detection in section 5.5, the experiment was setup with three 4 inch diameter pipeline sections of different lengths connected together. Figure 5.17 shows the experimental setup for the water pipe leak.

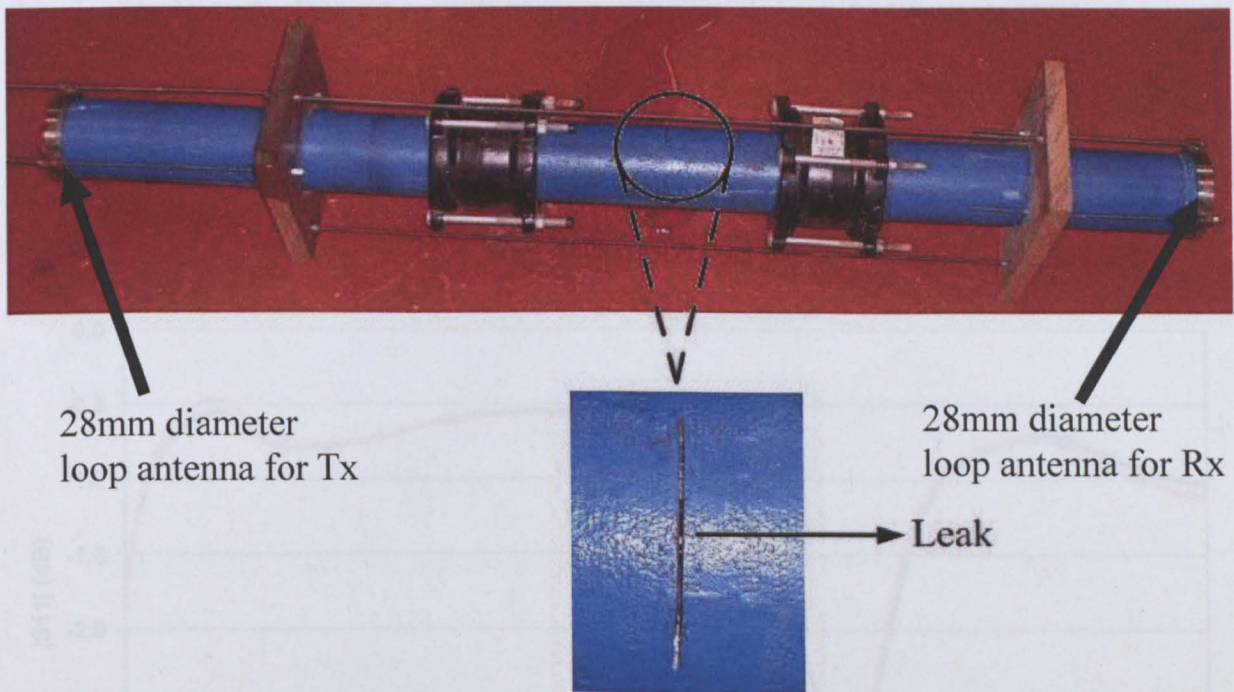


Figure 5.17: Experiment setup for water pipe leak, three pipeline sections, 4 inch diameter pipeline filled with water and with a cut through the central section of the pipe

The total length of these three pipelines sections was 1480mm and the pipe was totally filled with water. The same two mild steel end caps were used to house a loop antenna at both end, each attached to an N-type connector as shown in Figure 5.4 and 5.10. Then a 0.5mm crack was sawn in the central pipeline. The crack was sealed with tape to avoid water leaking from the pipe when the experiment was in progress and to make sure that

the pipe was always full filled of water. The coaxial cable was used to attach between the N-type connector and VNA. The $|S_{11}|$ and $|S_{21}|$ were measured using a VNA and compare the experimentally measured signals with the HFSS simulation results. The comparison results for this experiment with and without the crack are presented in Figures 5.18 and 5.19.

Figure 5.18 shows $|S_{11}|$ versus frequency for the water pipe leak experiment. The amplitude of the signals and the frequency of the resonance changes when the crack of the pipeline is made. From the result, the resonance peak is shifted from 468MHz to a lower frequency 464MHz and the amplitude is reduced from -2.89dB to -3.16dB when the crack is present.

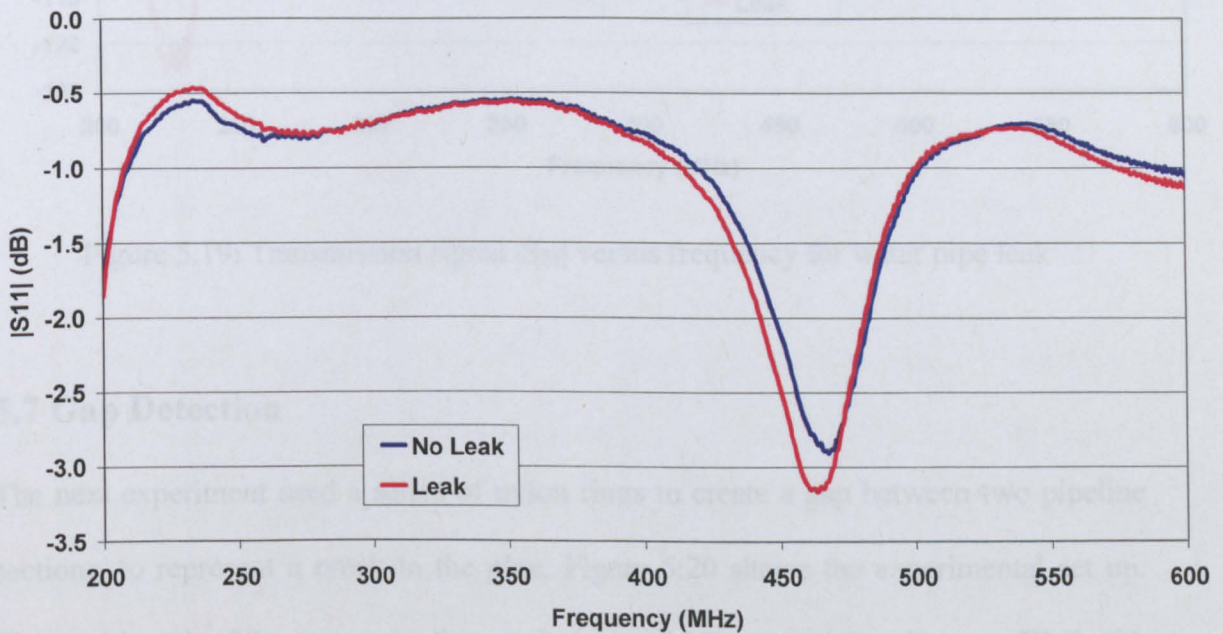


Figure 5.18: Reflection signal $|S_{11}|$ versus frequency for water pipe leak

Figure 5.19 shows the transmission signal $|S_{21}|$ versus frequency for water pipe leak experiment. The signal reduces due to the leak in the pipe both with the experimentation and using HFSS simulation software. The amplitude of the signals and the frequency of

the resonance changes when the crack of the pipeline is made. The signal is down for 30dB at frequency region 230MHz. Therefore, $|S_{11}|$ can also be used for determining if there is any fracture or discontinuity in the pipeline. It should be noted that in this experiment the RF transmission signal strength is only 1mW (0dBm) is comfortably transmitted over a distance of 1480mm.

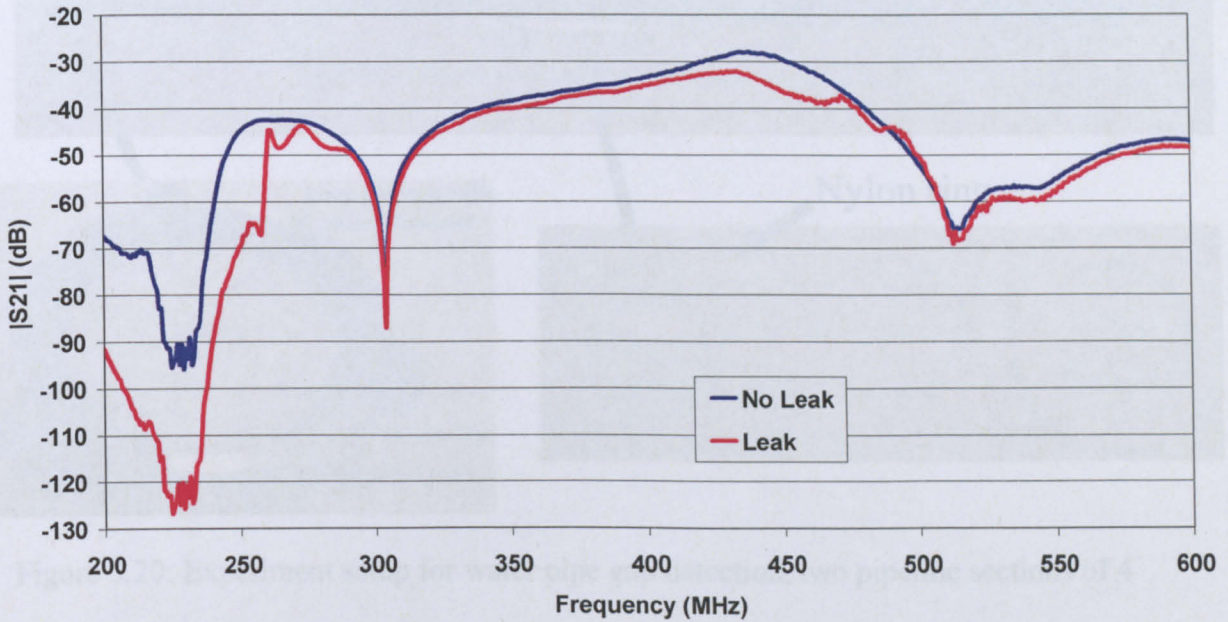


Figure 5.19: Transmission signal $|S_{21}|$ versus frequency for water pipe leak

5.7 Gap Detection

The next experiment used a series of nylon rings to create a gap between two pipeline sections, to represent a break in the pipe. Figure 5.20 shows the experimental set up. The total length of these two pipeline sections was 1060mm and the pipe was filled with water. The same two mild steel end caps with loop antennas attached to an N-type connector were used at each end. The nylon ring inserts which ranged from 3 to 15mm in thickness were used to increase the gap between the two pipes. The coaxial cable was used to attach between the N-type connector and VNA. The measurements for both $|S_{11}|$

and $|S_{21}|$ were taken by VNA at each of the gaps as shown in Figures 5.21 and 5.22 respectively.

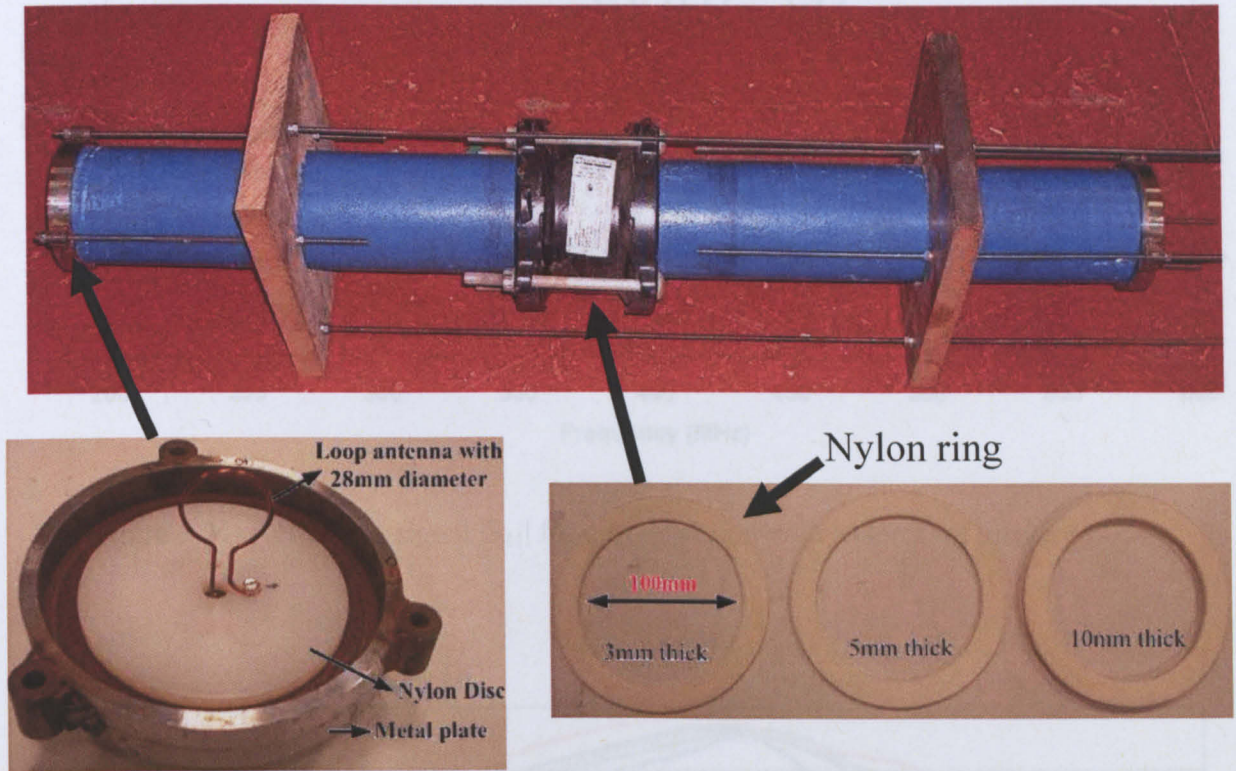


Figure 5.20: Experiment setup for water pipe gap detection, two pipeline sections of 4 inch diameter filled with water with nylon ring inserts between the pipes

Both of the results in Figure 5.21 and 5.22 show a distinct difference in spectrum signatures with a varying gap. For the reflection signal $|S_{11}|$ in Figure 5.21, it can be seen that the resonance frequency is reduced as the gap increases from 3mm to 15mm at frequency region 400MHz. With a 3mm gap, the frequency of the first resonance is at 410MHz and for 15mm gap it is at 385MHz. The shift is linear with distance with the resonance changing. Therefore, the frequency is shifted 2.1MHz per millimetre (mm) gap.

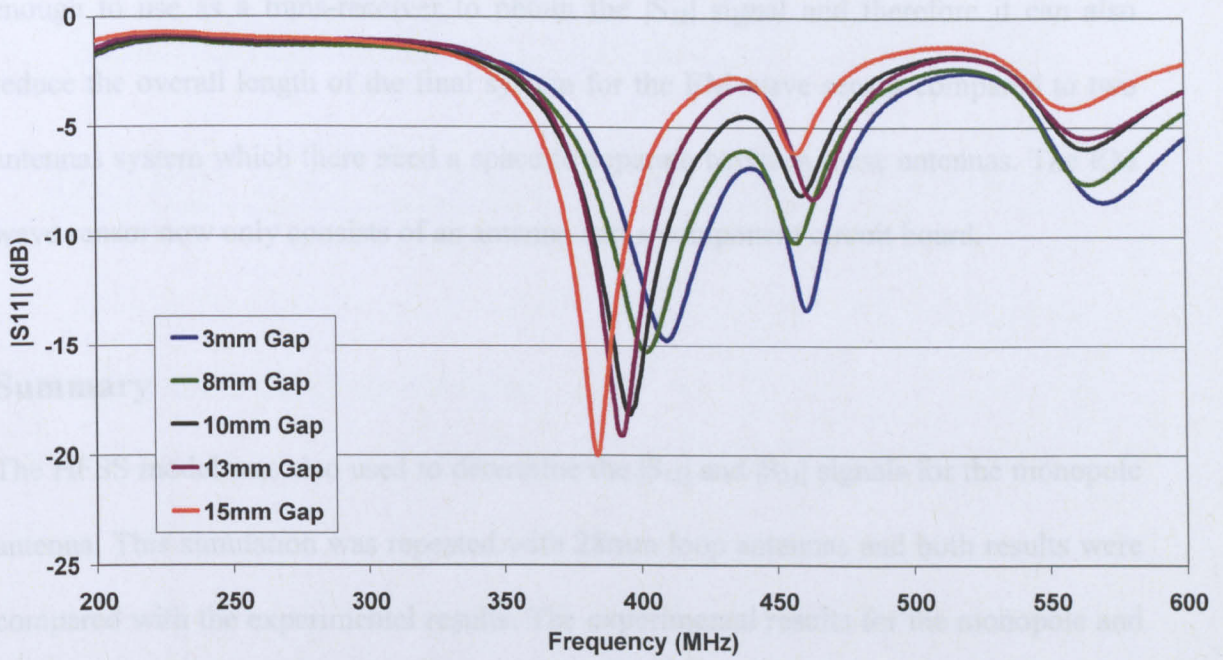


Figure 5.21: Reflection signal $|S_{11}|$ for gap detection with nylon ring inserted

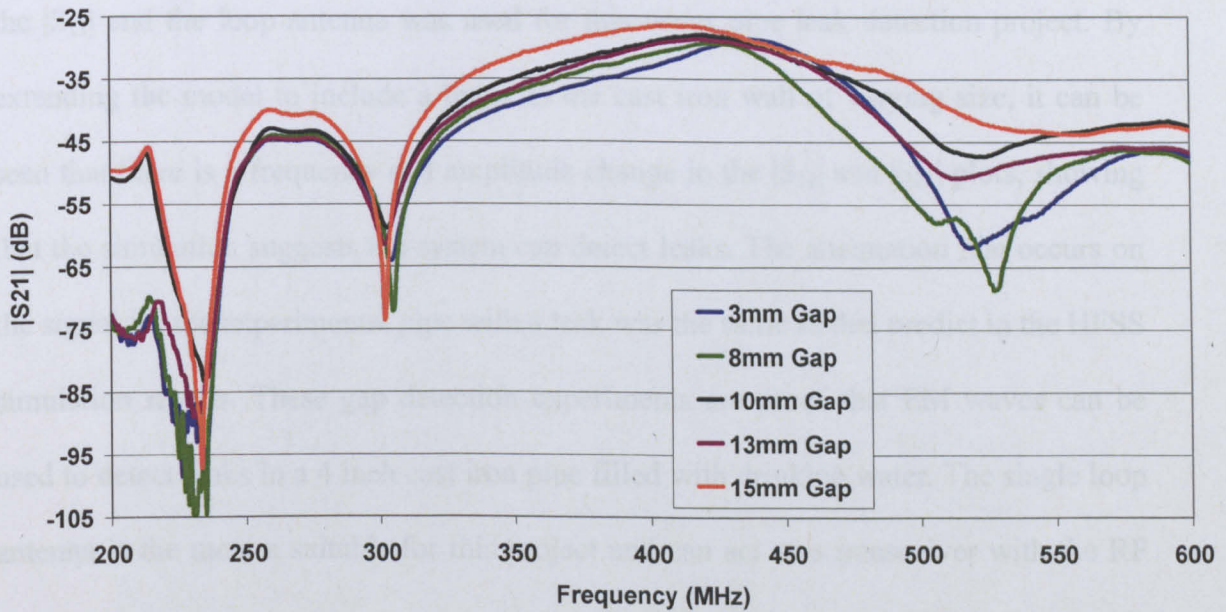


Figure 5.22: Transmission signal $|S_{21}|$ for gap detection with nylon ring inserted

The resonance frequency for $|S_{21}|$ in Figure 5.22 is not clearly shown and is difficult to use to determine a leak for this project. Therefore, $|S_{11}|$ is chosen for use in this project because the resonance peak is clearly shown in Figure 5.21. Hence, one loop antenna is

enough to use as a trans-receiver to obtain the $|S_{11}|$ signal and therefore it can also reduce the overall length of the final system for the EM wave sensor compared to two antennas system which there need a space to separate between these antennas. The EM wave sensor now only consists of an antenna and a component circuit board.

Summary

The HFSS model was also used to determine the $|S_{11}|$ and $|S_{21}|$ signals for the monopole antenna. This simulation was repeated with 28mm loop antennas and both results were compared with the experimental results. The experimental results for the monopole and the loop antennas for both $|S_{11}|$ and $|S_{21}|$ signals have been shown to be in good agreement, in both frequency and amplitude, with the results obtained by the HFSS simulation. Only the $|S_{11}|$ with the loop antenna gives a clear peak, however, therefore the $|S_{11}|$ and the loop antenna was used for this water pipe leak detection project. By extending the model to include a break in the cast iron wall of varying size, it can be seen that there is a frequency and amplitude change in the $|S_{11}|$ and $|S_{21}|$ plots, showing that the simulation suggests the system can detect leaks. The attenuation that occurs on the signal for the experimental pipe with a leak was the same as that predict in the HFSS simulation results. These gap detection experiments are proof that EM waves can be used to detect leaks in a 4 inch cast iron pipe filled with drinking water. The single loop antenna is the most a suitable for this project and can act as a transceiver with the RF electronics.

Chapter 6: Prototype Demonstrator

Design and Construction for Industry

6.1 90 Degree Bent Loop Antenna

All the previous experiments and simulations are setup using laboratory test sections with the antennas attached to the end caps on the pipeline which act as a transmitter (Tx) and receiver (Rx) for the EM wave sensor. However, the next stage was to develop a prototype demonstrator to be constructed that will fit through the hydrant deployment system used by Balfour Beatty. The limitation of the loop antenna design was reduced from the ideal diameter of 28mm to 22mm. The antenna was also bent and rotated by 90 degree to the pipeline axis which shown in Figure 6.1.



Figure 6.1: Loop antenna bent to 90 degrees from the axis of the pipe to fit with Balfour Beatty's requirements

The reasons for using the bent loop antenna were due to the specification of the sensor which required maximum dimension of 100mm in length and 22mm in diameter, so that it could pass through the Balfour Beatty hydrant delivery system, and that the centre of loop would allow a forward facing camera to be used and the loop could incorporate light emitting diode (LED) ring for illumination. A further benefit with using a 90 degree bent loop antenna is to reduce the possible damage when the sensor was put down the hydrant.

To determine how the bent loop antenna will affect the electromagnetic signal, the experimental setup shown in Figure 5.20 was repeated but with only one bent loop antenna as shown in Figure 6.1. The signal for the experiment was measured using the VNA. The measurement for $|S_{11}|$ was taken at several gap distances as shown in Figure 6.2.

As can be seen from the bent loop antenna experiment results in Figure 6.2, there are still distinct frequency shifts with gap increase in the pipeline. However the resonance peak is now shifted forwards and the resonance frequency increases as the gap increases from 3mm to 15mm, but the frequency is now 250MHz instead of 385MHz in the previous experiment with the normal single loop antenna. This means that the 90 degree bent loop antenna also can be used as a trans-receiver for the final system for the EM wave sensor. With no gap, the frequency of the first resonance is at around 250MHz and at 15mm it is at around 287MHz. Therefore, there is still a linear shift, with the resonance changing at 2.5MHz per millimetre (mm). This is still within the frequency range of the original specification as found in the laboratory feasibility stage.

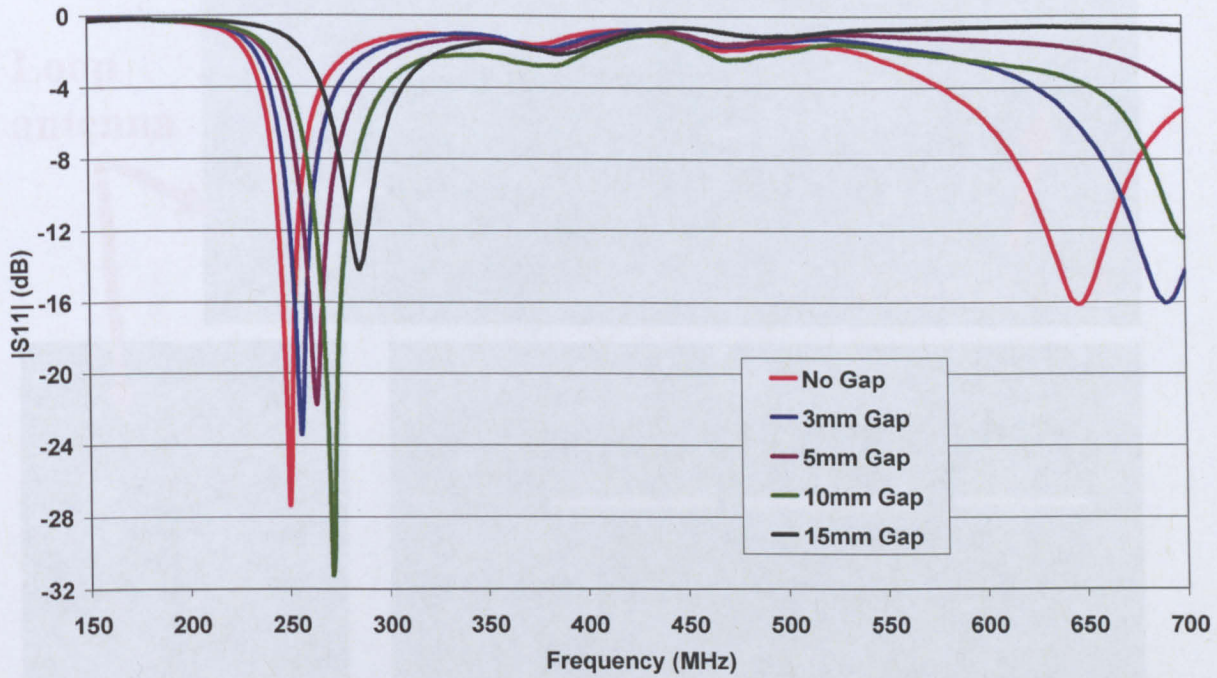


Figure 6.2: Reflection signal $|S_{11}|$ for bent loop antenna with nylon ring inserted

Figure 6.3: Setup of industrial prototype with 90 degree bent loop antenna

6.2 Prototype Demonstrator Design

The next step is to construct a stainless steel body to house the electronics with a nylon spacer and the loop antenna at the front. Figure 6.3 shows the setup of the industrial prototype with a 90 degree bent loop antenna. The overall length of the EM wave sensor is 90mm and the diameter is 22mm. The 90 degree bent loop antenna with a 22mm diameter is placed at the front of the assembly and spaced 15mm from the main body. The electronic housing allows the electromagnetic radiation to radiate efficiently from the antenna. The antenna is connected to the VNA via a coaxial feed cable.

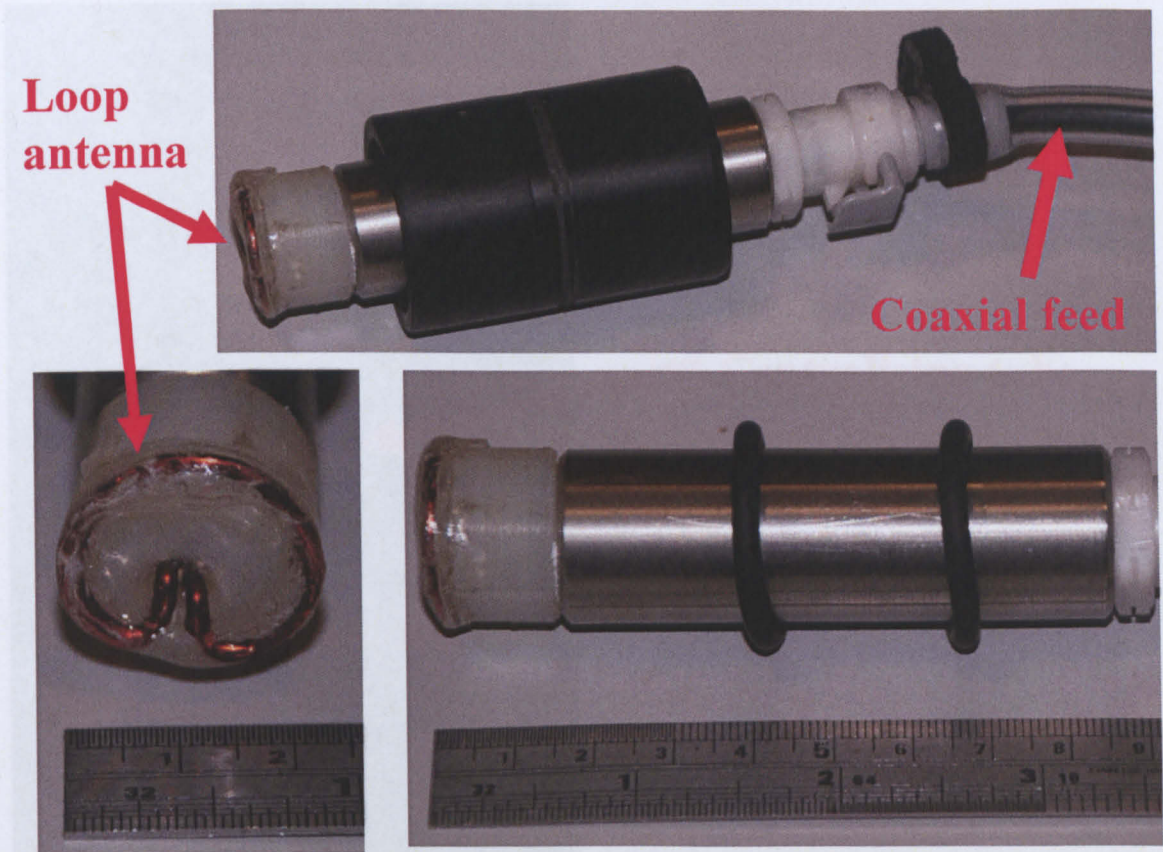
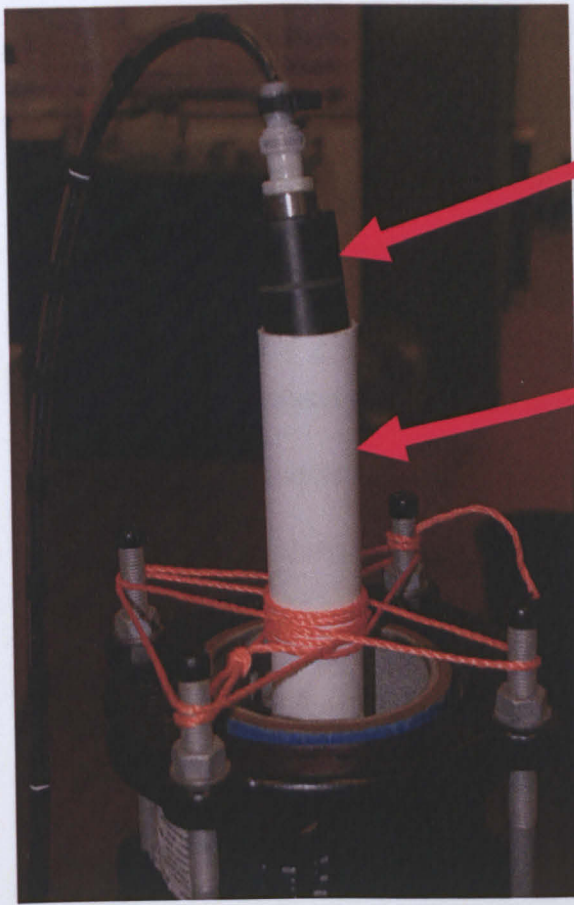


Figure 6.3: Setup of industrial prototype with 90 degree bent loop antenna

In order to test the prototype demonstrator system, the experiment was setup with two 4 inch diameter pipelines sections of different length connected together. Figure 6.4 shows the experimental setup to test the prototype demonstrator. The total length of these two pipelines sections is 1060mm. These two sections of pipeline were mounted vertically and filled with water. A plastic conduit with a 25mm diameter was used to ensure that the EM wave sensor passed through the centre of the pipeline. The experiment held the sensor at a fixed distance down to the pipe with the nylon ring inserts (3mm to 15mm thick) were used to increase the gap between the two pipes. Again, the coaxial cable was used to attach between the EM wave sensor and VNA. The measurement for $|S_{11}|$ was taken by VNA with several gap distances as shown in Figure 6.5.



**EM wave Sensor
with coaxial feed**

Centralising tube

Figure 6.4: Experimental setup to test prototype demonstrator

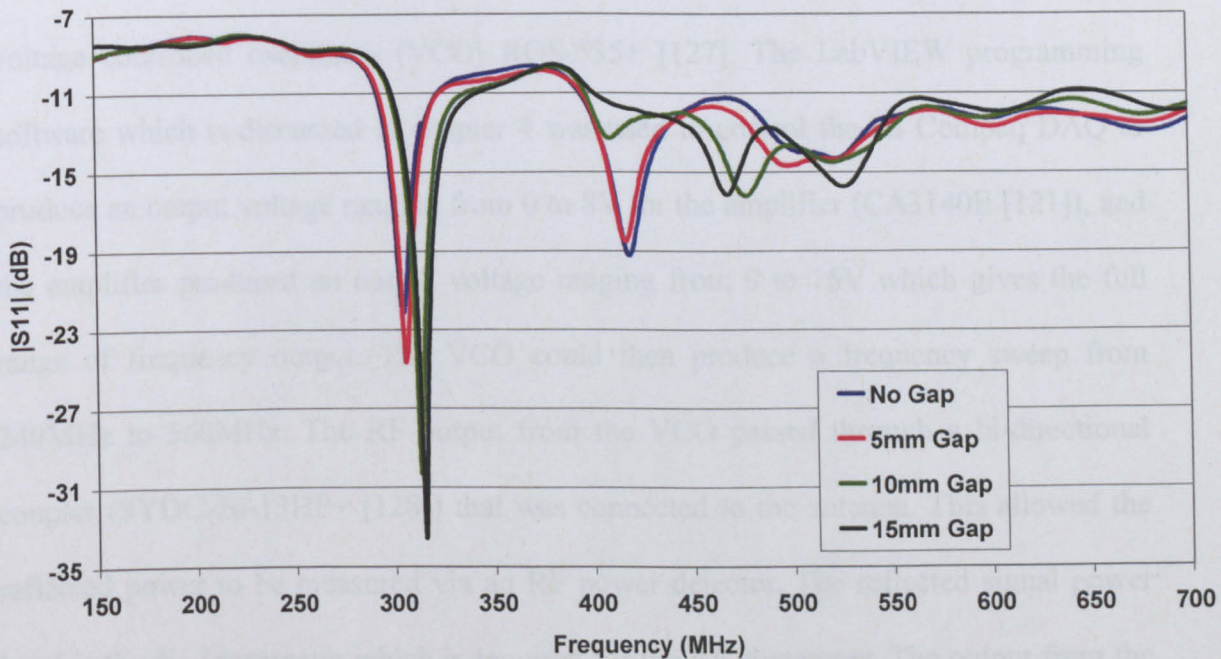


Figure 6.5: Reflection signal $|S_{11}|$ for the prototype demonstrator with nylon ring inserted

The signal in Figure 6.5 was comparable to the previous bent loop antenna experiment result shown in Figure 6.2. It can be seen that the electromagnetic spectrum clearly changes with the resonance peak shifting forward and the resonance frequency increasing as the gap increases from 5mm to 15mm. The starting frequency is now 305MHz instead of 250MHz in the previous experiment. This situation is due to the reduction in the diameter for the bent loop antenna. With no gap, the frequency of the first resonance is at around 305MHz and at 15mm it is at around 315MHz. Therefore, there is still a linear shift, with the resonance changing at 0.7MHz per millimetre (mm).

6.3 Prototype Demonstrator Design with Electronics Subsystem

The next stage was to design a surface mount version of the electronics that could fit within the stainless steel housing shown in Figure 6.3. The final schematic diagram for the electronics of a standalone EM wave sensor is shown in Figure 6.6. This system was driven by a 24V supply. Two voltage regulators (LM317 [125]) were used to produce a 5V and 12V output voltage for the RF power detector (MAX2015 [126]) and the voltage controlled oscillators (VCO) ROS-535+ [127]. The LabVIEW programming software which is discussed in chapter 4 was used to control the NI Compaq DAQ to produce an output voltage ranging from 0 to 8V for the amplifier (CA3140E [121]), and the amplifier produced an output voltage ranging from 0 to 16V which gives the full range of frequency output. The VCO could then produce a frequency sweep from 240MHz to 560MHz. The RF output from the VCO passed through a bi-directional coupler (SYDC-20-13HP+ [128]) that was connected to the antenna. This allowed the reflected power to be measured via an RF power detector. The reflected signal power level is the $|S_{11}|$ parameter which is required for the RF signatures. The output from the RF power detectors was a DC voltage in the range of 0 to 2V which was connected to the NI Compaq DAC and used by LabVIEW to plot out the spectrum.

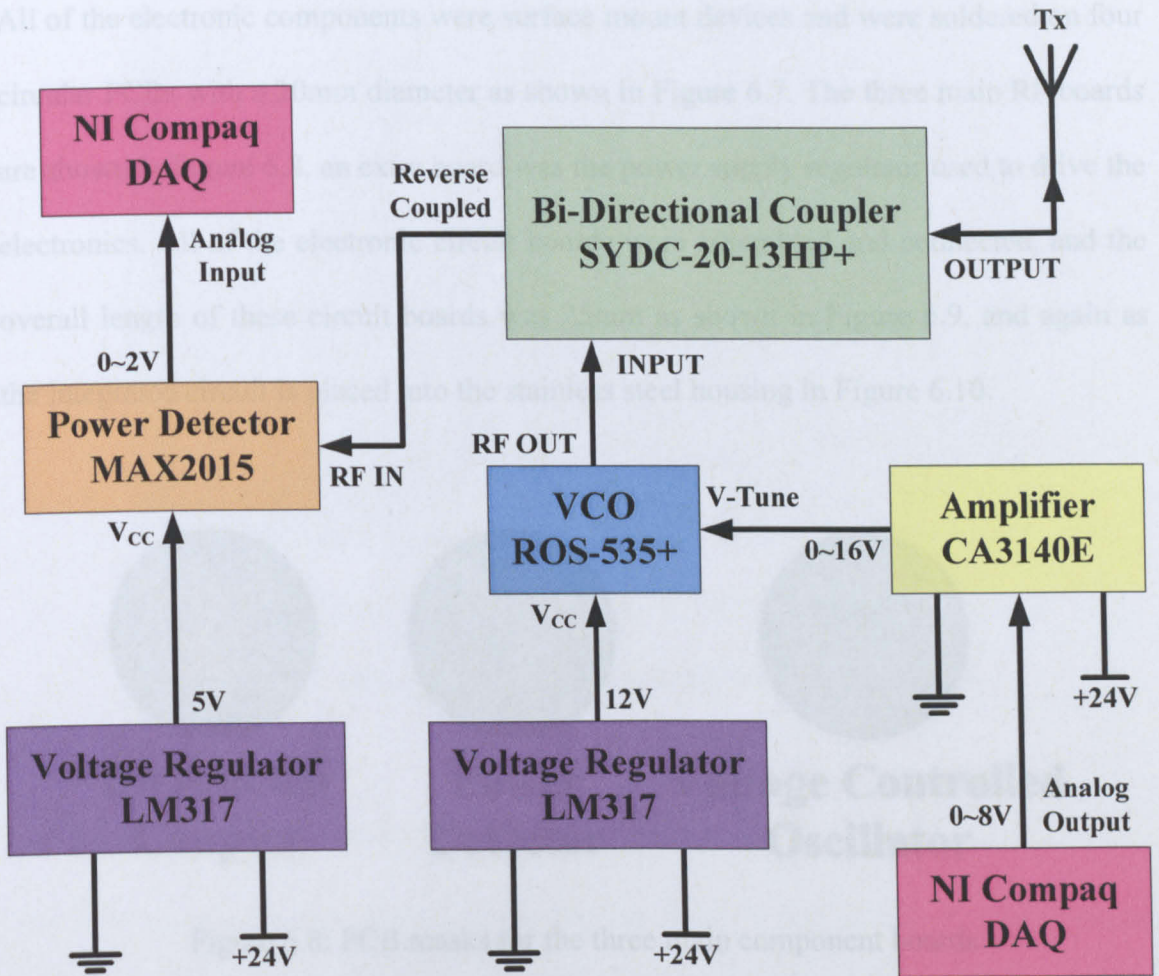


Figure 6.6: Electronics schematics for standalone EM wave sensor

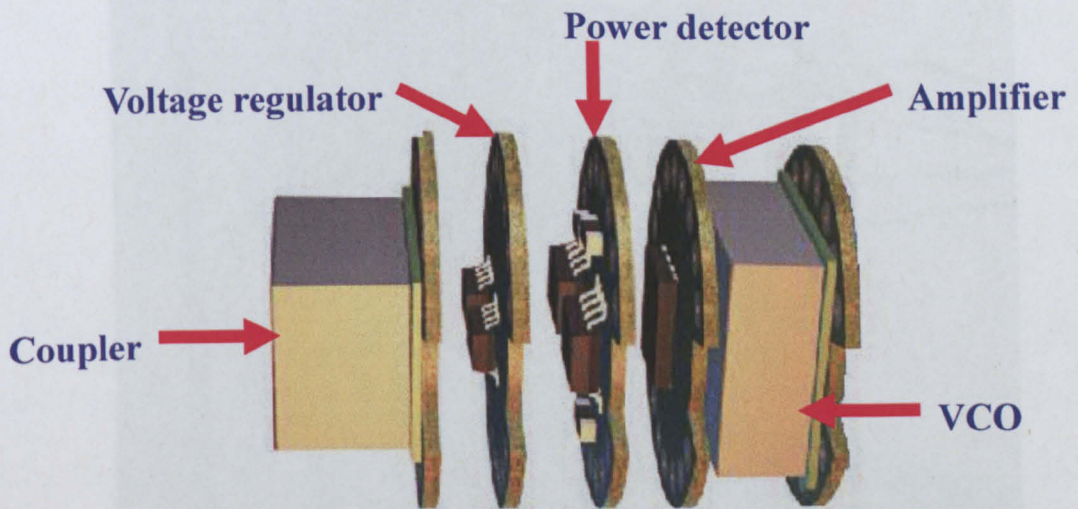


Figure 6.7: Four electronic circuit boards assembled for EM wave sensor

All of the electronic components were surface mount devices and were soldered on four circular PCBs with a 20mm diameter as shown in Figure 6.7. The three main RF boards are shown in Figure 6.8, an extra board was the power supply regulator used to drive the electronics. All of the electronic circuit boards were assembled and connected, and the overall length of these circuit boards was 25mm as shown in Figure 6.9, and again as the integrated circuit is placed into the stainless steel housing in Figure 6.10.

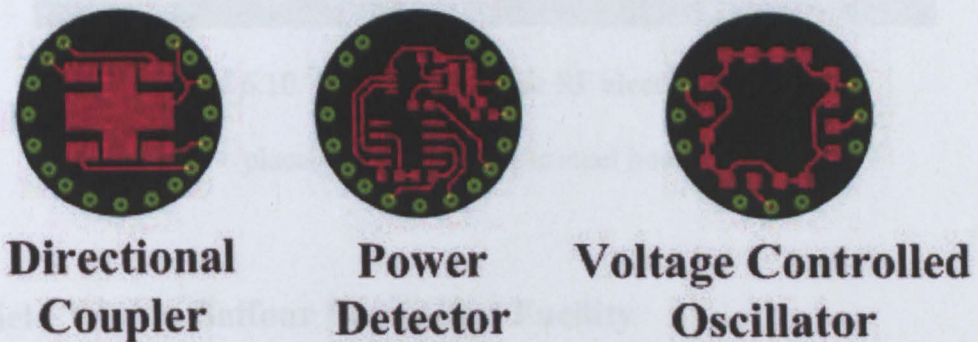


Figure 6.8: PCB masks for the three main component boards

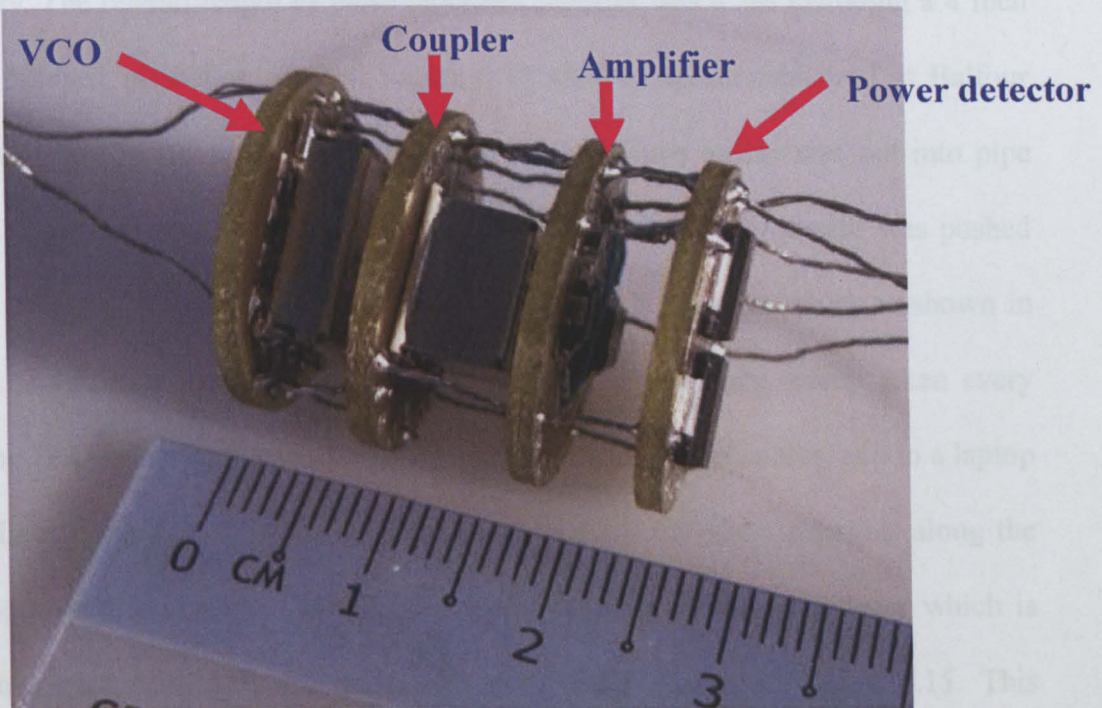


Figure 6.9: Photograph of the RF electronics for the integrated sensor, 25mm in length

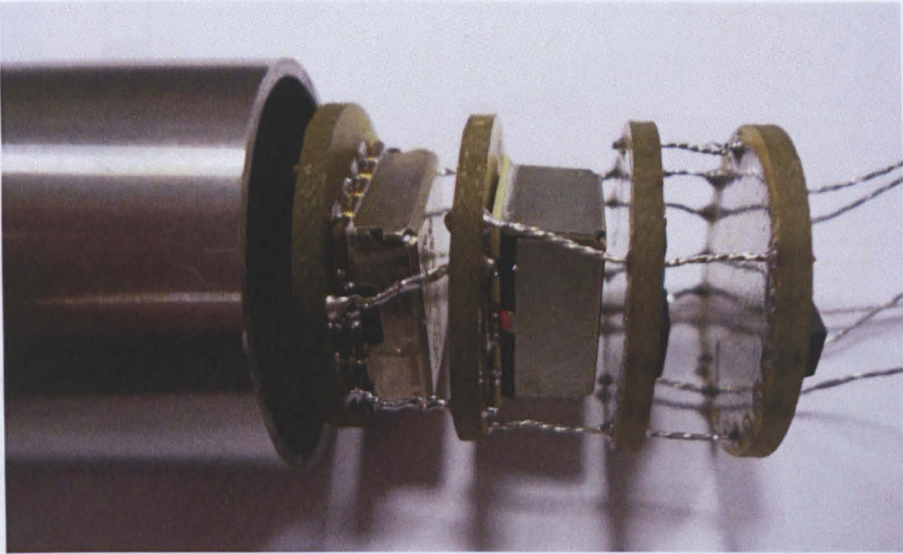


Figure 6.10: Photograph of the RF electronics being placed into the stainless steel housing

6.4 Field Trial at Balfour Beatty Test Facility

The next experiment was carried out at Balfour Beatty's test facility in Derby. Figure 6.11 shows the block diagram for the overall length of the pipelines in Balfour Beatty's test facility. The overall length of these pipelines sections was 4.3m including a 4 inch diameter Perspex inspection section. Figure 6.12 shows experimental trial at Balfour Beatty's test facility. To setup the experiment, the EM wave sensor was put into pipe through the access port. The EM wave sensor with the electronics circuit was pushed from the access port to the end of the system towards the reducer which is shown in Figure 6.13 and then systematically pulled back and a frequency sweep taken every 10cm. The EM wave sensor was connected by power and control cables, and to a laptop running LabVIEW. The insulator tape was used to mark the 10cm intervals along the 4.3m length of the pipeline. The marking were placed between the reducer which is shown in Figure 6.14, and the red access port which shown in Figure 6.15. This experiment allowed 43 readings to take place along the test section and through a variety of different types of pipeline.

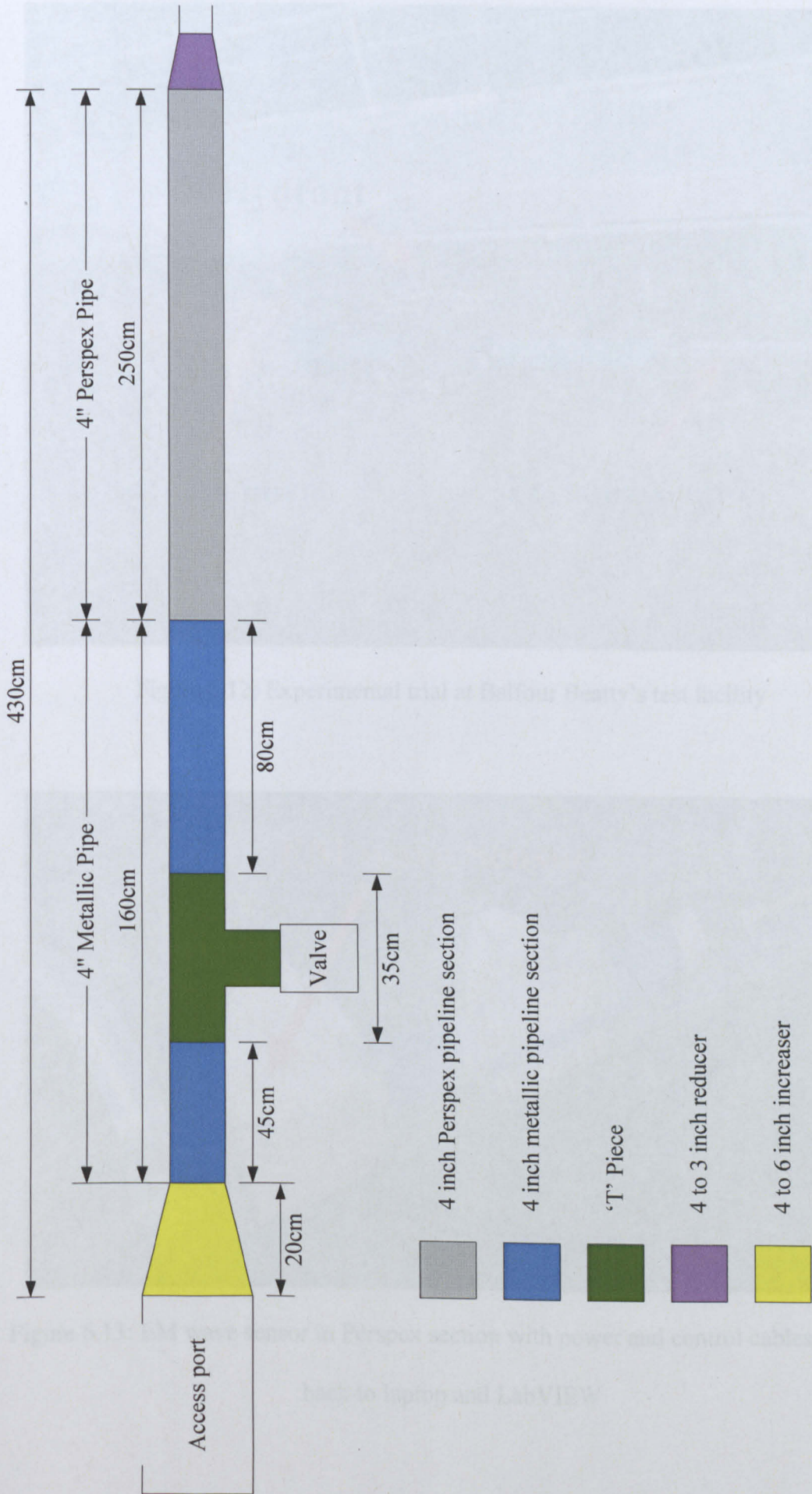


Figure 6.11: Block diagram for the overall length of the pipelines in Balfour Beatty's test facility

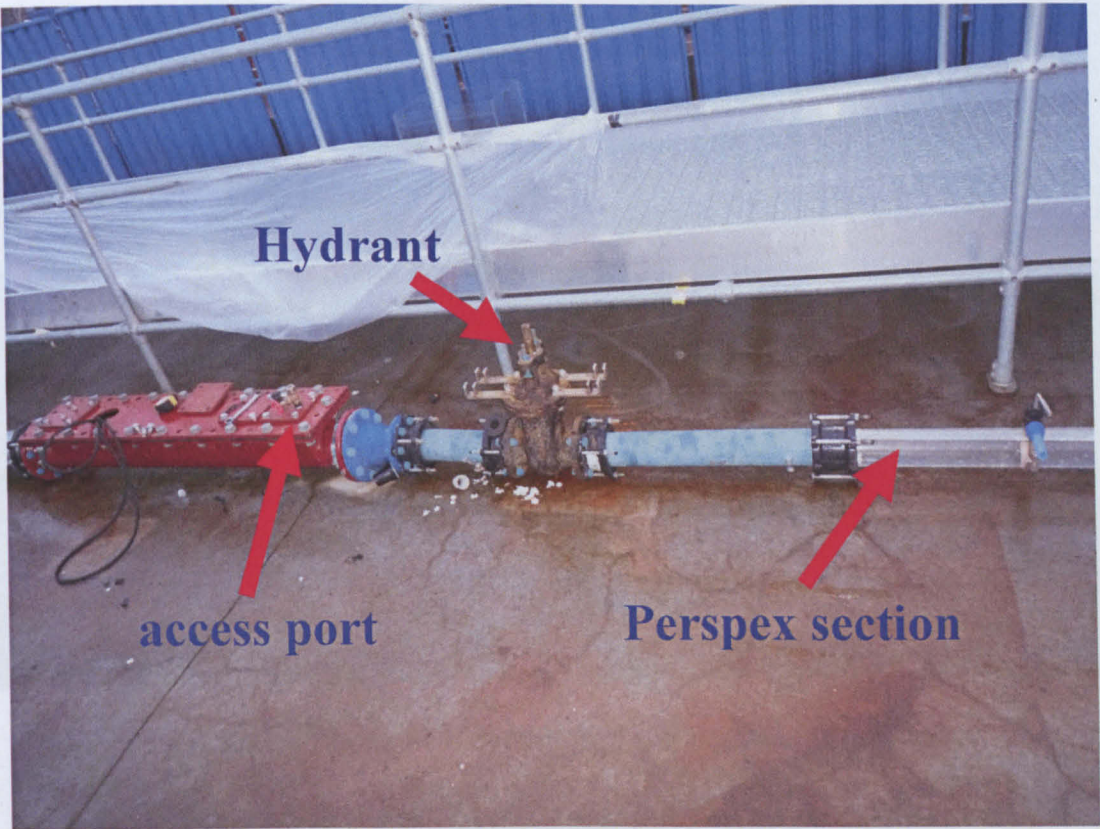


Figure 6.12: Experimental trial at Balfour Beatty's test facility

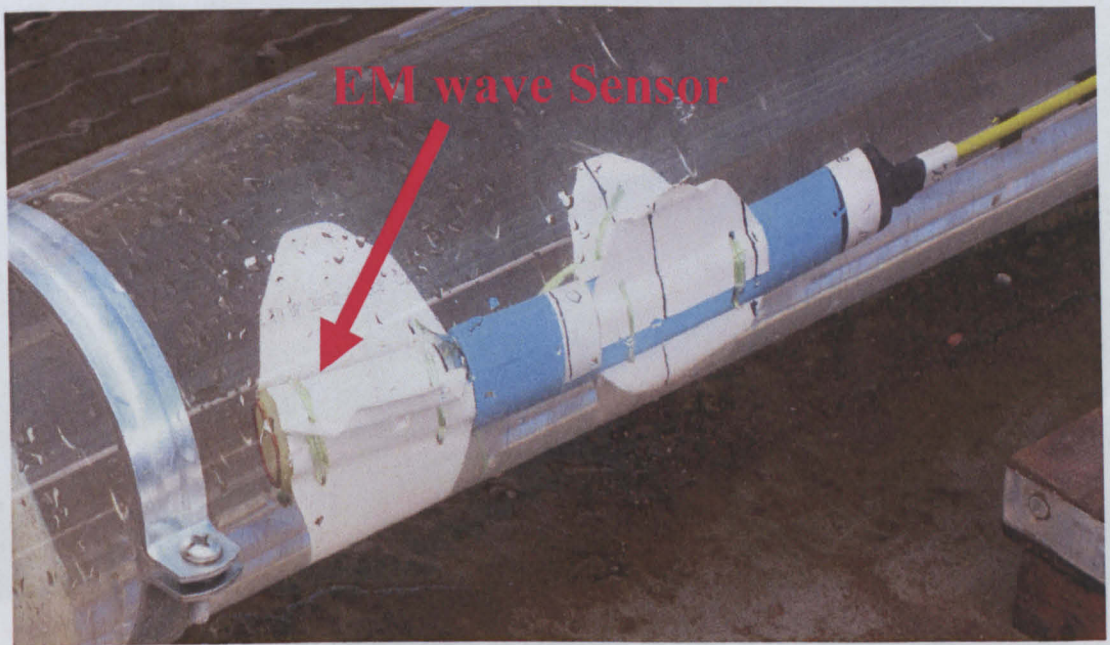


Figure 6.13: EM wave sensor in Perspex section with power and control cables feeding back to laptop and LabVIEW

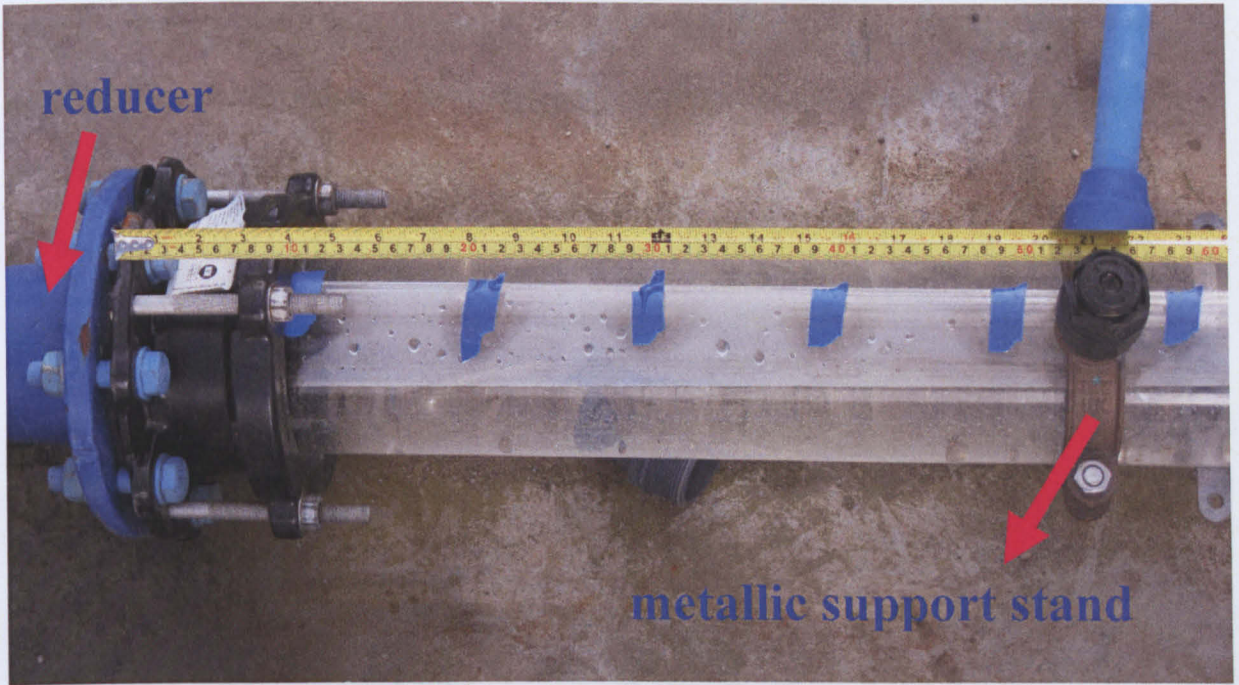


Figure 6.14: Photograph of markings starting from the reducer

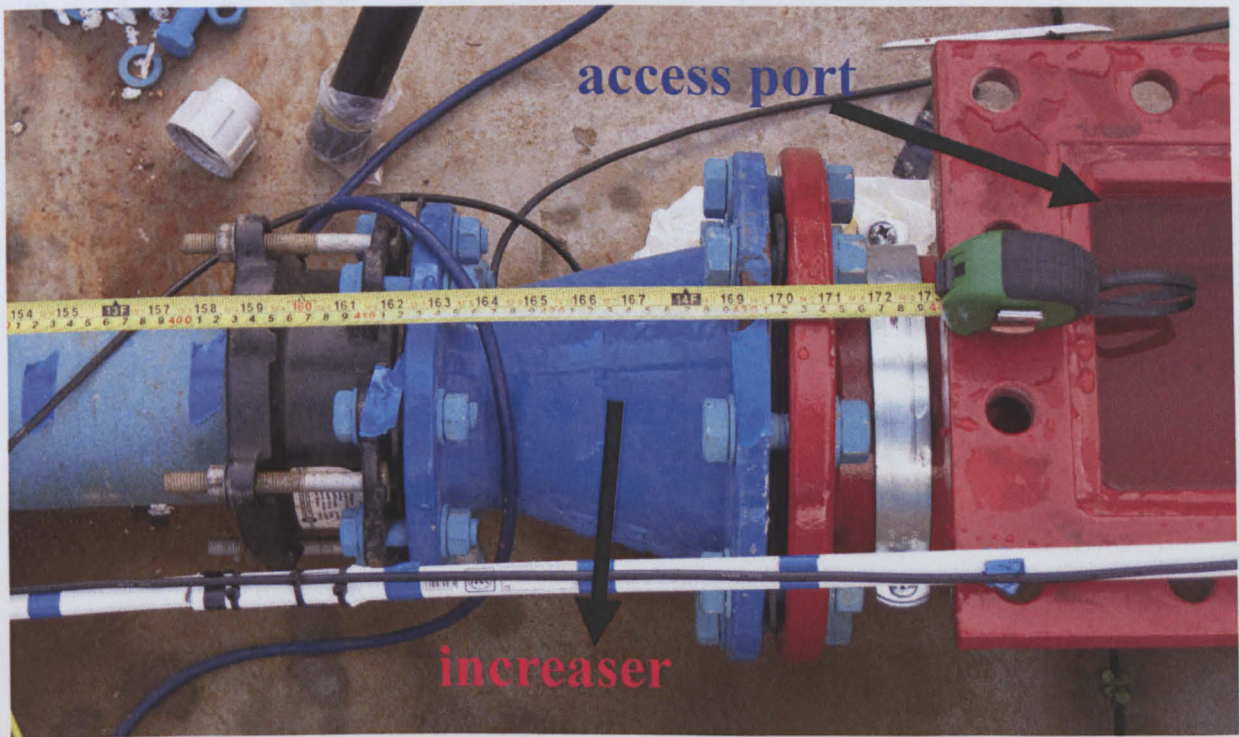


Figure 6.15: Photograph of marking ending at the access port

Figure 6.16 shows the results due to the reducer, the initial resonance peak for 0cm is at 275MHz, then the resonance peak is changes to 303MHz when the sensor is pulled back from the metallic reducer into the Perspex section. The spectrum then remains static as the sensor is pulled back along the Perspex section which is 2.5m long with only slight variances as the sensor is pulled over the metallic support stands.

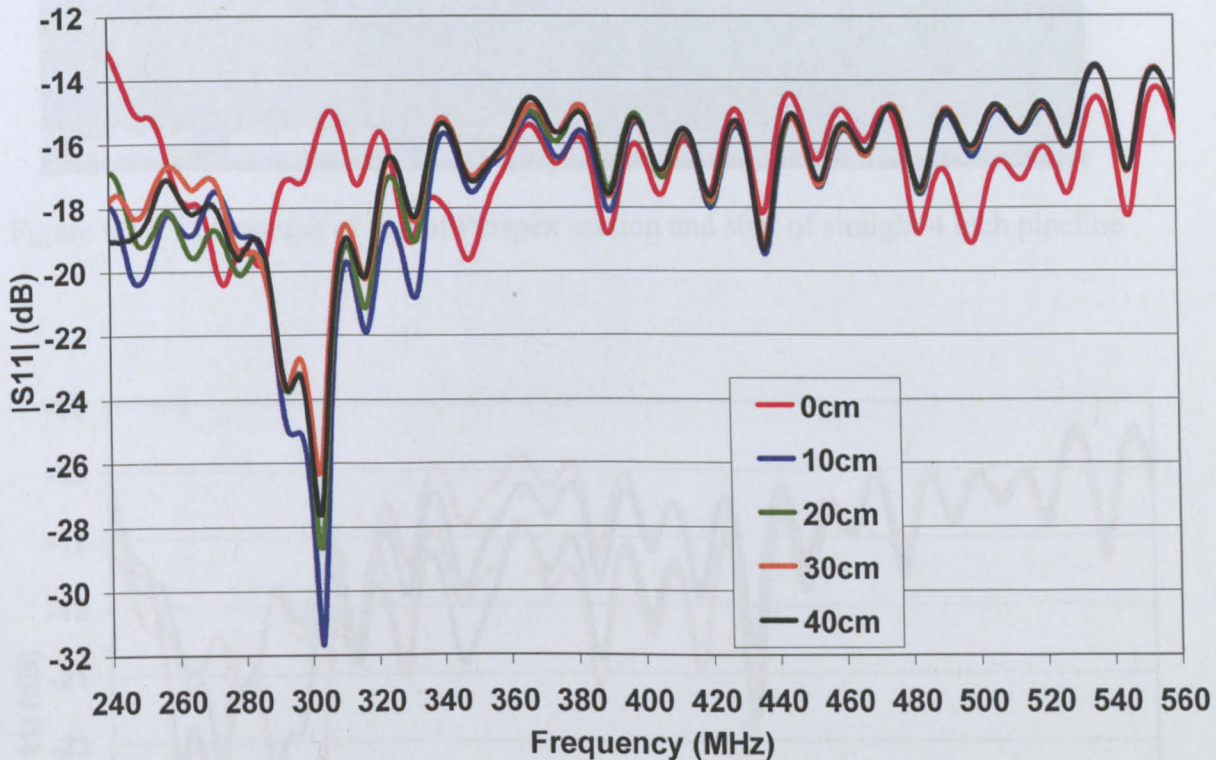


Figure 6.16: Results of reducer and start position of EM wave sensor

When the sensor is pulled from the end of Perspex section into the 4 inch cast iron pipeline section, which shown in Figure 6.17, the resonance peak in Figure 6.18 changes back from 303MHz at 2.3m to 275MHz at 2.5m as the sensor is now totally surrounded by metal.

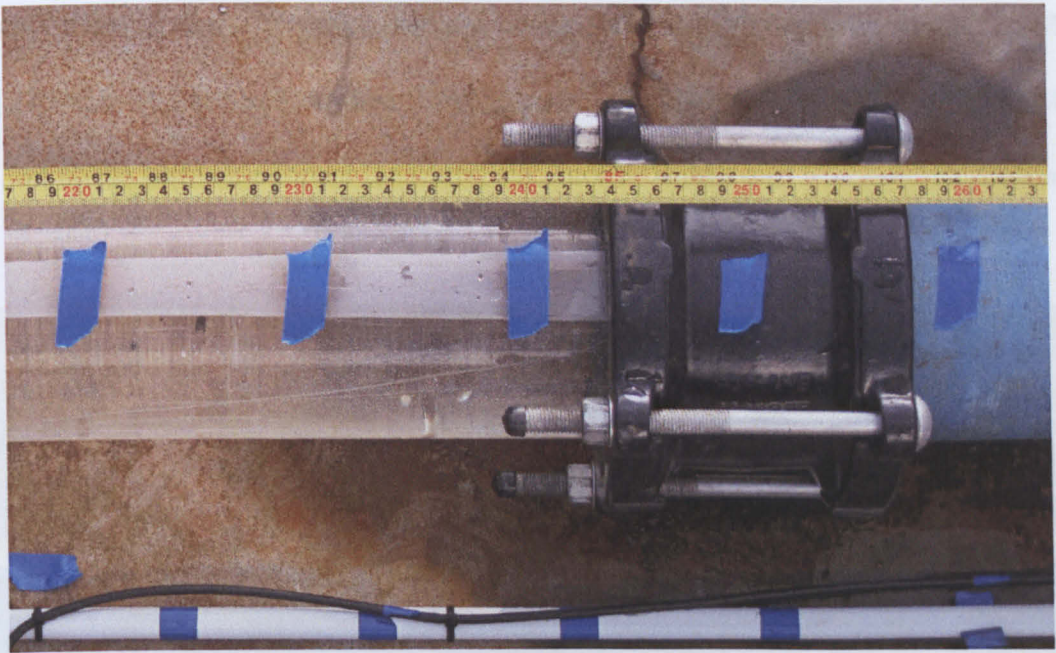


Figure 6.17: Photograph of end of Perspex section and start of straight 4 inch pipeline

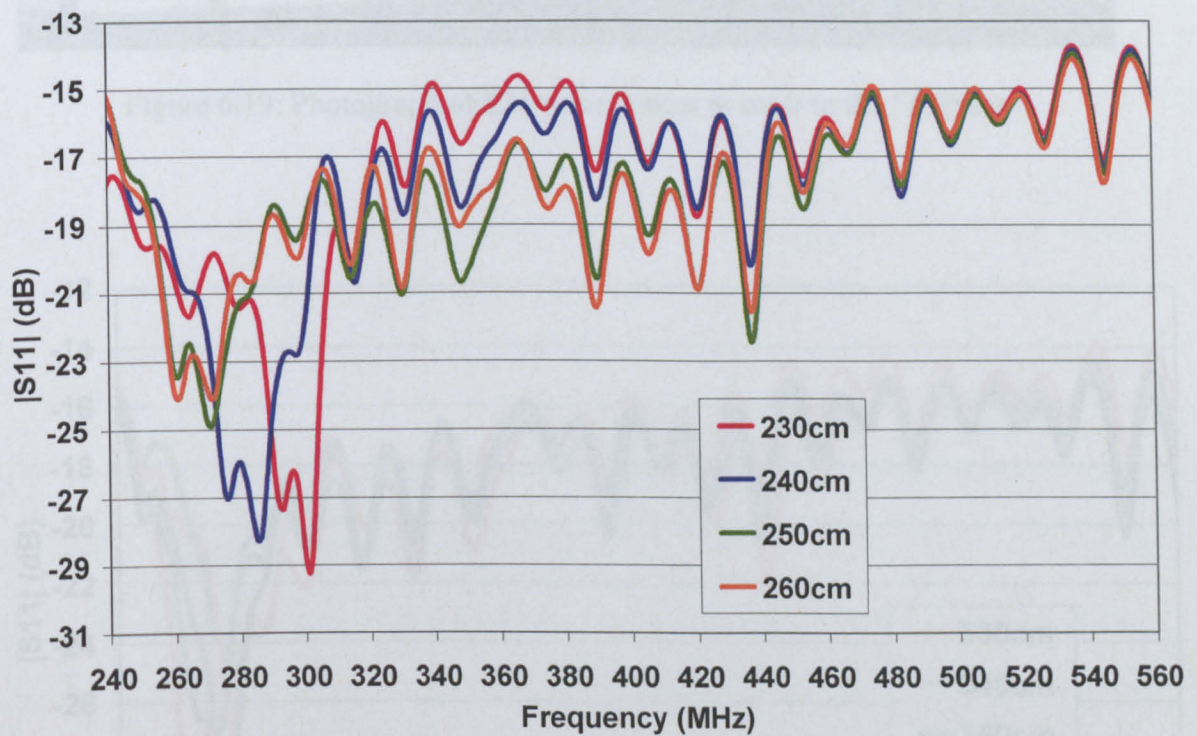


Figure 6.18: Results of end of Perspex section and start of the straight 4 inch pipeline

Figure 6.19 shows the EM wave sensor entering the 'T' piece at 3.3m, the resonance peak is constant at 275MHz as shown in Figure 6.20. When the EM wave sensor passes

through the arm of the 'T' piece, the resonance peak slowly changes between 270MHz and 277MHz at 3.4m to 3.6m and then the resonance peak returns back to the 275MHz at 3.7m as the EM wave sensor is return back into the 4 inch cast iron pipeline section.



Figure 6.19: Photograph of EM wave sensor is enter to the 'T' Piece

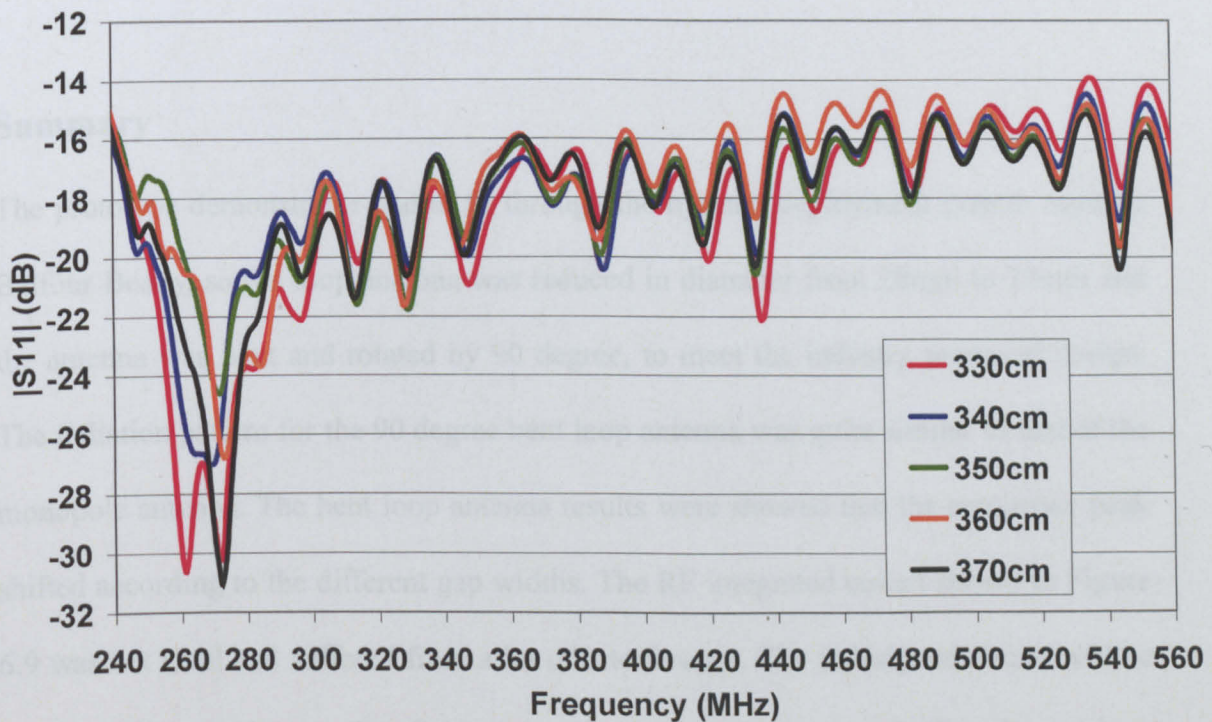


Figure 6.20: Results of EM wave sensor is enter to 'T' piece

When the sensor is pulled from the end of 4 inch cast iron section pipeline into the 4 to 6 inch increaser at 4.0m shown in Figure 6.15, the resonance peak in Figure 6.21 changes to 297MHz at 4.3m.

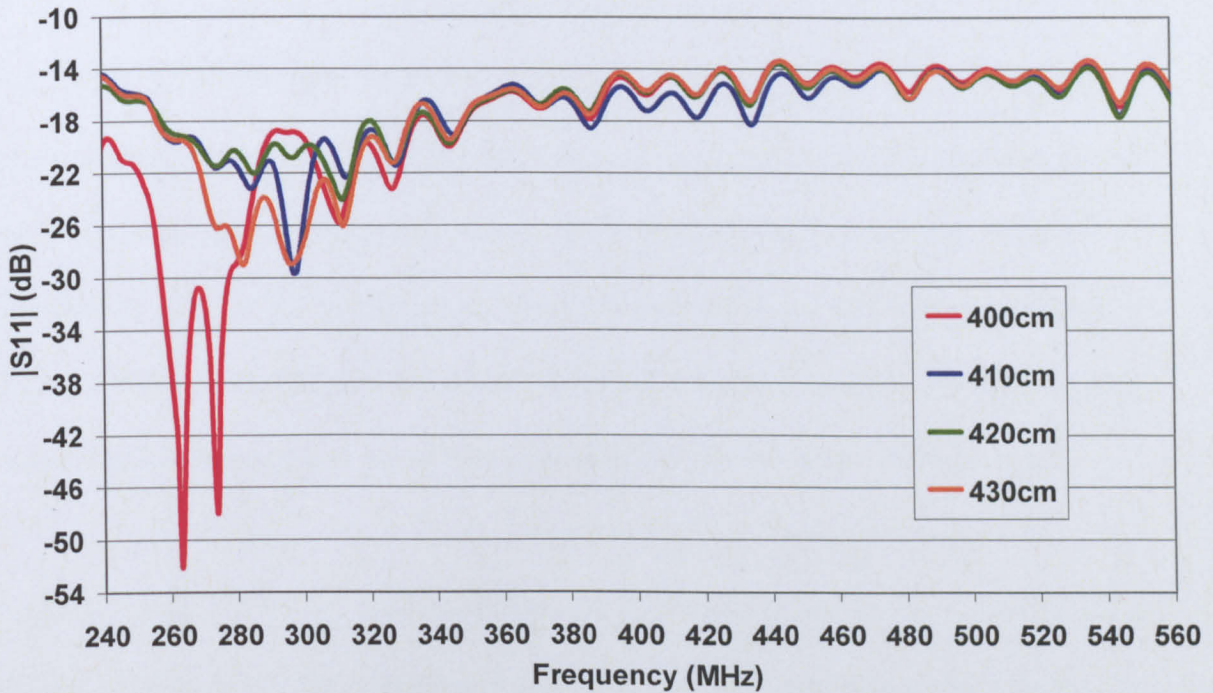


Figure 6.21: Results of increaser and end position at the access port of EM wave sensor

Summary

The prototype demonstrator had to fit through the hydrant deployment system used by Balfour Beatty, so the loop antenna was reduced in diameter from 28mm to 22mm and the antenna was bent and rotated by 90 degree, to meet the industry proposed design. The radiation pattern for the 90 degree bent loop antenna was quite similar to that of the monopole antenna. The bent loop antenna results were showed that the resonance peak shifted according to the different gap widths. The RF integrated circuit shown in Figure 6.9 was not ideal and suffered from a lot of interference. The redesigned circuit will be discussed in next chapter. The field trial at the Balfour Beatty test facility showed how

the resonance frequency changed in difference types of pipeline. The resonance frequency for the 4 inch metal pipe was 275MHz, for the 4 inch Perspex section it was 303MHz, and for the increaser it was 297MHz. When the sensor passed through the 'T' Pieces, the resonance frequency changed between 270MHz and 277MHz.

Chapter 7: PCB Design and

Leak Detection Trial

7.1 Eagle PCB Design Software

The next development stage was to build a second version of the PCB board with all the RF electronics for the integrated sensor. The previous version suffered from lot of interference and the RF signal is lost when transmitting via a wire which is shown in Figure 6.9 and 6.10. The new version PCB board was made using an FR4 prototyping board. The interference and signal loss were reduced using this new PCB design.

Eagle software [129] was used to design the PCB board. For the first step [130], a library for each of the RF components including the VCO, the directional coupler, the voltage regulator, the amplifier and the power detector was needed to be created as shown in Figure 7.1 before drawing the layout of the circuit. The second step was to draw the schematic diagram for the electronic circuit shown in Figure 7.2 by using the library that was created in previous step. The final step was to reorganize and place the component in the best position for the best wiring on the board and make the board as small as possible. Figure 7.3 shows the PCB layout for the integrated sensor. The size for this PCB board was 65mm in length and 20mm in width.

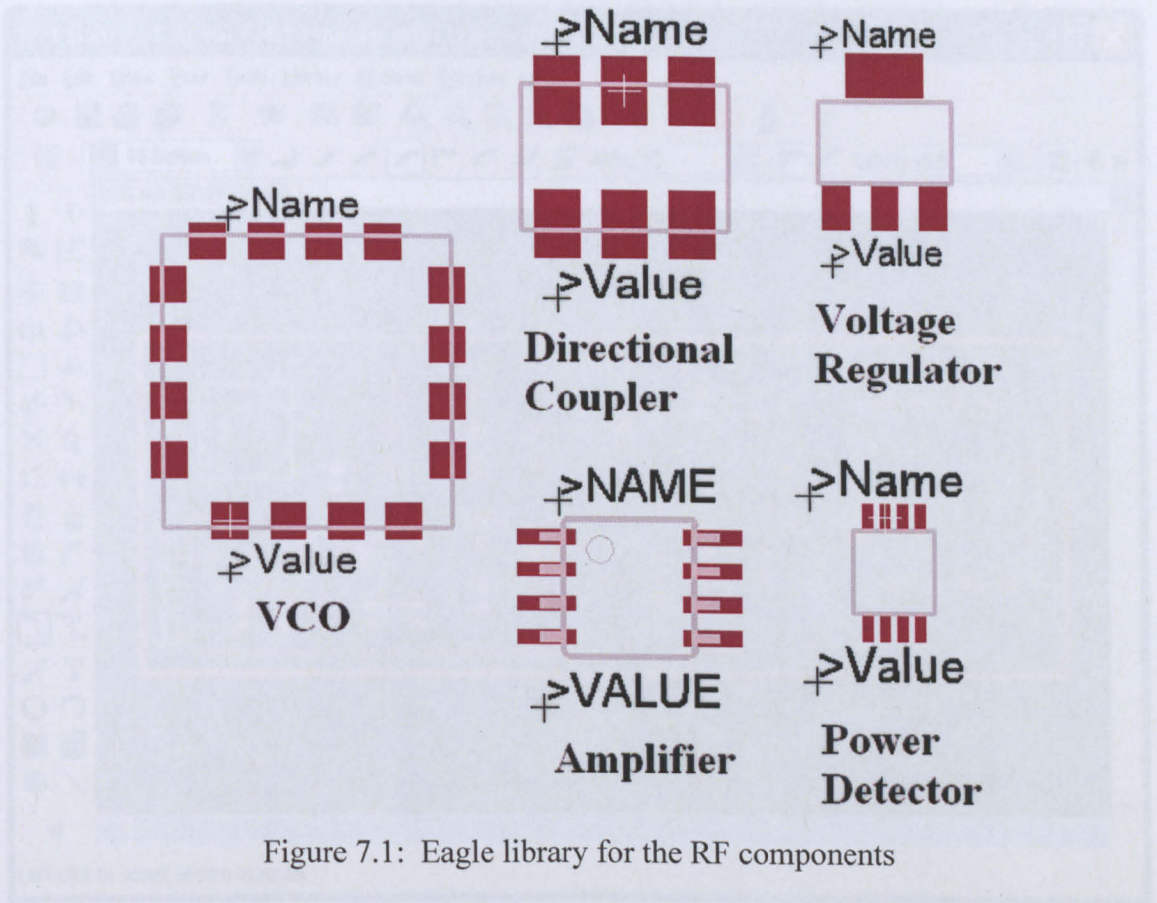


Figure 7.1: Eagle library for the RF components

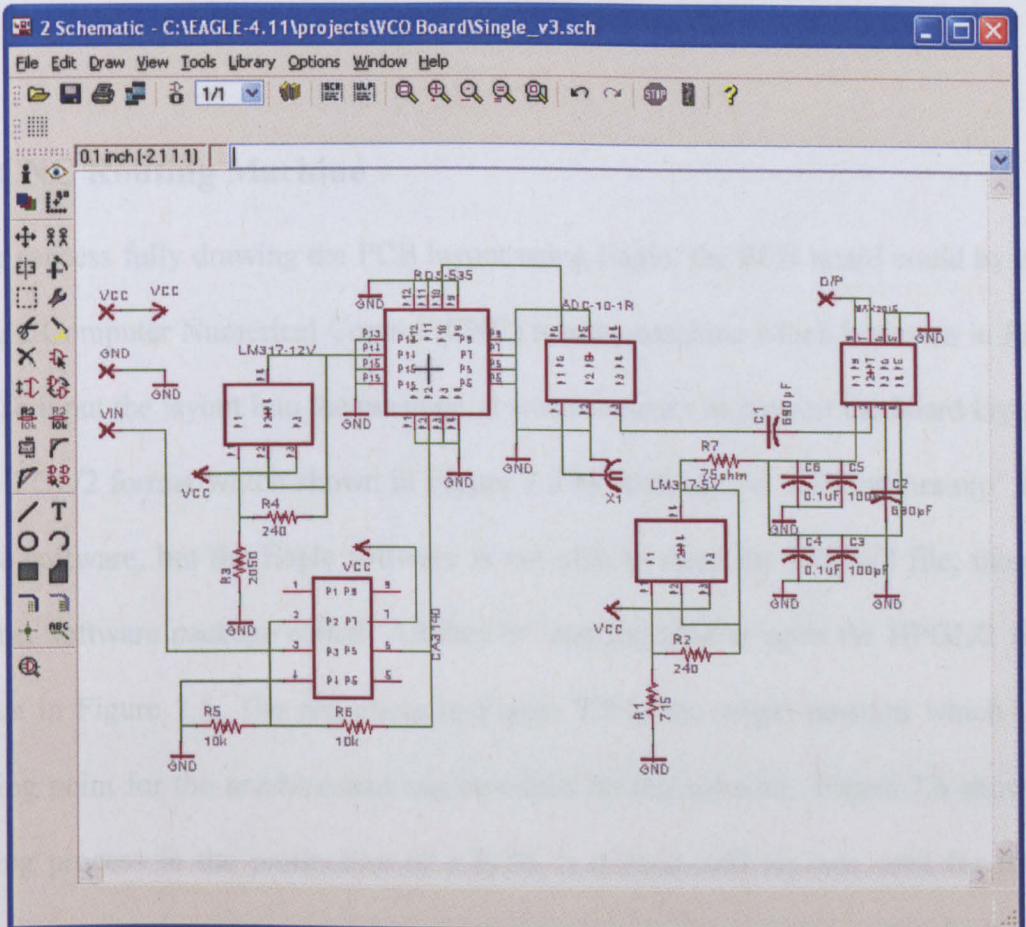


Figure 7.2: Schematic diagram for the integrated sensor

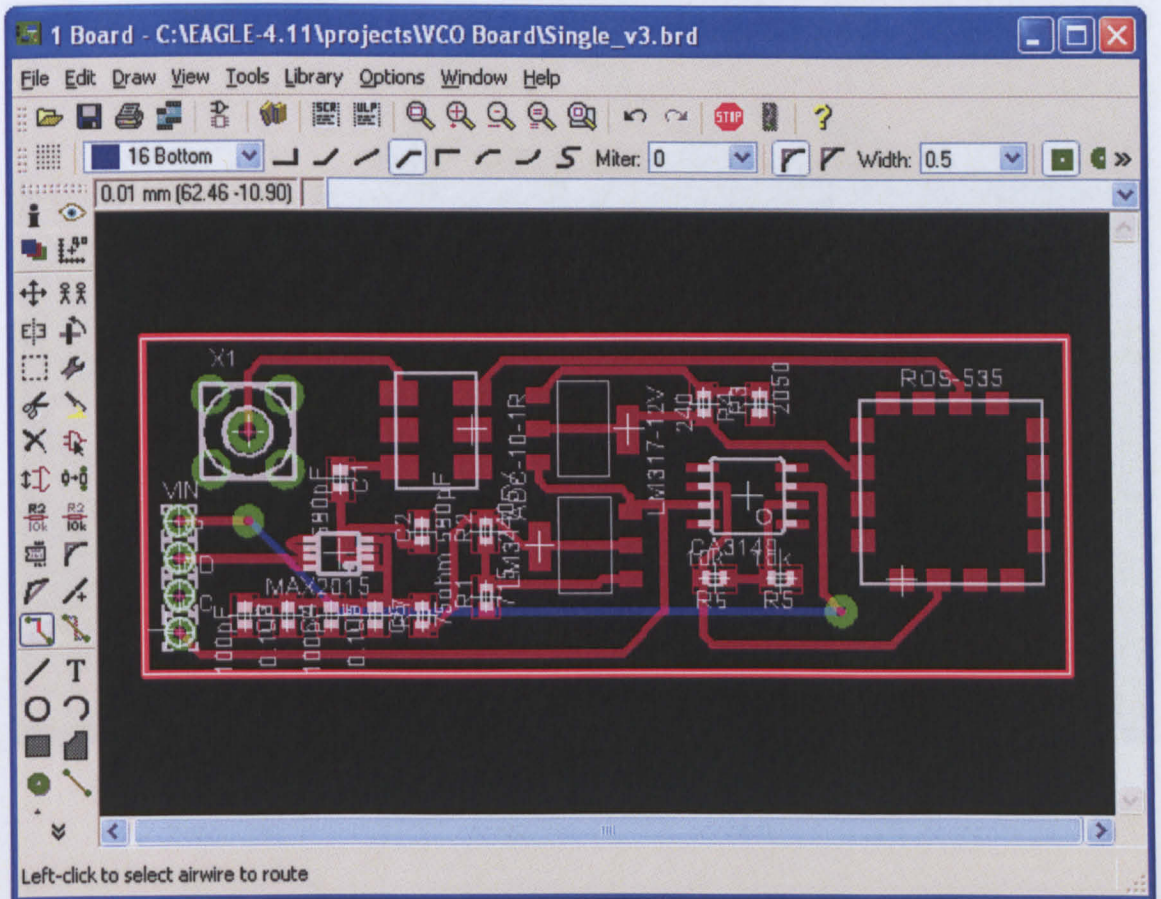


Figure 7.3: PCB layout for the integrated sensor

7.2 CNC Routing Machine

After successfully drawing the PCB layout using Eagle, the PCB board could be made using a Computer Numerical Control (CNC) routing machine which is shown in Figure 7.4. To input the layout into the machine, it was necessary to convert the board layout to the HPGL/2 format which is shown in Figure 7.5 by running the 'mil-outlines.ulp' in the Eagle software, but the Eagle software is not able to open the HPGL/2 file, therefore another software package called 'ABViewer' was required to open the HPGL/2 file as shown in Figure 7.5. The red circle in Figure 7.5 is the origin position which is the starting point for the machine and can be edited by the software. Figure 7.6 shows the routing process in the production of a PCB. A 0.1mm drill bit was used for routing because the spacing of the soldering pins for power detector is very narrow.

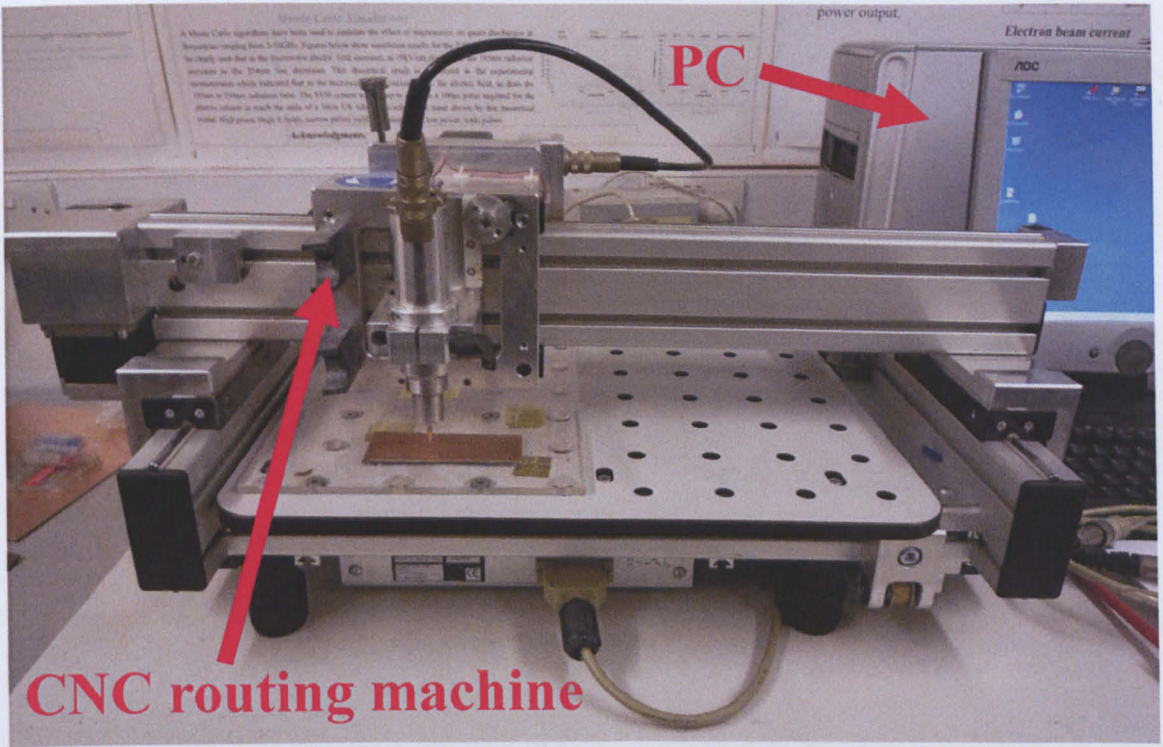


Figure 7.4: Bungard CCD2, CNC machine [131]

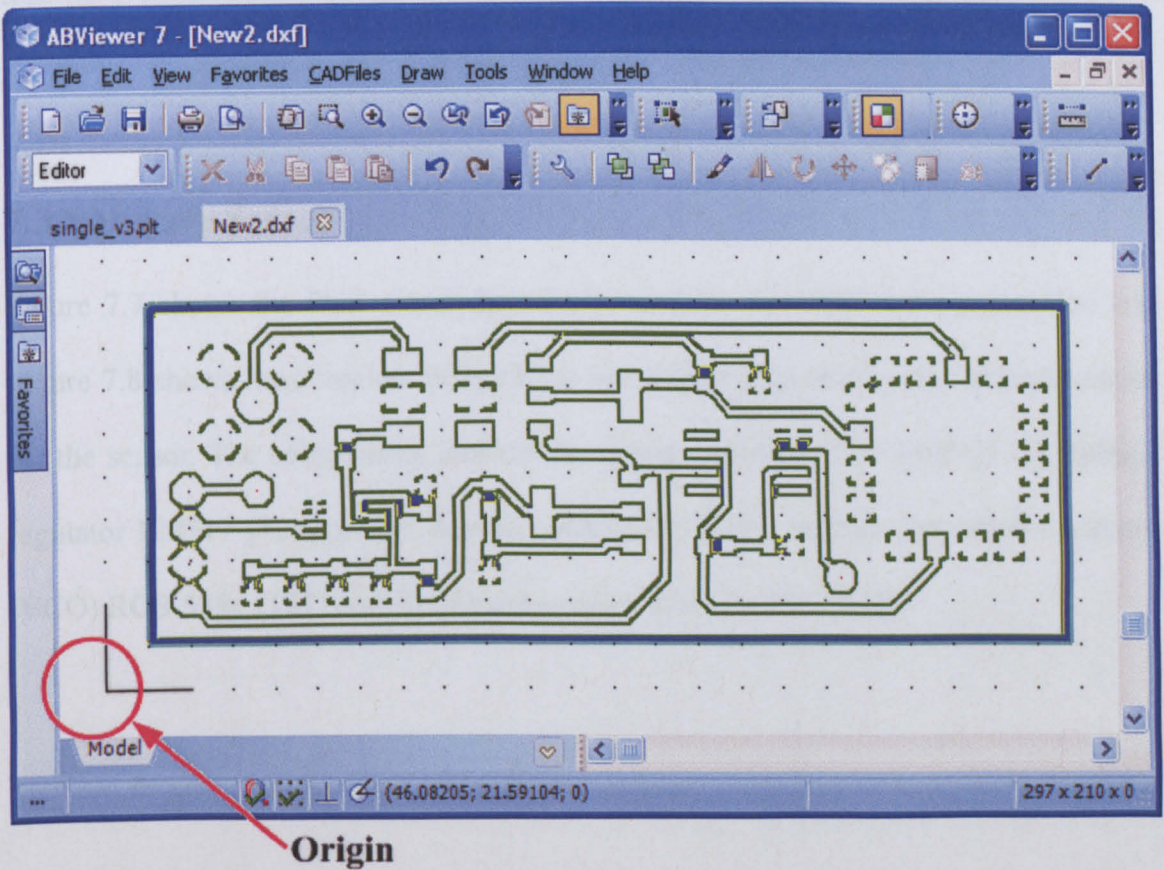


Figure 7.5: ABViewer use to open the HPGL/2 file

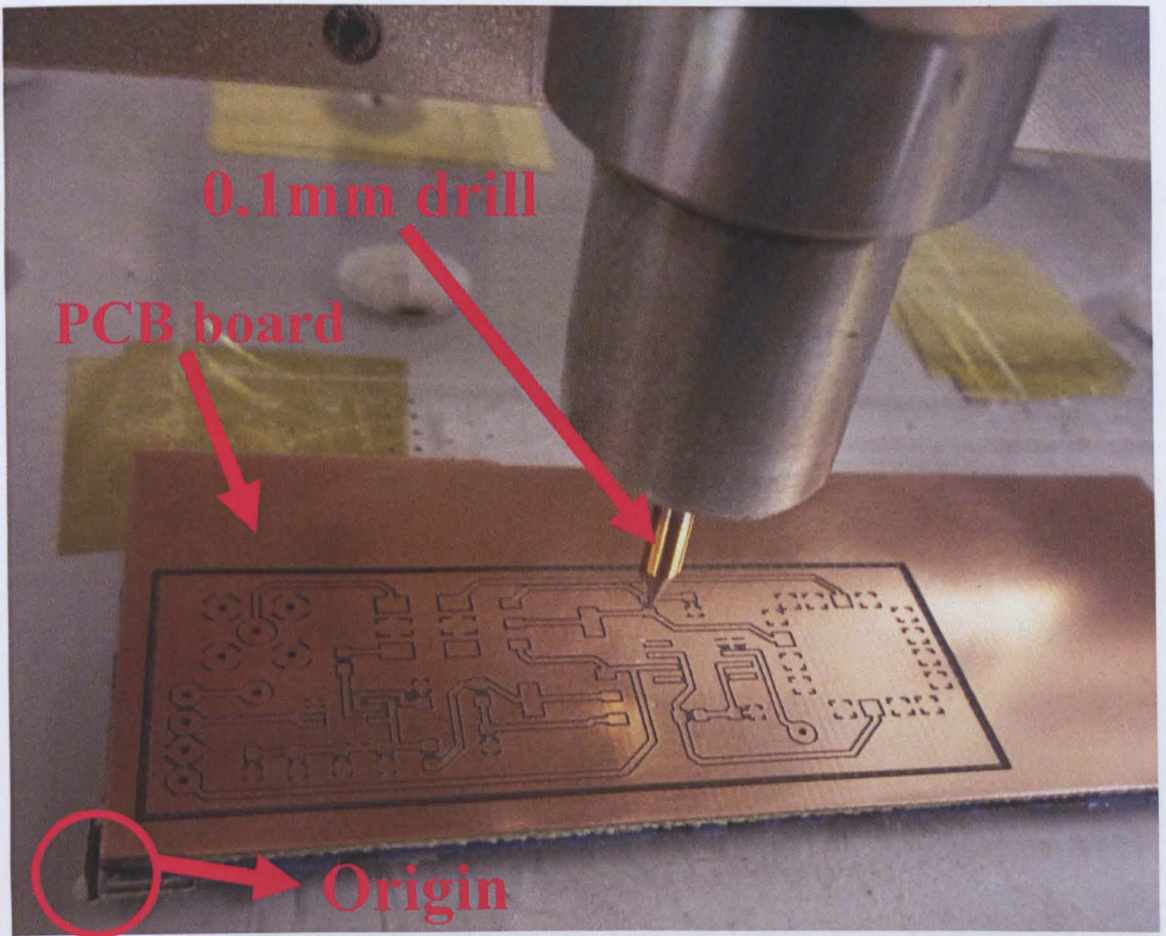


Figure 7.6: PCB board making by CNC routing machine

7.3 EM wave Sensor

Figure 7.7 shows the PCB circuit board produced by the CNC routing machine and Figure 7.8 shows the complete PCB circuit board fully populated with the components for the sensor. The components include the voltage amplifier CA3140E [121], voltage regulator LM317 [125], power detector MAX2015 [126], voltage controlled oscillator (VCO) ROS-535+ [127] and directional coupler ADC-10-1R+ [132].

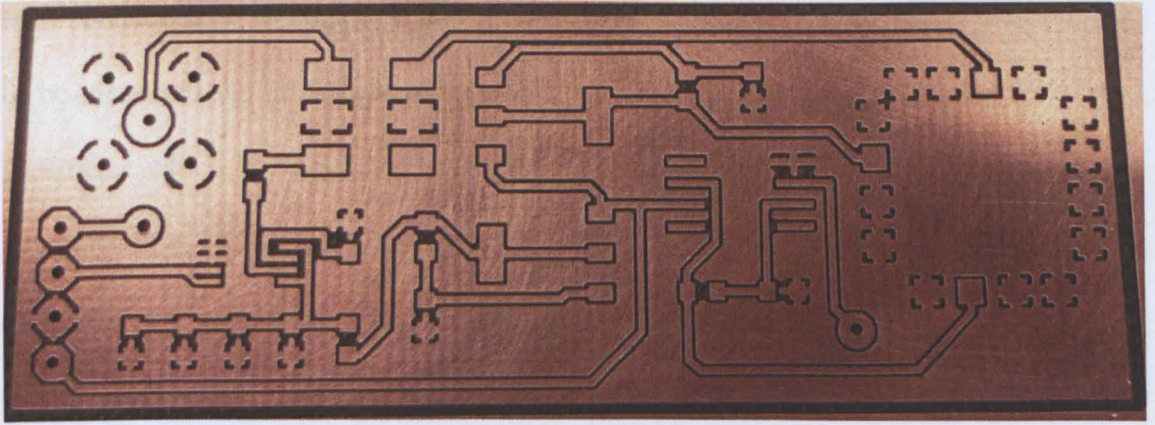


Figure 7.7: PCB circuit board for the sensor created by the CNC routing machine

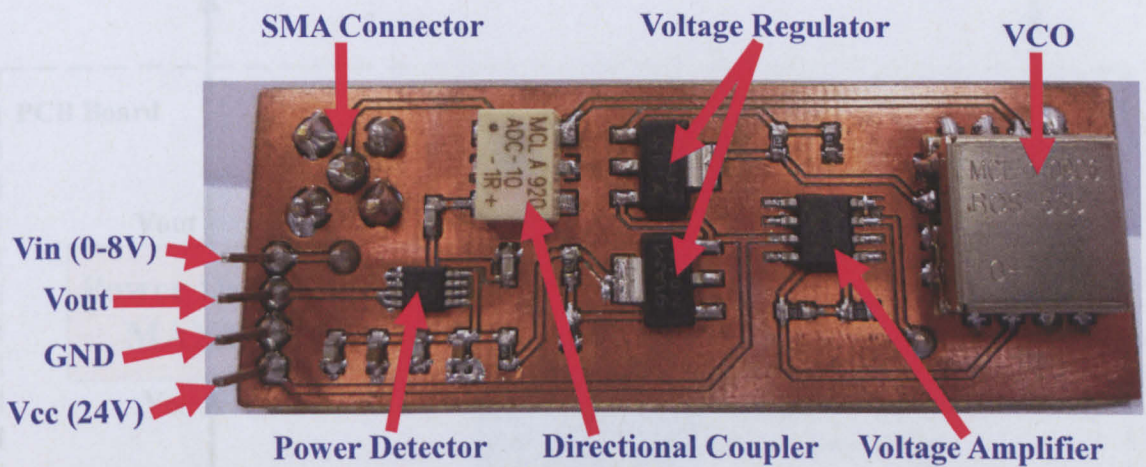


Figure 7.8: Complete PCB circuit board with full components for the sensor

Figure 7.9 shows the block diagram for the PCB circuit board sensor. For this circuit, a 24V power supply will supply the two voltage regulators LM317 and the amplifier CA3140E. The voltage regulators produce a 5V and 12V output voltages for the RF power detector MAX2015 and the voltage controlled oscillators (VCO) ROS-535+. The LabVIEW programming software discussed in chapter 4 was used to control the NI Compaq DAQ with analogue output module NI9264 to produce an output voltage range from 0 to 8V, which was then amplified from 0 to 16V which will give the full range of frequency output. The VCO produces a frequency sweep from 240MHz to 560MHz. The RF output from the VCO passes through a directional coupler ADC-10-1R+ and is

then connecting to the antenna via an SMA connector. This allows the reflected power to be measured via an RF power detector. The reflected signal power level is the $|S_{11}|$ parameter which is required for the RF signatures. The output from the RF power detectors is a DC voltage in the range of 0 to 2V which is then connected to the analogue input module NI9205 from which LabVIEW plots out the spectrum.

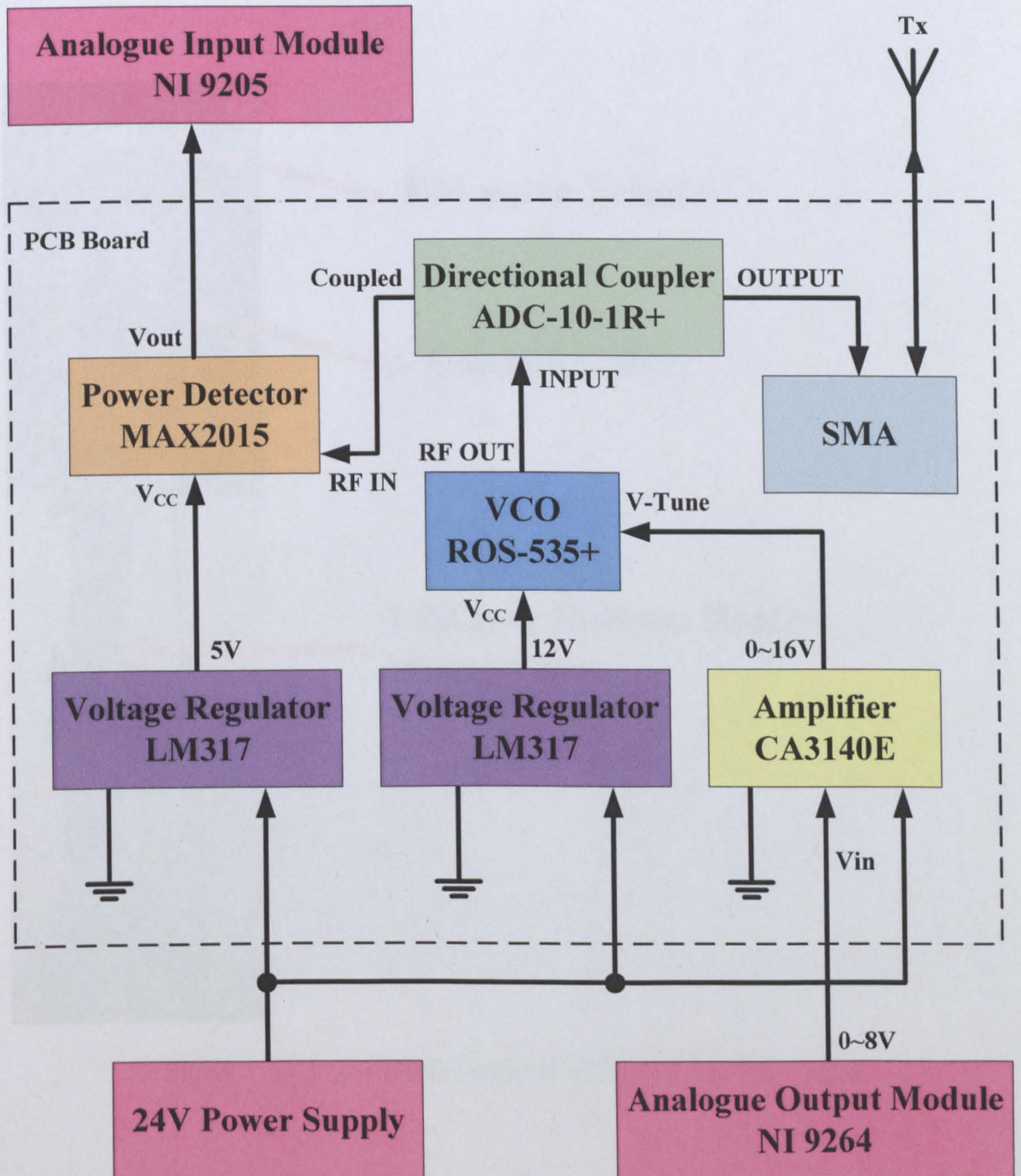


Figure 7.9: Block diagram for PCB circuit board sensor

7.4 Experiments for Reference Signal

The next stage is to prove that the EM wave sensor can detect a leak in the pipeline. The first step is to obtain the reference signal spectrum for the 4 inch metal pipeline, then the sensor is put into the pipeline and the signal spectrum is compared with the reference signal. The signals comparison is done by the LabVIEW programme and the programme will make a conclusion whether or not the pipeline needs further inspection.

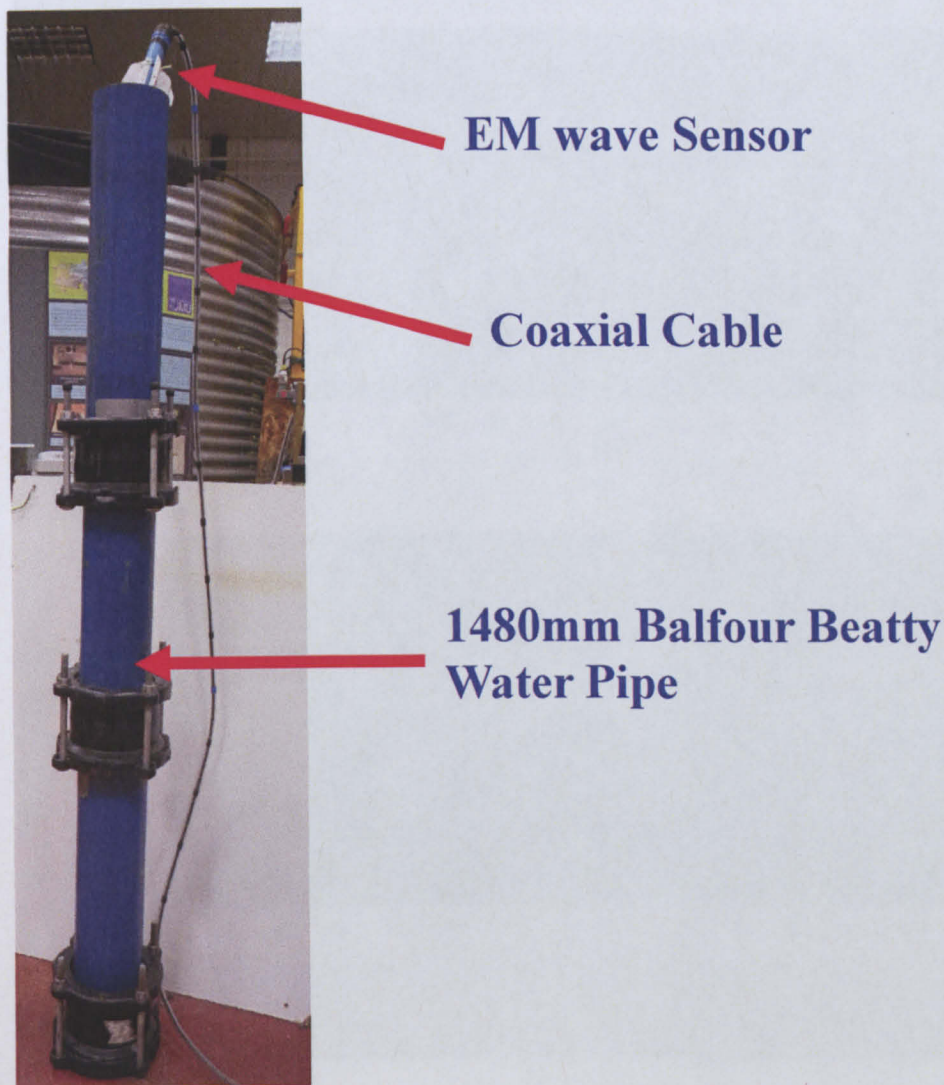


Figure 7.10: Experimental setup to obtain the reference signal

Figure 7.10 shows the experimental setup used to obtain the reference signal. This experiment is setup with three 4 inch diameter pipelines sections connected together.

These pipelines were mounted vertically and filled with water. The total length of the pipelines sections was 1480mm. The EM wave sensor with the final version of electronics circuit which is shown in Figure 7.8 was used. The EM wave sensor was put into pipeline from the top of the pipe and the EM wave sensor passed through the centre of the pipeline.

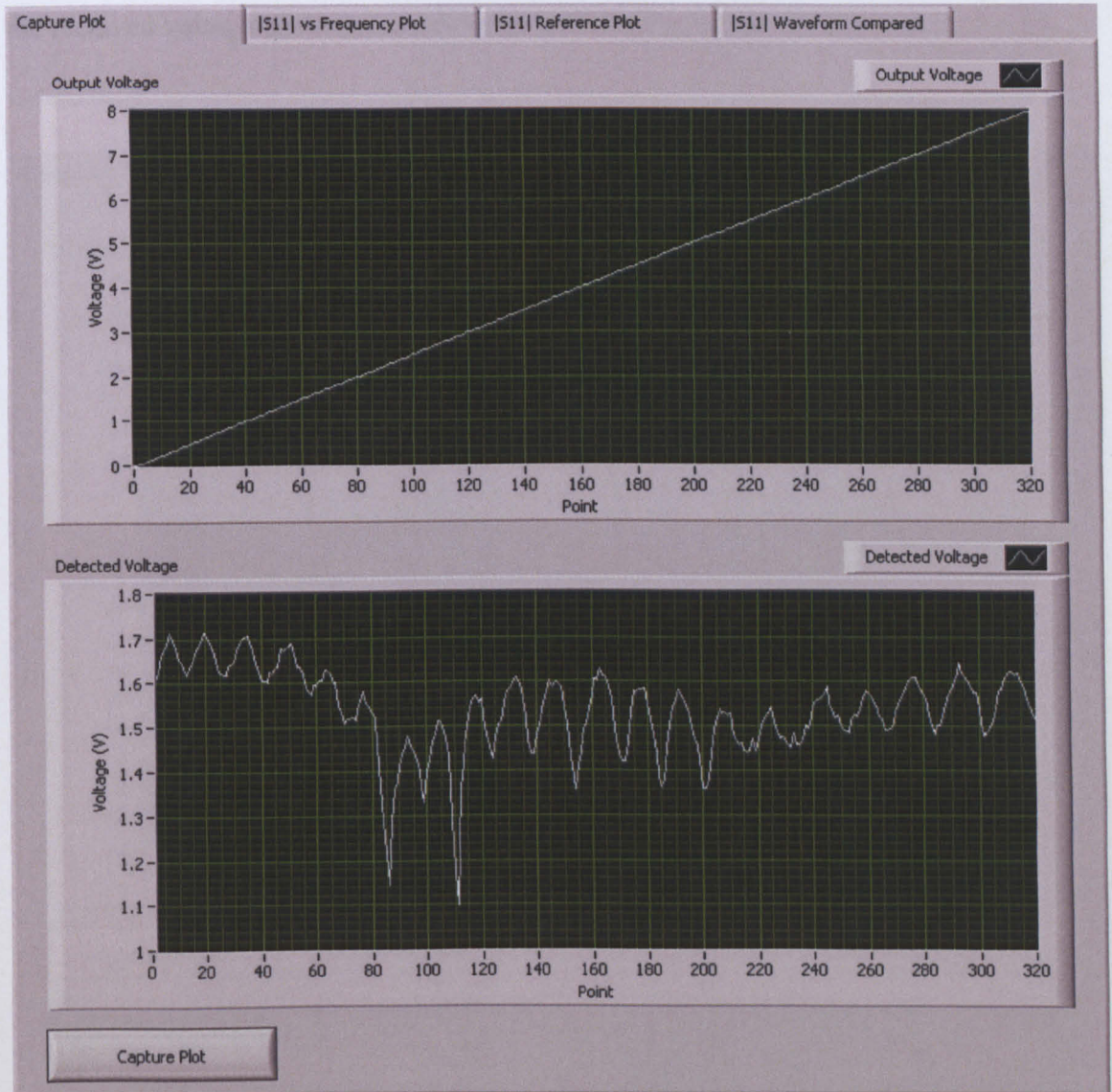


Figure 7.11: LabVIEW capture the signal from the sensor

This experiment allowed 14 readings to take place along the 1480mm test section. The measurements for the reflection signal $|S_{11}|$ was taken at 10cm interval using the LabVIEW programme. This was used as a reference signal for leak detection. Figure 7.11 shows the LabVIEW capture of the signal from the sensor. The programme captured the spectrum when the 'Capture Plot' button was pressed, the Output voltage is the voltage that supplied the VCO for frequency sweeping and the detected voltage is the received voltage of the sensor from the power detector.

leaks in this project.

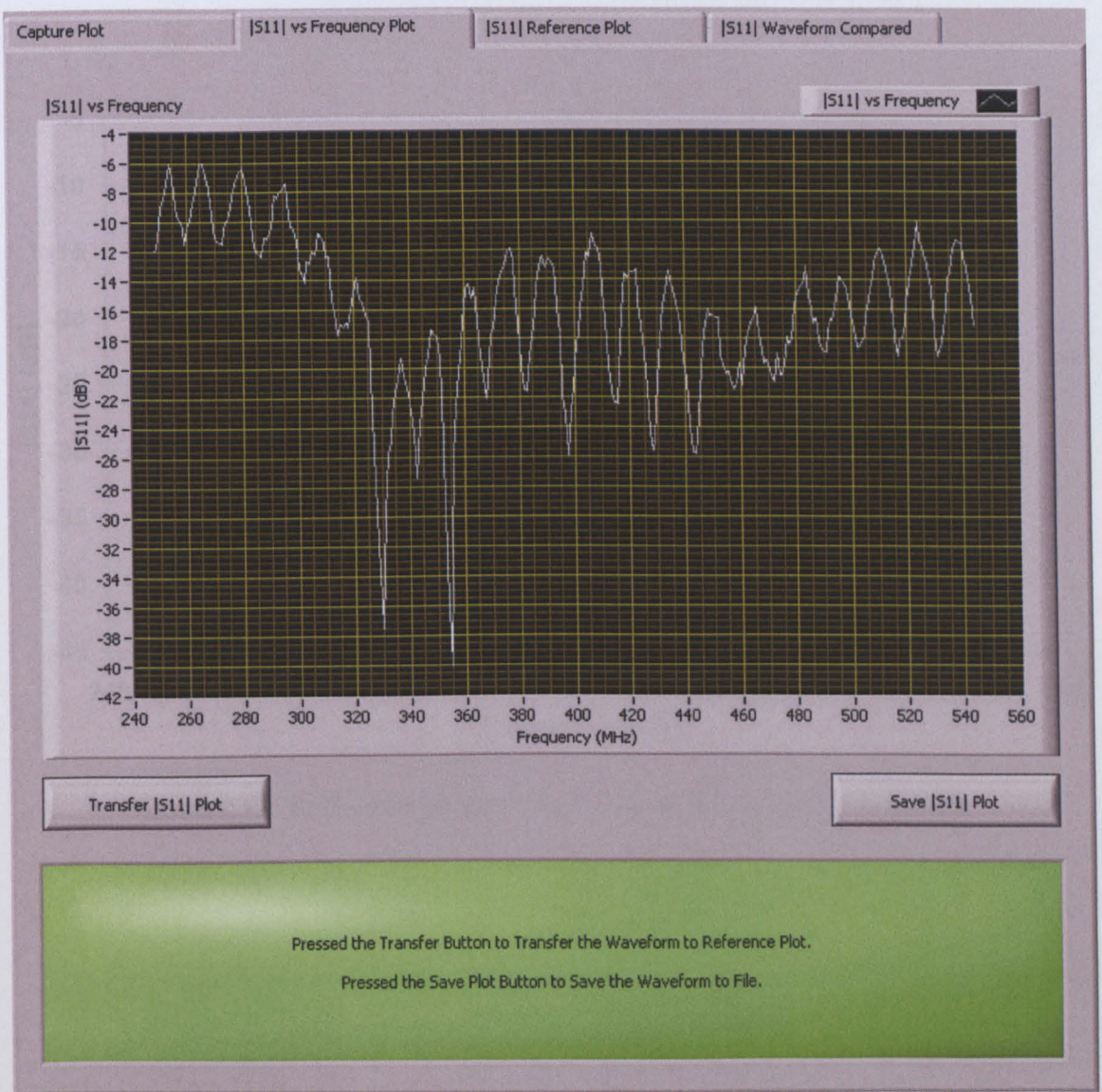


Figure 7.12: Frequency versus reflection signal $|S_{11}|$ from the sensor

The LabVIEW programme plotted the received signal strength versus frequency which in Figure 7.12. All of the reference signals were saved in a database by pressing the 'Save |S11| Plot' button.

The 14 reference signals from 10cm to 140cm are shown in Figures 7.13, 7.14 and 7.15. The resonance peak between 280MHz and 380MHz changed, but the remainder were the same shape. Therefore the $|S_{11}|$ between 280MHz and 380MHz was used to detect leaks in this project.

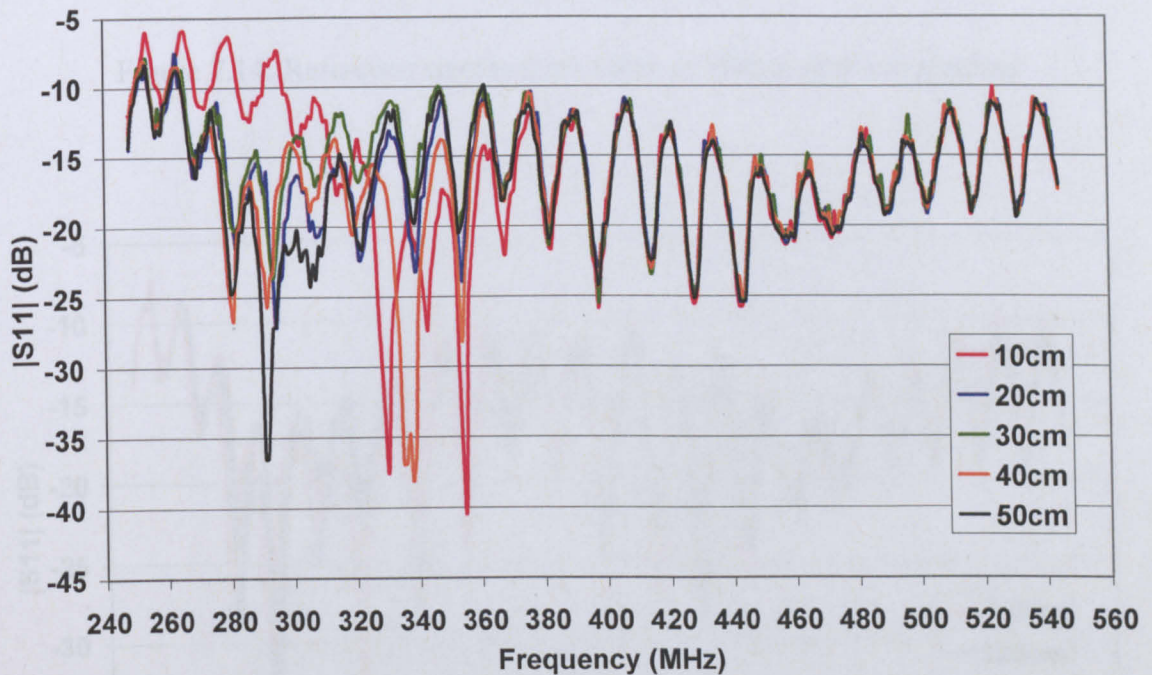


Figure 7.13: Reference signals from 10cm to 50cm depth in pipeline

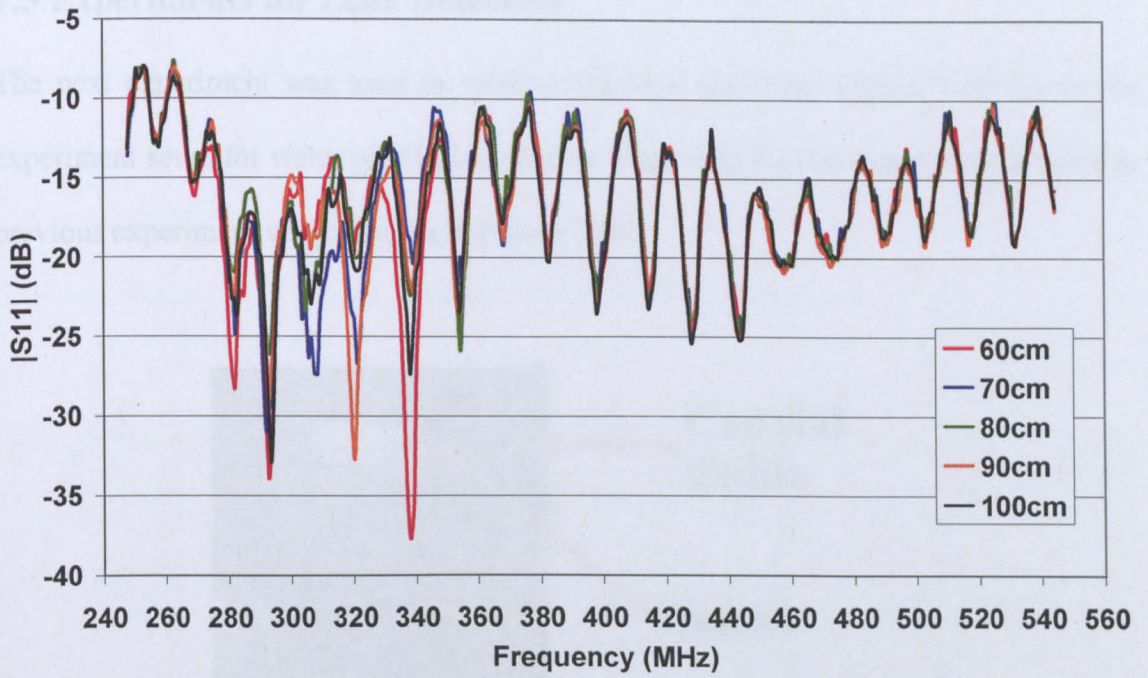


Figure 7.14: Reference signals from 60cm to 100cm depth in pipeline

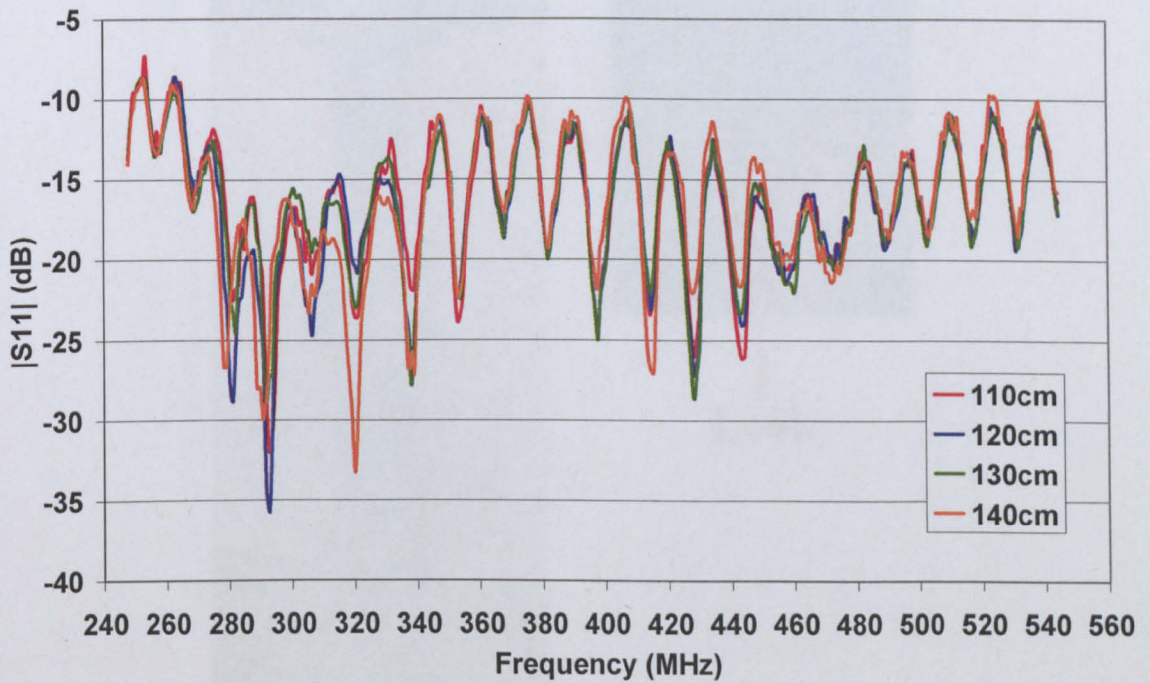


Figure 7.15: Reference signals from 110cm to 140cm depth in pipeline

7.5 Experiments for Leak Detection

The next experiment was used to validate the leak detection. Figure 7.16 shows the experiment setup for water pipe leak detection. The setup for this experiment is same as previous experiment which shown in Figure 7.10.

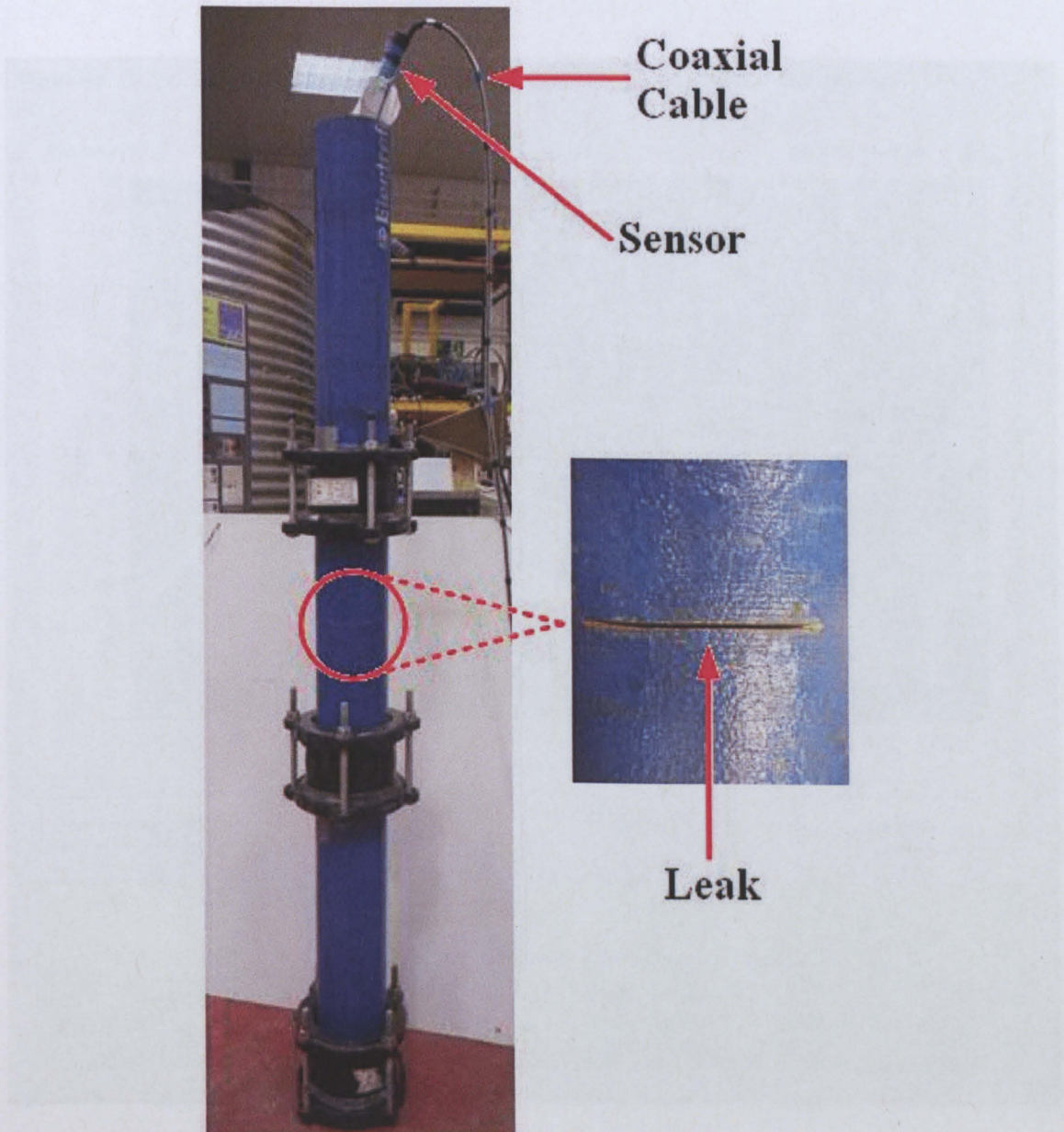


Figure 7.16: Experimental setup for water pipe leak detection

A crack was made in the central pipeline to demonstrate that the EM wave sensor was able to detect leakage in the water pipeline. The crack was sealed with tape to avoid

water leaking from the pipe when the experiment was in progress and to make sure that the pipe was always full filled of water. The crack was in centre position of the second pipeline section away from any of the joints and at 74cm from top of the pipeline. The EM wave sensor of electronics circuit was put into pipeline from the top of the pipe and the EM wave sensor passed through the centre of the pipeline.

In the previous experiment (Figure 7.16) the reflection signal

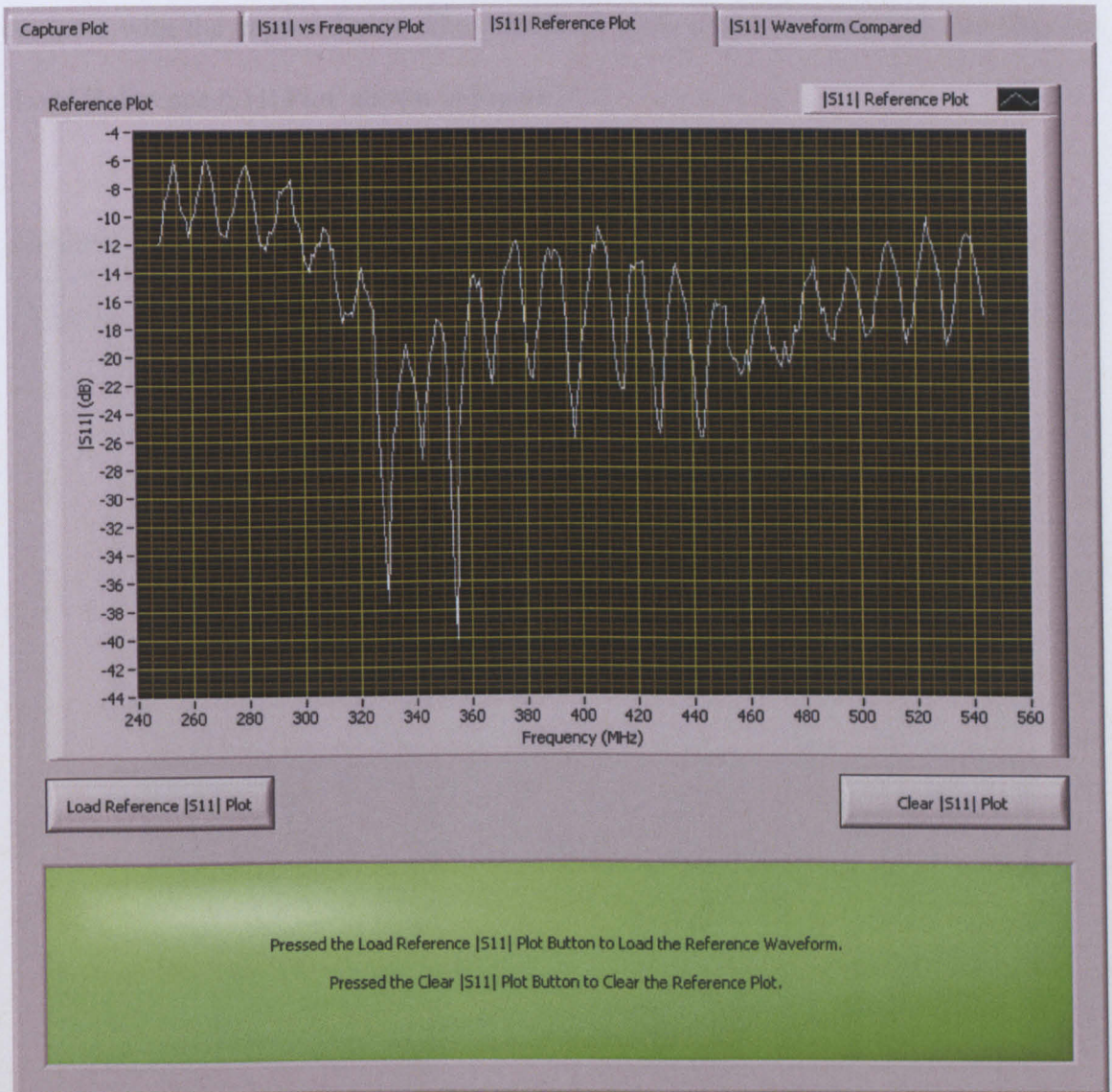


Figure 7.17: Reference $|S_{11}|$ plots loaded from database

The measurements for the reflection signal $|S_{11}|$ were taken at 10cm interval again by using the LabVIEW programme, and the reflection signal $|S_{11}|$ was compared with the

reference signals that were obtained in previous experiment. The LabVIEW programme then made a conclusion regarding whether the pipeline needed further inspection by using the Pearson correlation method which discussed in chapter 4.

The waveform comparison

The $|S_{11}|$ spectrum was captured by LabVIEW and the references plots that were saved in the previous experiment (Figure 7.13 to 7.15) were loaded from the database to compare with the captured plot. The references plots could be loaded by pressing the 'Load Reference $|S_{11}|$ Plot' shown in Figure 7.17.

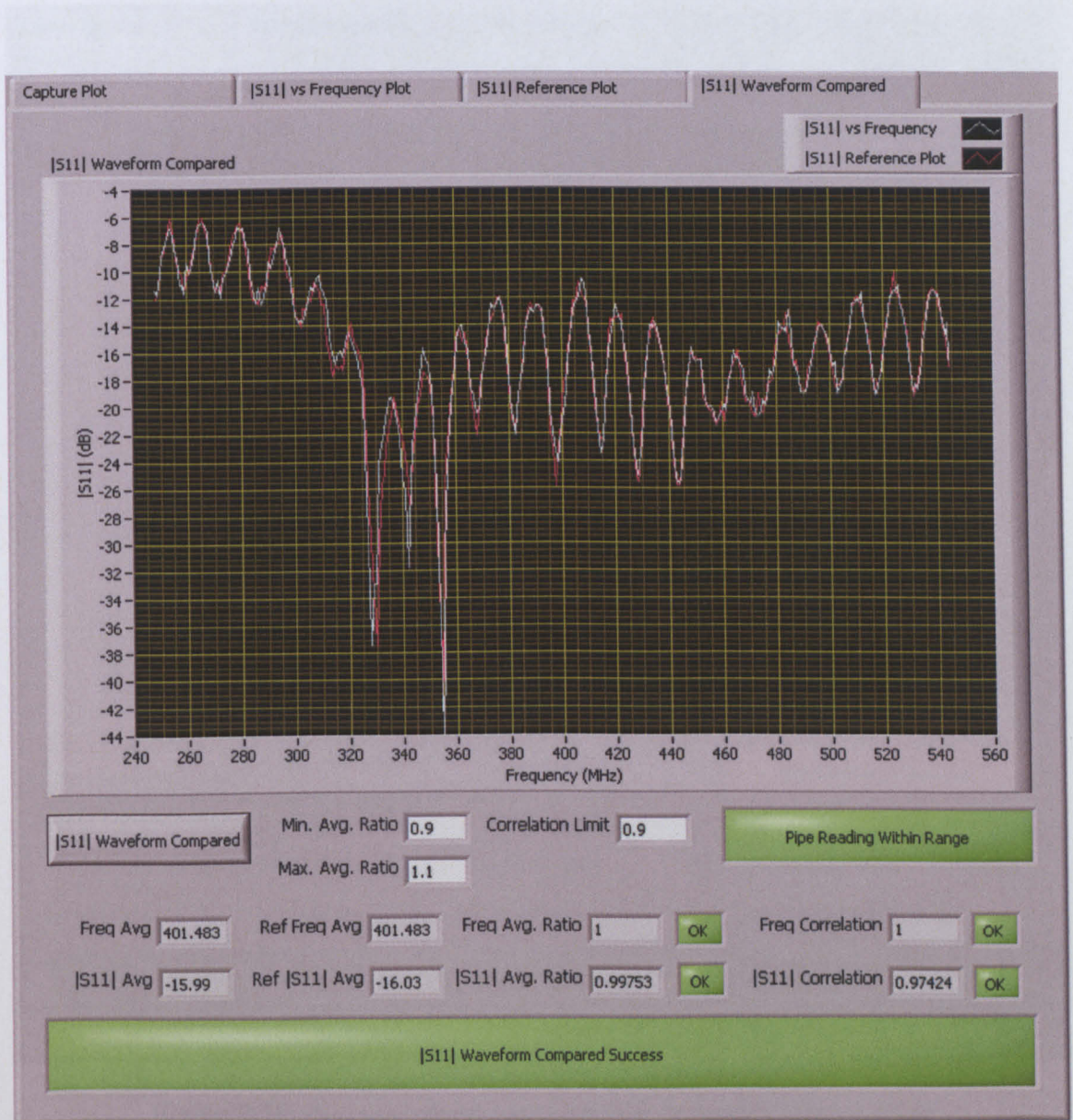


Figure 7.18: $|S_{11}|$ waveform compared for 10cm depth in pipeline

The 14 readings from 10cm to 140cm in the leaking pipeline were compared with the 14 reference signals in the database. Figure 7.18 to Figure 7.23 shows the waveform comparison for these signals from 10cm, 60cm to 90cm, and 140cm depth in pipeline. The waveform comparison for the rest of the signals was shown in appendix B. The signal comparisons were done by pressing the '|S11| Waveform Compared' button in the LabVIEW programme. The waveforms were compared by using the Pearson correlation statistic method.



Figure 7.19: |S11| waveform compared for 60cm depth in pipeline

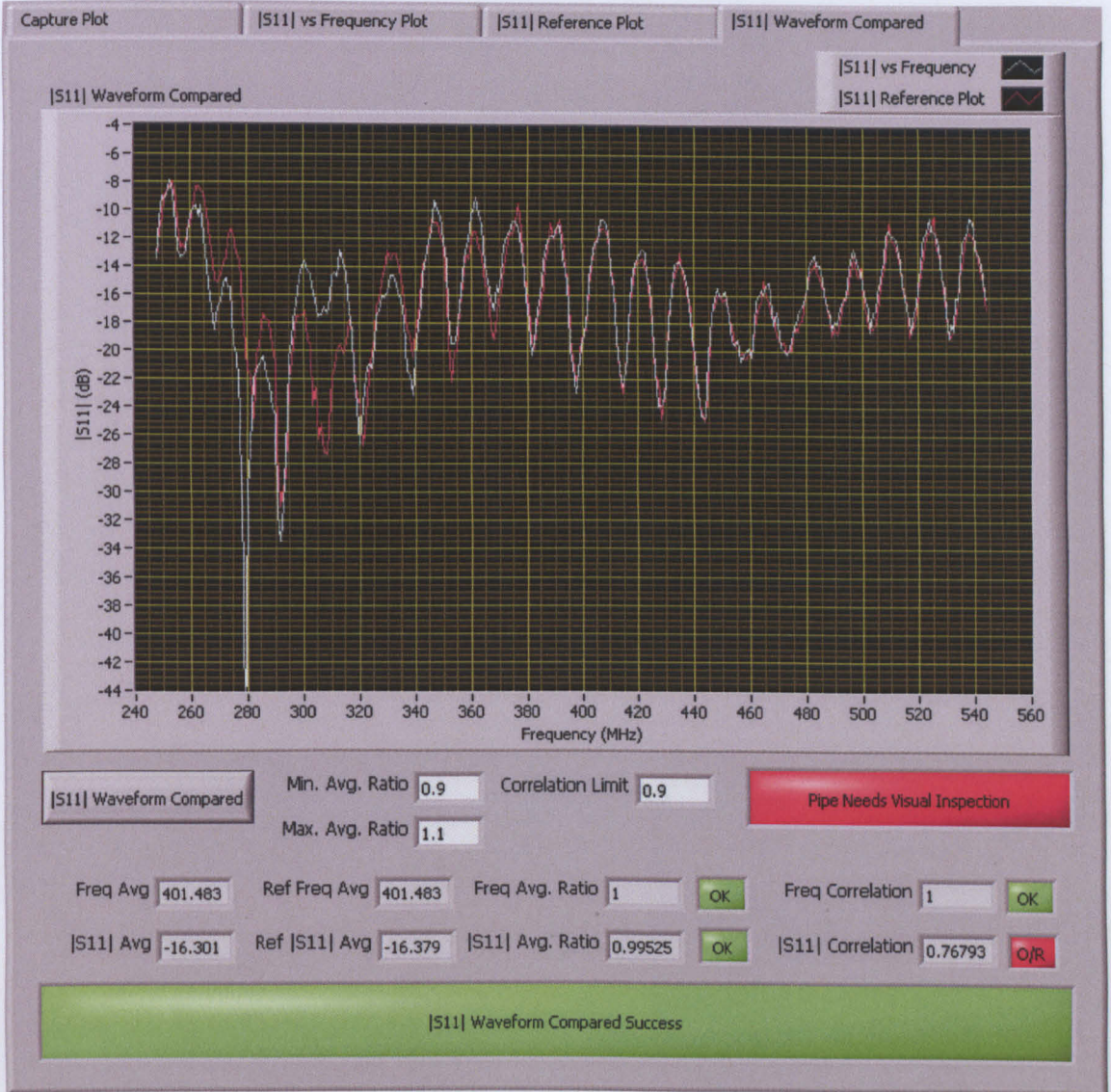


Figure 7.20: $|S_{11}|$ waveform compared for 70cm depth in pipeline

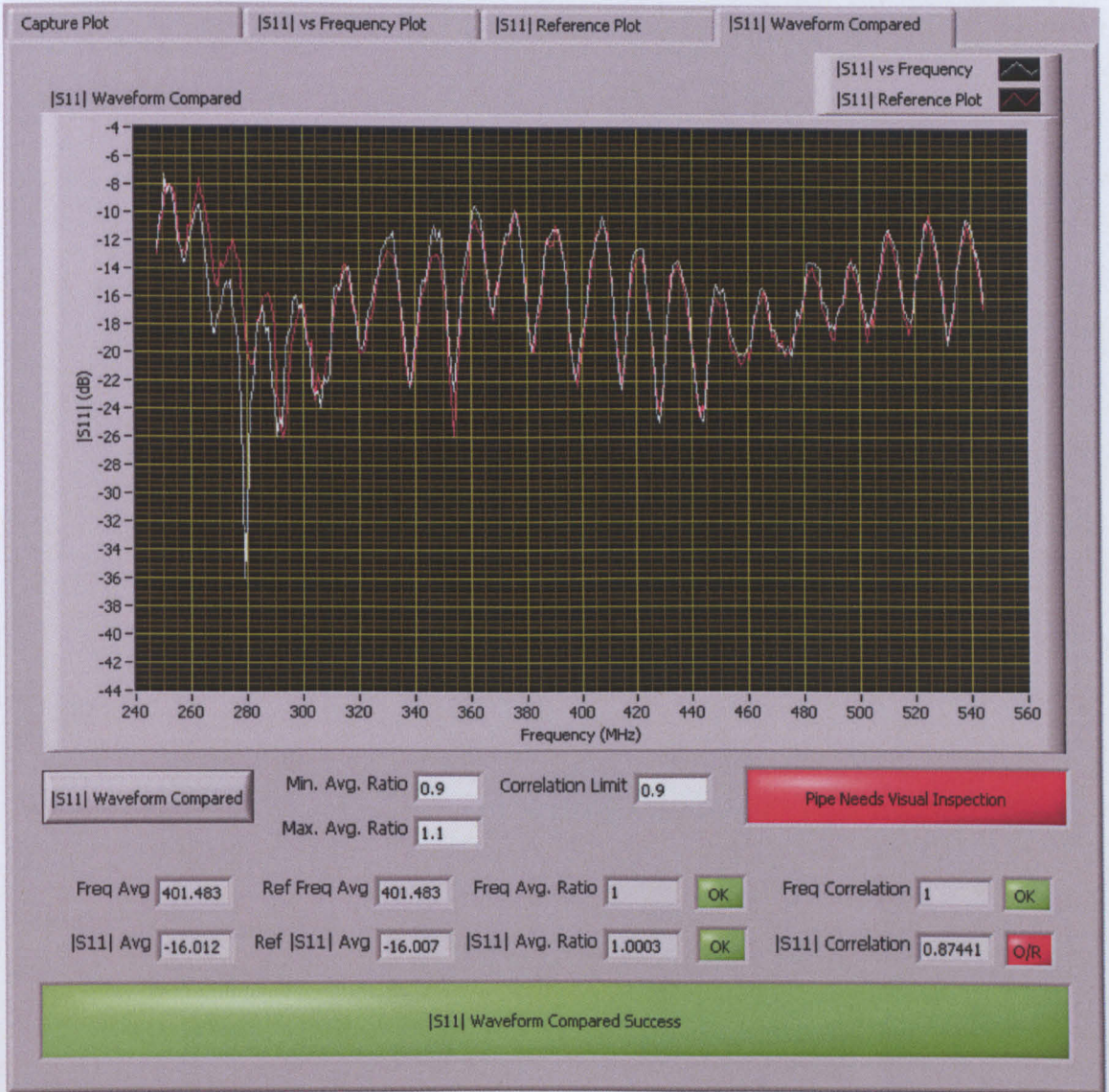


Figure 7.21: $|S_{11}|$ waveform compared for 80cm depth in pipeline

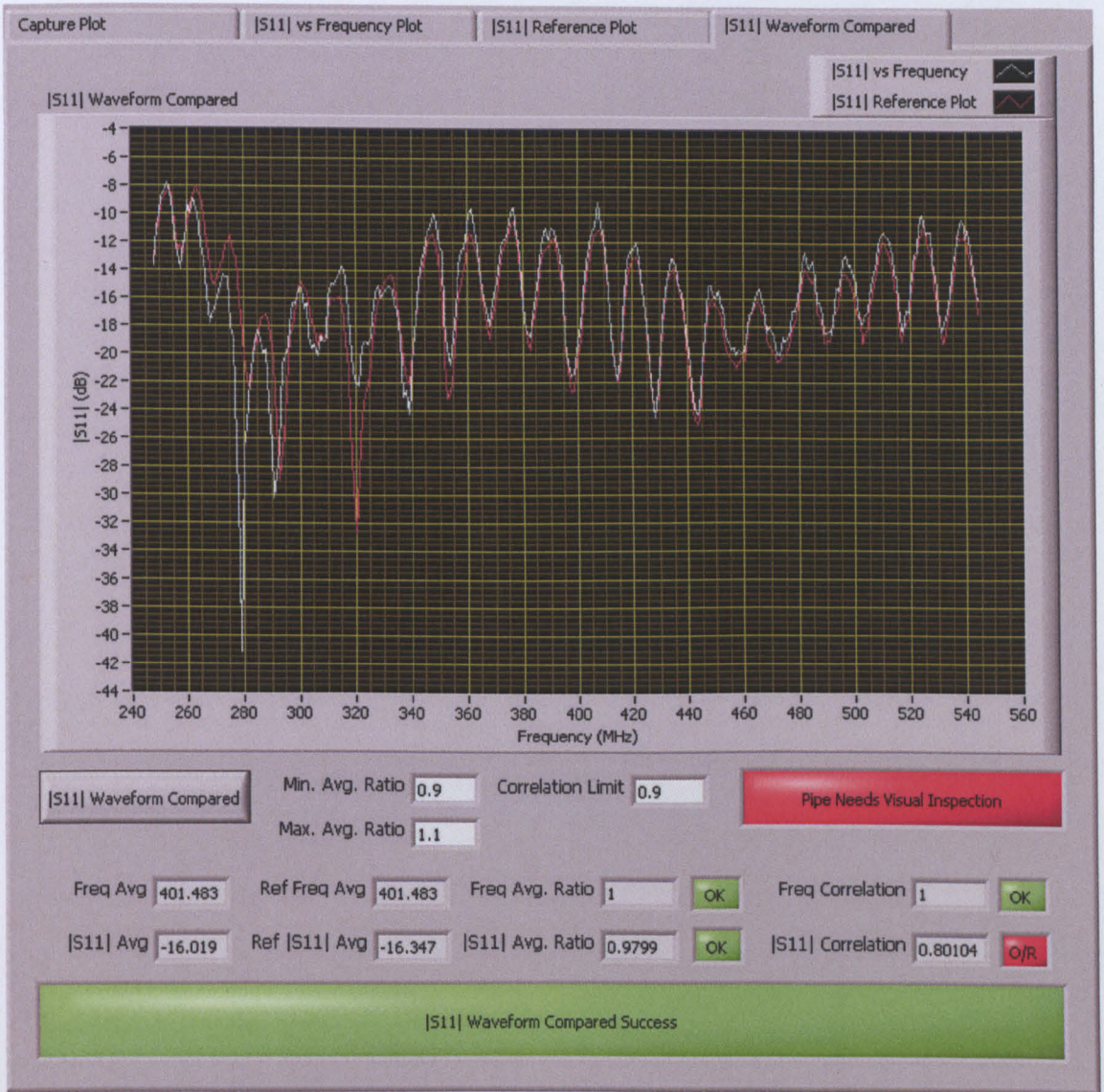


Figure 7.22: $|S_{11}|$ waveform compared for 90cm depth in pipeline

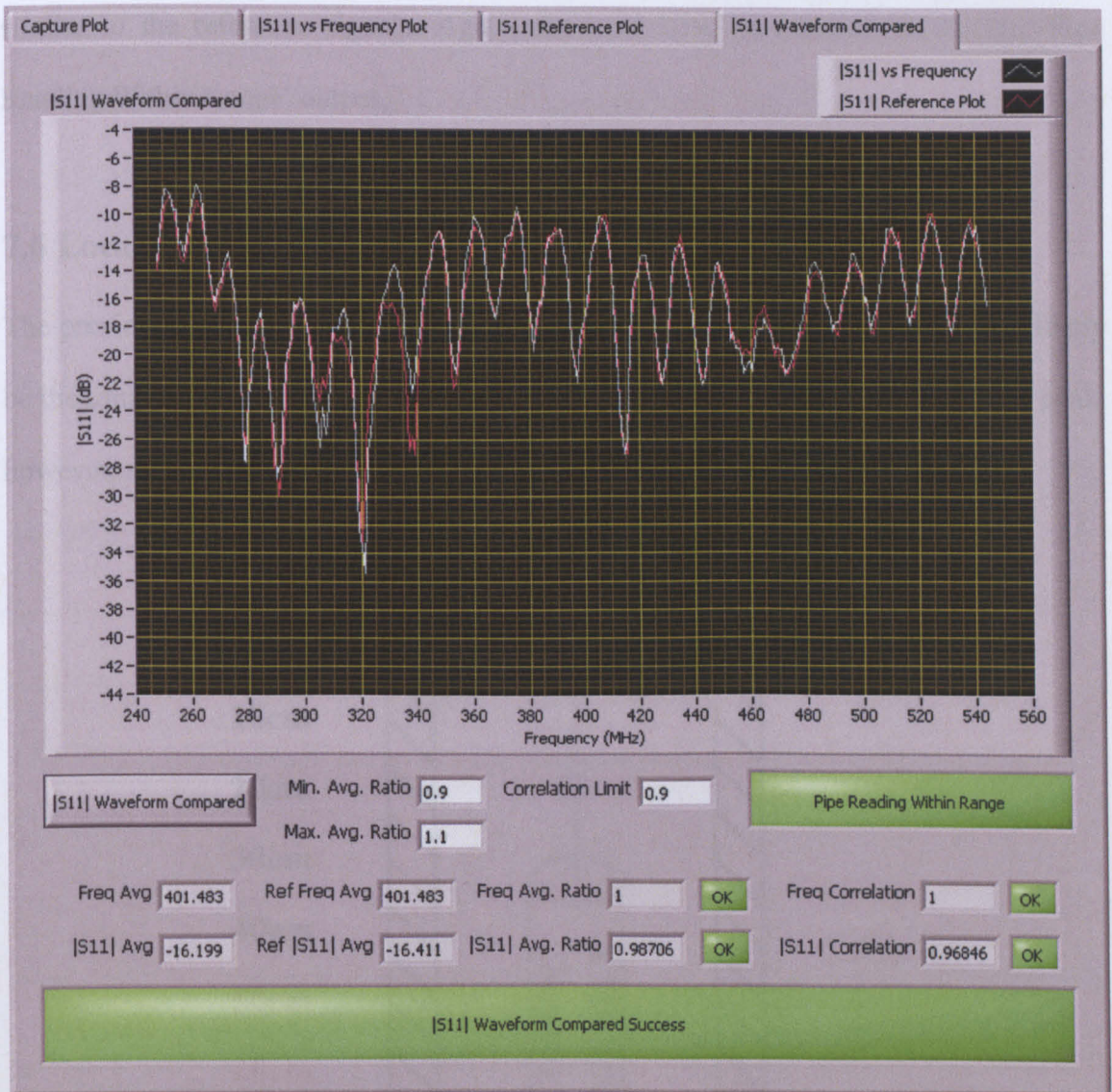


Figure 7.23: $|S_{11}|$ waveform compared for 140cm depth in pipeline

The signal spectrums for 10cm to 40cm depth were very similar to the reference signals. The LabVIEW programme shows the 'Pipe Reading Within Range' output, which means that no leaks have been detected in this region of the pipeline. The resonance peak has a huge change, the signal is reduced or/and resonance peak is changed for the signal spectrum between 50cm and 100cm depth compared to the reference signals. The LabVIEW programme shows the 'Pipe Needs Visual Inspection', which means that a leak has been detected at this region of the pipeline and needs further inspection. The signal spectrum for the 110cm to 140cm depth is back to normal again which is very

similar to the reference signals. Again, the LabVIEW programme shows the 'Pipe Reading Within Range' output.

7.6 Location for Leakage

The previous experiment for leak detection showed that the signal spectrums will likely be the same as the reference indicating with no leak in the pipeline. The resonance peak, however, shows huge changes and attenuation when there is leak in the pipeline.

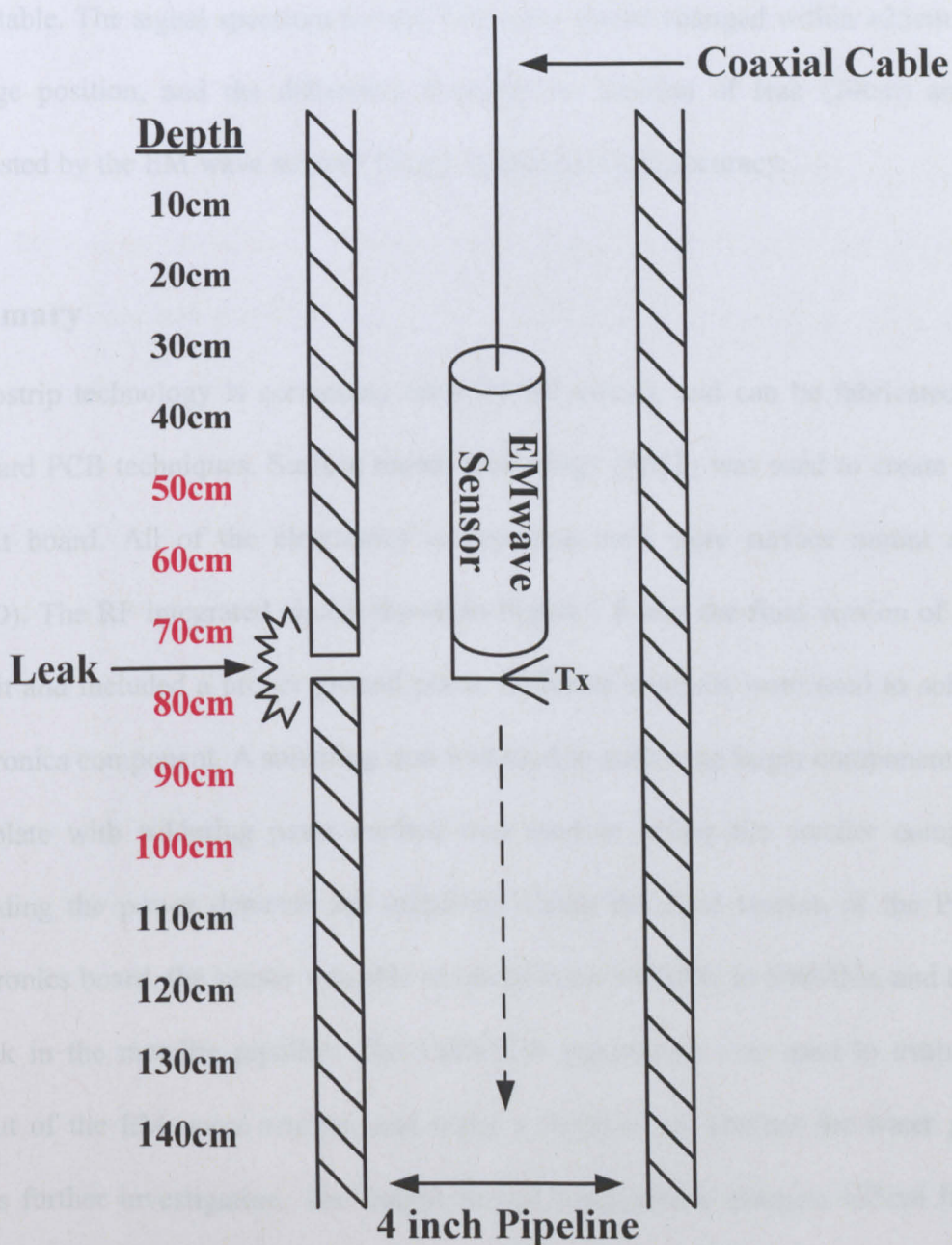


Figure 7.24: Location of the leak on the 4 inch pipeline

Therefore, the location of the resonance peak can be used to find the location of the leak. The first indication of these signals changing was shown by LabVIEW at 50cm, and the final location at which the signal changed was at 100cm, taking the average distance therefore suggested that the leak was at 75cm.

Figure 7.24 shows the location of the leak on the 4 inch pipeline. It was measured and found to be 74cm from top of the pipeline, so the above result was considered acceptable. The signal spectrum for this EM wave sensor changed within ± 25 cm of the leakage position, and the difference between the location of leak (74cm) and that suggested by the EM wave sensor (75cm), implied a ± 1 cm accuracy.

Summary

Microstrip technology is commonly used for RF circuit, and can be fabricated using standard PCB techniques. Surface mount technology (SMT) was used to create a PCB circuit board. All of the electronics components used were surface mount devices (SMD). The RF integrated circuit shown in Figure 7.8 was the final version of the RF circuit and included a proper ground plane. Different methods were used to solder the electronics component. A soldering iron was used to solder the larger components, but a hot plate with soldering paste method was used to solder the smaller components including the power detector and amplifier. Using the final version of the PCB RF electronics board, the sensor was able to sweep from 240MHz to 560MHz, and to sense a leak in the metallic pipeline. The LabVIEW programme was used to evaluate the output of the EM wave sensors, and make a decision on whether the water pipeline needs further investigation. The output of EM wave sensor changes ± 25 cm from the leak position, and the sensor was able to find a leak location at 75cm from top of the water pipe with ± 1 cm tolerance.

Chapter 8: Conclusion

A unique method for mains water leak detection within cast iron pipes was proposed in this thesis, utilising electromagnetic (EM) waves. As this project was an industrial collaboration with Balfour Beatty, the sensor was required to be deployed using their pressurized hydrant. This placed design constraints on the sensor, limiting the overall dimensions to 22mm in diameter and 100mm in length.

As no previous research had been done on water filled pipeline integrity using EM waves, the first objective was to investigate whether EM waves would propagate down a water filled cast iron pipeline. This was successfully achieved using a combination of HFSS simulation and laboratory experiment.

Using HFSS it was possible to model the cast iron pipeline and determine that the propagation of the first two TE_{11} and TM_{01} modes in a circular water pipe was possible. HFSS was also used to determine the loss and resonant frequencies within the pipeline using both monopoles and loop antennas. A series of experiments were also conducted to validate the HFSS model which showed good agreement with both frequency and amplitude between the experimental results and the simulation, and could therefore be used for designing the sensor.

From the simulation and experiment, it was found that the loop antenna showed a clearer peak for $|S_{11}|$ compared to the monopole antenna, the other signals had either no resonance peak or the signal had more than one resonance peak. Therefore the signal $|S_{11}|$ and the loop antenna were used for this water pipe leak detection project. The

results also showed that the best operating frequency for the sensor system was 480MHz. HFSS and the experimental results also showed the attenuation and resonance frequency changed when a leak was present, and this could be concluded as the attenuation observed as an indication for water pipe leaks. A series of nylon rings with different thickness were used to create a virtual gap between the two sections of pipelines, and the results showed the resonance frequency is shifted for different gap widths.

An industrial sensor for leak detection has been successfully designed to meet the required dimensions of 22mm in diameter and 100mm in length. This sensor was able to sweep frequencies from 240MHz to 560MHz, and this range covered the resonance frequencies which corresponded to a change in the pipeline properties as discussed in chapters 5 and 6. A rectangular shaped PCB boards with a ground plane was designed with all the RF electronics on it. The LabVIEW programme created for this project evaluated the output of the EM wave sensors and gave a recommendation about whether the water pipeline needs further investigation. This utilised the Pearson correlation algorithm up to 0.9 correlation limit. The LabVIEW system also proved that using Compaq DAQ and RF electronics device could successfully replace the expensive (£20,000 [133]) VNA.

The next stage of this project was to conduct field trials at the Balfour Beatty test site in Derby. The results from this demonstrated that the sensor could not only be used for leak detection but also as a possible asset management device. It was also demonstrated that each of the elements of the sensor worked correctly. The industrial trial showed that the resonant frequency in the 4 inch metallic pipeline with concrete lining on the inner surface was 275MHz whereas the resonant frequency in the 4 inch Perspex section was

303MHz. For the final stage, the signal spectrum for the 4 inch metal pipeline without a leak was shown to be repeatable, and that the resonance peak shows a significant frequency change and attenuation when a leak is present in the pipeline. This EM wave sensor is able to sensing $\pm 25\text{cm}$ from the leak position with $\pm 1\text{cm}$ accuracy.

Table 10.1: Comparison between EM waves sensor and present technology

Technology Attribute	Listening Stick	Ground Microphone	Acoustic	Ground Penetrating Radar	EM Waves Sensor
Respond Time	Time consuming	Time consuming	Time consuming	DSP analysis take hours to complete	Fast Response
Reliability and Sensitivity	Not very efficient	Not very efficient	Contact point with the water pipeline	Cannot differentiate the buried object	Put into water pipeline through any existing hydrant
Accuracy	Moderate success	Moderate success	Satisfactory	Over 80% [4]	90%
Cost	Low Cost £25 [5]	Expensive £2500 [6]	Moderate £400 [7]	Very Expensive £8000 [8]	Low Cost £50

This thesis has lead to a much greater understanding of the way EM waves propagates in metallic water distribution pipes. It is clear that different types of pipelines have a different spectrum based of the diameter and the pipeline material. This development of a unique EM wave sensor that was a significant improvement on the standalone technique. Table 10.1 shows the comparison between EM waves sensor and present technology. The EM wave sensor using low cost RF electronics devices could provide better accuracy up to 90% and a faster respond time compared to other techniques.

10.1 Future Work

For further work and development, leaks at different positions and the pipes with more than one leak should be investigated. Further work should also be done to improve the matching of the antenna to 50Ω which should improve signal strength. Furthermore, the sensor should also be tested on different types of pipeline materials such as plastic, stainless steel etc, with different common diameters of water pipeline such 6 inch, 12 inch etc. The microstrip patch antenna could be used in future to create a different polarization such as circular or elliptical. The double sided PCB method could apply in the future and this will reduce the size of the circuit board allowing more space for further sensors. Finally a camera could be added into the EM wave sensor to visualize the scene inside the pipeline and this could help to determine the location for a leak. Also an acoustic sensor could be added to create a multi sensor fusion device.

References

- [1] Water for Life, <http://www.un.org/waterforlifedecade/background.html>, (accessed on May 2010)
- [2] UK Water Companies, <http://www.water-guide.org.uk/companies.html>, (accessed on June 2010)
- [3] Balfour Beatty Utility Solutions, West Service Road, Raynesway, Derby, DE21 7BG, UK
- [4] GRP | Ground Penetrating Radar, <http://www.advancedradartechnology.com/ground-penetrating-radar-faq.html#a19>, (access on December 2010)
- [5] MSF Engineering Ltd, 52 Chestnut Grove, Coleshill, Birmingham, B46 1AD
- [6] EDENBROS, LLC., PO Box 3987, Naperville, IL 60567-3987, USA
- [7] Surveyors Mart, 7 Briercliff, Rancho Santa Margarita, CA 92679, USA
- [8] CAL Services UK Limited, 47 George Street, Weston super Mare, Somerset, BS23 3AS, UK
- [9] R. Pilcher, "Leak Dtection Practices and Techniques: A practical Approach", Fourth article in a special series for Water21, IWA Water Loss Task Force, December 2003, pp. 44-45
- [10] Water Demand Management Project Rural Water Supply and Water, <http://www.docstoc.com/docs/68288107/Water-Demand-Management-Project-Rural-Water-Supply-and-Water>, (accessed on June 2010)
- [11] Water Product Ltd., 11 Queenscliff Court, Kallaroo, Perth, WA6025
- [12] D. B. Sharp and D. M. Campbell, "Leak Detection in Pipes Using Acoustic Pulse Reflectometry", Acta Acustica united with Acustica, Volume 83, Number 3, May/June 1997, pp. 560-566. ISSN 1610-1928
- [13] Y. Gao, M. J. Brennan and P. F. Joseph, "Time delay estimation of acoustic signals for leak detection in buried plastic pipes", Proceedings of the Eleventh International Congress on Sound and Vibration, St Petersburg, Russia, 5-8 July 2004, pp. 3113-3120
- [14] J. C. P. Liou, J. Tian, "Leak detection: a transient flow simulation approach", American Society of Mechanical Engineers, Petroleum Division, 1994, Vol.60, pp. 51-58

-
- [15] I. F. Akyildiz, D. Pompili and T. Melodia, "Underwater Acoustic Sensor Networks: Research Challenges", Broadband and Wireless Networking Laboratory, School of Electrical and Computer Engineering, Georgia Institute of Technology, Atlanta, USA, 2005, Ad Hoc Networks 3, pp. 257-279
- [16] A. I. Al-Shamma'a, A. Shaw and S. Saman, "Propagation of Electromagnetic Waves at MHz Frequencies Through Seawater", IEEE Transactions on Antenna and Propagation, Vol. 52, No. 11, November 2004, pp. 2843-2849
- [17] A. Shaw, A. I. Al-Shamma'a, S. R. Wylie and D. Toal, "Experimental Investigations of Electromagnetic Wave Propagation in Seawater", Proceedings of the 36th European Microwave Conference, September 2006, pp. 572-575
- [18] M. Nakhkash and M. R. Mahmood-Zadeh, "Water Leak Detection Using Ground Penetrating Radar", IEEE Tenth International Conference on Ground Penetrating Radar, 21-24 June, 2004, pp. 525-528
- [19] S. Hyun, Y. Jo, H. Oh and S. Kim, "An Experimental Study on a Ground Penetrating Radar for Detecting Water-Leaks in Buried Water Transfer Pipes", IEEE Antennas, Propagation and EM Theory, 2003, pp. 597-599
- [20] S. R. Pennock, M. A. Redfern, and Q. Shan, "Subsurface Illumination And Propagation In Ground Penetrating Radar", Department of Electronic & Electric Engineering, University of Bath, IEEE Antennas and Propagation, 2006, pp. 1-5
- [21] J. L. Davis and A. P. Annan, "Ground-Penetrating Radar for High Resolution Mapping of Soil and Rock Stratigraphy", Geophysical Prospecting, Volume 37, Issue 5, July 1989, pp. 531-551
- [22] A. M. Thomas, C. D. F. Rogers, D. N. Chapman, N. Metje, J. Castle, "Stakeholder needs for ground penetrating radar utility location", Journal of Applied Geophysics 67, 2009, pp. 345-351
- [23] Y. Wen, P. Li, J. Yang and Z. Zhou, "Information Processing in Buried Pipeline Leak Detection System", College of Opto-electronic Engineering, University of Chongqing, IEEE Information Acquisition, 2004, pp. 489-493
- [24] Pensacola Testing Laboratories, Inc., 217 East Brent Lane, Pensacola, FL 32503, USA
- [25] GPR, <http://www.chipr.sunysb.edu/eserc/summereducationalinterns/linda/gpr.html>, (accessed on October 2010)
- [26] A. Catenaccio, Y. Daruich, C. Magallanes, "Temperature Dependence of the Permittivity of Water", Laboratorio de Dielectricos, Departamento de Fisica,

- Universidad Nacional de San Luis, Ejercito de los Andes 950, 5700 San Luis, Argentina, Chemical Physics Letters 367, 2003, pp. 669-671
- [27] D. K. Cheng, "Field and Wave Electromagnetics, 2nd Edition", Addison-Wesley Publishing Company, 1989, pp. 569-571. ISBN 0201528207
- [28] D. H. Staelin, A. W. Morgenthaler and J. A. Kong, "Electromagnetic Waves", Prentice Hall International, Inc, 1994, pp. 1-11. ISBN 0131768689
- [29] J. D. Kraus and D. A. Fleisch, "Electromagnetics: with applications, 5th Edition", McGraw-Hill, 1999, pp. 1-7. ISBN 0071164294
- [30] NWS JetStream – Introduction to the National Weather Service, http://www.srh.noaa.gov/jetstream//remote/remote_intro.htm, (accessed on October 2010)
- [31] J. F. White, "High Frequency Techniques: An Introduction to RF and Microwave Engineering", A John Wiley & Sons, Inc, 2004, pp. 209-211. ISBN 0471455911
- [32] Y. Huang, K. Boyle, "Antennas from Theory to Practice", John Wiley & Sons, Ltd, 2008, pp.16. ISBN 9780470510285
- [33] D. K. Cheng, "Field and Wave Electromagnetics, 2nd Edition", Addison-Wesley Publishing Company, 1989, pp. 77-85. ISBN 0201528207
- [34] Charles Augustin Coulomb – Coulomb's Law, http://ffden-2.phys.uaf.edu/212_fall2003.web.dir/don_bahls/coulombs_law.html, (accessed on October 2010)
- [35] D. K. Cheng, "Field and Wave Electromagnetics, 2nd Edition", Addison-Wesley Publishing Company, 1989, pp. 87-92. ISBN 0201528207
- [36] Y. Huang, K. Boyle, "Antennas from Theory to Practice", John Wiley & Sons, Ltd, 2008, pp.18. ISBN 9780470510285
- [37] Magnetic Fields, <http://www.acecrc.sipex.aq/access/page/?page=75ee44de-b881-102a-8ea7-0019b9ea7c60>, (accessed on October 2010)
- [38] Magnetic and Electric Fields, http://ffden-2.phys.uaf.edu/212_fall2003.web.dir/Aaron_Behnen/mag_elecfields.html, (accessed on October 2010)
- [39] D. K. Cheng, "Field and Wave Electromagnetics, 2nd Edition", Addison-Wesley Publishing Company, 1989, pp. 308-310. ISBN 0201528207
- [40] F. T. Ulaby, "Fundamentals of Applied Electromagnetics", Prentice Hall, 1999, pp. 231-233. ISBN 0130115541

-
- [41] Molecular Expressions: Electricity and Magnetism, <http://micro.magnet.fsu.edu/electromag/java/faraday2/index.html>, (accessed on October 2010)
- [42] F. T. Ulaby, "Fundamentals of Applied Electromagnetics", Prentice Hall, 1999, pp. 22. ISBN 0130115541
- [43] The Electromagnetic Spectrum, http://www.antonine-education.co.uk/physics_gcse/Unit_1/Topic_5/topic_5_what_are_the_uses_and_ha.htm, (accessed on October 2010)
- [44] Electromagnetic Spectrum, http://www.knowledgerush.com/kr/encyclopedia/Electromagnetic_spectrum/, (accessed on October 2010)
- [45] The UK Frequency Allocations, http://www.onlineconversion.com/downloads/uk_frequency_allocations_chart.pdf, (accessed on May 2010)
- [46] Y. Huang, K. Boyle, "Antennas from Theory to Practice", John Wiley & Sons, Ltd, 2008, pp.80-82. ISBN 9780470510285
- [47] J. J. Carr, "Practical Antenna Handbook, 4th Edition", McGraw-Hill, 2001, pp. 57. ISBN 0071374353
- [48] V. Rojansky, "Electromagnetic Fields and Waves", Dover Publication, Inc., 1979, pp. 389. ISBN 0486638340
- [49] Y. Huang, K. Boyle, "Antennas from Theory to Practice", John Wiley & Sons, Ltd, 2008, pp.82-83. ISBN 9780470510285
- [50] E. Hecht, "Optics, 3rd Edition", Addison-Wesley Publishing Company, 1998, pp. 319-323. ISBN 0201304252
- [51] Wireless Network Products, <http://www.wirelessnetworkproducts.com/nonline-of-sightnloscircular-polarizedantennas.aspx>, (accessed on October 2010)
- [52] Classification of Polarization, <http://hyperphysics.phy-astr.gsu.edu/hbase/phyopt/polclas.html>, (accessed on October 2010)
- [53] E. da Silva, "High Frequency and Microwave Engineering", Butterworth-Heinemann, 2001, pp. 45-47. ISBN 075065646X
- [54] K. F. Sander and G. A. L. Reed, "Transmission and propagation of electromagnetic waves, 2nd Edition", Cambridge University Press, 1986, pp. 153-156, ISBN 0521311926

- [55] W. Sinnema, "Electric Transmission Technology, Lines, waves and antennas", Prentice-Hall, Inc, 1979, pp. 5-7. ISBN 0132522217
- [56] Data Transmission – Cabling, <http://www.intelligenceunited.com/?p=2381>, (accessed on October 2010)
- [57] K. F. Sander and G. A. L. Reed, "Transmission and propagation of electromagnetic waves, 2nd Edition", Cambridge University Press, 1986, pp. 221-223, ISBN 0521311926
- [58] Y. Huang, K. Boyle, "Antennas from Theory to Practice", John Wiley & Sons, Ltd, 2008, pp.58. ISBN 9780470510285
- [59] Y. Huang, K. Boyle, "Antennas from Theory to Practice", John Wiley & Sons, Ltd, 2008, pp.59. ISBN 9780470510285
- [60] D. K. Cheng, "Field and Wave Electromagnetics, 2nd Edition", Addison-Wesley Publishing Company, 1989, pp. 430. ISBN 0201528207
- [61] T. C. Edwards, "Foundations for Microstrip Circuit Design, 2nd Edition", Wiley, 1992, pp. 42-43. ISBN 0471930628
- [62] Y. Huang, K. Boyle, "Antennas from Theory to Practice", John Wiley & Sons, Ltd, 2008, pp.60-62. ISBN 9780470510285
- [63] RF Cafe, Microstrip Substrate Equations Formulas, <http://www.rfcafe.com/references/electrical/microstrip-eq.htm>, (accessed on May 2010)
- [64] D. K. Cheng, "Field and Wave Electromagnetics, 2nd Edition", Addison-Wesley Publishing Company, 1989, pp. 437-443. ISBN 0201528207
- [65] Y. Huang, K. Boyle, "Antennas from Theory to Practice", John Wiley & Sons, Ltd, 2008, pp.49. ISBN 9780470510285
- [66] Integrated Publishing, "Voltage Standing Wave Ratio", http://www.tpub.com/content/neets/14182/css/14182_155.htm, (accessed on May 2010)
- [67] D. K. Cheng, "Field and Wave Electromagnetics, 2nd Edition", Addison-Wesley Publishing Company, 1989, pp. 460-462. ISBN 0201528207
- [68] L. F. Chen, C. K. Ong, C. P. Neo, V. V. Varadan and V. K. Varadan, "Microwaves Electronics, Measurement and Materials Characterization", John Wiley, 2004, pp. 97. ISBN 0470844922
- [69] D. H. Staelin, A. W. Morgenthaler and J. A. Kong, "Electromagnetic Waves", Prentice Hall International, Inc, 1994, pp. 310-319. ISBN 0131768689

- [70] J. D. Kraus and D. A. Fleisch, "Electromagnetics: with applications, 5th Edition", McGraw-Hill, 1999, pp. 456-467. ISBN 0071164294
- [71] D. K. Cheng, "Field and Wave Electromagnetics, 2nd Edition", Addison-Wesley Publishing Company, 1989, pp. 547. ISBN 0201528207
- [72] K. F. Sander and G. A. L. Reed, "Transmission and propagation of electromagnetic waves, 2nd Edition", Cambridge University Press, 1986, pp. 71, ISBN 0521311926
- [73] D. M. Pozar, "Microwave Engineering, 2nd Edition", John Wiley & Sons, Inc, 1998, pp. 129. ISBN 0471170968
- [74] K. F. Sander and G. A. L. Reed, "Transmission and propagation of electromagnetic waves, 2nd Edition", Cambridge University Press, 1986, pp. 75, ISBN 0521311926
- [75] D. H. Staelin, A. W. Morgenthaler and J. A. Kong, "Electromagnetic Waves", Prentice Hall International, Inc, 1994, pp. 323-329. ISBN 0131768689
- [76] J. D. Kraus and D. A. Fleisch, "Electromagnetics: with applications, 5th Edition", McGraw-Hill, 1999, pp. 468-471. ISBN 0071164294
- [77] D. K. Cheng, "Field and Wave Electromagnetics, 2nd Edition", Addison-Wesley Publishing Company, 1989, pp. 567. ISBN 0201528207
- [78] K. F. Sander and G. A. L. Reed, "Transmission and propagation of electromagnetic waves, 2nd Edition", Cambridge University Press, 1986, pp. 83, ISBN 0521311926
- [79] D. M. Pozar, "Microwave Engineering, 2nd Edition", John Wiley & Sons, Inc, 1998, pp. 140. ISBN 0471170968
- [80] D. M. Pozar, "Microwave Engineering, 2nd Edition", John Wiley & Sons, Inc, 1998, pp. 135. ISBN 0471170968
- [81] D. M. Pozar, "Microwave Engineering, 2nd Edition", John Wiley & Sons, Inc, 1998, pp. 137. ISBN 0471170968
- [82] S-parameters-Microwave Encyclopedia,
<http://www.microwaves101.com/encyclopedia/sparameters.cfm>, (accessed on May 2010)
- [83] D. M. Pozar, "Microwave Engineering, 2nd Edition", John Wiley & Sons, Inc, 1998, pp. 204-205. ISBN 0471170968
- [84] Merriam-Webster Dictionary, "Antenna Definition",
<http://mw1.merriam-webster.com/dictionary/antenna>, (accessed on May 2010)
- [85] J. J. Carr, "Practical Antenna Handbook, 4th Edition", McGraw-Hill, 2001, pp. 123-140. ISBN 0071374353

-
- [86] J. D. Kraus and R. J. Marhefka, "Antennas For All Applications, 3rd Edition", McGraw-Hill International Editions, 2002, pp. 165-178. ISBN 0072321032
- [87] F. T. Ulaby, "Fundamentals of Applied Electromagnetics", Prentice Hall, 1999, pp. 358. ISBN 0130115541
- [88] Y. Huang, K. Boyle, "Antennas from Theory to Practice", John Wiley & Sons, Ltd, 2008, pp.130. ISBN 9780470510285
- [89] W. L. Stutzman, G. A.Thiele, "Antenna Theory and Design, 2nd Edition", Wiley, 1998, pp. 92-94. ISBN 0471025909
- [90] C. A. Balanis, "Antenna Theory: Analysis and Design, 3rd Edition", John Wiley & Sons, Inc, 2005, pp. 195-197. ISBN 047166782X
- [91] Y. Huang, K. Boyle, "Antennas from Theory to Practice", John Wiley & Sons, Ltd, 2008, pp.138-141. ISBN 9780470510285
- [92] T. Macnamara, "Introduction to Antenna Placement and Installation", John Wiley and Sons, 2010, pp. 145. ISBN 9780470019818
- [93] M. M. Weiner, "Monopole antennas", CRC Press. 2003, pp. vi. ISBN 9780824704964
- [94] C. A. Balanis, "Antenna Theory: Analysis and Design, 3rd Edition", John Wiley & Sons, Inc, 2005, pp. 231-232. ISBN 047166782X
- [95] J. J. Carr, "Practical Antenna Handbook, 4th Edition", McGraw-Hill, 2001, pp. 299-312. ISBN 0071374353
- [96] Y. Huang, K. Boyle, "Antennas from Theory to Practice", John Wiley & Sons, Ltd, 2008, pp.143. ISBN 9780470510285
- [97] J. D. Kraus and R. J. Marhefka, "Antennas For All Applications, 3rd Edition", McGraw-Hill International Editions, 2002, pp. 211. ISBN 0072321032
- [98] T. C. Edwards, "Foundations for Microstrip Circuit Design, 2nd Edition", Wiley, 1992, pp. 353-359. ISBN 0471930628
- [99] C. A. Balanis, "Antenna Theory: Analysis and Design, 3rd Edition", John Wiley & Sons, Inc, 2005, pp. 811-815. ISBN 047166782X
- [100] J. D. Kraus and R. J. Marhefka, "Antennas For All Applications, 3rd Edition", McGraw-Hill International Editions, 2002, pp. 23-25. ISBN 0072321032
- [101] C. A. Balanis, "Antenna Theory: Analysis and Design, 3rd Edition", John Wiley & Sons, Inc, 2005, pp. 44-45. ISBN 047166782X
- [102] Y. Huang, K. Boyle, "Antennas from Theory to Practice", John Wiley & Sons, Ltd, 2008, pp.115. ISBN 9780470510285

- [103] C. A. Balanis, "Antenna Theory: Analysis and Design, 3rd Edition", John Wiley & Sons, Inc, 2005, pp. 65-67. ISBN 047166782X
- [104] Y. Huang, K. Boyle, "Antennas from Theory to Practice", John Wiley & Sons, Ltd, 2008, pp.116. ISBN 9780470510285
- [105] Y. Huang, K. Boyle, "Antennas from Theory to Practice", John Wiley & Sons, Ltd, 2008, pp.14. ISBN 9780470510285
- [106] Ansoft Corporation, "Parametrics and Optimization using Ansoft HFSS", Product Feature, Horizon House Publications, 1999.
<http://www.ansoft.com/news/articles/MWJ.11.99.pdf>, (accessed on May 2010)
- [107] D. M. Park and J. J. Choi, "Three-Dimensional Simulation of X-Band Coupled Cavity Traveling Wave Tube Amplifier", Journal of the Korean Physical Society, Vol.43, No. 6, Dec 2003, pp.1150-1111
- [108] Ansoft Corporation, "Electronic Design Automation Software: user's guide - High Frequency Structure Simulator, version 9.2", Four Station Square Suite 200, Pittsburgh, PA 15219-1119
- [109] Ansoft Corporation, "Electronic Design Automation Software: user's guide - High Frequency Structure Simulator, version 10", 225 West Station Square Suite 200, Pittsburgh, PA 15219-1119
- [110] R. A. Stuart, "TM01 transmission through a water pipe", Internal Report, General Engineering Research Institute, Liverpool John Moores University, 22nd July 2008
- [111] J. Travis, J. King, "LabVIEW For Everyone: graphical programming made easy and fun, 3rd Edition", Prentice-Hall, Inc, 2007, pp. 3-9. ISBN 0131856723
- [112] G. W. Johnson, R. Jennings, "LabVIEW Graphical Programming, 4th Edition", McGraw-Hill, 2006, pp. 1-11. ISBN 0071451463
- [113] C. F. Dietrich, "Uncertainty, calibration, and probability: the statistics of scientific and Industrial Measurement, 2nd Edition", Taylor & Francis Group, 1991, pp. 331. ISBN 0750300604
- [114] K. A. Stroud, D. J. Booth, "Foundation Mathematics", Palgrave Macmillan, 2009, pp. 561-563. ISBN 9780230579071
- [115] Basic Statistic, <http://www.statsoft.com/textbook/basic-statistics/#Correlationsb>, (accessed on October 2010)
- [116] Pearson product-moment correlation coefficient, "Pearson Correlation", http://my-bankruptcy-help.com/?b=Pearson_product-moment_correlation_coefficient, (accessed on May 2010)

- [117] Biz/ed - Correlation Explained [Time Web],
http://www.bized.co.uk/timeweb/crunching/crunch_relate_expl.htm, (accessed on October 2010)
- [118] National Instruments Corporation, 11500 N Mopac Expwy, Austin, TX 78759-3504
- [119] NI 9205 – 32-Channel Analog Input Module,
<http://sine.ni.com/nips/cds/view/p/lang/en/nid/208800>, (accessed on May 2010)
- [120] NI 9264 – 16-Channel Analog Output Module,
<http://sine.ni.com/nips/cds/view/p/lang/en/nid/208807>, (accessed on May 2010)
- [121] Intersil – CA3140MZ – Datasheet,
<http://datasheet.octopart.com/CA3140MZ-Intersil-datasheet-7407.pdf>, (accessed on May 2010)
- [122] ZOS-300 Model Detail Technical Information: Mini-Circuits,
<http://www.minicircuits.com/pdfs/ZOS-300.pdf>, (accessed on May 2010)
- [123] ZDC-10-1+ Model Detail Technical Information: Mini-Circuits,
<http://www.minicircuits.com/pdfs/ZDC-10-1+.pdf>, (accessed on May 2010)
- [124] ZX47-60+ Model Detail Technical Information: Mini-Circuits,
<http://www.minicircuits.com/pdfs/ZX47-60+.pdf>, (accessed on May 2010)
- [125] National Semiconductor LM317 - 3-Terminal Adjustable Regulator,
<http://www.national.com/ds/LM/LM117.pdf>, (accessed on May 2010)
- [126] MAX2015 0.1GHz to 3GHz, 75dB Logarithmic Detector/Controller,
<http://datasheets.maxim-ic.com/en/ds/MAX2015.pdf>, (accessed on May 2010)
- [127] ROS-535+ Model Detail Technical Information: Mini-Circuits,
<http://www.minicircuits.com/pdfs/ROS-535.pdf>, (accessed on May 2010)
- [128] SYDC-20-13HP+ Model Detail Technical Information: Mini-Circuits,
<http://www.minicircuits.com/pdfs/SYDC-20-13HP+.pdf>, (accessed on May 2010)
- [129] CadSoft Computer, 19620 Pines Blvd., Pembroke Pines, FL 33029
- [130] M. H. Olsen, “PCB Design Tutorial with Eagle”, Technical University of Denmark, March 19, 2004.
http://dmi.uib.es/~jguerrero/labSistemas/eagle_tut.pdf, (accessed on May 2010)
- [131] Bungard Elektronik GmbH & Co.KG, Rilkestrasse 1, D-51570 Windeck, Germany
- [132] ADC-10-1R+ Model Detail Technical Information: Mini-Circuits,
<http://www.minicircuits.com/pdfs/ADC-10-1R.pdf>, (accessed on May 2010)
- [133] Rohde & Schwarz UK Ltd., Ancells Business Park, Fleet, Hampshire, GU51 2UZ, UK

Appendix A:

Source Code for LabVIEW Programme

CONTAINS

PULLOUTS

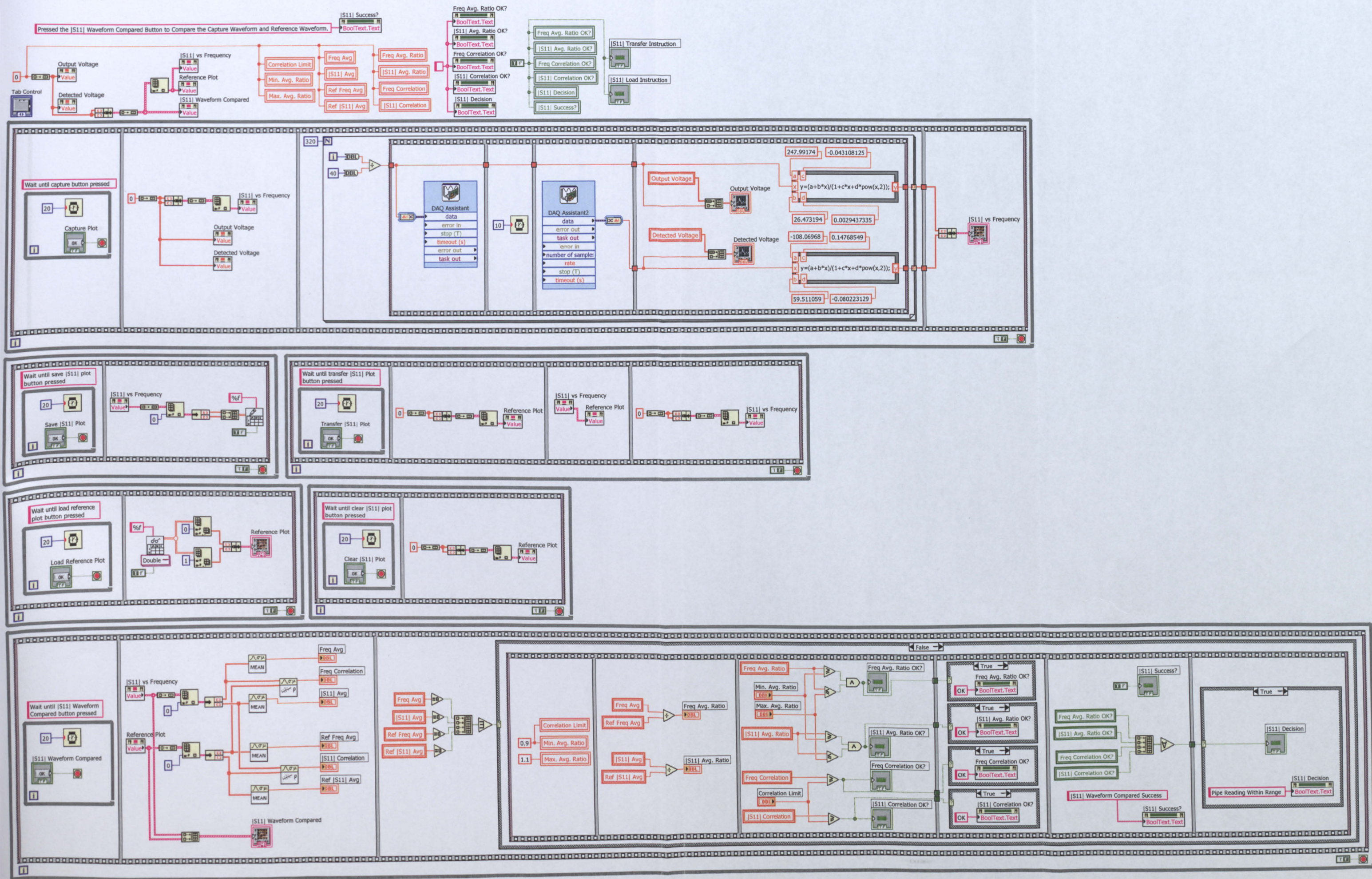


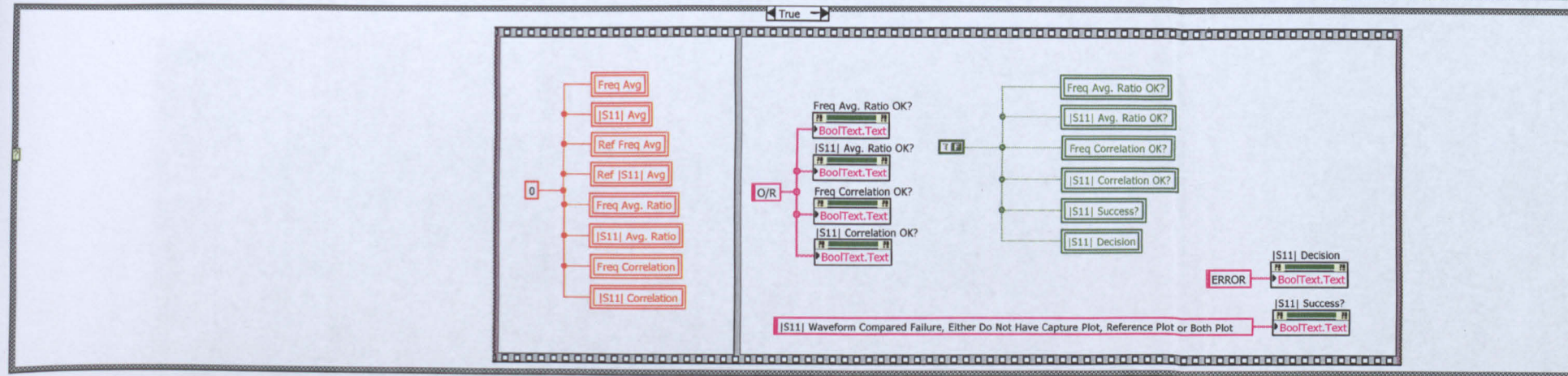
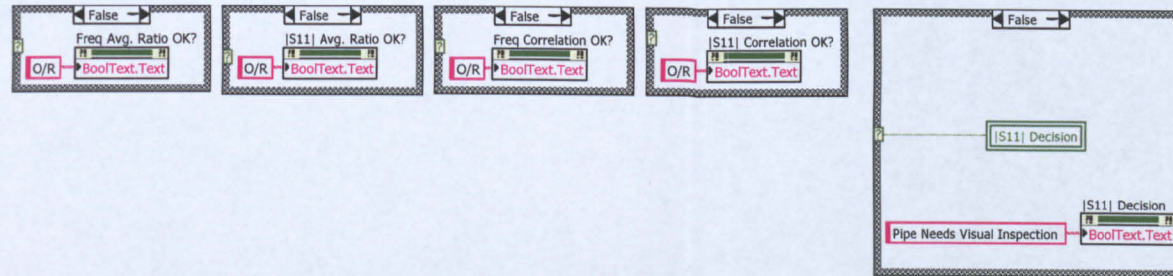
Waveform Compared v4.1.vi

C:\Documents and Settings\Goh\My Documents\LabVIEW\Waveform Compared v4.1.vi

Last modified on 12/04/2010 at 16:37

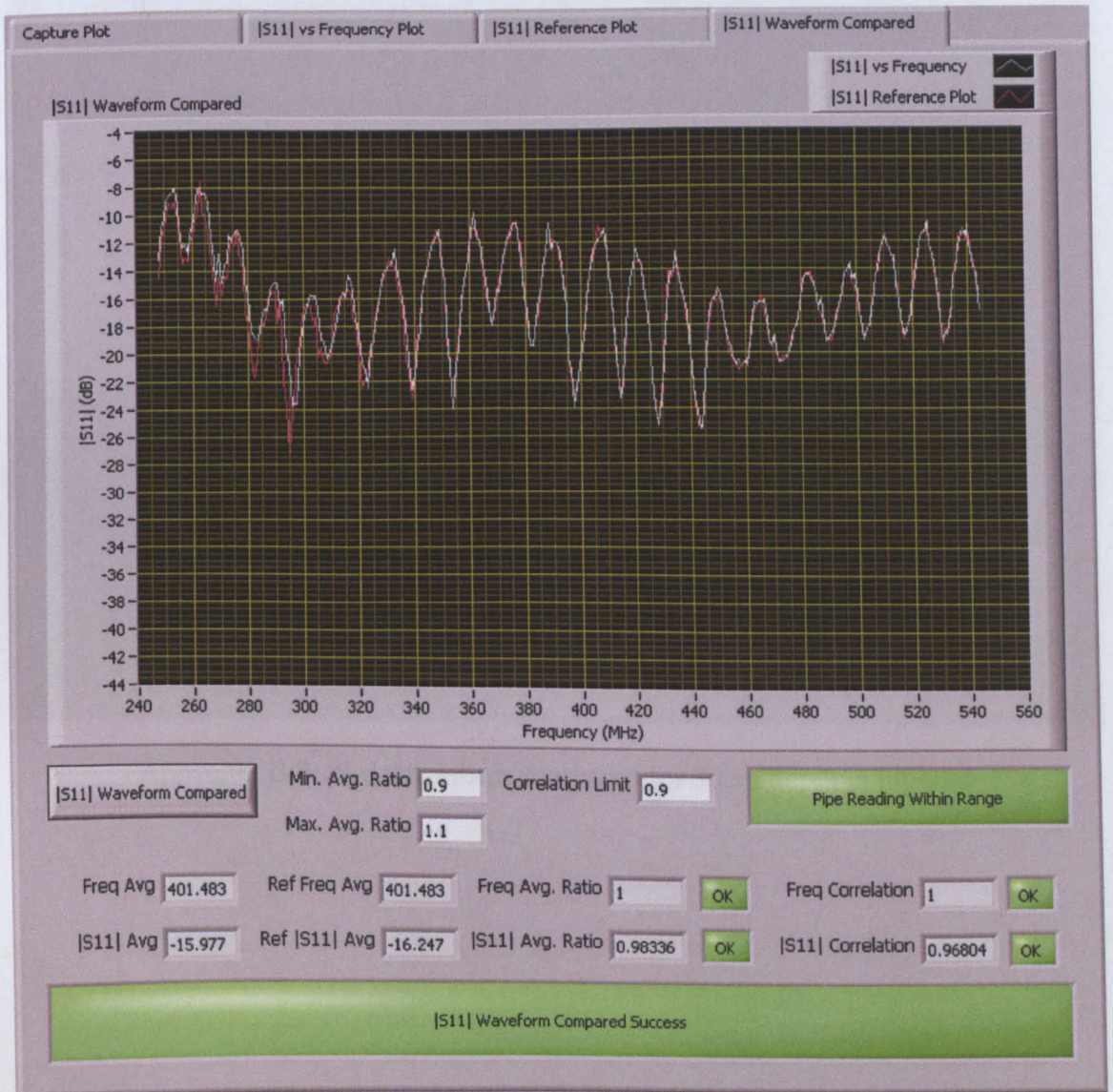
Printed on 09/05/2011 at 16:43





Appendix B:

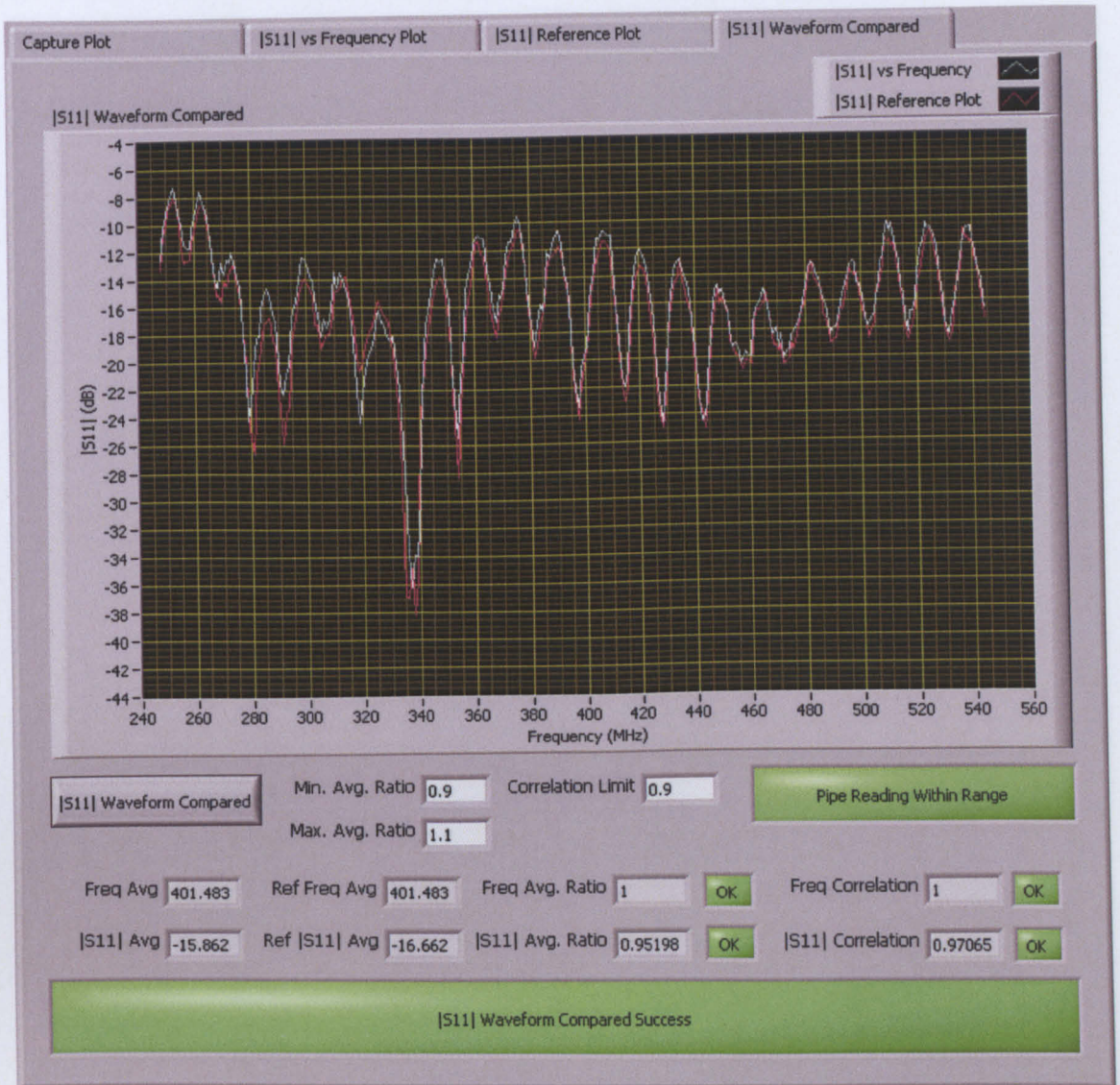
Results for Leak Detection



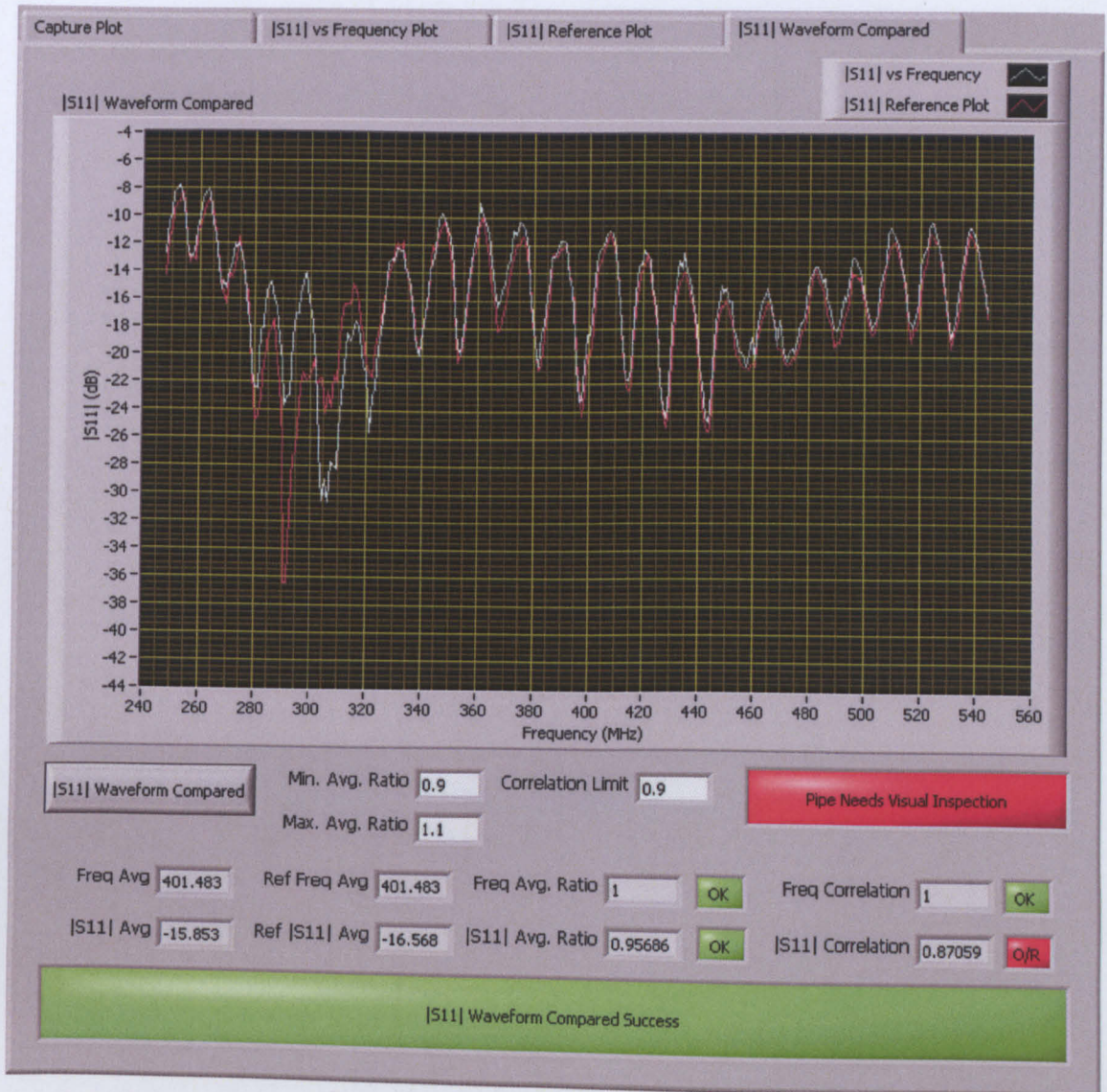
Appendix B.1: $|S_{11}|$ waveform compared for 20cm depth in pipeline



Appendix B.2: |S₁₁| waveform compared for 30cm depth in pipeline



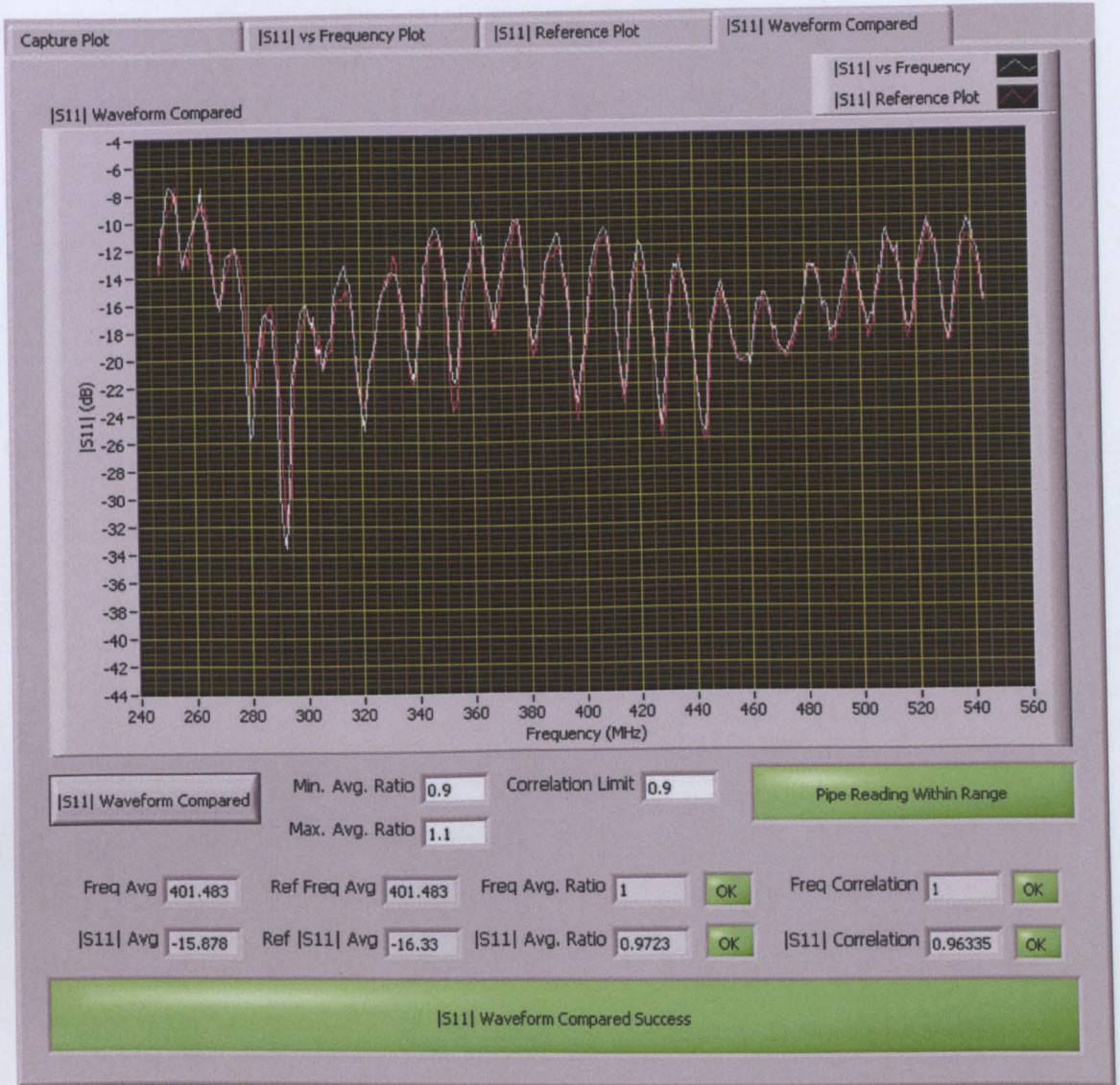
Appendix B.3: $|S_{11}|$ waveform compared for 40cm depth in pipeline



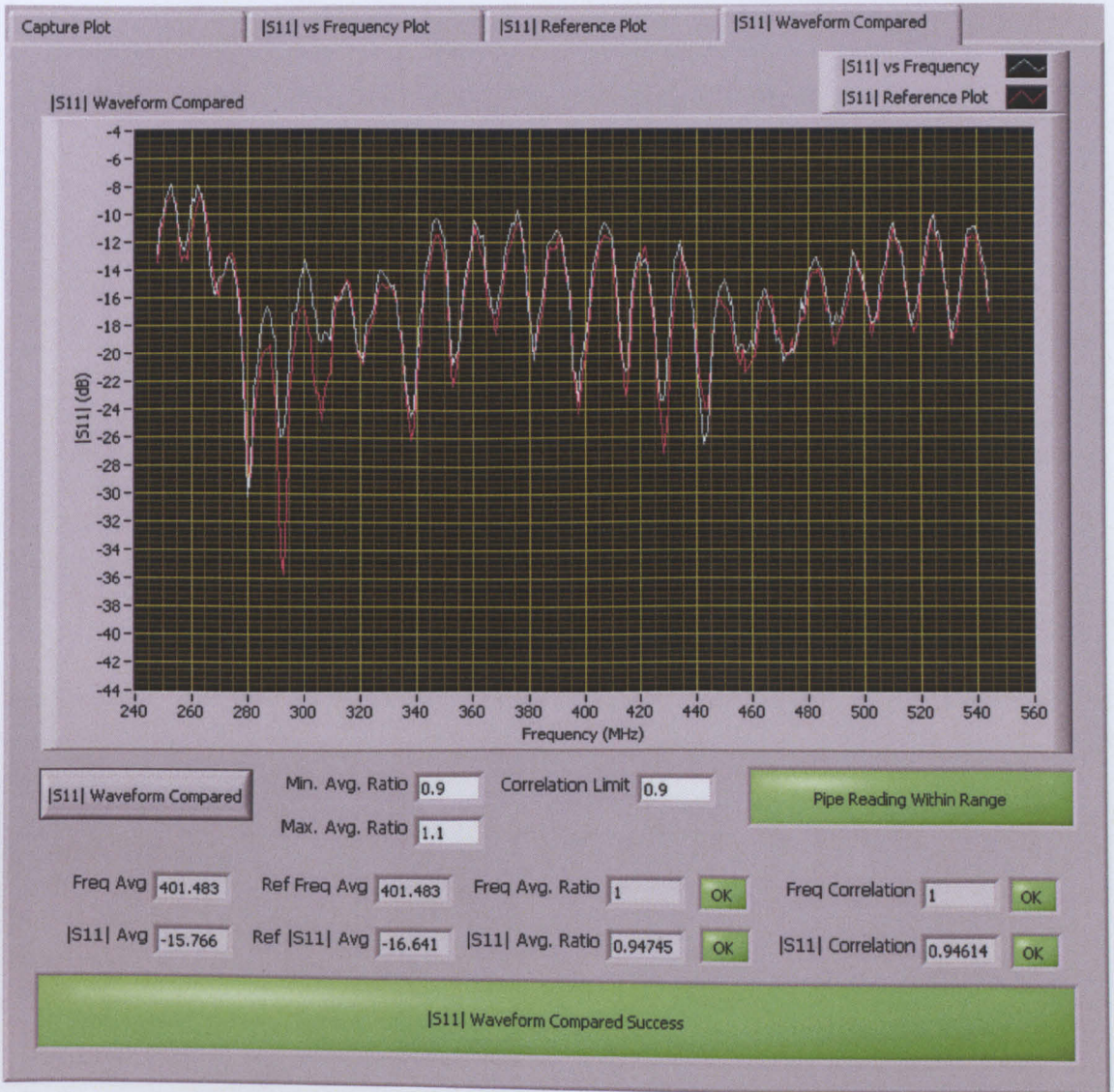
Appendix B.4: $|S_{11}|$ waveform compared for 50cm depth in pipeline



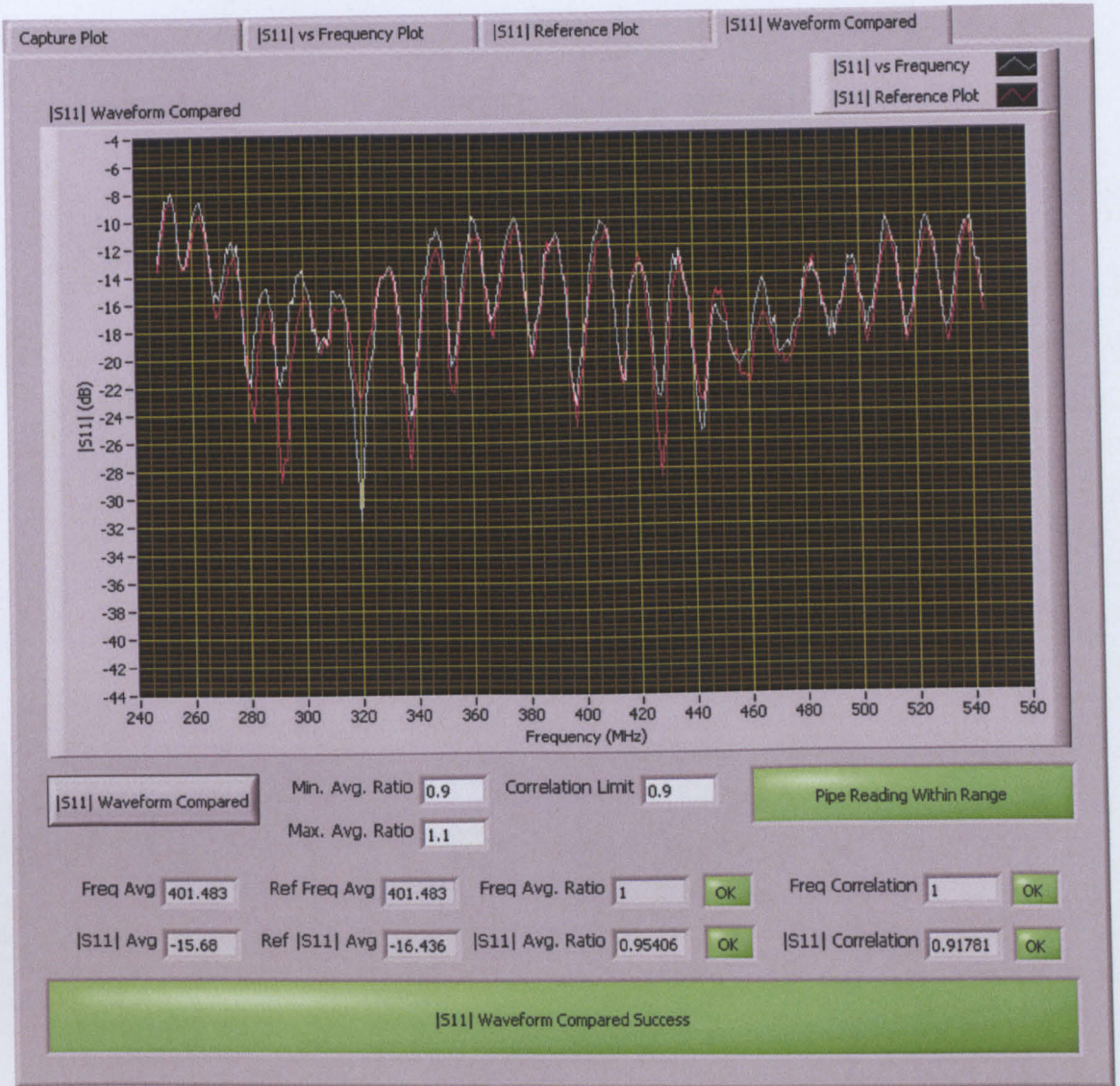
Appendix B.5: $|S_{11}|$ waveform compared for 100cm depth in pipeline



Appendix B.6: |S₁₁| waveform compared for 110cm depth in pipeline



Appendix B.7: $|S_{11}|$ waveform compared for 120cm depth in pipeline



Appendix B.8: $|S_{11}|$ waveform compared for 130cm depth in pipeline